UNIVERSITY OF SOUTHAMPTON
FACULTY OF ENGINEERING AND PHYSICAL SCIENCES
NATIONAL CENTRE FOR ADVANCED TRIBOLOGY

Materials and wear modelling of a cobalt-chromium alloy in self-mated reciprocated sliding

Paul Sebastian George Cross

Thesis for the degree of Doctor of Philosophy
April 2020

Materials and wear modelling of a cobalt-chromium alloy in self-mated reciprocated sliding

Paul Sebastian George Cross

Abstract

Many sliding applications depend upon cobalt-based hard-facing materials, due to their excellent friction and wear properties, where it is not possible to lubricate the mating surfaces. However, wear produced in such systems present a significant health risk and so there is motivation to understand cobalt-based wear to aid the development of cobalt-free alternatives. The focus of this work is to build a mechanistic model of sliding wear for a given cobalt-based hard-facing alloy. The chosen numerical approach was informed by a series of delineating simple reciprocated sliding wear tests, in accordance with Rolls-Royce research aims, as a stepping stone to more complex environments.

Wear testing of a cobalt-based hard-facing alloy, Stellite 6^{TM}, was performed under self-mated reciprocating dry room-temperature conditions. The wear-rate as a function of load was not constant, suggesting a different model of wear than typical linear models of wear. Probing the debrWis morphology, surface topography, and subsurface behaviour of the alloy revealed plate-like particle formation and separation via subsurface material rupture. Unique to this thesis, the sliding wear behaviour for the load range of 400 N to 1000 N was interpreted as belonging to a ratcheting-type wear mechanism.

A multiscale model of sliding wear was developed as part of this project. This model incorporates a modified microscale ratcheting wear subroutine into a standard finite element model of sliding wear via statistical homogenisation. This approach is a novel extension to the typical numerical models of sliding wear, and allows the user to see how macroscopic wear is affected as the result of material properties, evolution of surface roughness, or microscale imperfections. The model predicts the correct scale of wear, close to a wear-rate of $1 \times 10^{-14}\ m^3/Nm$. Presently this model only accounts for the purely mechanical aspect of wear, but may be adapted for use in synergetic tribocorrosion models to better understand how Stellite 6^{TM} behaves in a nuclear environment.

Contents

List of Figures

List of Tables

List of Abbreviations

BSI	Back-scattered imaging
COF	Coefficient of friction
COMSOL	COMSOL 5.3a Multiphysics
EDX	Energy dispersive x-ray spectroscopy
FCC	Face-centered cubic
FEA	Finite element analysis
FEM	Finite element method
HCP	Hexagonally close packed
HIP	Hot-Isostatically Pressed
HV	Vickers hardness
MATLAB	MATLAB 2016b
MML	Mixed mechanical layer
OM	optical microscopy
PDF	Probability density function
PWR	Pressurised water reactor
RT	Room Temperature
RR	Rolls-Royce
RVE	Representative volume element
SEI	Secondary electron imaging
SEM	Scanning electron microscopy
SFE	Stacking fault energy
SIT	Strain induced transformation
STF	Strain-to-failure

TEM	Transmission electron microscopy
TIG	Tungsten inert gas
UTS	Ultimate tensile strength
XRD	X-ray diffraction

Nomenclature

A	Amplitude
A_c	Asperity number per unit area
A_p	Projected area
A_r	Real area of contact
b	Contact width
b_H	Hardening rate
c	Strain-per-cycle
C	Back-stress constant
C_0	Corrosive wear
d	Separation
d_g	Hall-Petch grain diameter
dF	Microscale normal load
E	Young's Modulus
E^*	Reduced Young's Modulus
f	Friction force
F	Macroscale normal load
h	Frictional heat
H	Hardness
H_V	Saturation stress
k	Shear strength
k_T	Thermal conductivity
k_w	Wear coefficient
k_{eff}	Effective shear strength

k_g	Hall-Petch material constant
K_w	Dimensionless wear coefficient
K	Ludwik hardening constant
L	Contact length
N_{max}	Maximum load
n	Load step
n_H	Ludwik hardening constant
N	Cycles
m	Hardness factor
p	Pressure
p_r	Ratcheting threshold
p_s	Shakedown pressure
Pe	Peclet number
R	Mean asperity radius
s	Sliding distance
s_{ij}	Stress deviator
S'	Synergistic wear term
t	Time
T	Total wear
v	Velocity
W_v	Wear volume
W_d	Wear depth
W_0	Mechanical wear
z	Depth
α	Heat partition fraction
δ	Contact penetration
η	Deformed angle

ε	Total strain
$\varepsilon_p l$	Plastic strain
γ_c	Critical strain to failure
γ_r	Strain due to ratcheting
γ_b	Back-stress constant
$\gamma, \gamma_x y$	Shear strain
κ	Thermal diffusivity
μ	Coefficient of friction
ϕ	Asperity height distribution
ψ	Plasticity index
ψ_s	Plasticity index for dry sliding
σ	Mean asperity height
σ_b	Back stress
$\sigma_1, \sigma_2, \sigma_3$	Principle stresses
$\sigma_x y, \tau_x y$	Shear stress
σ_0	Initial yield strength
σ_Y	Yield stress
θ	Undeformed angle

Declaration of Authorship

I, **Paul Sebastian George Cross**, declare that this thesis, titled **"Materials and wear modelling of a cobalt-chromium alloy in self-mated reciprocated sliding"**, and the work presented in it is my own and has been generated by me as the result of my own original research.

I confirm that:

1. This work is done wholly while in candidature for a research degree at this University;
2. Where any part of this thesis has previously been submitted for a degree or any other qualification at this University or any other institution, this has been clearly stated;
3. Where I have consulted the published work of others, this is always clearly attributed;
4. Where I have quoted from the work of others, the source is always given. With the exception of such quotations, this thesis is entirely my own work;
5. I have acknowledged all main sources of help;
6. Where the thesis is based on work done by myself jointly with others, I have made clear exactly what was done by others and what I have contributed myself;
7. Parts of this work have been published as:

Journal Publications:

- [1] P.S.G. Cross, G. Limbert, D. Stewart, and R.J.K. Wood, Ratcheting wear of a cobalt-chromium alloy during reciprocated self-mated dry sliding. *Wear*, **426-427**: p.1142-1151 (2019).
- [2] P.S.G. Cross, G. Limbert, D. Stewart, and R.J.K. Wood, Extraction of material properties for a cobalt-chromium alloy using inverse analysis. Submitted to: *International Journal of Solids and Structures*

- [3] P.S.G. Cross, G. Limbert, D. Stewart, and R.J.K. Wood, A finite element model of wear for materials undergoing ratcheting deformation. Submitted to: *Wear*

Conference presentations:

- P.S.G. Cross, G. Limbert, D. Stewart, and R.J.K. Wood, Ratcheting wear of a cobalt-chromium alloy during reciprocated self-mated dry sliding. Presented at:
  - 22nd International Conference on Wear of Materials, Miami, Florida, USA, 30th April 2019.
- P.S.G. Cross, G. Limbert, D. Stewart, and R.J.K. Wood, An investigation into the effects of load and velocity on the dry sliding wear properties of a cobalt-chromium alloy. Presented at:
  - NORDTRIB 2018, Uppsala, Sweden, 18th-21st June 2018.

Signed: Date:

Paul Sebastian George Cross

Acknowledgements

Firstly, I would like to thank my supervisors, Professor Robert Wood and Dr Georges Limbert for their continued guidance and support throughout this project. I thank you both for the opportunity and the experience.

Secondly, I would like to thank Dr David Stewart for his sponsorship, through which the funding of Rolls-Royce allowed this project to manifest.

I would like to thank Professor Tomas Polcar and Professor Ling Wang, who, as my internal examiners, provided important and necessary feedback. Likewise, thank you to Professor Daniele Dini who accepted the role of external examiner.

I would also like to thank Dr Terry Harvey for his training on the lab equipment, support within and outside the project, and for indulging me in conversations about the project. Likewise, Dr Shuncai Wang and Dr Mark Light for their respective SEM and XRD training. Dr Richard Cook also has my thanks for setting up and performing the sheer amount of nano-indentation requests for which I am hugely grateful. I also thank Barry Burdett for his advice with regards to the available literature and the preparation of samples.

I would also like to thank Sue Berger and Katherine Day for their formidable administration skills, and thank you Dr Andrew Chipperfield for providing advice and support when I was unable to see the way forward.

Before last, I would like to thank my friends and colleagues for supporting me through this PhD. Though I cannot name all of you, I would like to thank, in no particular order: Alvaro Sanchez; Michael Giles; Dina Ma; Stephen Herd; Aleksander Marek; Angelos Evangelou; Alex Richardson; Charles Burson-Thomas; Sari Octaviani; Joshua Steer; Timothy Kamps; Behrad Mahmoodi; Luis Pena. And of course, thank you to all my friends from back home and overseas.

And finally, I cannot forget my family nor Satja for supporting me, not just through

the PhD, but throughout all my ups and downs. Without you, I would not be the person I am today.

Chapter 1
Introduction

1.1 Problem statement

Much of the world's energy is dependant upon nuclear reactors. In particular, pressurised water reactors (PWRs) generate energy by heating a primary coolant (lithium-doped de-ionised water), whereupon this heat is transferred from its primary circuit to a secondary circuit. The primary circuit is pressurised to ∼150 bar which prevents the 300°C water from boiling, however the secondary circuit is not pressurised, thus allowing the water to boil resulting in steam, which is used to turn turbines for energy generation, as shown in Figure 1.1.

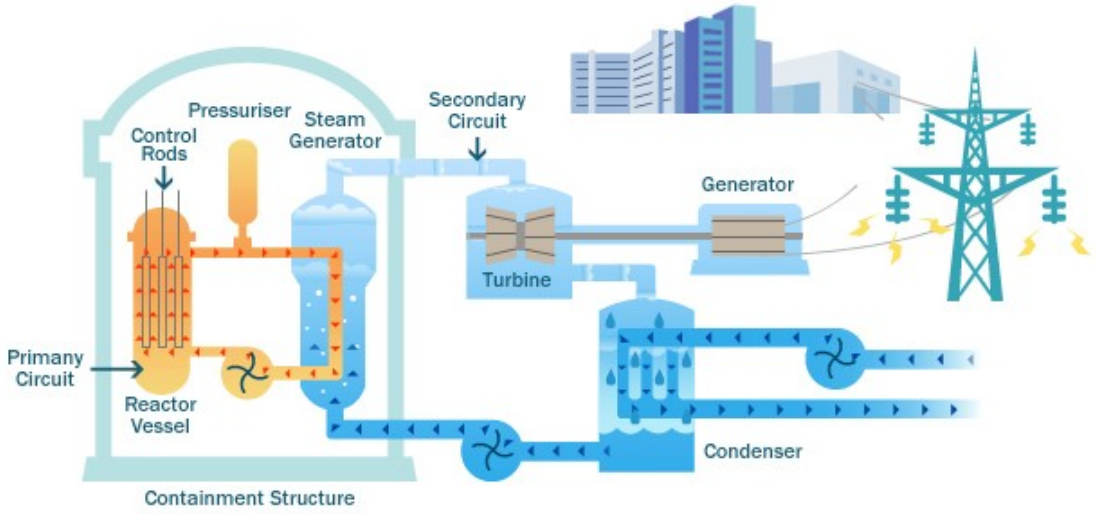

Figure 1.1: A schematic showing the operation of a PWR, taken from [4].

The environmental conditions of the PWR are one of a corrosive, radioactive, and high temperature aqueous environment. The water is doped with lithium to reduce radiolysis of the water from ionising radiation [5, 6], and materials typically sit within regions where water flow is often turbulent [7]. Furthermore, the PWR environment is also mechanically complex. In particular valves and control rods, when actuated, experience mated sliding contact, typically reciprocating, leading to wear [8]. Finally, vibrations resulting the turbulent flow and moving parts leads to fretting of mechanical parts, particularly the control rod guides [9, 10]. These extreme, highly complex,

conditions then require highly reliable low friction and low wearing materials that can perform in this environment, as failure to any of the operating components is not only dangerous, but potentially catastrophic.

A class of cobalt-chromium alloys, called Stellites™, are known to be performant in such extreme conditions, and are consequently of interest to Rolls-Royce Nuclear. These metals are known to be both heat, corrosion, and wear-resistant [11], and are unlikely to experience galling — a severe form of adhesive wear — under the load conditions experienced within a reactor. However, wear generated between two components in mutual sliding contact is an inevitable process and any cobalt wear particles generated are ejected into the primary coolant water. Here they pass through high neutron flux regions of the reactor, where they activate to the potent radioactive gamma emitter of Cobalt-60 with an approximate half-life of 5.27 years. This wear deposits onto parts of the reactor circuitry, where the resulting radiation fields present a dosage risk to plant workers performing routine maintenance [12], as summarised in Figure 1.2.

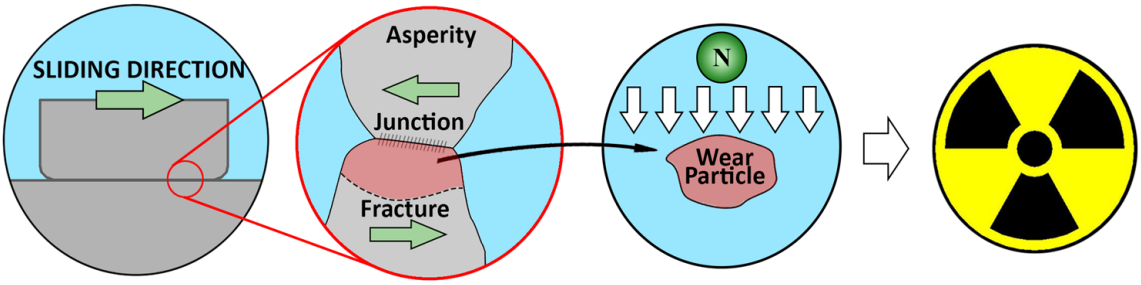

Figure 1.2: A schematic showing how macroscale geometry produces wear particles during sliding due to surface roughness interactions, which then pass through high neutron flux regions that activate to become a dangerous cobalt-60 gamma emitter.

Given the health risks of Stellites™, there is motivation from Rolls-Royce Nuclear to eliminate cobalt with the development of cobalt-free alternatives [13, 14, 15, 16]. This desire to understand Stellites™ in recent years is reflected in the quantity of sliding wear research, shown in Figure 1.3, though a majority of this work has been experimental with little focus on modelling [17]. However, a suitable cobalt-free alternative is yet to be established. Instead, Rolls-Royce initially suggested encapsulating Stellite™ components with thin-film ceramic coatings to reduce cobalt wear loss, as studies showed promise in this area [18]. However, it emerged that little understanding of the material properties, and physics behind the wear performance, of Stellites™ existed. It was agreed that an understanding of the mechanical sliding wear performance, in a simplistic dry environments, was a necessary path to developing a model

to predict the wear performance of this alloy in more complex environments.

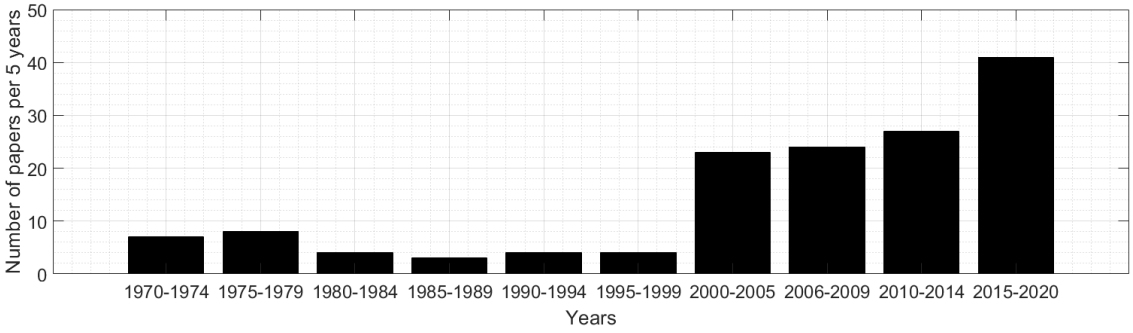

Figure 1.3: Quantity of research papers every 5 years involving the dry sliding Stellites™ since the 1970s, from Scopus [17]. Keywords used: *Wear, Sliding and Stellite*. Out of these papers, a total of 6 papers concerning the modelling of Stellite™ were published over a period of 2005 to 2015, in contrast to 10 for nuclear.

Thus, the aim of this thesis is to build an understanding of the purely mechanical dry sliding of Stellites™, through a combination of systematic wear testing and computational modelling. As many wear mechanisms can operate on Stellite at once, it would be useful to build a *degredation* model of wear capable of capturing the influence of different wear mechanisms throughout the components lifetime. In conjunction with the research aims of Rolls-Royce, the material of interest was a Stellite™ 6 alloy in a hot isostatically pressed (HIPed) form, as it had been shown that this processing method resulted in improved corrosion and wear resistance [19, 20]. Previous research work focused on welded, cast, or laser-clad forms of the alloy. The focus was placed on situations where a Stellite™ 6 component came into periodic sliding contact with other Stellite™ 6 components (like-on-like sliding).

1.2 Project aims and objectives

As a starting point, it was decided that developing a model to predict the dry room temperature sliding wear behaviour of HIPed Stellite™ 6 was a necessary stepping stone to modelling a more complex water lubricated sliding case. While unlike the in-service environment, the model would act as a basis to subsequent models incorporating the PWR behaviour — particularly because tribocorrosion occurs within the PWR [21] — and wear-corrosion models require knowledge of both purely mechanical wear and corrosive wear [22]. The thesis objectives are therefore:

1. **Gain a better understanding of the physics behind the dry sliding wear behaviour of HIPed Stellite™ 6.**

2. **Build a model to predict the purely mechanical dry sliding wear performance of HIPed Stellite™ 6.**

First, to develop an understanding of the dry sliding wear behaviour of HIPed Stellite™ 6, a systematic series of reciprocating flat-on-flat wear tests were performed, and a unique interpretation of a dominant wear mechanism, known as ratcheting wear, was established. The geometry, loads, and sliding speed were chosen to replicate in-service conditions. These tests were conducted in order to determine the influence of the tribological test parameters on the wear mechanisms of Stellite™. Above loads of 400 N, the dominant wear mechanism of ratcheting was observed, while around 40 N mostly oxidative mechanisms were observed.
Upon establishing the existence of ratcheting wear, a numerical model known as the Franklin-Kapoor model of ratcheting wear [23] was chosen to model Stellite™ 6, due to its success in modelling rail steels. Such a model required knowledge of the constitutive behaviour of Stellite™ 6, so standard materials testing had to be performed. Additionally, only simplistic geometries, i.e. cylindrical or spherical, could be model. The previous tribological testing also revealed a dependency on the heterogeneous microstructure. Therefore, several studies were conducted as to apply and extend the Franklin-Kapoor model for Stellites™:

1. **Standard materials testing was performed to determine the stress-strain response of Stellite™ under both tension and cyclic tension-compression.**

2. **Using a finite element simulation of the microstructure, and the materials testing, the material properties of the individual metallic phases were extracted.**

3. **An asperity-level model of Stellite™ 6 ratcheting wear, with and without microscale heterogeneity, was developed.**

4. **A numerical multi-scale incremental wear model, using the previous analysis as a subroutine and a statistical model of rough contact, was developed to compare wear-rates to laboratory tests.**

The benefits of this approach allow for a purely mechanistic, i.e. determined by the evolution of material properties and surface roughness, determination of wear-rates. The clear physical interpretation behind wear allows for the addition of heating effects, as present in a PWR, on the wear prediction of Stellite™ 6, which is a benefit afforded

over other models of wear. As such, this thesis accounts for the purely mechanical aspect of wear, present in tribocorrosion [22].
This project has been funded by Rolls-Royce Nuclear, with travel costs covered in-part by the ESPRC.

1.3 Structure of this thesis

To ensure clarity, each chapter in the thesis has the following format:

- A brief introduction to the chapter.
- The objectives of the chapter.
- The main body of the chapter.
- Conclusions of the chapter.

This thesis is separated into three sections, shown in Figure 1.4. Primarily: chapters 2 through 4 consist of the literature review, 5 through 6 the experimental work, and 6 through 9 the modelling work.
Chapter 1 presents an introduction to the thesis. It gives a problem statement and the motivation for the work behind this thesis. Directions towards achieving the goal set out by the problem statement are given as the project aims and objectives. Finally, the structure of the thesis is given.
Chapter 2 gives an overview of the literature concerning the crystallographic structure of cobalt-chromium alloys as well as relevant concepts necessary to understand how these alloys behave. In particular, as stress is an undeniably important aspect in wear, the physics behind the strain-induced transformations of cobalt are also given.
Chapter 3 focuses on the performance of Stellite™ 6, and other alloys of the cobalt-chromium alloy, when subjected to tribological situations. This chapter seeks to clarify the state-of-the-art understanding on Stellite™ 6 sliding wear. Focus is given to how different processing routes change the microstructure of the alloy, as this has implications on the tribological performance of the alloy. The frictional response of these alloys is also briefly discussed.
Chapter 4 reviews the literature regarding wear, contact, and materials modelling relevant to the project aims. In particular this section covers the Archard wear model and whether or not it is expectable for the problem at hand. Furthermore, statistical models of contact, models of metallic wear, and material modelling approaches are

reviewed as these are necessary in understanding the wear performance of Stellite™ 6.

Chapter 5 gives a broad overview of the testing and numerical methodologies used throughout the thesis.

Chapter 6 details the experimental test matrix of the tribological tests, and discusses the post-wear results of the dry reciprocated tests. A new interpretation — known as ratcheting wear — of Stellite™ 6 sliding wear is given. Primarily, microstructural heterogeneity such as subsurface voids and carbides appear to control this ratcheting mechanism. A numerical model of ratcheting wear, known as the Franklin-Kapoor model, capable of modelling wear when one knows the constitutive response of the alloy, is highlighted. In order to model Stellite™ 6 sliding wear, this thesis will address 3 limitations with the Franklin-Kapoor model: incorporation of microscale heterogeneity, determining rgw strain-per-cycle induced by the mutual sliding contact of asperities, and a multi-scale approach to observe how ratcheting wear produces the macroscale wear as seen within a laboratory environment.

Chapter 7 addresses the first limitation of the Franklin-Kapoor model. The ratcheting model requires knowledge of the full constitutive response of the alloy under strain, and so standard testing is performed to identify an appropriate hardening law for Stellite™ 6. Furthermore, to incorporate microscale heterogeneity, one must know the mechanics of each metallic phase. A finite element model of the microstructure, known as a representative volume element, is created. This model then simulates the standard uniaxial tension test, and is compared to an equivalent experiment conducted as a part of this thesis. By minimising the least squares difference between the simulated and experimental curves, it is possible to extract material properties for an individual phase thus allowing one to simulate microscale heterogeneity. To date, no such analysis has been conducted for Stellite™ 6

Chapter 8 compares the ratcheting wear of Stellite™ at the microscale with and without a subsurface imperfection, using the results of the previous section. Of interest is the void morphology, as prior to this thesis, the influence of imperfections on the wear-rate was unknown. Particularly, voids may be circular or 'diamond-like' in appearance. In addition to the comparison, the Franklin-Kapoor model relies on a simplified strain analysis to determine the strain-per-cycle. In an effort to address this, a finite element model of a sliding asperity incorporating plasticity is developed and the difficulties in its construction and execution are discussed. To compare microscale ratcheting to macroscale lab results, a multi-scale model of sliding wear is then built. The Franklin-Kapoor model is incorporated as a subroutine, with and

without microscale heterogeneity, using a statistical model of rough contact. This approach replaces the old method of using the Archard wear equation, and has the benefit of allowing one to see how wear is controlled by changes in material properties or microstructure.

Finally, **Chapter 9** gives the conclusions to the thesis and the potential avenues of future work as a result of the methods employed within this thesis.

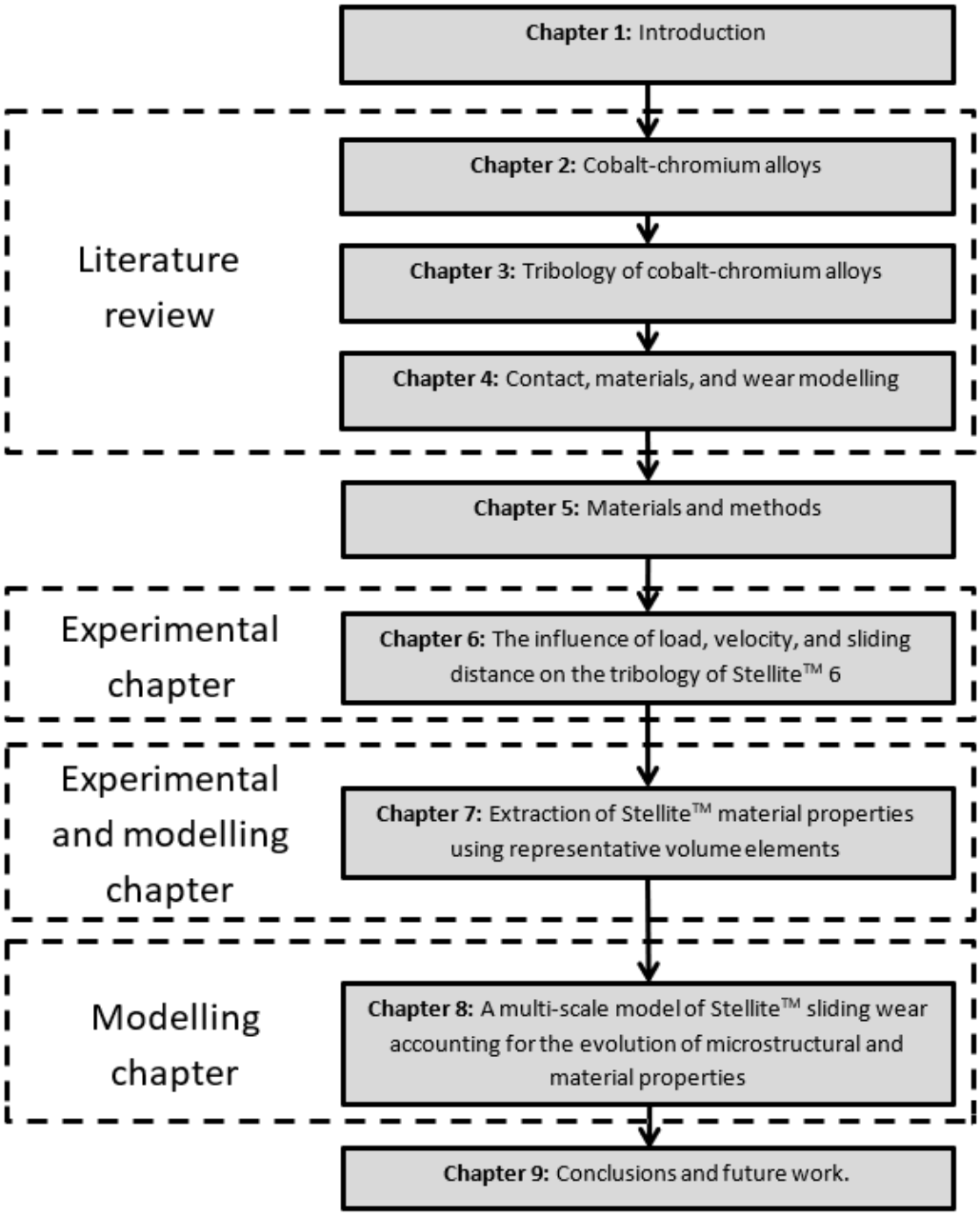

Figure 1.4: A overview of the thesis structure.

Chapter 2
Cobalt-chromium alloys

2.1 Introduction

The crystal structure of cobalt, its family of alloys, and response to external stresses is important in understanding whence these alloys gain their beneficial frictional and wear responses in dry sliding. This chapter gives a brief overview of the crystal structure of cobalt, the theory necessary to understand these transformations, the material phases common in cobalt-chromium alloys, and the mechanical response of the crystal structure when subjected to external stresses.

2.2 Objectives

- Review the basic crystallographic mechanics relevant to cobalt.
- Determine the crystal structures of cobalt.
- Understand how this crystal structure transforms when subjected to external stresses.
- Give an overview of the crystallographic phases present in cobalt-chromium alloys.
- Understand how introduction of new phases alters the transformation properties of cobalt.

2.3 Crystal plasticity

It is important going forward to understand the basic mechanics of dislocation movement, so a brief review is given here.
Dislocations are imperfections in a given crystal lattice of a material [24], as shown in Figure 2.1. Of interest in this thesis are the line dislocations: the 'edge' and 'screw' dislocations. These defects are referred to as such because they propagate as a line,

known as a slip-line, through a given crystallographic 'slip' plane. Associated with the dislocation is the Burgers vector, $\vec{b}$, which is a measurement of how much the crystal deviates from perfection due to the presence of a dislocation.
An edge dislocation, as shown in Figure 2.1(b), can be thought of as an additional planes of atoms introduced into a material when compared to the planes of a perfect crystal in Figure 2.1(a). When subjected to stress, these additional planes of atoms aid the shearing of atomic planes by propagating the defect through the material, until the edge of the crystal structure is reached. Propagation of this defect results in a much lower shear-strength of the material than otherwise expected. The direction in which the dislocation propagates is known as the *slip direction*, and the planes on which the slip occurs are known as the *slip-plane*.

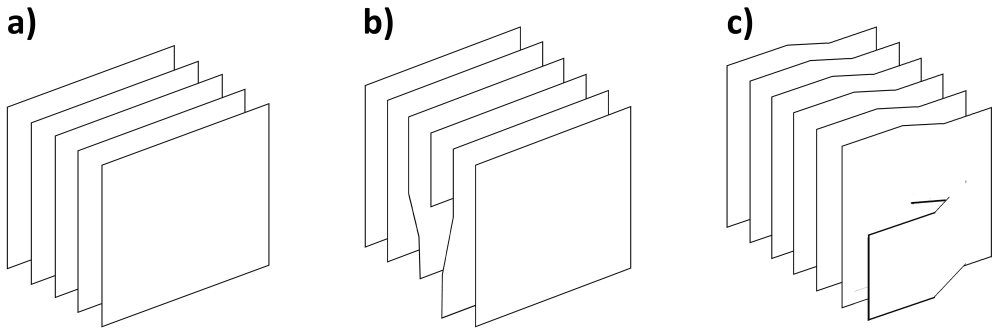

Figure 2.1: A diagram showing (a) planes of atoms in a perfect crystal, (b) planes of atoms with an 'edge dislocation' defect, and (c) a screw dislocation where atoms spiral around a slip-line.

A screw dislocations, shown in Figure2.1(c), can be thought of as atoms tracing a helical path around the slip line. Screw dislocations are important as they can lead to a phenomena known as cross-slip [25], as shown in Figure 2.2. This type of movement can aid further plastic deformation, as the dislocation can move out of a plane where movement is difficult, and so is unfavourable as they may compromise material strength. Importantly, the screw dislocation may only be able to move out of plane if it is possible to propagate along an oblique plane than has the same Burgers vector [24].
All dislocations have an energy associated with them, which is known to be proportional with the Burgers Vector, $\vec{b}$. Importantly, the Burgers vector helps explain what happens when dislocations meet. If the Burgers vector of one dislocation is equal and opposite to another, then the dislocations will annihilate and vanish from the material when they meet. Otherwise, they will repel. Thus, some dislocations, along with other defects, may act as obstacles and prevent further dislocation movement. This

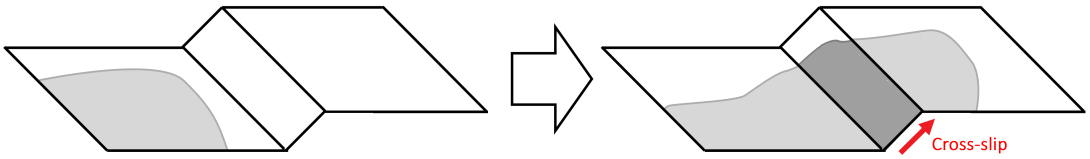

Figure 2.2: A schematic showing how a screw dislocation, as shown by the grey surface, can propagate and move along an oblique plane to a new plane.

property of crystals is important, as it explains the work-hardening of cobalt-based systems.

The schematic in Figure 2.3 shows how the propagation of edge and screw dislocations, within a respective slip plane, through a material can lead to a new deformation state when subjected to stress.

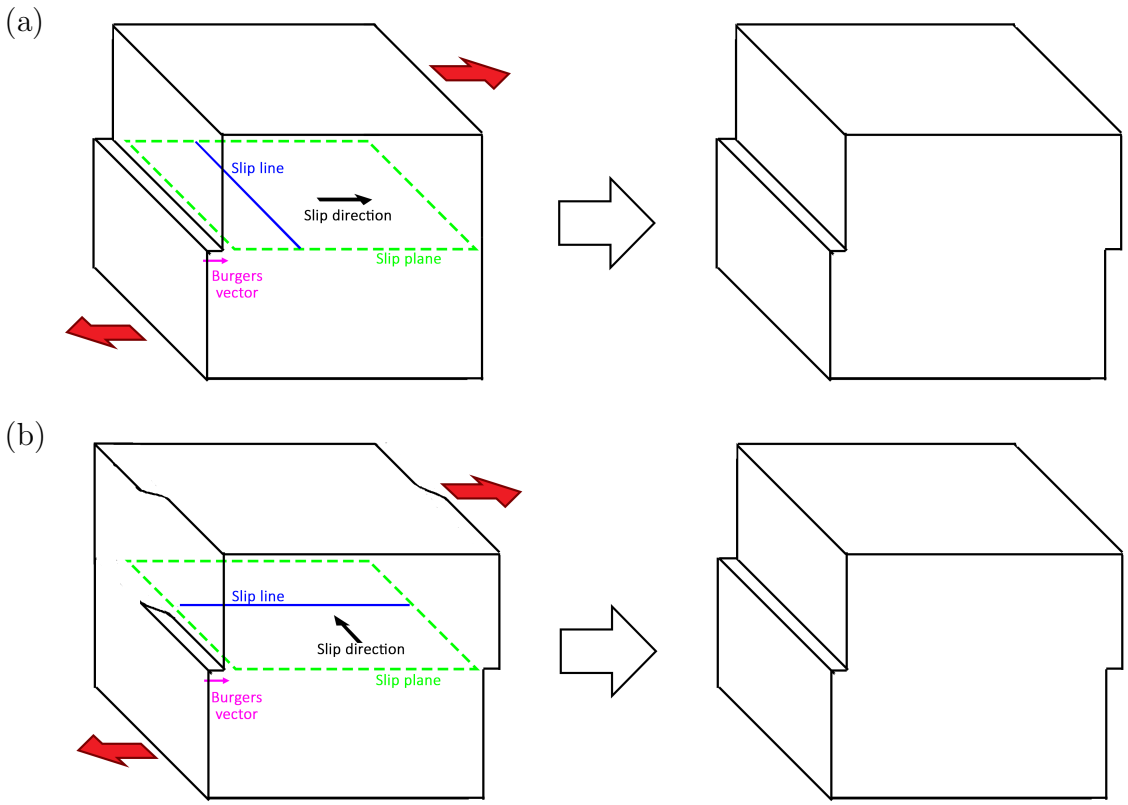

Figure 2.3: A schematic showing how, under shear stress shown by the red arrows, an (a) edge dislocation and (b) screw dislocation propagate through the material to a new permanently deformed state.

2.4 Crystal structure of cobalt

Understanding the crystal structure of cobalt is important in comprehending the structure of cobalt-chromium alloys and their transformation responses when subjected to mechanical stress. These transformations are important in understanding the sliding wear response of its alloys, where stress is active at the wear interface.
The crystal structure of cobalt is hexagonally close-packed (HCP) [26] at room temperature. The unit cell of this crystal can be seen in the left-hand of Figure 2.4. This crystal structure is known to be relatively resistance to plastic deformation (hard) when compared to other crystal structures, such as face-centred cubic (FCC) as shown on the right of Figure 2.4. The reason for this is due to cobalt only having 3 slip systems, when compared to the 12 of FCC. A slip system, simply put, are the planes and directions through which dislocations may move. These systems are typically constrained to crystal planes with the highest atomic density. Slip directions occur along the densest lines of atoms.

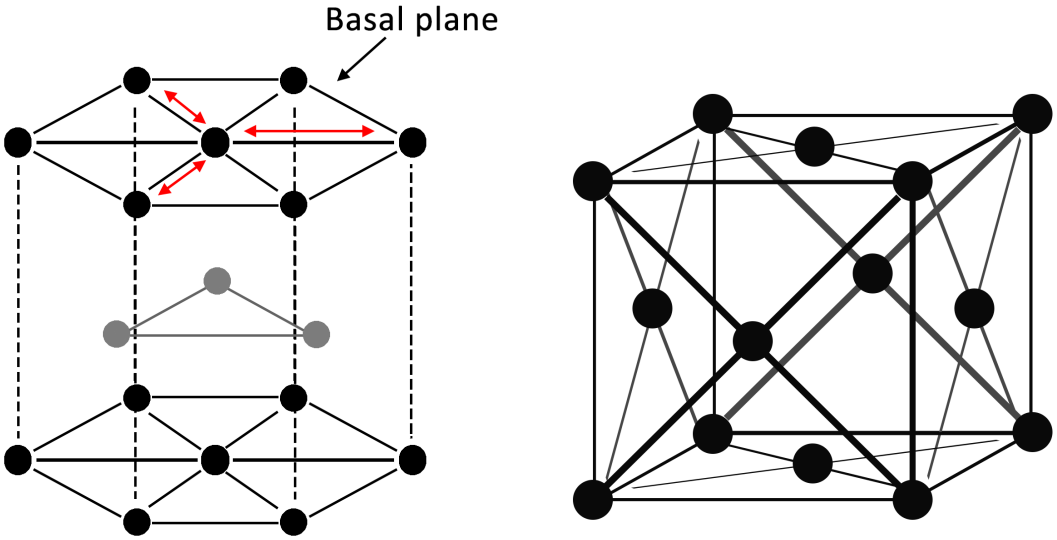

Figure 2.4: A schematic showing (left) the unit cell for a hexagonally close-packed structure. The red arrows correspond to the slip directions on the basal plane. Right) the unit cell of the FCC structure.

For cobalt, this slip system occurs on the basal plane as shown in Figure 2.4. As a result of the restricted movement for dislocation slip in the HCP crystal, when compared to the FCC crystal, then it is less easy for cobalt to deform plastically thus resulting in a higher hardness. However, if cobalt is heated sufficiently high, transformation from the HCP phase into a FCC phase can occur wherein plastic

deformation of the material becomes favoured [27].

2.5 Strain induced transformations in cobalt

When cobalt is subjected to mechanical stress, several transformations can occur in the crystal structure leading to changes in material properties. These alterations can have implications on the sliding wear and friction performance of cobalt alloys.
Two strain-induced transformations of importance in cobalt are deformation twinning and martensitic transformations, both of which are summarised in Figure 2.5. Twinning deformations occur when atoms move relative to other atoms within their plane; intermediate atoms are then sheared in the 'twinning' direction as to form a mirror image of the original atomic structure about the 'twinning plane', with well-defined boundaries between the two [28]. Martensitic transformations can occur within the FCC crystal when dislocation slip occurs. Essentially, planes of atoms shift from the FCC stacking order into an energetically favourable HCP order. This is known as a martensitic transformation [28].

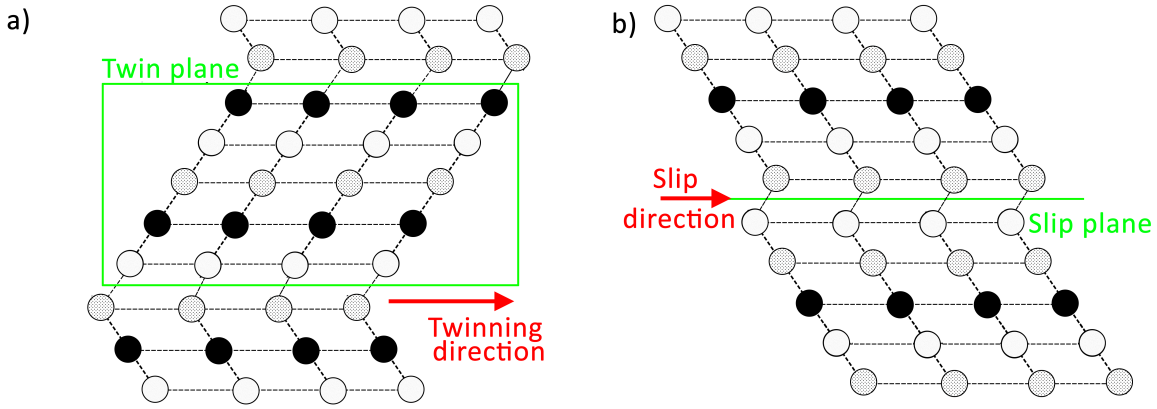

Figure 2.5: Schematic showing the two primary transformations that occur for cobalt. a) demonstrates twinning which occurs when part of the crystals shears relative to itself. b) A schematic showing how an entire plane of atoms has slipped through the crystal as to form a new stacking order.

Wu et al. [29] subjected polycrystalline cobalt with a mixture of FCC and HCP phases to mechanical surface attrition using shot-peening. They observed 3 transformations, with the aid of transmission electron microscopy (TEM), in the cobalt structure: deformation twinning, slip along the HCP basal plane, and grain refinement by sub-division of grain boundaries leading to the formation of nano-crystals. For the HCP phase, the dominant mechanism grain refinement was said to occur as the result

of dislocation slip. Martensite formed intra-granular boundaries and resulted in the formation of extremely fine nano-grains. Likewise, for the FCC phase twinning deformation dominated with a martensitic transformation occurring at higher strains. HCP crystals developed in the FCC phase and contributed to the grain refinement.
In understanding the work hardening of certain materials, it is necessary to understand the Hall-Petch effect. This simply states that the yield stress, and thus hardness, increases with a decrease in the average grain-size of the material [30, 31]. This particular phenomena is described by the equation:

$$\sigma_Y = \sigma_0 + \frac{k_g}{\sqrt{d_g}} \tag{2.1}$$

where d_g is the average grain diameter, k is some constant relating to the given material, and σ_0 is the initial yield strength of the material. The physics behind why grain refinement results in an increase in hardness is simple; intra-granular dislocations pile up at grain boundaries as they cannot overcome the energy potential at the grain boundary. Therefore, in order to plastically deform the material, more stress is needed to generate more dislocations, such that the total energy of the piled up dislocations is enough to overcome the inter-granular potential. If the grains refine too much, however, then it becomes impossible to generate enough dislocations within the grains to overcome the boundary energy and instead deformation continues as the result of creep or other plasticity mechanisms [32].

2.6 Crystal structure of cobalt-chromium alloys

In conjunction with the research aims of Rolls-Royce, a particular class of cobalt-chromium alloys called Stellites™ are of interest. This section will briefly overview the crystal structure of these cobalt-chromium alloys as it is important for understanding their friction and wear behaviours, as well as interpreting relevant x-ray characterisation data of the chosen material.
The typical phase diagram for a cobalt-chromium alloy is shown in Figure 2.6. The region of this phase diagram, of interest to Rolls-Royce, is around 30% chromium. As the melting temperature is brought down, the alloy solution begins to solidify into different crystalline structures as to minimise the free energy. The equilibrium phases of interest in this alloy are an HCP (ϵCo) phase, an FCC (αCo) phase, and an intermetallic phase (σ) [33]. The presence of chromium can be seen to help stabilise an FCC phase [19], as the higher percentage of chromium leads to intermetallic phases.

If carbon is introduced into the alloy system, the FCC phase is stabilised at lower temperatures [19], meaning that Stellites™ exist in a metal-stable FCC structure at room temperature.

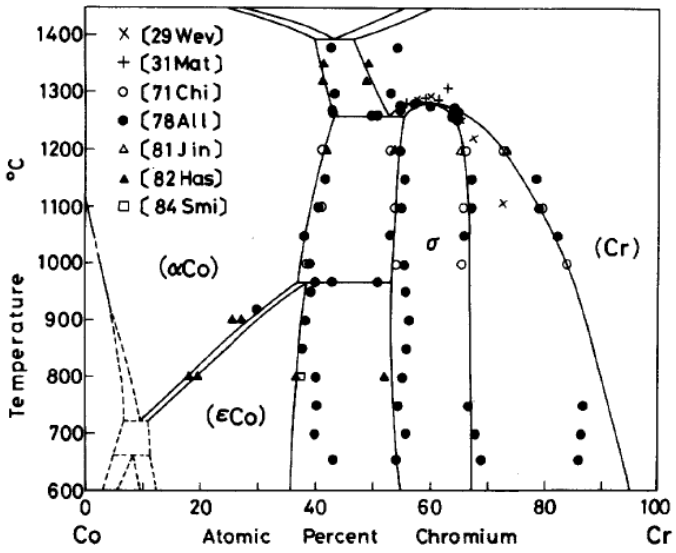

Figure 2.6: Taken from Ishida and Nishizawa [33]. A phase diagram determine for cobalt-chromium alloys with varying percentage of chromium, calculated using Thermo-Calc.

Of particular interest in the wear of cobalt-chromium alloys are the presence of stacking faults [34]. Stacking faults occur when the FCC crystal structure (ABC) is interrupted by a missing plane of atoms [24]. This results in a difference stacking arrangement of the crystal, which is identical to the stacking arrangement of a HCP crystal (ABA). These "errors" in stacking arrangement give stacking faults their name, and are depicted in Figure 2.7.

Associated with stacking faults is the stacking fault energy (SFE). The energy per stacking fault has an inverse relationship to the width of the stacking fault, as a result low SFE materials exhibit wider stacking faults. Stacking faults are important because if they are present they can prevent the cross-slipping of dislocations onto crystallographic planes where dislocation guide is less-prohibited [35]. This simply means that the low SFE reduces slip, thereby prohibiting further plastic deformation. Stellite™ 6 is a particular example of a low SFE alloy. The implications of this on the tribology of Stellite™ 6 is explored in the next chapter.

An important defect, leading to the formation of stacking faults and the FCC to HCP transformation crystals, is the Shockley Partial dislocation [36]. When the total energy, E_{ab}, of a dislocation is greater than the energy sum of two smaller dislocations, E_a and E_b, then it is more energetically favourable to decompose into

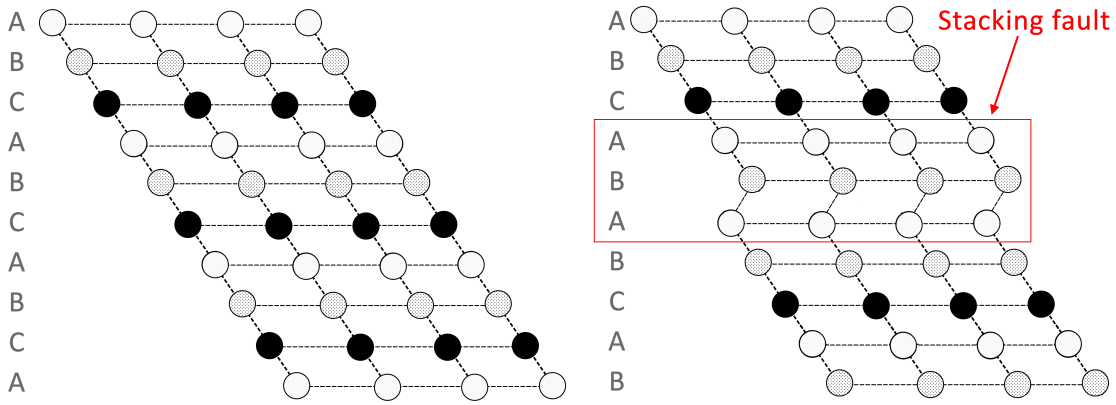

Figure 2.7: A diagram showing how stacking faults are an interruption in the stacking order of FCC materials. Left) the original structure. Right) The structure with a stacking fault. Importantly, this order is the same as that for the martensitic transformation.

the smaller dislocations. Simply put:

$$E_{ab} > E_a + E_b \tag{2.2}$$

Thus, when an edge dislocation, propagating in an FCC crystal, is able to decompose into a Shockley partial, then the two dislocations may propagate away from one another leaving an entire plane of free of atoms, as shown in Figure 2.8, thereby creating the HCP stacking order and forming hard martensite within the crystal. The formation of martensite in the crystal can improve the work-hardening of the material, not only due to the fewer slip-systems in HCP, but also because stacking faults can act as obstacles to further dislocation movement [37].

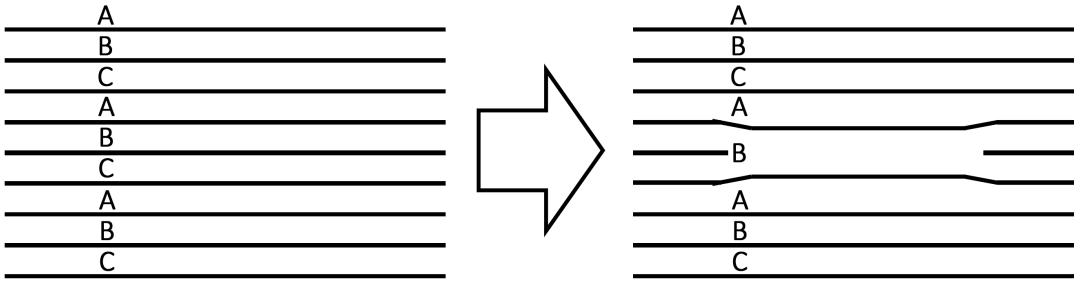

Figure 2.8: A diagram showing how a partial dislocation can leave a missing plane of atoms that results in an interruption of the FCC stacking order.

2.7 Strain-induced transformations in cobalt-chromium alloys

Insight into the deformation behaviour during the wear of Stellites™ can be provided by examining the literature on a variety of cobalt-chromium based alloys undergoing strain. This section briefly overviews the strain-induced microstructural and crystal transformations that can occur for these alloys.

Mani et al. [38] subjected a polycrystalline Co-Cr-Mo alloy to plastic straining and observed a strain-induced transformation from FCC to HCP. This martensitic transformation was promoted at room temperature and gave rise to intra-granular ridges of martensite which increased in density with strain. They showed that the yield behaviour of the alloy was a linear function of the martensite volume fraction. Thus, as more HCP forms within the material, the material becomes harder. The presence of martensite resulting in a harder material reflects the fact that fewer slip systems are active in HCP when compared to FCC, 3 versus 12 respectively, and thus leads to more restricted dislocation movement and therefore plasticity deformation. The presence of HCP also prevents further slip within the FCC phase, as boundaries between FCC and HCP within the same crystal experience dislocation pile-up, therefore creating a higher energy barrier to the movement of dislocations through the FCC material resulting in the pinning down dislocation movement [37].

Knezevic et al. [39] performed mechanical testing on polycrystalline Haynes 25. Haynes 25 is interesting given its similar composition to Stellite™ alloys, with the exception of a much reduced carbide content, essentially giving insight into matrix-only deformation behaviour. They observed that no deformation twinning occurred within the material and instead only intra-granular stacking faults formed resulting from a martensitic transformation. This tendency for Haynes 25 to transform to a HCP structure was previously found by Tawancy et al. [40].

Huang and Lopez [41] studied the influence of grain size on the HCP to FCC transformation in a cobalt-chromium alloy. In summary, they observed a saturation in HCP volume fraction to 50% for the coarse alloy. Conversely, they saw a 5% saturation in the volume fraction for the finer grained alloy. This suggests that for finer grains, the martensite transformation is suppressed. Importantly, they could not discern a relationship between hardness and grain size except when the grain size became exceptionally small.

In the context of strain-induced transformations as a result of sliding contact for

cobalt-chromium alloys, work by Namus et al. [42] and Kashani et al. [43] can provide some insight. Namus et al. observed the formation of a nano-crystalline layer after sliding under normal loads of 5N to 80N. For 40N to 60N, the nano-crystalline layer was thin and only a couple hundreds of nanometres thick. However, above 40N a transition was observed, whereupon the nano-granular layer became several microns thick (3-5 μm). At these loads, a typical doubling in material hardness was observed. Kashini et al. observed the formation of martensite seemingly independent to the testing temperatures (room temperature to 500°C). Furthermore, they observed alignment of the HCP basal plane to the sliding direction with a resulting reduction in friction force.

If carbon is introduced into the cobalt-chromium system, then the formation of carbides can occur [19]. These 'secondary hard-phases' can result in the depletion of chromium in the metallic matrix. These chromium-poor regions can aid in the formation of stacking faults during strain-induced transformations [44], due to the lack of chromium not stabilising the FCC phase. Furthermore, the carbide-matrix boundary can lead the presence of stress-raisers which further aid the formation of a HCP phase.

2.8 Conclusions

The typical crystal structure of cobalt and its alloys is a combination of FCC and HCP crystalline phases. The primary transformations that these alloys can experience are a combination of mechanical twinning and a martensitic transformation. Some important consequences of these transformations are the formation of intragranular boundaries due to the martensitic FCC to HCP transformation. This type of deformation appears to be ubiquitous for both cobalt and its alloys. In particular, the formation of intragranular boundaries by this deformation mechanism allows for cobalt to form extremely small grain structures known as nano-crystals and appears to be favoured in the case of mechanical attrition at the surface, either by sliding or shot peening. The existence of nano-crystals has been noted as important within the medical industry [45] as being responsible for the formation of a wear-reducing layer and may be considered one of the major reasons for the excellent wear performance of Stellite™ 6. The effect of grain refinement can impact the wear-rate, as the relative hardness of materials is known to influence the steady-state behaviour of the alloy [19]. Models that account for hardness on the wear-rate may then model this effect by relating the Hall-Petch equation [30, 31] to material hardness and alloy wear to grain

size evolution. Thus, the importance of microstructure on the influence of material properties on the wear-rate and its evolution during wear is thus explored in the next section in the context of Stellites™.

Chapter 3
Tribology of Stellite™ 6

3.1 Introduction

The sliding wear and friction response of the cobalt-chromium alloy family, and specifically Stellite™ 6, is complex; the type of wear response depends heavily on the load conditions, environmental conditions, and processing conditions. The aim of this section is therefore to inform the testing procedure by reviewing the current state-of-the-art in wear and friction testing of Stellites™ in dry room temperature environments. From this the test procedure, and consequently the modelling approach, is informed.

3.2 Objectives

- Understand the processing methods used in the production of Stellite™ 6 alloys and their microstructures.
- Determine the typical mechanical properties of these alloys under different processing routes.
- Overview the importance of oxides in the sliding wear response of alloys.
- Review the typical dry frictional response, and the physics governing these responses, for Stellites™.
- Determine the typical wear mechanisms seen in the literature for a variety of test cases and processing routes.
- Establish differences or similarities between HIPed Stellite™ 6 and the other processing methods.

3.3 Stellite™ alloys

This section briefly overviews some of the typical processing routes for Stellite™ and the mechanical consequences of each. Particular focus is given to the HIPing method,

a focus of this thesis.

Stellites™ are a family cobalt-chromium based super alloys. They consists of a variety of elements, but their highest element percentage is cobalt followed by chromium. For instance, Stellite™ 6 has a nominal composition of 25-32% Chromium, 4-6% Tungsten, 0.9-1.4% Carbon, and other elements. However, more than 60% of the alloy is cobalt [46]. It is this composition of Stellites™ that gives them increased temperature, corrosion, and wear resistance [11, 47]. Particularly, Stellite™ 6 is known to perform best in the regimes most suited to PWR operation due to its tungsten and carbon content. The general microstructure of Stellite™ consists of a cobalt-based matrix with different material carbides embedded throughout. The most prevalent carbide is chromium-carbide, however tungsten-carbides can also form. The shape and frequency of carbides depend heavily on the carbon, chromium, and tungsten concentration as well as the manufacturing routes used to produce the Stellite™ alloy, see Figure 3.1. A review into the micro-structural and wear properties of cobalt-based super alloys was done in 1993 by Atamert and Stekly [19]. Further studies seeking to delineate the influence of alloy processing methods on the material and wear properties of cobalt hard-facing alloys have been done by Ahmed et al. [48, 49, 50] over a period of 2009 to 2016. Studies looking into the influence of carbon [51], yttrium [52] and molybdenum content [53] on the wear characteristics of Stellites™ have also been performed. The influence of temperature on the wear-rate and material properties of Stellites™ have also been studied by Kapoor [47] and more recently in 2019 the influence of high temperature aqueous environments on the wear differences between Stellite 6 and 3 have been done by Ratia et al. [54, 98].

3.3.1 Processing methods

The most common processing methods for Stellites™ are casting, laser-welding, and tungsten inert gas (TIG) arc-welding. Casting is the process wherein dissimilar elements are heated to a liquid phase and mixed together to form a molten alloy. This is then poured into a mould, typically sand, where the metal cools to form a solid in the shape of the mould [55]. Laser-cladding is the process whereby a powdered form of an alloy or metal is melted by a laser onto a given substrate where it cools into a solid-form. Likewise, TIGing involves feeding a Stellite™ 6 rod into the an electrical arc generated between a tungsten electrode shielded with an inert gas and the weld surface [56]. For Stellites™, these routes tend to result in large brittle M_7C_3 carbide phases, consisting primarily of chromium or tungsten, with flaws in the microstructure

being common. These hard phases are often tree-like dendrites in form, see Figure 3.1. Typically, laser-cladding results in a finer more uniform microstructure and is known to improve corrosion and wear resistance [57], when compared to casting.

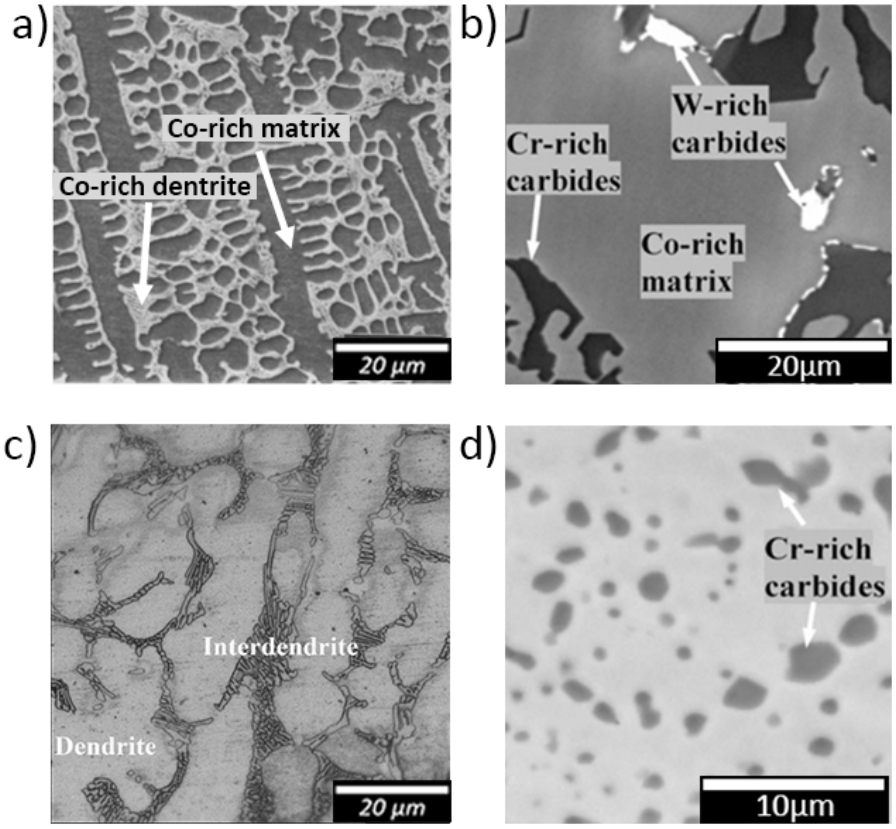

Figure 3.1: A showcase of different Stellite™ 6 microstructures as a consequence of the manufacturing process. a) Laser-clad structure; The dark phase is the cobalt matrix, whereas the lighter dendrite phase is a metallic-carbide structure, taken from [58]. b) cast-formed Stellite™, taken from [48]. c) Tungsten Arc Welded Stellite™ 6, taken from [59]. d) HIPed Stellite™, taken from [48].

Hot isostatic Pressing (HIPing) is a manufacturing process whereby an alloy in powder form is placed into a bespoke container and subjected to high pressures and temperatures [60]. This causes the powder particles to fuse together in a process known as *sintering* into a solid taking the container shape as shown in Figure 3.2. Consequently, as the powder particles are fused together, pores form throughout the alloy. However, the high energy input of the processing method causes most of these voids to seal up and results in fewer pores when compared to other processing routes [20]. Not all the pores can be sealed up, however, resulting from the energy required to seal the pore being inversely proportional to the pore radius [60], suggesting that

as the radius tends to zero that the energy required to seal it tends towards infinity.

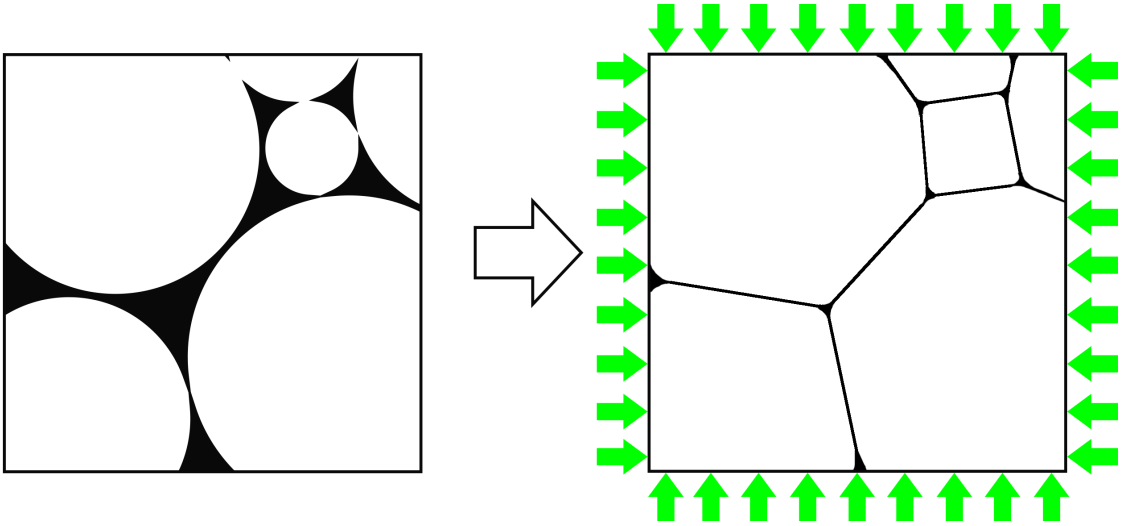

Figure 3.2: A schematic showing the fusing together of powdered particles as the result of a hipping cycle. The green arrows represent pressure applied externally to the container, which would additionally be heated above 1000°C.

Particularly, the HIPing method for Stellite™ has been known to improve the mechanical performance, abrasive, and corrosive resistance of Stellite™ [20]. Tungsten is dissolved into the cobalt-rich matrix which aids mechanical performance [61, 19] and heat resistance [19] up to 450°C. Bonding between matrix and carbide is also improved, in particular the smaller carbide side means that corrosion is less likely to occur in the matrix-carbide boundary, unlike the cast or clad methods [48, 49, 62]. This also results in improved sliding wear resistance, which shall be explained in further detail later. HIPing of Stellite™ alloys is a relatively novel process being explored by Rolls-Royce, hence its focus in this thesis.

Notably, the sizes of carbides is different depending on the chosen processing method, as shown in Figure 3.1. The carbide size can have an important influence on the corrosion behaviour of such alloys. Particularly, near chromium-carbide boundaries there is a depletion in the total chromium content in the metallic matrix [44]. Given the importance of chromium in corrosion resistance [63], these regions are particularly prone to degradation [64]. Typically, the larger the carbides, the larger surface area of corrosion-poor material. The over-all smaller carbides, seen in the HIPing method, give a higher corrosion resistance [62].

3.3.2 Mechanical properties

The general mechanical properties of Stellite™ 6 can be seen in Table 3.1. Through this cursory analysis, it can be seen that the typical hardness and Young's Modulus of Stellite™ 6 are approximately 4.9 GPa and 220 GPa respectively.

Table 3.1: A table of the friction values of Stellite™ sliding against different matings.

Material	Young's Modulus (GPa)	Yield (MPa)	Hardness (GPa)	Strain-to-failure (%)	Ref.
Laser-clad	–	–	4.89–6.47	–	[58]
Laser-clad	–	–	5.8	–	[65]
Laser-clad	–	–	5.08	–	[66]
Cast	–	–	4.08	–	[48]
Cast	209	700	3.8–4.9	1	[46]
HIPed	–	–	4.14	–	[48]
HIPed	237	750	3.8–4.9	3-5	[46]
HIPed	237		5.6	3.6	[61]

Kapoor demonstrated [47] that for Stellites™, wear resistance for higher temperatures was improved for alloys with a higher tungsten content. The reason for this is that tungsten having a high melting point stabilised the solid-phase of the alloy. Carbide size is known to affect the mechanical response of alloys. Ahmed et al. [48] report that HIPed Stellite™ 6 performs slightly better on hardness tests than the cast form at room temperature. The improvement in hardness is attributed primarily to an increase in carbide fraction. The dependency of environmental heating on the hardness and yield of Stellite™ 6 is shown in table 3.2.

Table 3.2: A table of the mechanical response of Stellite™ due to heating, from ref. [47]

Material	Temperature (°C)	Hardness (GPa)	Percent reduction (%)	Ref.
Cast Stellite™ 6	RT	4.1	0	[47]
	300	3.7	9	
	425	3.5	14	
	650	3.4	17	

It is clear from this table that, due to an increase in temperature, the ductility of Stellite™ 6 has increased meaning plastic deformation will occur more easily. While an ambient temperature of 300°C is typical within a PWR, high temperatures may

also be experienced at room temperature as the result of frictional forces heating the contact area during sliding. This occurs as a result of the high pressures and the transient nature of asperity contacts during sliding leading to the generation of flash temperatures [67]. Importantly, these so-called flash temperature have implications regarding the wear performance, as the high temperatures can help drive the necessary chemical reactions local to the asperity and form an oxide layer, which can be wear reducing [68].

The implications of oxide on the wear-rate of a Stellite™ 20 ball sliding against a Haynes 25 disc was explored by McCarron et al. [69]. They found a greater percentage of oxygen present on the ball after sliding with room temperature wear-rates in the range of 1×10^{-4}mm^{2}Nm than compared to the disc which had less oxide formation and a greater volume of wear in spite of the theoretical wear values for the disc being lower than the ball. They concluded that a model capable of incorporating the influence of other variables, such as oxide formation and geometrical changes, on the wear-rate would improve prediction accuracy.

3.4 Oxidational response of alloys

Understanding the oxidational behaviour of alloys, particularly Stellites™, is important if one wishes to understand the wear and friction behaviour of cobalt-chromium alloys across different sliding speeds and loads. In particular, the existence of mechanically mixed layers (MMLs) [70], named as such because they are the result of metallic and oxidative material mixing within the wear interface due to mechanical motion, are well documented for such alloys at high temperatures [71]. Naturally, the formation of oxides plays an important role in the creation of such layers. The existence of these layers can be thought of as self-forming thin-film coatings, which naturally have implications with regards to wear resistance.

When two metals slide against one another, their respective asperities form junctions and experience local heating effects due to frictional heating. While these asperities flatten into plateaus due to the initial running in behaviour, this heat leads to highly local flash temperatures. These temperatures greatly exceed the ambient surface temperatures of the material and become the driving force for the chemical reactions necessary to oxidise the surfaces of the sliding metals [72]. During wear, the result of mechanical attrition due to ploughing from hard asperities, or adhesive effects, will allow for the progressive removal of oxide as it forms [73] with the ability of the oxide to resist attrition depending upon its thickness and adherence to the substrate metal.

However, if these oxides are well adhered and able to grow reasonably thick, then they can protect the surface and lead to wear-rates less than 1×10^{-5}mm^3/Nm [74], deemed 'mild wear'.

Particularly, chromium is known to be prone to oxidation [26]. This leads to the formation of a thin nano-scale surface layer known as a passivating film, which can help prevent further corrosion of the system, and also leads to a reduction in cobalt at the surface for cobalt-chromium alloys [75]. In the case of sliding, due to the introduction of frictional heat, the energy driving the chemical processes necessary to create oxides is much greater leading to thicker oxides[76, 77]. It is commonly thought that these oxides grow to a 'critical thickness', during which they fracture off to form wear debris [78]. However, in studies on steel by So et. al [73], it was revealed if a well-adhered oxidation layer existed on the material, that such a layer would not fracture off as a whole. Rather, only parts of the oxide would spall off due to the progressive cycling of the contact interface, instead suggesting that oxides fail by a fatigue mechanism.

Carbides, if proud enough, may sit above the oxidised layer as to support some degree of the normal load. In particular, Vardavoulias [79] suggested that if the oxide is much more proud than the hard-phase, then it is more likely to fracture off the surface. In the case of non-HIPed processing methods, it may be possible for the carbides to remain more proud than the oxide. However, in the case of HIPed materials, the carbide size (1 μ m to 3 μ m) is much smaller than the typical tribo-oxide thicknesses seen for this alloy [73], meaning it is unlikely that such a phenomena will occur.

3.5 Frictional response of Stellites™ in dry environments

The typical friction response of a variety of Stellites™ under dry conditions can be seen in Table 3.3. Overall, the frictional response of Stellites™ appear to improve with load, dropping from as high as 0.6 to as low as 0.15.

Using transmission electron microscopy (TEM) Persson [83] was able to reveal the mechanism behind the improvement of friction in Stellites™. It was observed that a strain-induced martensitic transformation occurs for Stellite™ when it was subjected to high pressures. The basal planes of the newly formed HCP crystals were strained into positions where their slipping planes aligned parallel with the wearing interface, as shown in Figure 3.3. Furthermore, the active slip direction within this plane turned

Table 3.3: A table of the friction values of Stellite™ sliding against different matings.

Material	Counter face	Temperature (°C)	Load (N)	Velocity (m/s)	Coefficient of Friction	Ref
Laser-clad S6	AISI Steel	RT	40	1	0.52	[65]
			160		0.48	
			40	2	0.46	
			160		0.42	
Laser-clad S6	WC-Co	RT	50	2	0.7± 0.1	[58]
Cast S6					0.5 ± 0.2	
Welded S6	Steel	RT	10	0.025	0.7	[80]
		300			0.4	
Laser-clad S21	Laser-clad S21	RT	500-2000	0.013	0.265 ± 0.115	[81]
Laser-clad S21	Laser-clad S21	RT	500-2000	0.065	0.24-0.20	[82]
Laser-clad S6	Laser-clad S6	RT	500-2000	0.065	0.35-0.30	[83]
Cast S6	WC-Co	RT	25	0.05	0.42	[48]
HIPed S6					0.47	
Laser-clad S6	Laser-clad S6	RT	5000	0.08	0.19	[66]

S6: Stellite™ 6.

to the direction of sliding. With the preferential slip system aligning in the direction of sliding, the wearing interface consumed considerably less energy and resulted in a drop a friction force as low as 0.15% of the total normal force. This same behaviour was observed in Stellite™ 21 [81]. For lower pressures, the severity of this strain induced transformation was much reduced and marked slightly higher friction values. With the slip systems existing along the direction of sliding, then resistance to plastic deformation may be much reduced. It is likely that this easily deformed nano-layer, sitting on top an exceptionally hard martensite matrix, is what leads to the reduction in coefficients of friction with load. The work of Bowden and Tabor [68] showed that, for a sliding system undergoing plastic deformation:

$$\mu = \frac{m}{\sqrt{1 - m^2\alpha_1/\alpha_2}} \tag{3.1}$$

where m is the relative strength between the interface (the easy shear layer) and the bulk (some several micrometers thick martensite), and α are experimental constants. Of further interest is the reduction in adhesion between self-mated cobalt systems, when the HCP crystals align with the sliding direction. Buckley [85] observed for cobalt sliding against itself in a vacuum that the frictional force between them, when compared to other HCP materials with less-ideal packing densities, was at it's lowest and this corresponded to a reduction in adhesion between the mated parts. When the sliding speed increased however, heating at the interface caused a transformation from

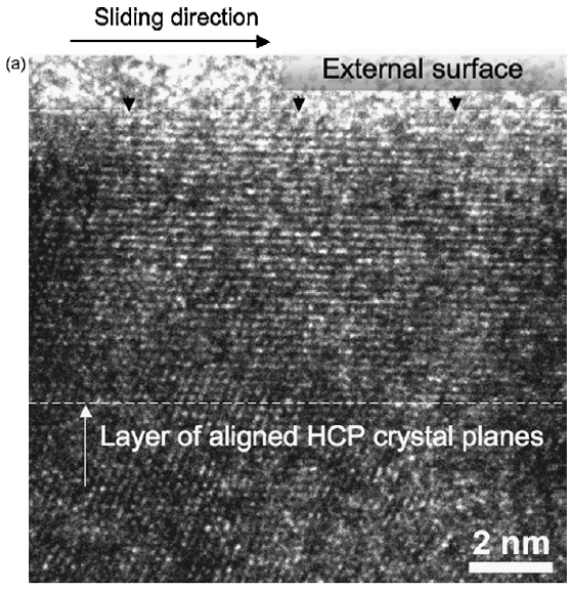

Figure 3.3: A high-resolution TEM image demonstrating the alignment of HCP planes parallel to the sliding surface, taken from Jacobson et al. [84]. Stellite™ 6 was observed to strain harden to depths between 30μm and 150μm, where the 30nm deep surface layer aligned parallel to the surface plane.

HCP back to FCC, which caused the material pair to seize together. This suggests that the natural close packing order of the martensite within cobalt, and its class of alloys, has low adhesion and therefore experiences lower frictional forces.
The importance of the martensitic transformation in Stellites™ cannot be overstated. Bhansali and Miller [34] demonstrated a clear relationship between low SFE alloys and a resistance to galling. Galling is a type of severe adhesive wear during which the friction force between metals greatly exceeds unity and causes seizure between moving parts. For low SFE alloys, such as Stellite™, the strain-induced martensitic transformation is promoted by the already high volume of stacking faults which has been shown to suppress galling, though the mechanisms behind exactly why HCP should prevent galling is unclear.

3.6 Sliding wear of Stellite™ alloys in dry environments

The typical wear values for a variety of Stellite™ alloys in dry environments can be seen in Table 3.4. Generally, the wear of Stellites™ is low and occupies the mild wear regime of 1×10^{-13} to 1×10^{-15} m^3/Nm. A whole range of mechanisms of wear can be

in play at any one time. These included carbide pull-out or fracture, with evidence of abrasion from a hard material in the interface in the form of wear grooves[48]. Oxide also forms on Stellite™ at low loads [65] resulting in lower wear-rates, but was destroyed at higher loads.

Table 3.4: A table of the wear-rates for Stellite™ sliding against different matings.

Material	Counter face	Temperature (°C)	Load (N)	Velocity (m/s)	Distance (m)	Wear-rate (m^3/Nm)	Ref
Cast S6	WC-Co	RT	25	0.10	100	1.60×10^{-14}	[48]
HIPed S6						1.20×10^{-14}	
Cast S6				0.01	500	1.60×10^{-14}	
HIPed S6						2.80×10^{-14}	
HIPed S6	WC-Co			0.01	500	2.80×10^{-14}	[49]
Re-HIPed S6						2.80×10^{-14}	
Laser-clad S6	AISI Steel		40	1.0	10000	$\sim1.50\times10^{-14}$	[73]
			160			$\sim2.50\times10^{-15}$	
			40	2.0	6000	$\sim1.50\times10^{-14}$	
			160			$\sim1.25\times10^{-14}$	
Cast S6	WC-Co		50	2.0	320	$\sim1.0\times10^{-13}$	[58]
Laser-clad S6	WC-Co					$\sim2.0\times10^{-13}$	
Welded S6	Steel		5	0.025	90	$\sim2.0\times10^{-13}$	[80]
			15			$\sim2.5\times10^{-13}$	
		300	5			$\sim5.0\times10^{-13}$	
			15			$\sim4.75\times10^{-13}$	
Annealed S6B	SiO_2 Abrasive	RT	–	–	–	3.13×10^{-15}	[86]
Laser-clad S6	Laser-clad S6		3000	0.07	1440	5.5×10^{-14}	[66]

S6: Stellite™ 6.

Further to this, it has been shown that when subjected to abrasive wear processes, that the larger relative carbide size within the alloy leads to an improvement in abrasion resistance [87].

To better understand the wear behaviour of the Stellite™ alloy family, it is necessary to look at the wear debris. For the majority of wear tests seen in the literature, the wear debris of Stellite™ takes a flake-like or plate-like appearance, as in Figure 3.4. This morphology is quite common, with spalling wear more likely at lower loads in the oxidative regime [65].

Of particular interest is the sub-surface strain behaviour after wear, as this can indicate modifications in material properties. Changes in the subsurface mechanical response can have implications for the stress field. In Figure 3.5, the subsurface straining of laser-clads Stellites™ can be seen. Importantly, using the analysis of Dautzenberg [88], one can determine the extent of shear-strain in the subsurface. Strikingly, the deformation at 5000 N load exceeds 1000% strain. For loads of ∼2000,

(a) 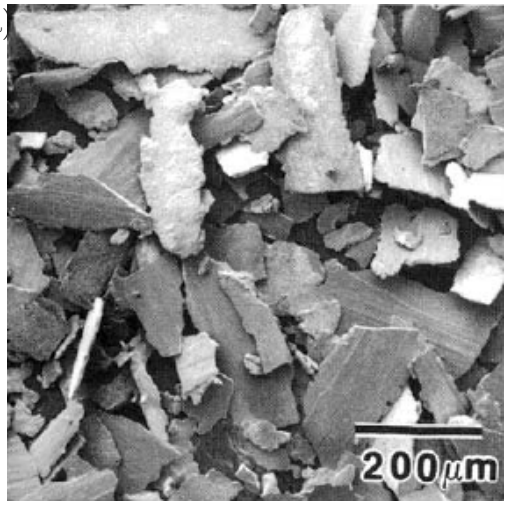

(b) 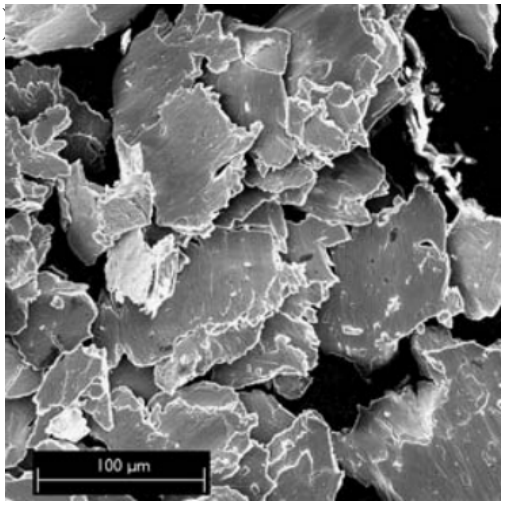

Figure 3.4: Wear debris resulting from different wear tests found in the literature, from (a) Frenk et al. and (b) Persson [58, 83]. Depending on the test parameters, the common morphology for the wear of Stellites™ under sliding is plate-like or flake-like.

this is 500%. Finally, 50% for 50N. These incredibly high strains greatly exceed the strain-to-failure seen in monotonic tension tests. Reasons for this can be attributed to the high hydrostatic pressures under the point of contact, some 1.0 GPa in order, suppressing fracture [89].

This intense straining of the material under the point of contact is also associated with a corresponding increase in material hardness. This would be expected as Stellites™ undergo work-hardening when subjected to strain, which is typically attributed to the formation of finer grains and martensite as in the previous chapter. The extend at which the material work hardens depends on the loading parameters, with the high loads typically resulting in an almost-doubling of material hardness at the wear interface, as shown in Figure 3.6. This increase in hardness has wear-reducing properties [19], particularly in the steady-state.

During wear, the penetration and subsequent sliding of hard asperities through soft material will cause the softer surface to displace. In cases where this penetration is sufficiently high, the ploughed material can lead to the grooving of material and the formation of ridges, wedges and prows. In the most extreme cases, the soft material is able to flow substantially and fracture off as thin metallic extrusions known as cutting wear [90]. Hokkirigawa and Kato [91] used a nano-scratch system and tested several materials to determine the relationship between material hardness and penetration depth on the transition between ploughing, grooving, and cutting. They were able to rank the likelihood of cutting per material using the following 'Degree of Penetration' equation:

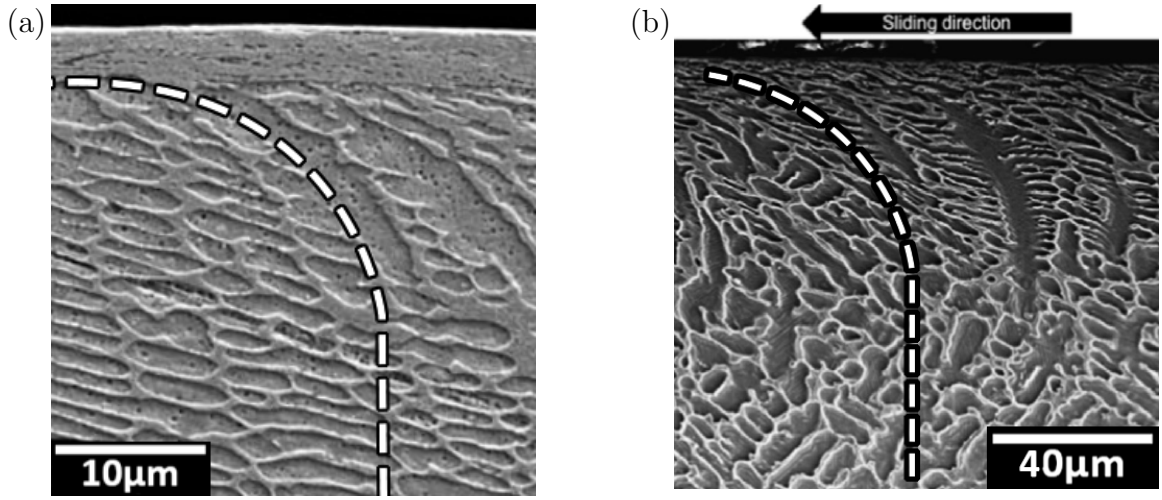

Figure 3.5: Subsurface deformation of grains for laser-clad Stellite™ 6 after sliding tests at 2000N and 5000N taken from (a) Persson [83] and (b) Cabrol et al [66] respectively. The dashed line has been added to show the deformation of the grain structure between the interface and the bulk.

$$D_p = \frac{2d}{w} \tag{3.2}$$

where d is the depth of the scratch and w is the width of the scratch. For Steel they discovered that a value of $D_p = 0.40$ gave rise to cutting. Ahmed et al. [92] employed the same analysis when investigating the nano-scratch response of Stellite™ 21. They observed no cutting debris at a value of $D_p = 0.13$, though ploughing and wedge formation were seen. In another study, they performed nano-scratching on Stellite™ 6, both HIPed and cast, with a value of $D_p = 0.15$ suggesting that Stellites are very unlikely to experience cutting behaviour during abrasion from a hard counter-face.

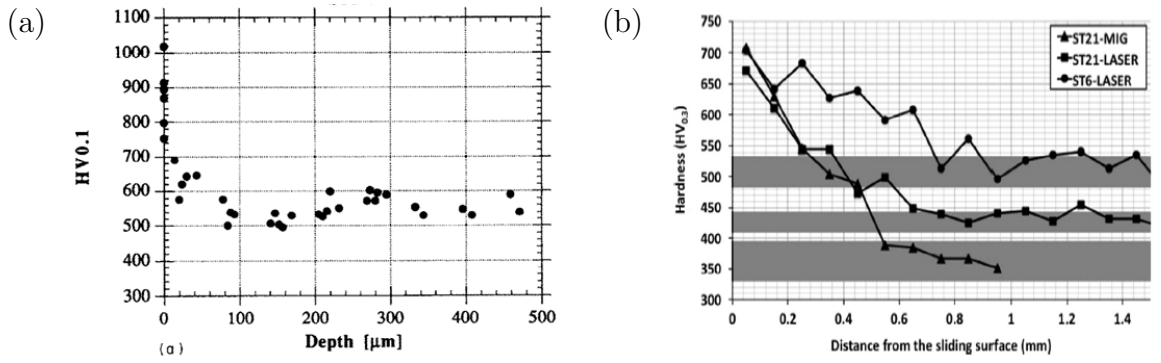

Figure 3.6: Subsurface hardening for laser-clad Stellites™ after sliding tests at 50N, and 5000N taken from (a) Frenk et al. [58] and (b) Cabrol et al [66] respectively. Both hardnesses were determined using a Vickers indenter under a force of 0.1 and 0.3 kgf respectively.

Similar wear particle morphology, surface topography and cross-sectional deformation as seen on Stellites™ has also been seen on rail steels, where the ratcheting wear model has been used to explain wear under rolling-contact fatigue [23] albeit on a larger scale due to the relative ductility of rail steel. Figure 3.7 shows some examples of the wear mechanisms experienced on these steels during rolling and sliding contact. Particularly, subsurface cracking parallel to the wear interface, thin platelet wear particles, and formation of flakes or metallic 'tongues' on the surface can be seen with the subsurface experiencing a high degree of deformation. The debris and fracturing of thin extruded 'tongues' are similar to that seen by Frenk and Persson for laser-clad Stellite™.

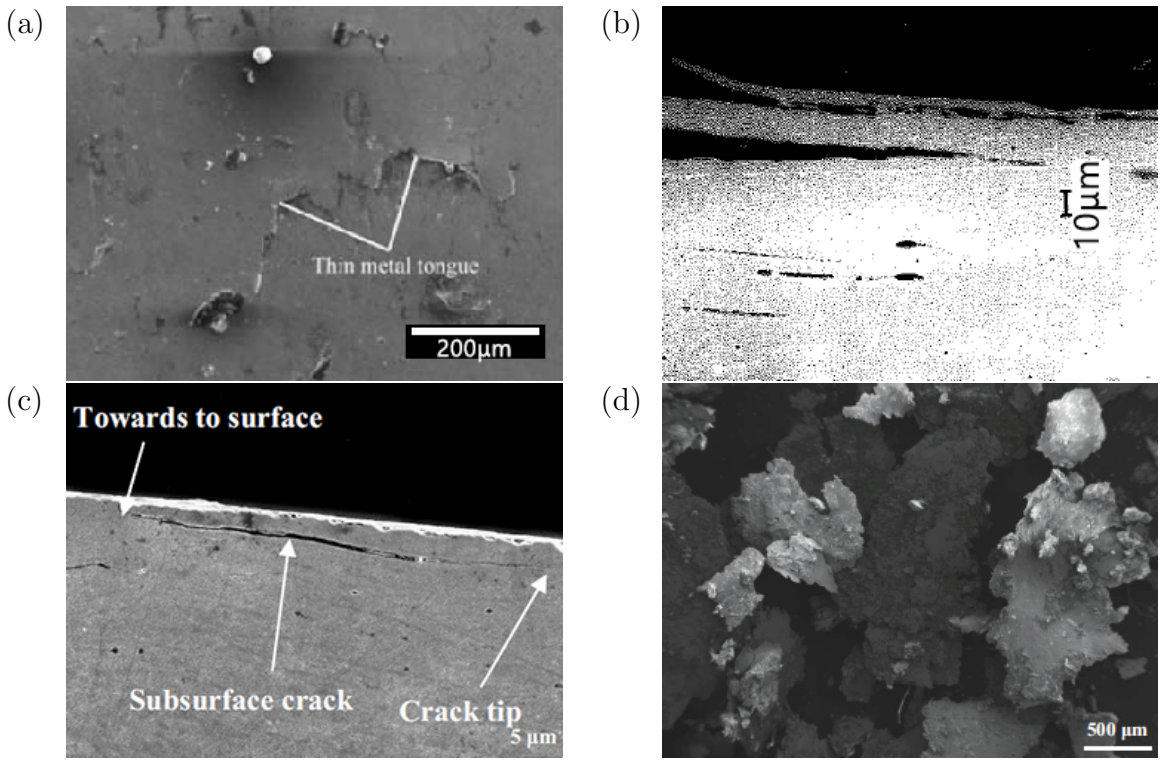

Figure 3.7: A series of SEMs demonstrating the effect of rolling/sliding contact on the wear mechanisms and debris seen on rail steels, where ratcheting wear is said to occur. The SEM from the work of Wang et al. [93] (a) shows the wear surface, forming thin metallic extrusion known as a 'shear tongue', (b) work by Tyfour [94] demonstrates how debris can be formed by the removal of a layer by fracturing as the result of subsurface cracks propagating in the subsurface. Similarly, a more complex crack morphology can be seen in (c) from the work of Ma et al. [95]. Finally, the flake-like debris resulting from this contact condition is shown in (d) from the work of Wang et al. [96]

.

3.7 Sliding wear of Stellite™ in complex environments

One of the desired outcomes of this thesis is to build a wear model of Stellite™ that can potentially integrate complex environmental effects on the wear process. Therefore, a review of one such environment, the PWR, is given.

The reactor core of a PWR operates around pressures of 15 MPa (150 bar). The water within the core, typically doped with lithium hydroxide and boron to limit further generation of corrosive species [5], reaches temperatures of 300°C. During operation, the primary coolant water is bathed in radiation from the core. This induces a variety of reactions under which H_2O decomposes into corrosive species of which Hydrogen Peroxyl (HO_2), Hydrogen Peroxide (H_2O_2), and Oxygen (O) are some [6]. Lithium hydroxide and boric acid within the reactor water helps reduce the number of corrosive species generated [5]. Therefore, the PWR environment is highly aggressive both mechanically and chemically.

In a study on the wear of Stellite™ 6 on a control rods latch arm in a PWR, Lemaire et al. [8] hypothesised that during periods when the wearing surface was not in contact, the surface would form a thin passive layer due to the corrosive nature of the environment, which would then be stripped off the surface with ease when the counterface was brought into contact and slid over the passivated surface. They observed a non-linear trend in the wear data, as shown in Figure 3.8(a), and determined the equation of total wear loss, T:

$$T = kNt^{1-n} \tag{3.3}$$

where k and n are constants, N is the number of cycles, and t is time. They noted highly polished surfaces from the wear specimen, as shown in Figure 3.8(b), and wear-rates in the range of 1×10^{-6} mm^3/Nm.

Formation of a thin passive layer in a nuclear environment was well known and had been explored by Hocking et al. [63]. They saw that, upon exposing Stellite™ 6 to litigated high temperature water, after 600 hours an oxide film, composed of Co-rich oxides via diffusion processes, grew to a thickness of approximately 30 nanometres. Such a thin layer would easily be removed during mechanical wear.

Sliding wear of a HIPed Stellite™ 6 specimen in high temperature lithiated water under self-mated reciprocated sliding, with focus on how this wear changed as a function of temperature, was undertaken by Ratia et al. [54]. A significant increase in

(a)

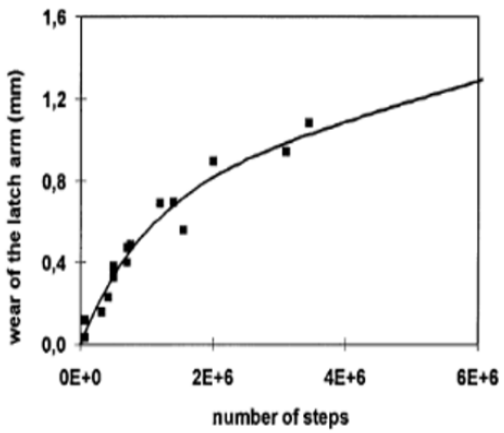

(b)

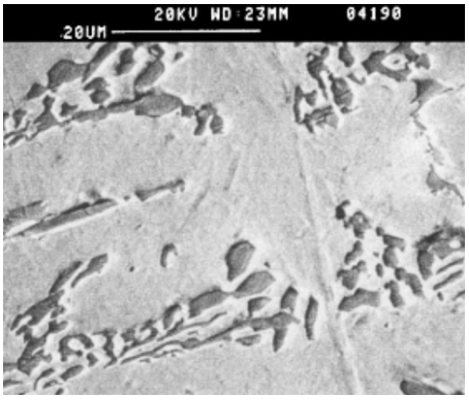

Figure 3.8: (a) The wear trends observed on a control rod latch arm submerged in a pressurised water reactor and (b) micrograph of the wear surface showing a highly polished topography.

wear was observed above 150°C, reasons for this were attributed to the higher temperature accelerating corrosion-rates of the cobalt-chromium system, and therefore allowing the material to undergo harsher wear due to removal of passive films. Similar wear-temperature sensitivity was seen by Taylor and Armson [97]. A further study by Ratia et al. [98] was done to observe the differences in self-mated wear between HIPed Stellite$^{\text{TM}}$ 6 and 3. The latter alloy has a higher weight percentage of 12.07% Tungsten, 2.32% Iron, 2.52% Carbon and 0.75% Molybdenum. This leads to a greater density of carbides and a mixture of M_12C carbides amongst the M_7C_3 carbides such that alloy 3 has three times as much carbide content than 6. Similar to the previous experiment, both materials had worn surfaces that did not see much surface deformation, with the carbide structure still being clearly visible, though carbide pullout and ploughing marks were apparent. It was noted that the high carbide content of 3 allowed for more load to be supported by carbides and resulted in the metallic matrix undergoing less martensitic transformations. Nevertheless, Stellite$^{\text{TM}}$ 3 wore less than 6 further suggesting the importance between carbide content and wear-rates [19].

In addition to this, the effects of the FCC to HCP transformation were explored. After sliding in lithiated water at room temperature (20°C), a much higher HCP fraction was seen at the wear interface indicating that sliding wear promotes the formation of HCP crystals, even under water lubrication. The high temperature results also promoted HCP formation, but saw a lower fraction than in the room temperature tests. It was concluded that increase corrosion rates due to temperature were the dominant factor in controlling wear.

The type wear seen by Lemaire et al. and Ratia et al., could then be determined

to be the result of wear-corrosion synergy, or tribocorrosion [21]. It is hypothesised that the rate of material loss from a system, undergoing mechanical and chemical attrition, is related to tribological wear and corrosion by the formula [99, 22]:

$$T = W_0 + C_0 + S' \tag{3.4}$$

where T is the rate of material loss, W_0 is the mechanical wear produced independently from corrosion, C_0 is material loss independent from wear, and S' is a coupling term denoting the synergy between wear and corrosion. One then may be able to determine the synergistic term, S', with this method by isolating the independent corrosion and wear terms through separate experimentation and using total wear loss data as determined from contextual studies to give $S' = T - W_0 - C_0$, where models could then be designed that capture the evolution of this S' term.

While this equation summarises the corrosion-wear interplay, it does little to build a quantitative understanding of wear in harsh environments. Particularly, it assumes that wear and corrosion mechanisms can act independently and in addition to the synergistic term, whereas total wear could simply be a function of both wear and corrosion such that $T = T(W, C)$. Perhaps a more informed approach to modelling complex environmental wear would be to build a wear map that controls for these variables and to identify wear transitions within the experimental matrix. Even if this method is employed, this nevertheless emphasises the need iterative testing that builds upon simplistic experiments via the introduction of new mechanical and chemical variables to truly understand how these processes interplay and lead to the wear-rates as observed in highly complex environments.

3.8 Conclusions

The HIPed form of Stellite™ 6 benefits from improved corrosion resistance, as well as improved abrasive wear resistance. It can be seen that the cobalt-chromium alloy system produces an exceptional frictional response due to the formation of martensite at the surface. The slip-systems of the HCP crystals in this layer can align preferentially with the sliding direction, more so with higher loads, to allow for little resistance to plastic deformation, and therefore a lower coefficient of friction.

Stellite™ 6 also undergoes relatively little wear under dry sliding conditions, experiencing a range of 1×10^{-15} to 1×10^{-13} where other materials would suffer. Particularly, the solid solution strengthening tungsten and presence of carbides improve its

abrasive wear resistance, while the chromium allows for the preferential formation of oxide. Such oxides aid in the reduction of wear for the Stellite™ system.
In spite of its high hardness, Stellite™ 6 can be seen to undergo extreme strains under tribological contact conditions, as evidenced in the work of Cabrol and Frenk, before failing.
All of these qualities contribute to the effectiveness of Stellite™ as a wear-resistant and anti-galling material in dry sliding environments.

Chapter 4
Contact, materials, and wear modelling

4.1 Introduction

This chapter focuses on the modelling of contact, materials, and wear. Prediction of Stellite™ performance during operation life-time is important, and so a lot of work has been done in order to develop predictive models of wear in the literature. This section aims to elucidate on the models necessary to gain a better understanding into the tribological performance of Stellites™ in reciprocating sliding contacts, as well give insight into the conditions experienced at the micro-scale during sliding contact.

4.2 Objectives

- Overview statistical methods that incorporate the surface roughness into the load analysis between two bodies in contact.
- Overview the shakedown theorems of plasticity and their importance to the wear of metals under cyclic contact.
- Understand how homogenisation schemes are used to relate the influence of microscale heterogeneity on constitutive macroscale material behaviour.
- Develop an understanding of the Archard model of wear and its physical assumptions, as well as an alternative model of metallic wear known as "ratcheting wear"
- Understand the role that frictional heating can play in the wear of two materials in contact.
- To determine the state-of-the-art in numerical models of wear.

4.3 Modelling of rough contact

While there is an *apparent* macro-scale area of contact, in reality surfaces of materials have micro-scale extrusions known as *asperities*, see Figure 4.1 as a result of surface roughness. Rather, the area of contact is formed by asperities most proud in the contact interface leading to a *real* area of contact. This area is much smaller than the apparent area of contact which has implications on the contact mechanics at the interface.

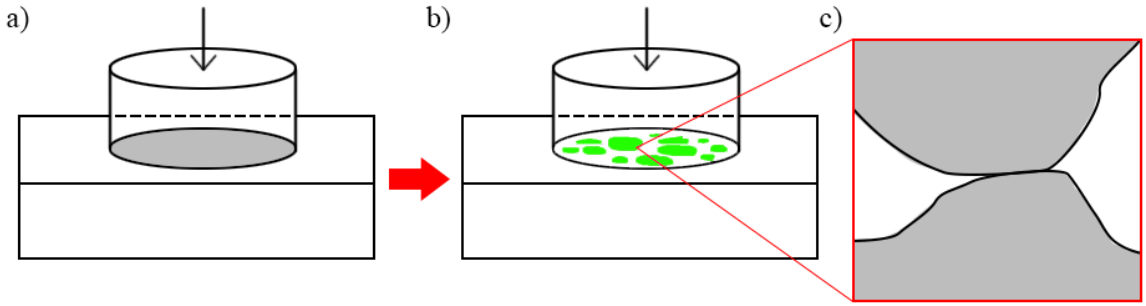

Figure 4.1: A schematic showing a) the apparent area of contact, shaded dark grey. b) the real area of contact as a result of microscale surface perturbations. Zooming into the contacting interface, c) we see contact is actually formed between asperities in contact.

An obvious consequence of the real area of contact is that the load carried by the interface is not shared across the entire apparent area, but rather the real area of contact. As a result, the contact pressures experienced at the interface are much greater under the point of contact than would be if one were to perform a calculation for the apparent area of contact. For example, using the geometry in Figure 4.1(a), for a load of 400 N and a cylinder of 8 mm diameter, one acquires 5.0 MPa. This value is about 0.6% of the yield stress which is unreasonable given the degree of plastic deformation typically experienced during sliding wear.

The accurate modelling of rough contact continues to present a challenge to the tribology community [100]. Starting with the Greenwood-Williamson model of rough contact [101], the influence of surface roughness on the real area of contact is modelled using a statistical distribution of asperity heights, as determined through profilometry data, where proud asperities experience greater levels of deformation. This approach determines its statistical distribution from a single-length scale and treats the deformation of asperities as independent from one another. However, it was noted by Whitehouse and Archard [102] that surface roughness can proceed as a self-affine fractal, i.e. the surface appears as rough at one length scale as it is when one zooms in to a

smaller length scale and referred to them as 'protuberance upon protuberance'. This fractal nature of some surfaces naturally prevents one from easily determining the real area of contact, as finer profilometry measurements will result in a different real area of contact and acquiring data at any scales is limited by the type of apparatus used. A different approach, starting from different considerations, was given by Persson [103], where the surface is initially treated as smooth and 'fully-closed' but introduces sinusoidal variations gradually by adjusting a scale-parameter ζ as to influence the pressure distribution $p(N, \zeta)$. In 2006, a simplistic non-fractal semi-analytical model using the principle of Archard, where asperities at different scale-lengths are modelled such that they share the same load as asperities at different scale lengths, was used to model the real area of contact [104]. Furthermore, purely numerical simulations have been conducted where the rough surfaces in contact have been modelled explicitly [105] to determine the influence of load on real area of contact. Comparison of these different approaches was done by Müser et al. [106], where the goal of each of these models is to capture the linear variation between contact area and normal load. All models were able to recreate the continuum mechanics solutions and all showed good agreement with one another.

For the sake of simplicity, this thesis chooses to focus on the Greenwood-Williamson model of rough contact [107] and so more detail is given. This method involves deriving a Gaussian statistical distribution relating to the heights of asperities which can be obtain using standard profilometry traces of the contact surfaces. This height distribution is then used to homogenise a physical quantity at the contact interface, such as a microscale area or load for a single asperity, to an overall global or macroscopic quantity. Typically, the area of contact or load carried by an asperity is assumed to be Hertzian in nature with the radius of the asperity once again obtained using profilometry data. This can then be homogenised using the following equation:

$$F = A_c \int_d^\infty \phi(z) dF(z-d) dz \tag{4.1}$$

where A_c is given d is the separation between surfaces, ψ is a Gaussian height distribution of asperities, and dF is the microscale quantity we wish to homogenise to the overall quantity F. This analysis is often simplified for a cylinder or spherical asperity indenting a flat surface by superimposing roughness from one surface onto the roughness of the other and integrating it into the probability distribution, ϕ. The separation between surfaces is then taken as the distance between the flat counter-face and the mean-line from the asperity height distributions, as in Figure 4.2. Impor-

tantly, if a maximum surface height is known, this may be used as a cut-off value instead of integrating to infinity.

An important parameter in determining the transition from elastic to plastic behaviour in the case of rough surfaces, which is necessary in understanding the wear response of metals, is the 'plasticity index' [68], which applies for static contact only. It is given as:

$$\psi = \frac{E^*}{H}\left(\frac{\sigma}{R}\right)^{0.5} \tag{4.2}$$

where E^* is the reduced modulus from Hertzian analysis [108], H is the hardness of the contacting material, R is the mean radius of curvature from the profilometry data, and σ is the mean height of asperities. If this value is in great excess of unity, then the material response under contact will be predominantly plastic. This parameter then acts as a design criterion, effectively allowing one to determine if plastic behaviour of the materials is necessary in understanding the damage performance of the alloy under contact. The reciprocal of coefficient E^*/H is taken as the elastic strain-to-failure [109], and has implications on the damage behaviour of the material. For instance, if the material hardens and becomes more compliant over the course of a given test, the value of ψ may fall below unity, meaning the damage response of the material becomes predominantly brittle with elastic fracture behaviour dominating.

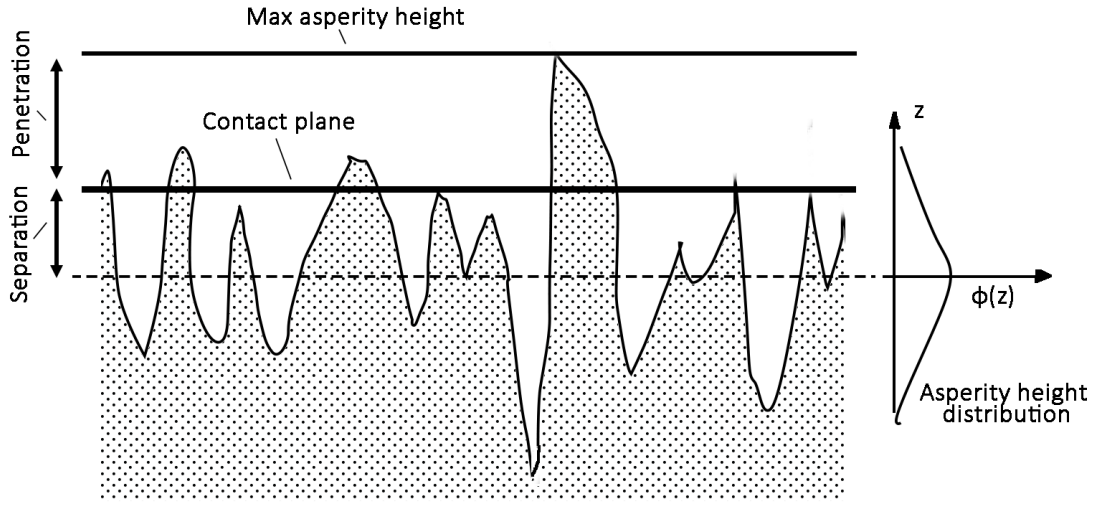

Figure 4.2: A schematic showing the separation between a rough surface, superimposed from the roughnesses of two surfaces in contact, and a flat counter-face.

4.4 Plasticity modelling

Plasticity refers to the permanent deformation induced after the monotonic application of load, i.e. deformations that are retained by the material after loads are removed [24]. Particularly, metals are known to undergo plastic deformation after exceeding the elastic regime by reaching a critical stress known as the *yield stress*, σ_y, after which the constitutive behaviour of the material becomes non-linear and history dependent, i.e. the evolution of strain is determined by the current state of strain during loading. Typically, the yield stress is determined using the Von-Mises criterion [24]:

$$(\sigma_Y)^2 = 3J_2 = \frac{3}{2}s_{ij}s_{ij} \tag{4.3}$$

where s_{ij} is the second invariant, i.e. independent of the coordinate system chosen, of the stress-deviator defined as $s_{ij} = \sigma_{ij} - (\sigma_{kk}\delta_{ij})/3$. The indices here correspond to the stress tensor directions in Cartesian co-ordinates such that $i = \{x, y, z\}$ and $j = \{x, y, z\}$. Reasons for this are because the majority of plastic deformations are volume-conserving, and instead concern only the change of shape in a material.

After the material has exceeded yield, the stress-strain curve deviates from elastic linearity for Stellites™, and the magnitude of yield stress has increased known as hardening. Descriptions of this non-linearity are defined by *hardening laws*. Only two hardening laws, applicable to metal plasticity, are shown here as other laws are merely modifications. They are Ludwik [110] and Voce [111] hardening, respectively:

$$f_{ludwik}(\varepsilon) = \sigma_Y + K\bar{\varepsilon}_{pl}^{n_H} \tag{4.4}$$

where $\bar{\varepsilon}_{pl}$ is the effective plastic strain (a monotonically increasing scalar that tracks the state of plastic strain), and K and n_H are phenomenological hardening constants, determined from experiment. The Voce law is:

$$f_{voce}(\varepsilon) = \sigma_Y + H_V(1 - e^{-b_H\bar{\varepsilon}_{pl}}) \tag{4.5}$$

where b_H is the rate of hardening, and H is the saturation stress. The saturation stress is the maximum possible value of flow stress in the material, and is best approximated as the endurance limit of the material. In contrast to Ludwik, the constants in the Voce equation have a more physical interpretation.

Presently, the discussion has only involved plasticity under monotonically increasing load. Such plasticity is captured by isotropic hardening models. In the case of cyclic

loads, where load oscillates between a maximum and minimum with time. The best description of the material behaviour under these loads are done using kinematic hardening models. Of particular interest, and applicable to Stellites™, is the *non-linear* kinematic hardening model, Armstrong-Frederik [112]:

$$\dot{\sigma_b} = \frac{2C}{3}\dot{\varepsilon}_{pl} - \gamma_b \dot{\bar{\varepsilon}}_{pl}\sigma_b \tag{4.6}$$

where C and γ are phenomenological constants, ε_{pl} is the rate of plastic strain, and σ_b is the back-stress. The back-stress determines the position of the yield surface locus in stress-space. The non-linear kinematic hardening model is able to capture the Bauschinger effect [112], where the material undergoes yield in compression sooner than would be expected after yielding in tension.

4.5 The shakedown theorems of plasticity

During sliding, where the contacting material undergoes repeated contact, the boundary load condition for any point under the zone of contact is cyclic. Furthermore, for metallic materials, the pressures typically experienced under the point of contact are high enough to cause the material to yield. The shakedown theorems of plasticity [113, 114] can then provide insight into the mechanical response of a metal under cyclic loading, which is important if one wishes to understand the sliding wear response of metals. The shakedown theorems are stated thusly:

1. **The lower bound shakedown theorem:** for any admissible field of cyclic plastic strain, if residual stresses and strain-hardening being introduced into the material for the first cycle of load are sufficiently high, then any subsequent cycles will not bring the material past yield. The material is said to have shaken down to a purely elastic response for the steady state.

2. **The upper bound shakedown theorem:** for any admissible field of cyclic plastic strain, if the rate of work done by a purely elastic material exceeds the rate of plastic dissipation in a material of identical geometry during each cycle of load, then the material will experience a net accumulation of plastic strain with each cycle. The material is then said to be ratcheting.

These theorems are important as they allow one to determine the material response of a metal under cyclic load purely in terms of the elastic behaviour. The consequence of these theorems can be seen in the stress-strain behaviour for a cyclically loaded

material in Figure 4.3. For sufficiently load loads, the stress-strain response is elastic, as in Figure 4.3(a). At loads capable of taking the material above yield, if the steady-state response is purely elastic as a result of work-hardening suppressing further yield, then the response is of Figure 4.3(b). If the loads are sufficiently high, then one can enter the plastic shakedown regime where the material response is that of a closed cycle of plastic strain, shown in Figure 4.3(c). Here, fatigue mechanisms of failure are likely to dominate. Beyond this, in Figure 4.3(d), we enter the ratcheting regime otherwise known as incremental collapse. Here the material accumulates a unidirectional plastic strain up until the material reaches a critical strain of failure.

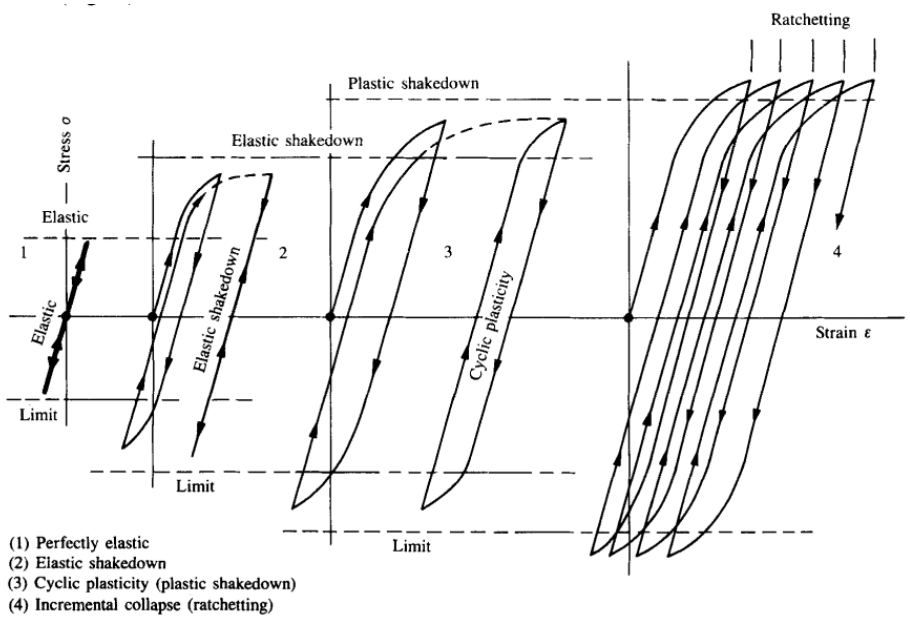

Figure 4.3: Taken from [115]. The stress-strain response of a cyclically loaded material under different loads, showcasing the effect of taking the material above the respective shakedown limits.

These shakedown theorems have since been applied to two asperities under sliding and/or rolling contact [116] for a kinematically hardening material, which allows one to better understand the mechanical response of material during sliding, and is shown in Figure 4.4. Particularly this shows how residual stresses introduced during asperity deformation can influence the shakedown pressures for an asperity under rolling/sliding contact. Consequently, the effect of friction is integrated into the cyclic load analysis. As a result of the shakedown theorems being determined purely with elastic analysis, the contact stress, p_0, can be evaluated in terms of elastic mechanics. This shakedown map demonstrates, for increasing values in the coefficient of friction, that ratcheting is more likely to dominate. As the coefficient of friction increases, the

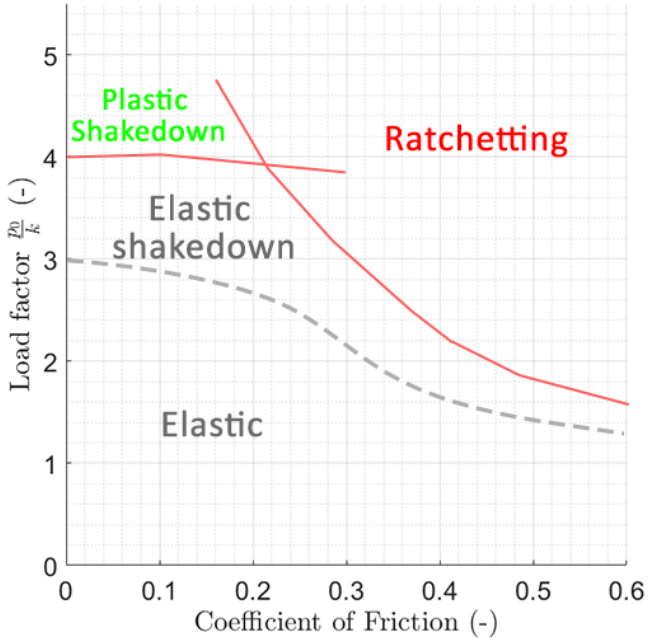

Figure 4.4: A shakedown map for a kinematically hardening solid, adapted from [108]. The y axis corresponds to the maximum Hertzian pressure, p0, divided by the shear strength of the interface, k.

maximum value of shear-stress is brought closer to the surface. The result of this is that residual stresses introduced during the initial deformation of an asperity do little to protect the material from further deformation and thus the ratcheting threshold is exceeded at lower values of contact loads [117].

4.6 Homogenisation in materials modelling

Determining the macroscopic mechanical behaviour in terms of the underlying microstructure is important as it can reveal the relative importance of the constituent elements of the material. For example, it may reveal the effect grain refinement may have on the overall material response or how the introduction of stress-raisers influence the overall macroscopic response. However, such analysis cannot be modelled explicitly as it is limited by computational power and memory [118]. This lead to the development of a 'multi-scale', i.e. different length scales, modelling approach to material modelling.

One particular approach, and the one explored in this thesis, is the sequential approach which is given as follows and shown schematically in Figure 4.5:

1. Construction of a micro-scale 'representative volume element' (RVE), where microstructural properties are modelled.

2. Solution of the RVE in terms of appropriate boundary conditions.

3. Derivation of macroscale material properties from the microscale response.

4. Solution of the macroscale problem.

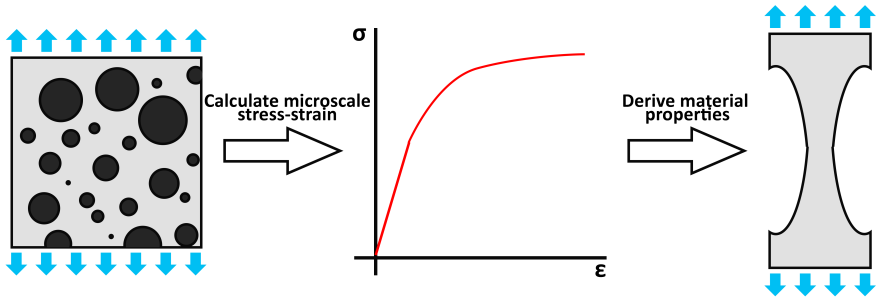

Figure 4.5: Sequential homogenisation procedure showing the derivation of microscale stress-strain response using a RVE and then deriving material properties for using in a macroscale simulation, such as a tensile test.

Importantly, this homogenisation procedure can be solved numerically, e.g the finite element method, thereby allowing one to implement a wide range of microscale heterogeneity; it nevertheless requires an a priori understanding of the macro-scale material model wherein the material properties are then determined using an RVE [118]. While this a priori understanding is a drawback, i.e. stress-strain response is not determined entirely from the microscale, it is computationally less costly than other approaches.

The definition of the RVE requires that: the structure is representative of the 'whole mixture on average' (i.e. spatially homogenous) and that the size of the RVE is such that enough microstructure effects are included (i.e. large enough) such that the derived material properties are independent from the boundary effects introduced during loading [119]. Typically, one can be certain of the second requirement when the microscale response becomes independent of the RVE size and should be selected such that computational time is reasonable.

4.7 Modelling of wear

4.7.1 The Archard wear equation

The Archard wear equation [120] finds a lot of use in tribology for both ranking material performance and wear modelling. The equation is stated thus:

$$V = K_w \frac{Fs}{H} \tag{4.7}$$

where V is the material volume lost due to wear, F is the normal load, s is the total sliding distance, H is the hardness of the wearing material, and K_w is the "dimensionless wear constant". For values of K_w/H above 1.0×10^{-4} mm^3/Nm wear is considered severe, with mild wear occupying wear-rates below this value. Derivation of this equation relies on several simplifying assumptions, primarily:

1. Two asperities slide over one another to form an 'adhesive junction' at their contact interface.

2. The asperity ruptures and creates a wear particle when a critical plastic flow stress, H, is reached.

3. The wear particle created is hemispherical in nature.

4. Wear particles are ejected from the contact immediately.

A description of these assumed processes can be seen in Figure 4.6. An important quality of this equation is that it predicts all wear to be some linear function of both sliding distance, s, and load, N. In principle this is not the case, as several studies to date have demonstrated the wear of metals to have periods of "running-in" or "wearing-out" where the relationship of wear to sliding distance is non-linear, before reaching some steady-state where the rate of wear appears to be constant [121] as shown in Figure 4.7. It is during the steady-state where an Archard description is most possible. Beyond this, many studies have been able to demonstrate a dependency of K_w on parameters such as friction, contact geometry, and wear mode. As a result, the variable K_w in equation 4.7 hitherto referred to as a constant will now be referred to as the wear coefficient.

There has been a deal of difficulty in determining the physical origin for the values of the dimensionless wear coefficient as determined through typical tribological lab tests. As a result, the use of this wear constant puts a limit on the predictability of

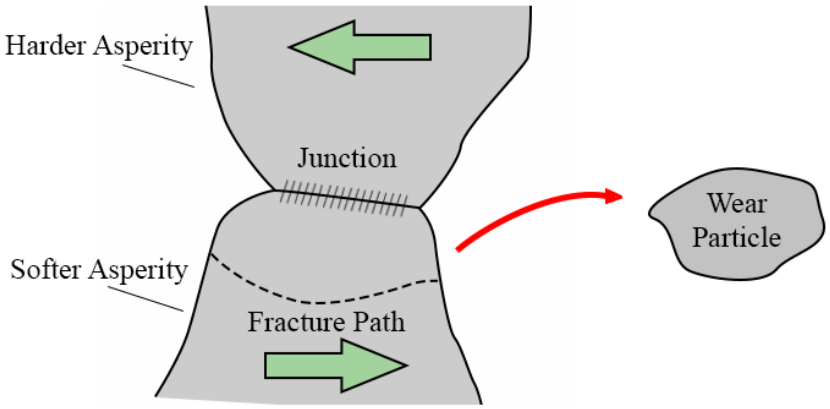

Figure 4.6: A schematic showing the formation of a wear particle. The green arrows denote sliding direction. Rupture of the softer asperity occurs along some fracture path leading to the creation of a wear particle.

any models that use it, as one cannot ascertain the role a physical parameter (such as sliding distance, mechanical properties of the mated tribological pair, or environment, etc.) has on the wear response of any given alloy. Difficulty in qualification of this coefficient has lead to over 200 plus experiment-specific wear equations [122]. This means values of K_w determined in a lab test cannot confidently be used in predicting the performance of Stellite$^{\text{TM}}$ 6 in a PWR environment, unless one is willing to build variability into K_w. This may done by performing lab tests that control for wear-rate in terms of various parameters. Such a method was employed by Molinari et al. [123] who built the influence of frictional heating into the wear-rate of a steel contact, or Sutton et al. [124] who built variability into K_w as a function of transfer layer thickness.

It would be informative if one could determine the sensitivity of the Archard wear-rate in terms of fundamental physical phenomena, such as material properties, as this would allow one to make predictions on the wear-rate without the need to adapt K_w to experiments. One such model, which describes the degradation, i.e. damage and deterioration of strength, of a material up until failure is the "ratcheting model of wear". This is model captures degradation of the material in terms of physical properties such as the rate of straining at the surface which is based on knowledge of how asperities deform during repeated frictional sliding. It is titled as such because it uses the phenomena of ratcheting to describe wear during the cyclic loading of asperities. In addition, it is important to note that one interpretation of K_w is that it is considered the likelihood of hemispherical wear particle creation during *cyclic* loading events of asperities [116]. Particularly, this model sought to explain the observation

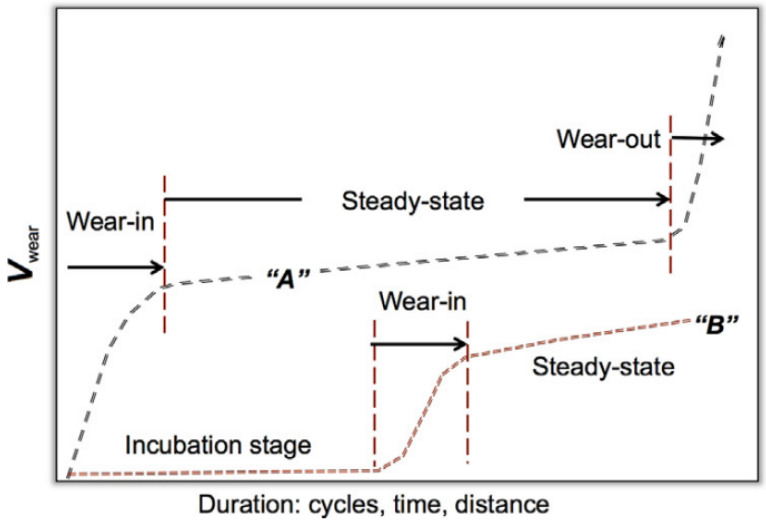

Figure 4.7: Taken from P.J. Blau [121], this graph shows the various typical non-linear wear trends experienced in sliding wear contacts.

that many metallic wear particles do form as platelets that delaminate from the contact interface as the result of material straining and appears to contradict the 3rd assumption of Archard [120]. Using this model one can determine a volume loss and then relate it to a wear-rate using equation 4.7. Further detail of this description is given in the next section.

4.7.2 The ratcheting model of metallic wear

As noted in chapter 3, there exists some physical results regarding the wear of Stellite™ that is not accounted for in the assumptions for Archard. Particularly in the experiments of Frenk and Kurz [58], Persson [82, 81, 83] and Cabrol [66], the material subsurface near the interface after wear appears highly strained for experiments of high load, much more than would be expected from monotonic tension data alone [46]. Persson [83] noted that the surface showed the existence of 'shear tongues', material that is extruded out to the side and then fractured off the edge of worn component. Furthermore, all of the wear debris appears to have a plate-like or lamellar morphology. Though, importantly, this is not always the case, as if the load is sufficiently low oxides may form a protective layer against wear [65] where material degradation may proceed as a fatigue [73] or fracture [79] mechanism. Together, this phenomena could suggest that ratcheting, the incremental increase of shear strain due to cyclic loading, is responsible for the formation of wear particles on a Stellite™ contact. This section outlines the ratcheting model of wear, which seeks to explain

metallic wear more deeply in terms of this observed phenomena.
In order to make the theory behind the ratcheting model of metallic wear as clear as possible, this section has been broken down into several parts necessary in understanding the ratcheting wear model, primarily: the physics behind the straining and wear of metals under sliding contact that lead to the discussion of ratcheting mechanism behind metallic wear, the response of a 'unit event' elasto-plastic half-space during the repeated sliding of an cylinder (asperity) and the failure criterion leading to wear particle generation, the steady-state response of rough surfaces during sliding, and finally the model of mild wear by plastic ratcheting. Two reviews by Johnson [116] and Kapoor [125] give overview of ratcheting deformation for rough surfaces and its associated wear.

The nature of metallic wear and the sliding response of an elasto-plastic half-space

It is commonly observed, during the wear of metallic materials, that wear particles take the form of thin platelets and have a lamellar-like structure [116]. Upon sectioning the worn materials, the existence of cracks parallel to the wear interface were seen in a highly strained surface material. This lead to the development of the "delamination" model of wear, that described these sub-surface parallel cracks to be stress-driven elastic fracture events. These cracks were considered as mode-II cracks and are driven by the intensity of elastic shear stresses. However, this could not be true as frictional stresses essentially suppress the propagation of elastic cracks in this mode. Instead, it was observed that these cracks propagate in high plastically strained sub-surface material. Instead, these cracks are more likely the result of ratcheting deformation in the sub-surface as a result of repeated asperity counters, where small plastic strains per cycle can accumulate into large permanent plastic strains [116]. Importantly, the plastic strains seen in the sub-surface material are much greater than the strain-to-failure for the same material in a monotonic tension test, and are a consequence of the high hydrostatic pressures in the sub-surface (typically above 1.0 GPa during rough contact) suppressing the strain-to-failure [89].
Bower and Johnson [126] analysed the ratcheting response of an elastic-plastic half-space in contact with an elastic cylinder with a friction coefficient of $\sim$0.25 (typical for Stellites$^{\text{TM}}$). They showed that, for a single surface element, the half-space would experience an initial compressive stress in the direction of sliding (σ_{xx}), and a shear stress (τ_{xy}). The initial compression (σ_{xx}) was then followed by a tension component as the cylinder passed over and out of contact with the surface element. Importantly,

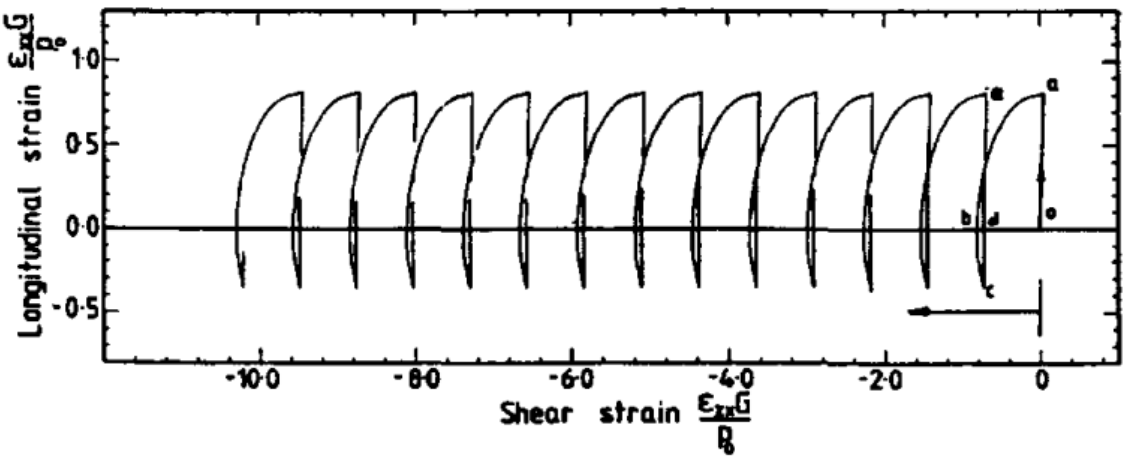

Figure 4.8: Taken from Bower and Johnson [126], this graph shows the strain history of a surface element undergoing repeated contact from an elastic sliding cylindrical asperity.

if the Hertzian pressure exceeded the shakedown limit as in Figure 4.3, then the surface element would experience plastic strains. These were a closed cycle of plastic strain induced by the compression-tension of the σ_{xx} stresses and a unidirectional accumulation of shear strain by the shear stress,τ_{xy}. The strain history for this contact situation can be seen in Figure 4.8. The closed cycle of strain is considered a fatigue component, where the number of cycles to material rupture is governed by a fatigue failure law [127]. For the shear (ratcheting) component, material failure is governed by the number of cycles necessary to ratchet the strain up to failure, defined as:

$$N = \frac{\gamma_c}{\Delta\gamma_r} \tag{4.8}$$

where γ_r is the shear strain due to ratcheting, and γ_c is the critical strain to failure for the surface material under appropriate hydrostatic pressure. The fatigue and ratcheting components are competitive, that is wear of the metal will be governed by the component of strain whose cycles to failure is less than the other. Before we can discuss the wear model, it is necessary to understand how surface roughness plays a role in ratcheting.

The steady-state sliding of rough surfaces

During sliding, we are primarily interested in the case where the load carried by the asperities induces pressures under the point of contact that are high enough to cause ratcheting. In particular, these will be stresses that exceed the lower bound shakedown theorem in section 4.5 as to induce plastic deformation, meaning the

majority of the analysis can be performed using Hertzian expressions of contact.

Kapoor et al. [128] studied the importance of surface roughness on the repeated plastic resulting from ratcheting. They used the Greenwood-Williamson model of rough contact (section 4.3), meaning the asperity height distribution was Gaussian in nature. Using this model, in conjunction with the contact force resulting from the Hertzian contact of a cylinder and the shakedown thresholds for an asperity (from Figure 4.4), they derived a relation termed "the plasticity index in repeated sliding":

$$\psi_s = \frac{E^*}{p_s}\sqrt{\frac{\sigma}{R}} \tag{4.9}$$

where E^* is the reduced modulus, p_s is the threshold of elastic shakedown shown as the red line from Figure 4.4, R is the mean radius of curvature, and σ is the mean asperity height. This equation essentially gives a threshold value, in terms of the surface roughness, under which repeated plastic flow(ratcheting) will occur. Importantly, it is adapted for sliding responses. If the pressure resulting from the load carried by the real area contact, i.e. the nominal pressure, exceeds this threshold value then ratcheting is likely to occur. Importantly, the rougher the surfaces are, the more likely ratcheting will happen which corresponds to a large value of ψ_s. For values of equation 4.9 below unity, the sliding response of the material is purely elastic and so one would expect wear to be negligible or controlled by fatigue mechanisms.

A model for the mild wear of metals by plastic ratcheting

Kapoor et al. [129] developed a model of metallic wear based off the ratcheting of metals. In order to do so, they first considered a 'unit event' of an asperity undergoing plastic deformation resulting from an initial compression in the direction of a normal load from a harder asperity, followed by shearing due to friction as the harder surface slid over the softer surface. This resulted in an extrusion of the asperity as shown in Figure 4.9. It is assumed for this model that the shaded area is removed as a wear particle.

Now, for a rough surface, only some of the asperities will be experiencing stresses high enough to go above the shakedown limit from Figure 4.4 during sliding. The proportion of asperities above the shakedown limit for sliding may be accounted for using equation 4.9, the plasticity index for sliding contact. Using this, in conjunction with the statistical model of rough contact from section 4.3, Kapoor et al. derived

an equation for the wear-rate of the material in terms of ratcheting:

$$\frac{VH}{Fs} = \frac{H}{E^*}\frac{k}{p_s}f(\bar{P}, \psi_s) \tag{4.10}$$

where the left hand side is the non-dimensional wear coefficient from Archard (equation 4.7. H is the hardness of the harder surface, E^* isd the reduced modulus, p_s is the shakedown limit for a given friction value in Figure 4.9, $\bar{P}$ is the nominal pressure i.e. the load carried by the real area of contact, ψ_s is the plasticity index in sliding, and k is the shear strength of the interface, which can be approximated using the equation $k = \sigma_Y/sqrt(3)$ as determined through the von Mises yield criterion. The full analysis and derivation of this equation can be found in the appendix of [129]. The function $f(\bar{P}, \psi_s)$ is a complex function owing to the height distribution of the profilometry data, and it's form is show in Figure 4.9. As the plasticity index reduces to 1 i.e. the material response becomes predominately plastic, the wear-rate becomes negligible.
This equation suggests that the wear-rate is instead proportion to $(\text{load})^{1.5}$ through the function $f(\bar{P}, \psi_s)$, unlike the Archard equation that suggests a linear relationship. Importantly, this equation allows one to integrate friction into the analysis in the form of the shakedown threshold p_s.
Some important caveats to this equation:

- The values in the wear-rate are sensitive to the material hardening response of the given alloy under high hydrostatic pressure; data on this is scarce.
- The statistical portion of the equation relies on the mean value of the asperity curvature which can be difficult to determine.
- Creation of the wear-particle, i.e. fracture of the extruded portion of the asperity, is not given.

Furthermore, this analysis where the deformation of the asperity is concentrated on its tip was done in reference to experiments by Kato et al. [130] for low friction lubricated contacts (approximately $\leq$0.2% of the normal force). This resulted in the definition of 'filmy wear', an extremely thin plate-like wear debris of thickness $\leq 0.1\mu$m. Nevertheless, this filmy wear can potentially agglomerate into larger compacted wear debris [90, 131] if entrapped in the wear interface. Beyond the low friction regime, into high friction un-lubricated sliding, the resulting thickness of wear debris is indeterminate and may take any size. Despite this, the laminar plate-like morphology remains.

4.7.3 Frictional energy dissipation and heat

Of great importance into understanding the wear processes of two metals under mated reciprocal sliding is the generation of heat in the interface due to friction processes. The heat generated not only affects the wear process through potential softening of the alloy, but can also drive the necessary chemical processes that lead to the formation of an oxide layer [72]. In particular, if this oxide layer is well adhered, it may act to reduce the total volume of wear. Otherwise, it may spall off and increase wear through abrasion of the interface [73].

Frictional heating may also explain why one contact element experiences more severe wear than the other. In reciprocated sliding, the moving component sees a greater portion of heat as a result of it always being in contact. The stationary component, however, may have dwelling periods where it is completely out of contact. During this time, heat is allowed to diffuse throughout the material itself and the atmosphere. It may also form the aforementioned wear-reducing oxide. Importantly, the stationary contact will re-experience heating due to the repetition sliding before the heat from the initial contact can diffuse away. As a result, the contacting surfaces experience a nominal rise in temperature that would not be present in unrepeated sliding [132].

Frictional heating may be described in terms of the work done by frictional processes as $\mu N s$, where μ is the coefficient of friction, N is the normal load, and s is the sliding distance. However, it is more appropriate to re-cast this equation in terms of a heat flux as this allows one to describe the transient influence of frictional heating [68]. The equation is:

$$h = \mu p v \tag{4.11}$$

where μ is the coefficient of friction, p is the normal pressure, and v is the relative sliding velocity between the moving and stationary pair. As a result of differences in material, and the fact one component will always experience heating through the duration of a test in reciprocated sliding, each of the bodies in contact will see a different percentage of this heat. For a moving specimen of width, b, a heat partitioning factor can be given as [132]:

$$\alpha = \frac{1}{1 + \frac{k_T^1}{k_T^2}\sqrt{1 + Pe}} \tag{4.12}$$

where k_T is the thermal conductivity of stationary body 1 and moving body 2, and Pe is defined as the Péclet number:

$$Pe = \frac{vb}{2\kappa_2} \tag{4.13}$$

where v is the velocity, b is the contact width, and κ_2 is the thermal diffusivity of the moving specimen. At high speeds, $\alpha \to 0$, meaning the majority of the heat is diffusing into the specimen *moving relative to the heat source*. The conjugate of equation 4.11, $1 - \alpha$, gives the portion of heat into the stationary (in the frame of reference to the heat source) body.

4.7.4 Numerical models of wear

This section covers the relevant numerical models of wear used in the development of a new model that captures the sliding wear response of Stellite™ 6.

Finite element modelling of wear

The typical method employed in the numerical modelling of wear is to couple a chosen wear or degradation model, such as Archard, to the finite element modelling method. This is useful, as it allows for one to account for the geometrical influences on geometry wear. It also permits one to integrate any desired multi-physical effect, such as frictional heating, in terms of material models or variations in geometry and has been employed successfully in the multi-physics wear modelling of steels [123].
The common methodology, as outlined in ref. [133], is described as follows. Broadly speaking, the wear volume is derived from the FEA model is acquired by adjusting the positions of finite element nodes at the wear interface corresponding to a wear depth calculated from a chosen degradation model. Typically, the Archard wear equation is chosen. First, the Archard wear equation must recast in terms of the wear depth, W_d:

$$W_d = k_w p s \tag{4.14}$$

where k_w is the specific wear-constant, equal to K_w/H, p is the contact pressure, and s is the total sliding distance. Furthermore, as one is interested in the evolution of the wear depth during the course of sliding, the wear equation is differentiated with respect to time:

$$W_{d(i)} = k_w p_{(i)} v dt \tag{4.15}$$

where v is velocity. The subscript (i) here now denotes that the wear depth is now

evaluated in terms of the pressure value per ith node. Using this equation, one can solve the finite element contact model to acquire a pressure distribution. This pressure distribution is then used in conjunction with equation 4.15 to calculate the wear-depth at a given node after sliding a distance $vdt = dx$. The finite element nodes are then adjusted by this wear depth, which can either be done in terms of an inward-facing normal at boundaries in the wear interface of the contacting geometries, or the nodes are simply moved perpendicular to the sliding direction into their respective geometries.

The advantages of this approach are that it can integrate the phenomena of running-in whereby an initially non-conformal geometry becomes conformal. While this doesn't change the fact the wear volume is assumed to be a linear function of load and sliding distance, it can capture the phenomena that the rate-of-change in wear depth decreases as the pressure distribution at the wear interface becomes more spread out due to improved conformity [124]. Due to its iterative nature, is also possible to map the evolution of other variables, such as material hardness, on the wear-rate. It also integrates the effects of friction on the pressure distribution, and therefore distribution of wear throughout the contact interfaces.

As argued before, the standard approach is to use a value of k_w as taken from a standard wear test. Naturally, when one uses a pre-established wear-rate, their model will always give the correct value of wear *for that specific test* and it is not possible to make concrete predictions on the wear-volume outside of that range. Instead, if one wishes to extend the predictability of their model they must build in the variability of k_w as a function of a given parameter by running several tests that control for it [123]. Furthermore, to update the pressure distribution at each step of the model is exceptionally costly. Several methods can overcome this; that the finite element solution is updated at set points during the wear simulation or the model only solves after a critical threshold in the change in wear depth is met. Parallel processing of the wear depth at each node has also been used to improve performance [134]. Lastly, unless one is willing to use a uniform mesh, the pressure distribution needs to be interpolated onto a uniform grid in order to use equation 4.15 and then interpolated back [135] which can prove costly.

Energy dissipation description

A different approach, concerned with the integration of friction into the wear-rate, was performed by Fouvry et al. [136], who observed in a previous work that if one surpasses the elastic shakedown boundary during fretting, a type of reciprocated

sliding motion whose stroke amplitudes are in the order of microns, one moves into the plastic shakedown regime [137] and that there is a marked increase in the wear-rate. Naturally, the conclusion here is that, as friction controls the threshold of that shakedown boundary as shown in Figure 4.4, that it is necessary to incorporate friction into the wear analysis if one wishes to quantify wear during repeated alternate sliding.
To incorporate friction into wear, Fouvry started from the principle of total frictional energy dissipated over N cycles, as integrated over the area of contact:

$$\sum E_d = \sum_{i=1}^{N} E_{di} \tag{4.16}$$

where E_{di} is the dissipated energy of the ith cycle. It was observed that this energy dissipation had a linear relationship to the wear volume. It was noted, however, that before wear would occur, the material would accumulate energy dissipation until a threshold energy was exceeded such that the metallic structure would transform and wear volume would proceed as:

$$W_V = \alpha_s(\sum E_d - E_{th}) \tag{4.17}$$

where α is the gradient of the wear volume as function of energy dissipated, $\sum E_d$, and E_{th} is the threshold energy required to transform the material and cause the formation of wear particles due to fracture.

Kapoor-Franklin model of ratcheting wear

In an effort to build a numerical ratcheting wear model, capable of capturing the effects of work-hardening, Kapoor and Franklin [23] developed a 'tribological layers' model, henceforth referred to as the "Franklin-Kapoor ratcheting wear model".
Essentially, the model works by simulating either a sphere, or cylinder, cycling over a half-space above yield resulting in the accumulation of shear-strain in the subsurface. For convenience, the cylinder or sphere shall be referred to as an asperity however the model is not limited to the microscale. The half-space is vertically divided up into virtual surface elements which, when the shear accumulated in these layers exceeds a critical strain to failure, is removed from the model as a wear particle and the asperity is brought back into contact with the layers underneath and the simulation continues. A schematic demonstrating this model is shown in Figure 4.10. The obvious difficulty in this approach is the method employed to get the plastic strain accumulated with each cycle of contact.

In order to get the strain accumulation-per-cycle of an asperity, Kapoor and Tyfour [94] employed a simplified analysis with regards to the subsurface strain behaviour in a post-test wear specimen after repeated sliding, which is given here for convenience. It is known that the ratcheting threshold may be described purely in terms of elastic contact mechanics [138] due to the shakedown theorems of plasticity only requiring elastic analysis to establish their limit during cyclic loading [116] and this can be applied to asperity contacts. Knowing this, one may calculate the proportion of load above which ratcheting occurs by taking the difference between the contact pressure p and the contact pressure at ratcheting $p0$ (as shown in the shakedown map in Figure 4.4), divided by the shear strength at the interface after work hardening, k_{eff}. It is then assumed, that this *effective* stress is experienced every cycle N of the asperity which leads to the observed subsurface shear strain as seen in Figures 3.5. This accumulation is assumed, though there is no reason it should be, as a linear function of the stress and is given as:

$$\gamma = c\frac{(p - p0)}{k_{eff}}N \tag{4.18}$$

where c is a linear constant, p and $p0$ are the contact pressures at the applied normal load and ratcheting threshold respectively, γ is the strain accumulated some set depth below the wear interface, typically calculated using the Duatzenberg method [88], and k_{eff} is the effective shear strength. This quantity can be found by taking the ratio of material hardness before wear, H_{before} and after, H_{after}, at the interface and multiplying it with the shear strength, $k = \sigma_y/\sqrt{(3)}$, such that $k_{eff} = k(H_{after}/H_{before})$. Unlike the Archard approach, the constant c here, though phenomenological, has an obvious physical interpretation. That is, it relates the strain-rate per cycle to the applied load. This parameter c can simply be derived by re-arranging the aforementioned equation in terms of the known physical quantities, p, $p0$, N, k_{eff}, and γ. This equation is then recast in terms of the elastic stress distribution under the point of contact and stress-per-cycle, to give:

$$\Delta\gamma_{xy} = c\frac{\tau_{xy}}{k(\gamma_{xy})} \tag{4.19}$$

This equation is then used in the Kapoor-Franklin model to calculate strain accumulation in the half-space with each cycle of the asperity. Importantly, the contribution of c on the accumulated strain for that cycle depends on the current value of material hardness at the interface and as such wear is not a linear function of load. The critical strain-to-failure, resulting in a wear particle, is assumed to be the total subsurface

strain accumulation after wear seen previously from Figures 3.5 using the approach of ref. [88]. Importantly, damage in the form of plastic fracture is not explicitly modelled, rather this model simply describes the *degradation of material* and it is implicitly assumed that the progressive propagation of ductile cracks occurs as the result of the plastic shear strain accumulation. It is suggested in reality, that material is deformed through this process to create extrusions at the geometry edge which then fracture off to form wear particles or ductile cracks propagate from subsurface imperfections which then turn up towards the interface to form a wear particle [125]. This numerical model of wear not only captures running-in effects when incorporating work hardening into the evolution of k_{eff} but has also been very successful in the wear modelling of pearlitic rail steels [23].

One of the limitations of this model, is that the influence of plastic strain on the strain accumulation of other layers are effectively independent and not capture the role of other stresses on the strain accumulation, such as those that might result from buckling. Furthermore, the model treats the half-space as homogenous; which is appropriate if one is modelling macro-scale effects. However, the influence of hard-inclusions or voids result in known stress raisers which could have implications on the strain history, and therefore wear. Additionally, the assumption that strain is accumulated as a linear function of pressure is arguably oversimplified, and a description of strain accumulation could be improved using finite element simulations. Lastly, the model fails to account for surface roughness and variations in asperity size.

Franklin brick model

Franklin presented an extension to the Kapoor-Franklin model to 2-dimensions, titled the 'Brick model' [139]. Rather than tribological layers, the wearing material is now represented by a 2-dimensional array of elements, where each element strains independently to its neighbours. Despite this, the same relationship to relate the stresses experienced due to contact to a plastic shear strain is used. Once again, the strain accumulated in each brick is considered to be independent to its neighbours, though a simplifying assumption it allows the simulations to run up to several thousand sliding cycles comparable to real world applications.

Unique to this model is the use of a heuristic, which dictates that for elements that fails (i.e. reaches the critical strain to failure) in specific patterns, a probability of removal, related to an element and its combination neighbouring elements, is used to generate wear loss. In this way, it is possible to see failure occur and propagate through the material, similar to a crack. Elements that are on a boundary are scanned

in 3 across by 3 down groups and are considered 'removed' when the heuristic criterion is reached, and counts as wear loss; after which the elements beneath become the new boundary elements. However, determination of each heuristic, i.e. combinations of failure, must be established *a priori* to the simulation. The heuristics for rail steel were determined by Franklin et al. [139] and consist of 9 situations that can lead to element removal. Broadly speaking, an element can only be removed if its on a boundary and only weak or mixed, i.e. a combination of weak and undamaged, elements can be removed. The heuristics here do not appear to have any quantifiable reason for their usage beyond the reasonable conclusion that a weak or mixed element neighbouring more than 3 elements that are also weak or mixed will be removed. These heuristics could be improved by running finite element simulations of damage during shear deformations.

As a result of the added dimension, the brick model is capable of modelling microstructural features such as carbides and grain boundaries [140].

4.8 Conclusions

Wear is an exceptionally complex phenomena, and the existence of many wear models in order to understand it reflects this [122], often with many caveats. Several important factors play a role in wear, such as the stresses generated under the point of contact during sliding [141], surface roughness, and the mechanical properties of the material undergoing wear. Importantly, as mated sliding is an inherently cyclic loading process, the shakedown theorems of plasticity are necessary in understanding the mechanical responses of metals during wear.

Several procedures, such as the Greenwood-Williamson model of rough contact, among others, seek to understand the influence of roughness during contact. Likewise, homogenisation schemes in material modelling seek to bridge the gap between the mechanical response of materials at the microscale to the overall macroscopic of the same material during deformation.

Thus far, wear modelling has been dominated by the Archard wear equation, and has been successfully used in finite element packages to capture geometrical processes on wear [124], though little has been done to move away from this procedure towards more mechanistic forms of wear. In contrast, the ratcheting wear model stands in contrast to this, with wear being determined purely through material properties – such as hardening functions and critical strain, and is able to overcome a limitation of the Archard wear model in that friction is incorporated into the analysis. It is

noted however, that the model fails to account for surface roughness and suffers to be applied meaningfully to macroscopic test geometries, currently only being used for simplistic Hertzian cases. Furthermore, its assumption that the strain-rate per cycle is a linear function of load is perhaps too simplistic of an assumption. These limitations will be addressed in future chapters.

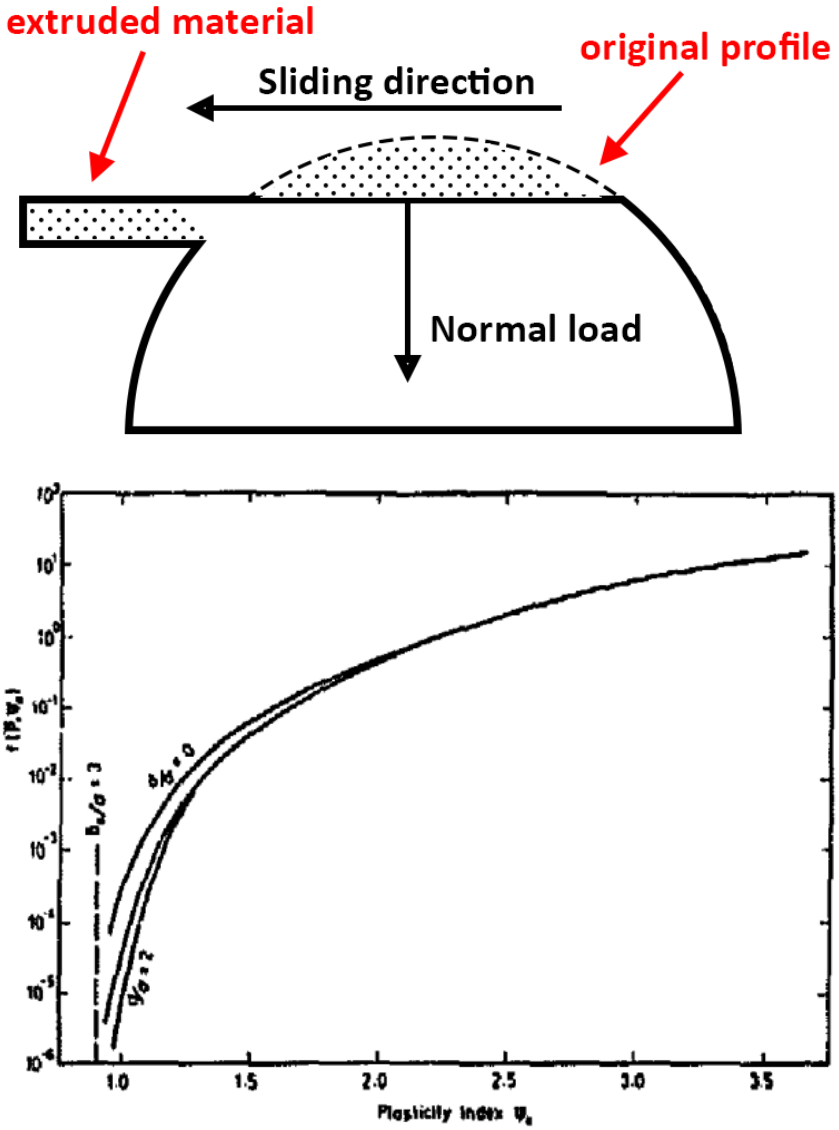

Figure 4.9: Top) Adapted from Kapoor et al. [129], an asperity undergoing ratcheting deformation resulting from the indentation and sliding from a hard counterface. Bottom) a graph showing the variation in the value of $f(\bar{P}, \psi_s)$ (see equation 4.10) with ψ_s. As the value of ψ_s falls to one (elastic shakedown) the value of the function becomes negligible causing little to no wear.

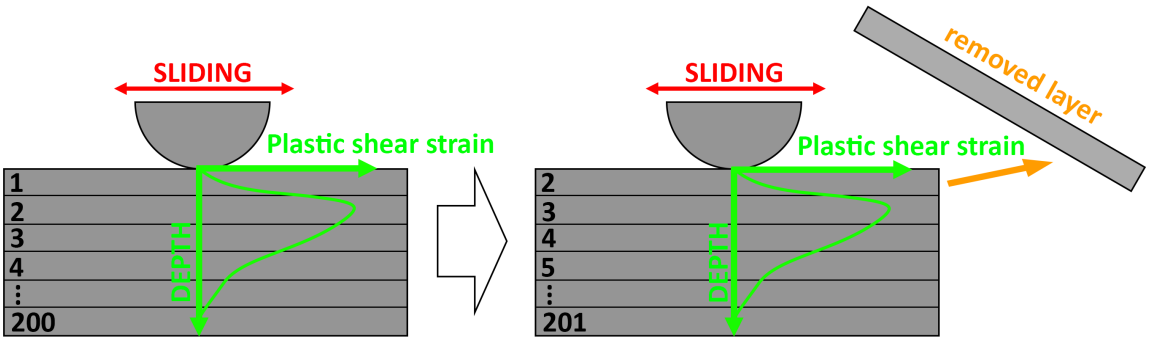

Figure 4.10: A schematic demonstrating the Kapoor-Franklin numerical model.

Chapter 5
Materials and methods

5.1 Introduction

This chapter aims to give detail of the chosen alloy and it's microstructure, the test rig used for the sliding wear tests, and experimental characterisation methodologies necessary to collect and analyse relevant tribological data of the chosen alloy before and after wear testing. Reasons for the selection of these characterisation methods are given in their respective sections.

5.2 Objectives

- Give detail on each of the characterisation methods and reasons for their usage in delineating individual material properties and tribological responses.
- Establish the materials used for testing throughout the thesis.
- Describe the preparation methodology for the materials used in the thesis.
- Explain the set-up of the reciprocating test rig and the reason for its usage.

5.3 Tribological test methods

It was decided that being able to mechanistically, i.e. from purely physical considerations, model the wear of Stellite™ 6 under simplistic room temperature conditions would provide a stepping stone towards more complex environmental simulations. From this, if the model could capture the wear of a simplistic case then it could be adapted to increasing environmental complexity. Therefore, this thesis focuses on the dry wear testing of Stellite™ 6.
The experimental rig for the frictional and wear testing used a Plint TE77 (Phoenix Tribology, Berkshire, UK) reciprocating sliding test rig under dry room conditions of ∼25°C and relative humidity ∼40%. A schematic for the test rig is shown in Figure 5.1. Frictional data was recorded via a transducer connected to the TE77 rig.

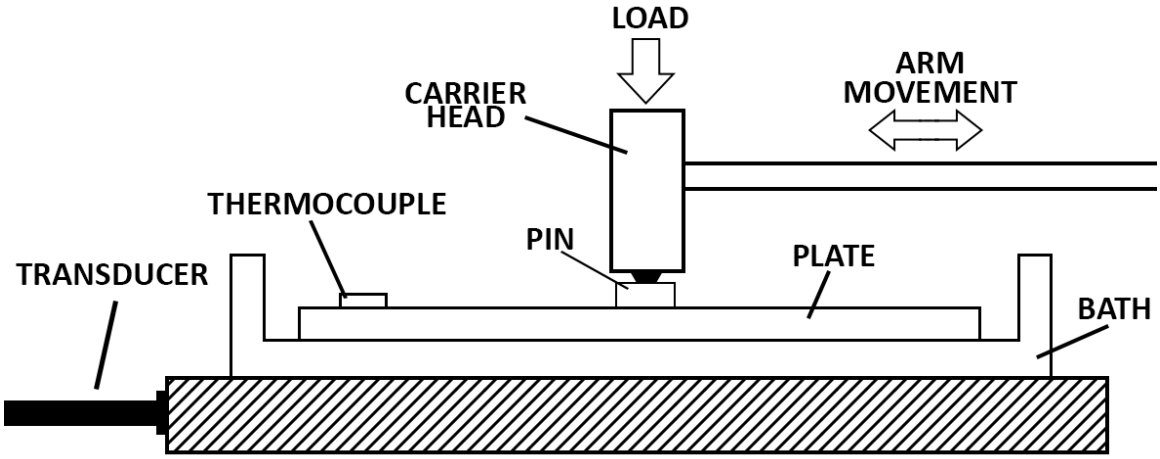

Figure 5.1: Schematic of the experimental rig.

The sliding geometry chosen was an area-on-flat with a cylindrical pin of 10 mm and 8 mm diameter for the variable velocity and load cases respectively to allow for higher nominal pressures in the latter experiments. These were slid against plates of dimension 20x60x3 mm^3. The chosen mating for each experiment was like-on-like. As chamfered pins can lead to edge effects, additional tests were performed using chamfered pin edges to delineate the differences in wear mechanisms between the two geometries. A schematic of the different test components are shown in Figure 5.2.

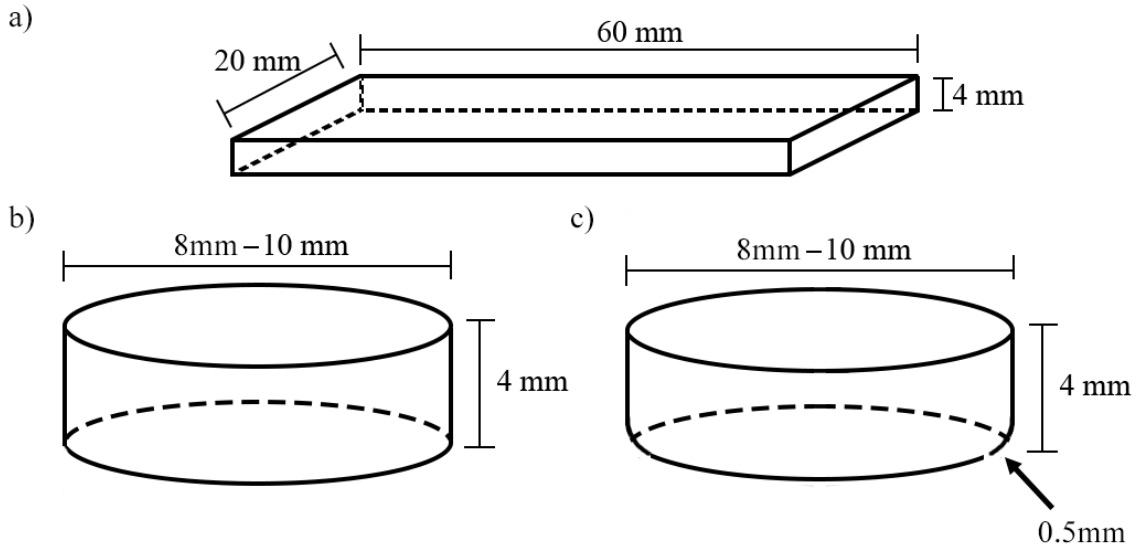

Figure 5.2: A schematic of the test geometries used in the reciprocated sliding wear tests. (a) the plate, (b) the un-chamfered pin and (c) the chamfered pin with a chamfering radius of 0.5 mm as shown by the arrow.

Several dry tests were conducted as part of this thesis, resulting in over 74 unique tests

for dry, with 148 tests minimum including repeats. These tests involved controlling for load, sliding speed and distance.

5.4 Materials testing methodology

Standard uni-axial structural tests were performed to gain an understanding of the bulk elastic-plastic response of the alloy, as well as the total strain-to-failure. The testing procedures undertaken were a standard uniaxial tension test and a standard uniaxial cyclic tension-compression test following British Standard "ISO 6892-1" [142] and "ISO 12106" [143] respectively.

The rate of displacement used in the monotonic tension test was 0.4 mm/min to eliminate any strain-rate dependant effects. The material was taken up to failure in tension where the ultimate tensile strength (UTS) and strain-to-failure (STF). Proof stress of the material was calculated using the 0.2% yield offset method.

The cyclic tension-compression tests were run under strain-control up to a maximum strain of 0.3% and 0.75% for the low-strain and high-strain tests respectively, and were cycled until 100 cycles or failure was seen. The waveform chosen was sinusoidal. An additional load-controlled test was performed up to a maximum amplitude of 600 MPa, slightly above the yield point, to demonstrate the ratcheting effect in Stellite™ 6.

5.5 Characterisation methods

Tribological tests result in worn surfaces of highly complex morphology, chemistry and new material properties. It is necessary then to outline several methods that can characterise each aspect of the material prior and post testing. 2D surface profilometry is used to quickly assess the changes in surface topography, while optical microscopy and scanning electron microscopy are used to identify features of morphological significance in the wear scar. Energy dispersive x-ray spectroscopy allows one to determine the percentage of different elements that exist within the material and can help highlight changes in chemistry. Likewise, x-ray diffraction studies can reveal phase changes within the material. Furthermore, indentation tests into the material can provide mechanical information such as how surface hardness and the Young's modulus has evolved at and near the worn surface. This section covers detail of the characterisation methods used to evaluate the tests conducted as part of this thesis.

5.5.1 Profilometry

Post-wear characterisation consisted of weight change measurements for the pin and profilometer data for the plate and pin. The profilometer used was a Taylor-Hobson Talysurf (Taylor-Hobson, Leicester, UK) using a 120L diamond tip (4 μm in diameter). This Talysurf is capable of resolving up to 0.08 μm. Post-wear surface texture data were also calculated from the profilometer data.

In order to calculate the wear volume of the plates, 3 profilometry traces were taken transverse to the sliding direction for the wear scars. The wear volume was approximated by taking the integral of the wear-scar below the mean-line of the unworn portion of the plate, shown in Figure 5.3. This area was then averaged between the two scars and multiplied by the stroke length in order to get the wear volume of the plates. This approach stands in contrast to the more accurate method of using 3D imaging, such as that performed using an 'Alicona InfiniteFocus' microscope (Alicona Imaging, Graz, Austria). However, given the number of samples and timescale required to image the entire wear scar, the 2D approximation was used to save on time.

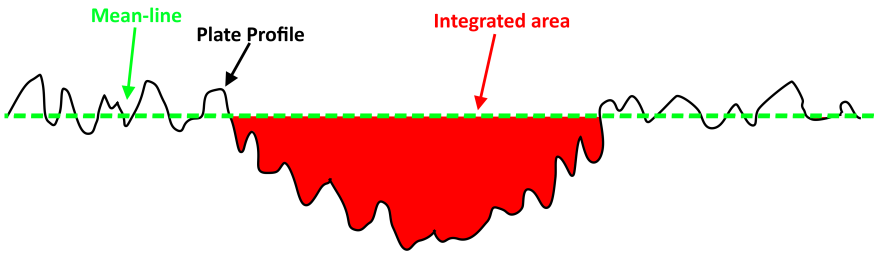

Figure 5.3: Schematic demonstrating the area integral of the wear scar used in the wear volume methodology for the plates.

The mean radius for asperities from the profile data was calculated using the mean radius of curvature equation [68]:

$$R = \left| \frac{(1 + z'^2)^{3/2}}{z''} \right| \tag{5.1}$$

where z is the surface roughness data, i.e. the profile minus the form. One should note that this equation merely approximates asperity radius, does not account for variation in radii, and is limited by the resolution of the measuring device [144].

5.5.2 Indentation

Micro-indentation was performed on polished cross-sections of the worn and unworn pins, and a polished unworn plate, using a Vickers micro indenter. Indentations were performed from the wear interface into the bulk of the pin with a spacing of 30 microns each. For a given depth, 3 indentations were made and the values of hardness were averaged. All indentations were taken at 50 gf. The micro-indentations were also supported by nano-indentation data.

Microscopic material properties were characterised using the nano-indentation method. A NanoTest Vantage (Micro Materials, Wrexham, UK) nano-indentation machine with a Berkovich diamond indenter was used in all cases controlled up to a depth of 500 nm. A 20 by 20 indentation map was taken for every sample pre- and post-test with a 15 μm spacing between indents. The Young's modulus and poisson ratio for the indenter were taken to be 1141 GPa and 0.07 respectively.

Some additional maps were performed for a depth up to 50 nm to better resolve the mechanical properties of each individual phases within the alloy. Deconvolution of the material phases was done by ranking the indents in terms of their recorded hardness and stiffness values. This resulted in several distinct peaks with each corresponding to the statistical distribution of the individual phases. Though not conducted as part of this study, this deconvolution strategy may be improved by mapping the individual indents to each metallic phase using scanning electron microscopy.

5.5.3 Scanning electron microscopy and Energy-dispersive x-ray spectroscopy

Scanning electron microscopy (SEM) was performed using a JEOL scanning electron microscope. Characterisation of the unworn surfaces was performed using back-scattered electron detection (BSI) to distinguish the individual phases in the material. Analysis of the worn surfaces, cross-sections, and wear debris was performed using the secondary-electron mode (SEI) which allows for easier identification of edges in the material. A series of magnifications of 500x, 1000x, 2500x, and 5000x were taken for a given area of interest.

Additional energy-dispersive x-ray spectroscopy (EDS) analysis was performed to identify the elemental composition of the unworn and worn surfaces. The software used was INCA. This was used primarily to identify the content of each material phase, as well as the presence of oxide on the worn surfaces.

5.5.4 X-ray diffraction

X-ray diffraction (XRD) analysis was performed using a "Rigaku SmartLab" x-ray diffractometer (Rigaku Europe, Neu-Isenburg, Germany). A tungsten anode was used in the machine to produce the x-rays, which meant extra time was needed to capture the XRD spectrograph due to an increased amount of noise from excess x-rays produced by the exciting of cobalt atoms. The XRD analysis was performed by targetting the unworn and worn interfaces using a 10 mm filter. To better distinguish the presence of peaks, the raw data was smoothed using a Gaussian window function and overlaid on the raw data.

5.6 Materials and microstructure

The material selected for this study was a cobalt-chromium based hard-facing alloy with a composition of Co-30Cr-5W-2Fe-1.1C-1.1Si. The powder particle size was in the range of 63-150 μm. The material was processed using a HIPing cycle of 100 MPa at 1200 °C for 4 hours. This resulted in a speckled microstructure as seen in Figure 5.4. The light grey phase corresponds to the cobalt-chromium matrix. Dark spherical chromium-rich M_7C_3 carbides sit within the matrix, as shown by the dark phase, and have an average size of 1 to 3 μm in diameter. The area fraction of the carbides correspond to roughly 19.5%. Tiny pores of less than 1 μm in diameter throughout the material are also evident, typically clustering around carbide-matrix boundaries. The typical hardness of this alloy is reported to be in the range 380-490 Hv [46], which corresponds to a 3.8-4.9 GPa range.

XRD analysis of the unworn specimens were also undertaken, in addition to EDX. The XRD pattern can be seen in Figure 5.5. The peaks corresponded to a combination of ϵ- (HCP) and α- (FCC) cobalt phases in the alloy.

Table 5.1: Material properties for the cobalt-chromium alloy tested. These were taken from the author's own measurements based off 3 or more repeats.

Young's Modulus (Tension test) (GPa)	Young's Modulus (Nano-indentation) (GPa)	Strain-to-failure (%)	Vickers Hardness (Hv)	Nano-hardness (GPa)
215 ± 27	215 ± 5.39	1.5 ± 0.19	423 ± 20	5.19 ± 0.45

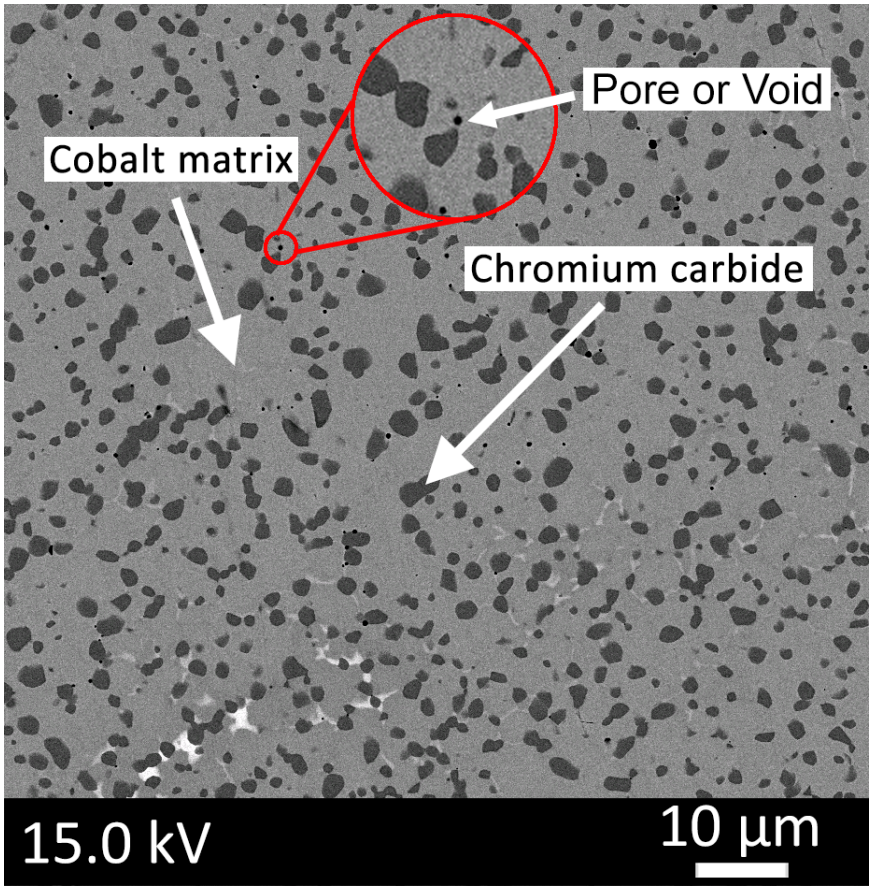

Figure 5.4: SEM micrograph showing the microstructure of the cobalt-chromium alloy.

5.7 Preparation methods

5.7.1 Lapping

Each test surface was diamond lapped to a surface finish of 0.2 ± 0.05 μm average roughness (Ra), using a 25 μm diamond suspension. The reason for selecting these parameters for the wear tests were to reflect a specific application within industry.

5.7.2 Polishing

For post-wear characterisation of the material cross-sections, the following polishing procedure was used:

1. Grinding at 200 grit.
2. Polishing at 9μm diamond suspension.
3. Polishing at 3μm diamond suspension.

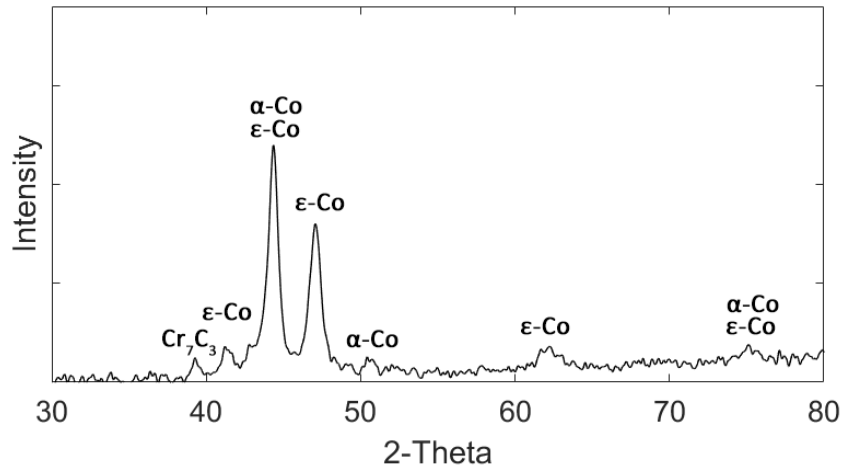

Figure 5.5: XRD spectroscopy pattern for the unworn cobalt-chromium hard-facing alloy.

4. Polishing at 0.02μm using silicon-oxide suspension.

This polishing process was selected following the standard for Stellite™ materials, and resulted in a mirror finish of the characterisation surfaces. Importantly, the polishing process at the end was performed longer than usual in order to remove the presence of un-wanted martensitic phases introduced into the material during the grinding phase.

5.8 Mean pressure

In order to estimate the mean pressure experienced over the *real area* of contact, as opposed to the apparent area, a straight-forward computational methodology was used. As mentioned, the Greenwood-Williamson statistical model of contact, given by equation 4.1 on page 41, was utilised in conjunction with the Hertzian, purely elastic, cylinder-against-flat contact situation. The cylindrical asperity geometry was chosen as a result of the lapping process, which gives a surface lay consisting of almost-unidirectional parallel lines [108]. The relation that gives force per asperity, dF, as a function of the indentation depth or penetration, δ, is:

$$dF/L \simeq \pi R E^* 0.31 \Big(\frac{\delta}{R}\Big)^{1.28} \tag{5.2}$$

where E^* is the *reduced modulus* [108], L is the out-of-plane cylinder length, and R is the cylinder radius. Derivation of this equation is given in appendix A.1. This equation can then be plugged into equation 4.1 in order to homogenise it (a more mathematically rigorous means to reach the following equation is given in ref [68]):

$$F/L \simeq \pi R A_c E^* 0.31 \int_d^\infty \psi(z) \Big(\frac{z-d}{R}\Big)^{1.28} dz \tag{5.3}$$

where d is the separation between surfaces, A_c are the number of asperities on the surface, and $\psi(z)$ is a Gaussian distribution of asperity heights. δ can be expressed in terms of the separation by $(z-d)$. Taking equation 5.3, as a function of the separation, d, we can see how the clearance between two surfaces in contact affects the over-all macroscopic force. This equation was then used in combination with an optimisation routine to select a value for the separation, d, that would give the force applied in the tribology experiments. In other words, there exists a value of separation, d, such that the difference between the total homogenised forces, F, experienced on the asperity level match the macroscopic experimental load, N_{exp}:

$$\exists d : \Pi = N_{exp} - F \to 0 \tag{5.4}$$

Once a value for the separation is determined, this can be plugged into the equation that homogenises the area of contact of a single cylindrical asperity to the over-all real-area, A_r, by:

$$A_r/L = 2R^{\frac{1}{2}} A_c \int_d^\infty \psi(z)(z-d)^{\frac{1}{2}} dz \tag{5.5}$$

where R is the mean radius of curvature, as determined through profilometry measurements. Then to get the real contact pressure experienced as a result of surface roughness, we take the equation, $p_0 = N_{exp}/A_r$.

5.9 Numerical simulations

For the majority of this thesis, numerical procedures have been used for data, finite element, and wear analysis.

MathWorks MATLAB, version 2016b, was used to analyse the majority of data. Primarily, data was plotted in MATLAB to take advantage of its wide arrange of tools within its libraries. Particularly, linear regression analysis was performed using the Optimisation Toolbox™. Additionally, MATLABs Image Processing Toolbox™ was used to process aspects of the microstructure for the chosen alloy, primarily area fraction of individual phases. Finally, numerical models that did not require the finite element method, such as those outlined in Section 4.7.4 and Section 4.3, were conducted in MATLAB.

For finite element simulations, COMSOL Multiphysics 5.3a was used. The primary physics analysed were performed using the Solid Mechanics module, with elastoplastic material models used to study structures under a variety of contact conditions. The majority of simulations were conducted under either plane-stress or plane-strain. Lastly, the simulations were performed under quasi-static conditions using the Stationary Study node. Quasi-static simulations are justified as the application of load, even during sliding, is slow enough as to make the influence of accelerations negligible. Cross-linking, for pre- and post- processing of finite element simulations, was performed using LiveLink™ for MATLAB. Preprocessing was used to construct geometries for a variety of the simulations. The Optimisation Toolbox™ was used in conjunction with COMSOL to optimise material parameters in response to loading. Post-processing of the stress or strain fields were conducted using MATLAB.

5.10 Statistical analysis methods

In order to quantify the goodness of fit for *linear* regression models, used primarily through Chapter 6, the coefficient of determination, R^2, is used:

$$R^2 = 1 - \frac{\sum_i (y_i - f_i)^2}{\sum_i (y_i - \bar{y})^2} \tag{5.6}$$

where y_i are the observed experimental values, $\bar{y}$ is the mean value of the data, and f_i is the fitted model. Typically, R^2 values lie between 0 and 1, and the higher values correspond to a better fit, i.e. the chosen model explains most of the variation in the experimental data.

Throughout this thesis a lot of *non-linear* mathematical models are fitted to experimental and simulation data. As a result of non-linearity, the coefficient of determination, R^2, is not a good measure of fit particularly because R^2 tends to be high even for poor fits in the case of non-linear models [145]. However, it is okay to use this factor when comparing *different* non-linear models to the same data set. The better model will simply have a higher coefficient of determination.

Chapter 6

The influence of load, speed, and sliding distance on the wear of Stellite™ 6 under dry self-mated conditions

6.1 Introduction

This chapter presents the tribological testing of self-mated Stellite™ 6 under dry room temperature conditions. From the literature review, very little work has focused on the evolution of wear mechanisms for hot-isostatically pressed Stellite™ 6, as a result of dry sliding speed, load, and distance. The aim here is establish a dominant wear mechanism by studying the range of interfacial phenomena experienced by Stellite™ 6 using mass-loss from the tribological pair, profilometry of the worn surfaces, nano- and micro-indentation of the subsurface and SEM/EDX of the surface and sub-surface. The wear-rate, which was expected to be constant as according to the Archard wear equation, varied with load and the SEM images revealed a highly strained surface at above loads of 160 N and wear particles that were plate-like and lamellar in nature with highly deformed edges of the pins with material rupturing in the subsurface. This phenomena of degradation at the wear interface may best be explained by ratcheting wear – a mechanism which has not been suggested for Stellites™ prior to this thesis – which seeks to account for wear as the result of incremental plastic straining under cyclic loading that occurs at the wear interface and takes the material up to failure as to create lamellar wear particles and would explain the highly deformed nature of the worn surfaces.

6.2 Objectives

- Outline the test methodology for the dry sliding wear tests.
- Analyse the wear data using in-depth analysis of surface topography, microscopy of near-surface and through-depth phenomena, and sub-surface material properties.
- Establish a dominant wear mechanism in a given test window to explain the wear behaviour of Stellite™.
- Link observed data to the dominant dry sliding wear mechanism, and give a new interpretation of the data, to inform a future modelling approach.

6.3 Test methodology

Before each wear test, the initial surface texture parameters (surface roughness, radius of curvature, height variance) were determined using two dimensional contact surface profilometry on the Taylor Hobson Talysurf. Gravimetric analysis of the pins prior to wear were also taken in order to measure the weight loss on the pin.
In order to delineate the role of the tribological parameters in producing the observed wear mechanisms and friction of Stellite™ 6, a study into load, sliding speed, and distance was conducted. The chosen distances were 100 m and 500 m as to recreate in-service operation time, with sliding speeds of 0.02 m/s to 0.50 m/s. The slow speeds replicate in-service performance, while high speed data sought to identify the sensitivity of frictional heating on wear. Loads of 40 N to 1000 N were chosen, as this reflected the potential range of loads experienced in a PWR. The wear tests conducted were performed using the reciprocating TE77 tribometer. All of the tests were performed under dry conditions at room temperature at relative humidity of $\sim$40%.
The wear tests were separated into two categories: one to observe the effects of sliding speed at lower nominal pressures, and another to observe the effect of high surface pressures at low speeds. The experimental test geometry is given in Figure 5.2 on page 66. The sliding speed and normal load values were chosen such that the power-density, pressure $\times$ velocity (PV), values for the lowest load at the highest speed was equivalent to the highest load at the lowest speed.

The experimental matrix is given in table 6.1. A total of two test runs were performed at minimum after determining the repeatability of the friction and wear results. If there was considerable variation, an additional test run was performed.

Table 6.1: The experimental test matrix for the tribological tests.

Pin Radius (mm)	Ra (μm)	Load (N)	Pressure $\times 10^6$ (Pa)	Speed (m/s)	PV $\times 10^6$ (W / m^2)	Distance (m)	Stroke Length (mm)	Frequency (Hz)
10	0.2	40	0.5	0.05, 0.10, 0.50	0.03, 0.05, 0.25	500	25	1, 2, 10
		160	2.0		0.10, 0.20, 1.00			
		240	3.0		0.15, 0.30, 1.50			
		320	4.0		0.20, 0.40, 2.00			
		400	5.0		0.25, 0.50, 2.50			
8	0.2	600	12	0.02	0.24	100	10	1
		700	14		0.28			
		800	16		0.32			
		900	18		0.36			
		1000	20		0.40			

Post-wear analysis consisted of optical microscopy of the worn specimens to get an over-all view of the wear-surface morphology. A deeper analysis of the worn surfaces was performed using SEM, at magnifications of 2500x and 5000x. EDS was also performed to gain insight into the chemical composition of the worn surfaces and to identify the presence of any oxide. Sub-surface mechanical behaviour was performed using the micro-hardness indenter, and for a select number of tests nano-indentation was performed. Post-wear surface texture parameters were determined using 2D profilometry, and 3D profilometry was performed to gain an understanding of the wear scar morphology with regards to the scar topography.

6.4 Results

The following section covers the results from the tribological tests. All of the data shown is necessary towards developing a model for the sliding wear of Stellite$^{\text{TM}}$ 6. Importantly, the results also help to show a range of validity for particular types of models, such as whether Archard is valid or if certain tribological parameters permit an oxidative wear mechanism to be modelled. These points will be discussed in further detail in section 6.5.

6.4.1 Friction

The average coefficients of friction, taken as the mean-line of the friction trace after running-in, are shown in Figure 6.1(a). To judge whether friction is a linear function

of load ($f = \mu F$), a linear regression analysis of the frictional curves was conducted.

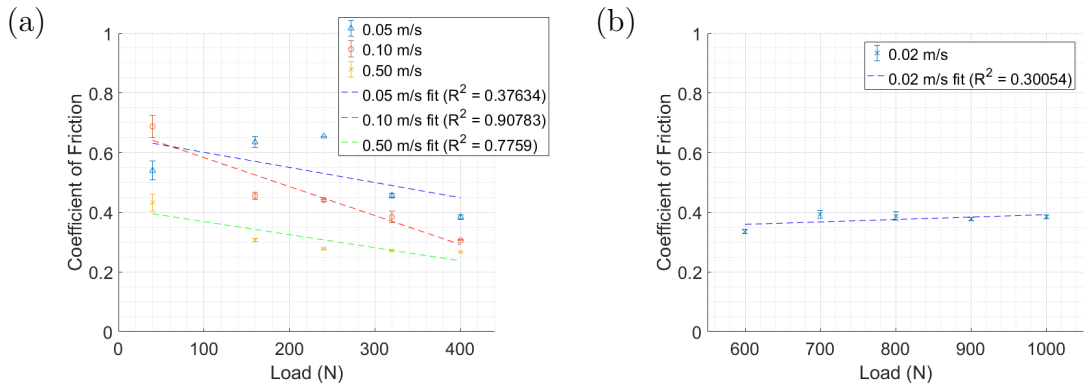

Figure 6.1: (a) The average friction coefficients for the variable speed tests and (b) The average friction coefficients for the high load tests at 0.02 m/s.

Immediately, it is obvious that as the load increases, the friction co-efficient decreases. This corresponds to the notion that Stellites™ improve their frictional properties with load [83]. The lowest coefficients of friction was about $\mu \simeq 0.25$ being reached at the highest load and speed, with highest coefficient of friction is experienced at lower speeds (0.1 m/s to 0.2 m/s) under 160 N.

The linear regression analysis shows that for speeds above 0.05 m/s, that frictional forces can adequately be represented as a linearly decreasing function of load corresponding to high R^2 values. However, for the 0.05 m/s test, a linear fit is considerably less accurate; above 240 N, the friction coefficient suddenly drops to decrease with load. Prior to this, the friction coefficient increased with load. For the high load data, 6.1(b), the average friction coefficients show little variation with load. All linear-regression studies indicate poor fit and suggest a different relationship is required for Stellites™.

The entirety of the frictional traces from which these values were derived can be seen in Appendix B.

6.4.2 Wear

Wear-rates

In order to determine if Archard, i.e. constant wear-rate, is a good model for cobalt-chrome, the specific wear-rate of Stellite™ material is given, which is calculated from equation 4.7 by taking $k_w = V/Ns$, where $k_w = K_w/H$. As with friction, a linear-regression analysis is conducted; arguably, if the wear-rate versus load has an R^2

value close to 1 for a straight horizontal line, then we can conclude Archard-like wear behaviour.

The specific wear-rates for the variable speed tests are show in Figure 6.2. It can be seen, with the exception of the high speed tests, indicating a linear model is not appropriate. The fit is poor, even for the near-invariant linear regression lines of 0.05 m/s and 0.1 m/.

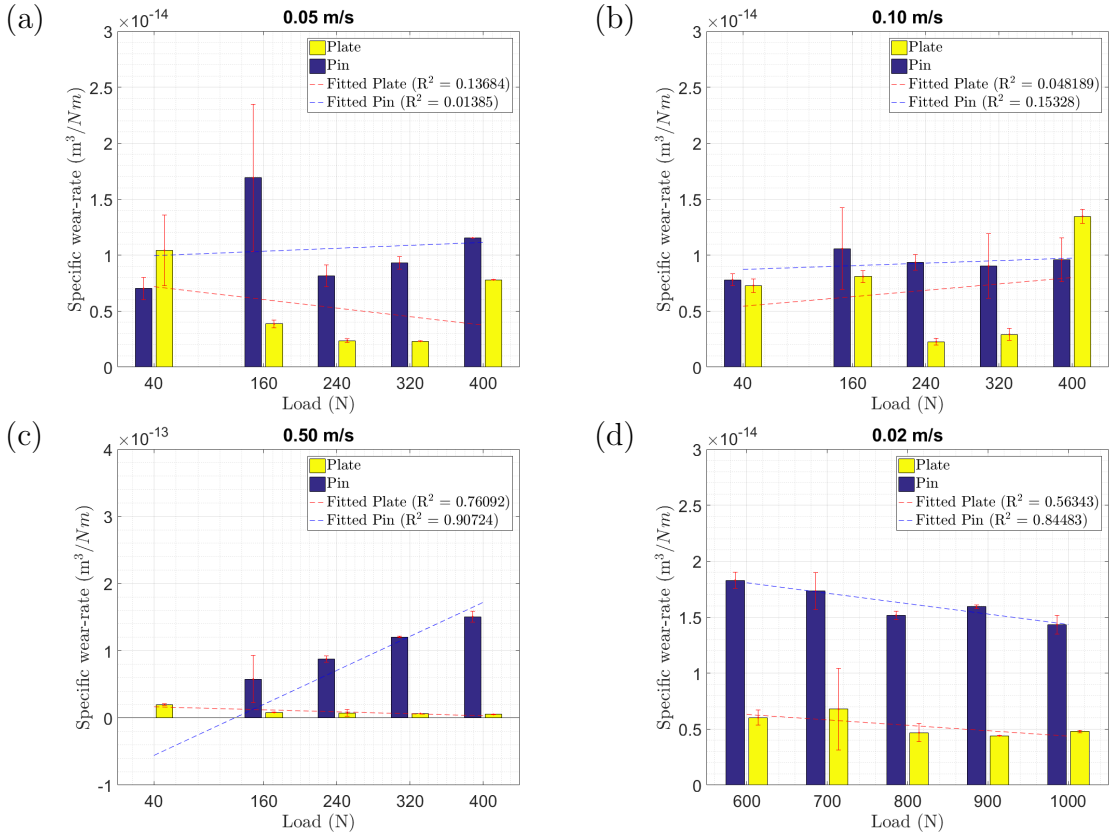

Figure 6.2: Wear-rates for the variable speed tests for both the pin and the plate. The coloured dotted lines correspond to a linear regression analysis for the wear-rates. The high speed 0.50 m/s data showed no wear loss on the pin at 40 N and instead mass gain thus it is not shown here.

For the majority of wear-tests, with the exception of 40 N at 0.05 m/s, and 400N at 0.10 m/s, the plate wore less than the pin. For the high load case, the wear-rate of the plate was some 60% lower than the pin.

Some wear-rate data concerning the evolution of wear with sliding speed is shown in Figure 6.3. The wear-rate begins initially large as would be expected, before settling down into a steady state. With the low speed 0.02 m/s tests between 600 N and 1000 N, the pin is shown to wear more than the plate though the same is not the case for the 0.10 m/s tests.

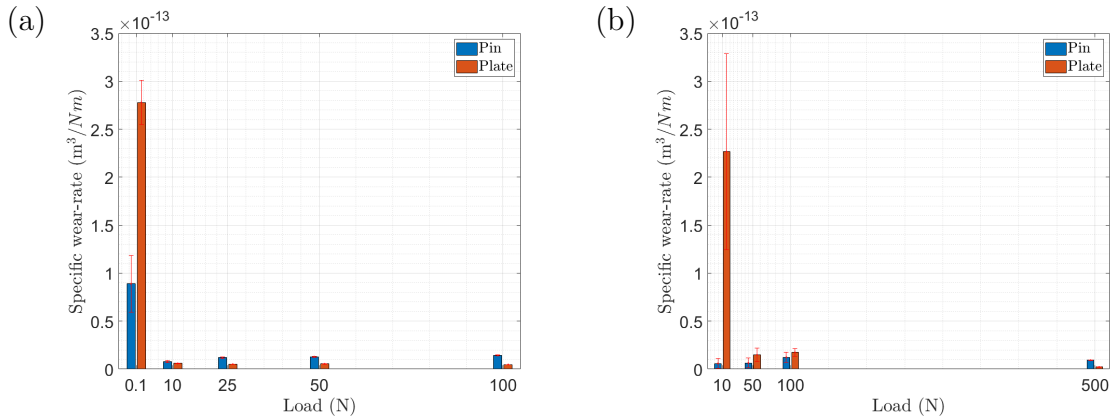

Figure 6.3: Wear-rate vs sliding distance for (a) tests at 0.02 m/s and (b) tests at 0.10 m/s for both pin and plate. The wear-rate begins initially large but decreases with time as a steady state is reached.

Surface texture and mean pressure analysis

Going forward, it is insightful to know the statistical distribution of asperity heights and their effect on the mean pressure experienced through-out the duration of a test. These were all calculated from the *surface roughness* using the methodology outlined in Chapter 5.

For the sake of argument, only the height distributions, calculated using the methodology of ref. [68], for 0.02 m/s and 0.50 m/s experiments are shown in Figure 6.4. For the 0.50 m/s test, the height distributions after wear were much broader than the 0.02 m/s test. The variation in the distribution as a function of load for the 0.02 m/s and 0.50 m/s did not show much variation individually, but the higher load of 1000 N at 0.02 m/s resulted in less high asperities for 400 N at 0.50 m/s. This would be expected as the higher load would prevent the creation of proud surface features.

Surface texture parameters for the variable speed tests and the high load test are shown in Figure 6.5. For the high loads at 0.02 m/s of 600 N to 1000 N gave overall lower asperity heights, whereas the asperity height distribution was more broad due to more proud asperities on the high speed low load data. Importantly, the mean asperity curvature, determined using the mean radius methodology outlined in section 5.5.1, remained at an approximately constant value, as a function of load and sliding speed, of $R_{mean} = 1.5\mu m$.

Using the methodology to look for the mean pressure, as in section 5.8, the corresponding surface parameters and textures were used to find an approximate value of the mean pressure, i.e. the load divided by the real area of contact, at the beginning and end of the tests. The maximum asperity height from Figure 6.5 was used to

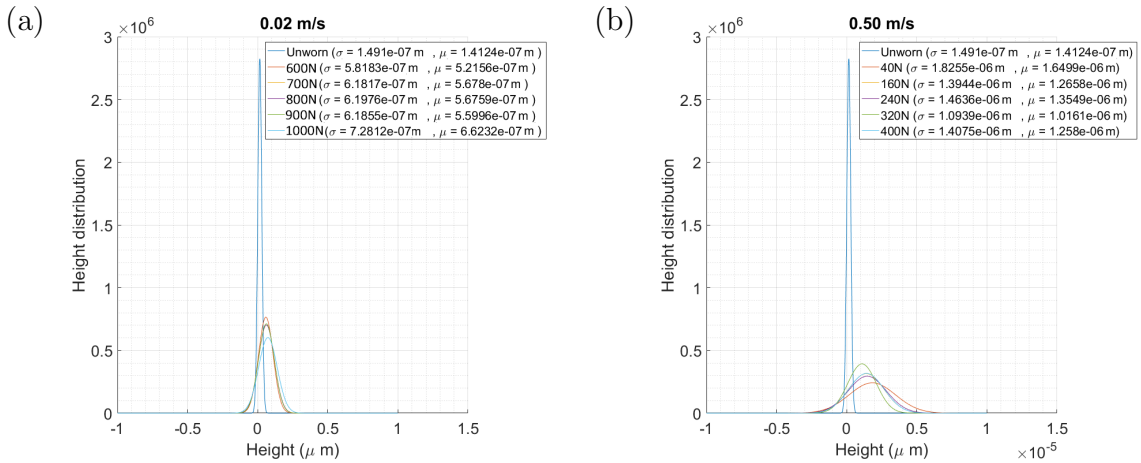

Figure 6.4: Statistical distributions of asperity heights for the sliding wear tests.

cut-off each respective distribution. The initial and final pressure values are shown in Figure 6.6. Strikingly, the mean pressure exceeded several GPa. At this scale, the material would undergo yield almost immediately.

As would be expected, the mean pressure increased generally with load and sliding speed. However, the mean pressure versus load for the 0.02 m/s tests in Figure 6.4(a) appears to be relatively insensitive to the level of load, with the mean pressure not showing an increase in magnitude with load. The converse is true for the low load and variable speed data. This may be owed to the fact that the mean pressure is both dependant upon the scale of the load, as well as the normal distribution representing the asperity height distributions, as shown in Figure 6.4. For the same load, a height distribution that has a smaller mean and variance will result in a lower pressure. In the case of the high load and low speed data, the mean and variance reduce while the load increases thus resulting in a mean pressure that appears constant with load.

Scanning electron microscopy

The SEM images, with corresponding EDS, for both pin and plate not shown for this section can be seen in Appendix B.

Figures 6.7 through 6.9 show the post-wear SEM micrographs from 0.05 m/s to 0.50 m/s for the pin wear surface, cross-section of the pin surface, and wear debris. EDX of these micrographs are also shown.

The surface SEM micrographs are shown in Figure 6.7. Primarily material transfer, as shown by the white highly electrically charged particles, can be seen in all tests. Likewise, material appears to have been pressed and displaced across the surface as evident in Figure 6.7(b) and (c). Interestingly, what appears to be a platelet is peeling

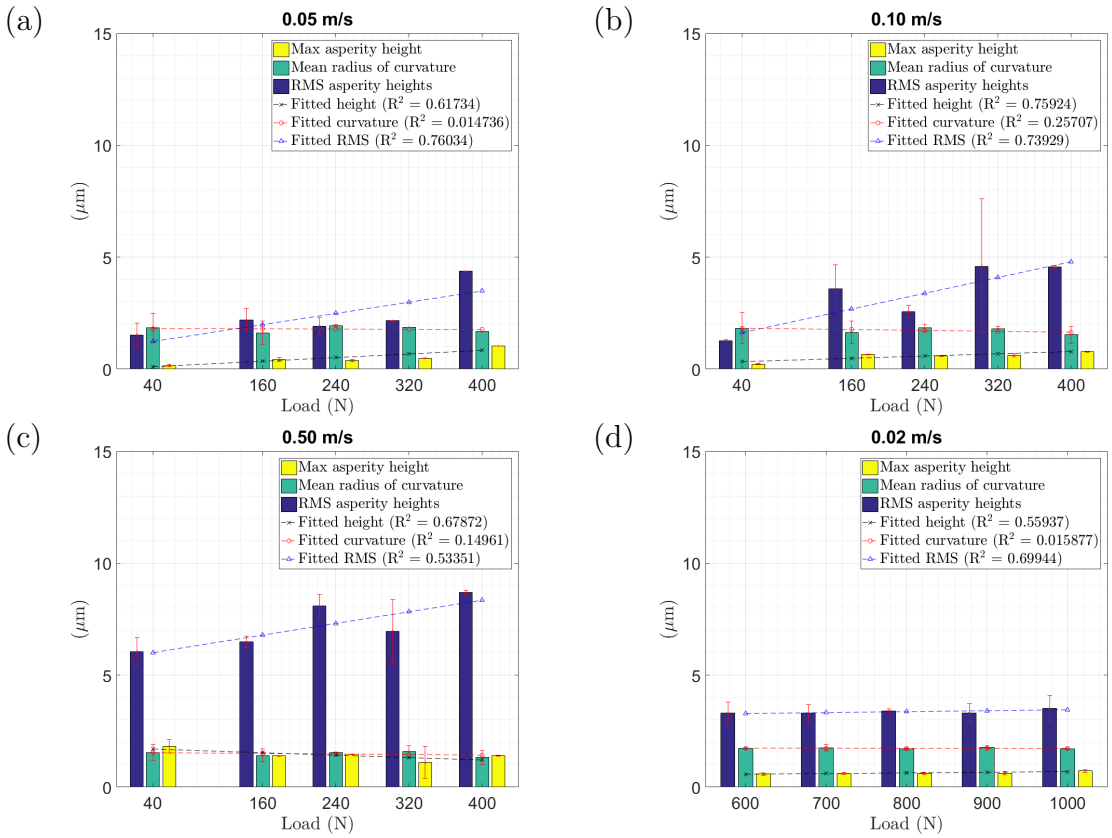

Figure 6.5: Surface texture parameters for the sliding wear tests.

from the surface as seen in Figure 6.7(b) for the 0.1 m/s test. This platelet is of the same order as the wear particle diameters seen for the corresponding experiment in Figure 6.9. A large plate-like piece of material appears to have adhered and been pushed along in the high 0.50 m/s test in Figure 6.7(c). EDX of the surface confirms that these wear surfaces consist primarily of Co, Cr, and W as expected. Oxygen is also present which is expected due to the passivating nature of chromium [64]. Several wear mechanisms operating at once is typical for this alloy [65, 48].

The cross-sections of the worn pin shown in Figure 6.8 show clear evidence of subsurface cracks forming parallel to the wear surface. The damaged surface appears to lift off and away from the pin forming a thin-lip before breaking off to become entrained in the contact interface as a wear particle. For the 0.1 m/s test in Figure 6.8(b) one can observe what appears to be a wear particle consisting of highly-strained oxidated material similar to what can be seen in mechanically-mixed-layers [83]. Figure 6.8(a) shows what appears to be detachment of material however there appears to be oxidated Co-Cr in between the separating material and the pin. All the cracks appear to occur no further than 10 μm below the surface. Every wear surface had evidence of

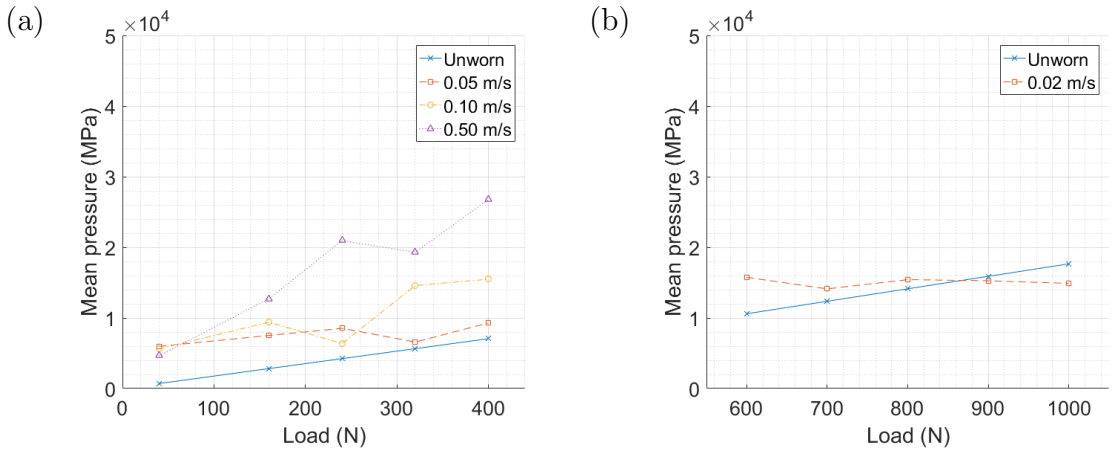

Figure 6.6: Mean pressure values, calculated by matching the Greenwood-Williamson model to the macroscopic experimental load as outlined in Chapter 5 for (a) the variable speed tests and (b) the high load tests.

small scratches, of the same order as the carbide radius, which suggests that carbide pull-out is occurring. Such a mechanism was observed by Yu et al. [48].

The debris, shown in Figure 6.9, observed throughout all of the 400N variable speed tests appears to be plate-like. The size of the debris consists of smaller broken up portions of debris no larger than 10 μm in diameter with the largest debris being above 50 μm. The wear debris show evidence of cracking and fracture throughout their surface which suggest they are brittle. Smaller chip-like wear particles are also seen. EDX shows that the debris is high in oxygen and chromium. The thickness of debris seen in the 0.05 m/s to 0.5 m/s tests all appear to be less than 10 μm in thickness. For 0.50 m/s, Figure 6.9(c), the wear debris appears to correspond severe metallic wear, as this type of wear typically has jagged edges, a clear directionality on its surface, and a lamellar morphology [131].

Figures 6.10 through 6.12 show the post-wear SEM micrographs for the 0.02 m/s tests for the pin wear surface, cross-section of the pin surface, and wear debris. EDX spectra of these micrographs are also shown.

Debris is shown to be highly strained and displaced across the wear surface in Figure 6.14. There is clear evidence of ridges induced by plastic displacement of material in Figure 6.14(a). The uniform distribution structure of spherical carbides cannot be seen at high magnifications, instead showing a mottled pattern of light greys. This suggests that mechanical attrition at the wear surface has destroyed the carbide structure possibly due to straining that has cause the carbides to become mixed with the metallic matrix.

As in the variable speed tests, Figure 6.11 shows subsurface damage and cracking

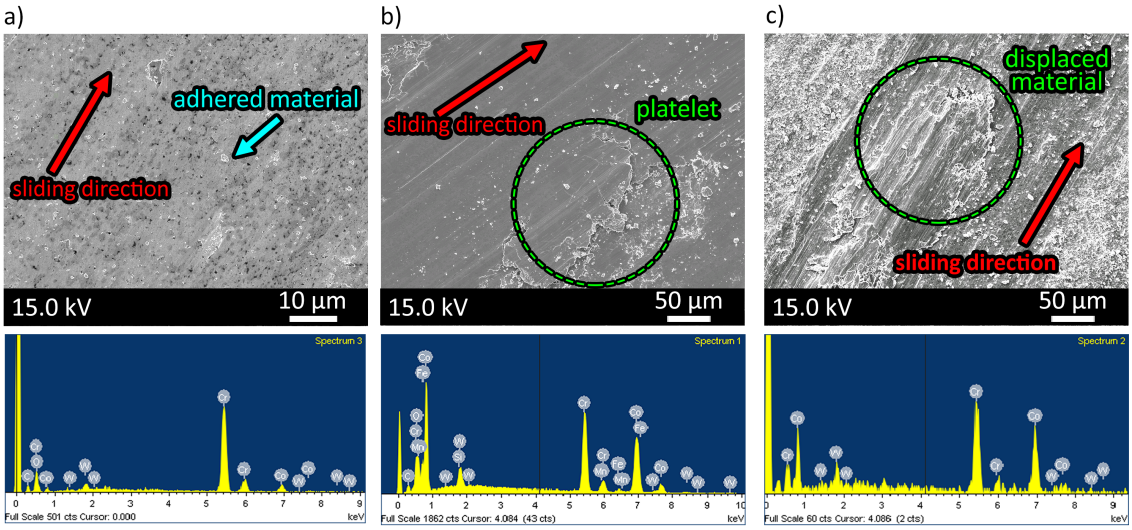

Figure 6.7: SEM micrograph of the wear surface on the pin for the variable speed tests with a corresponding EDX measurement below for (a) 0.05 m/s, (b) 0.10 m/s, and (c) 0.5 m/s. Oxygen is present in all EDX measurements, however the highest peaks are owed to cobalt, chromium, and iron.

occurring in the pin. Once again, highly-strained mechanically mixed material appears to be entrained in the fracture surface. All the fracture surfaces in the pin appear to occur approximately 3 μm below the wear interface with cracks nucleating and propagating around the carbide boundaries. This is further emphasized in the following section. In some cases, the fracturing material appears to be a combination of mechanically-mixed material and the bulk material of the pin.

Figure 6.12 shows debris from the high load tests. Similar to the lower load tests, the wear debris appears to be plate-like. The material is observed to be brittle and thin as shown by the cracks in the debris.

Figure 6.13 shows close ups of cracks propagating in the subsurface for a range of different experiments taken at various places on the worn pins. Branching can be seen on some of the cracks and the microstructure appears to be in contact in proximity to the crack suggesting that this is not reintroduced wear debris. The cracks appear to be propagating quite deep, typically near and around carbide boundaries.

To quantify the depth of the crack surfaces seen in the variable load and speed test – shown in Figures 6.8, 6.13 and 6.11 – some image analysis has been done and consequently tabulated in Table 6.2. In addition to this, some of the tests had the wear particle dimensions qualified. It can be seen for all tests that the crack propagation in the subsurface occurs approximately at a depth between 1.5 μm to 4.0 μm. Correspondingly, the wear particle dimensions can be seen to be of the same order of

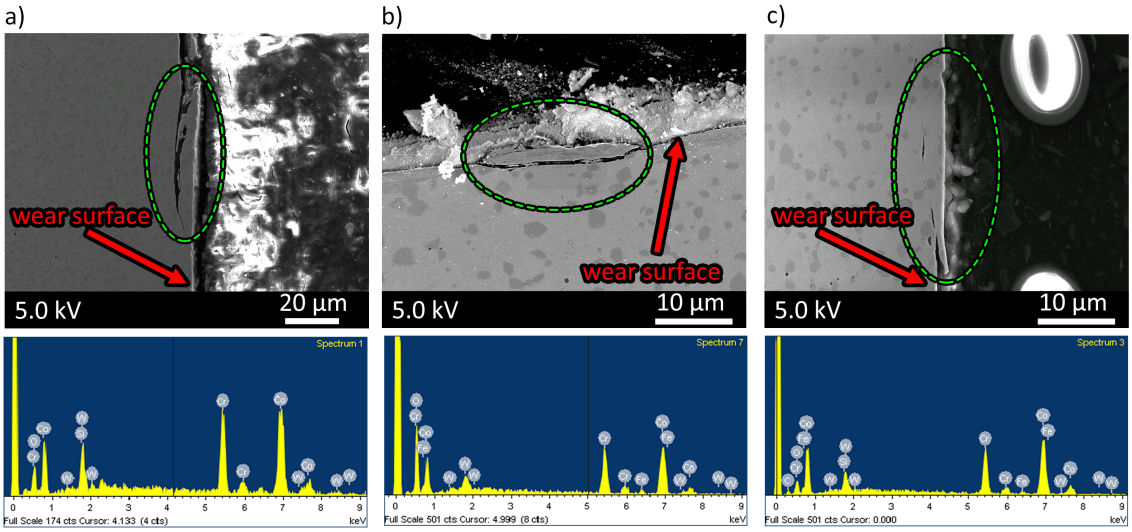

Figure 6.8: SEM micrograph of the pin cross-section for the variable speed tests with a corresponding EDX measurement below for (a) 0.05 m/s, (b) 0.10 m/s, and (c) 0.5 m/s.

magnitude, varying between 2.1 μm and 2.65 μm.

Table 6.2: Depth of fracture surfaces seen throughout the SEM surfaces with comparison to some wear particle depths.

Speed (m/s)	Load (N)	Fracture Depth (μm)	Wear Particle Depth (μm)
0.02	600	2.96 +/- 0.80	–
	800	3.34 +/- 0.33	–
	1000	2.27 +/- 0.20	2.5 +/- 1.0
0.05	400	2.15 +/- 0.30	–
0.10		2.97 +/ 1.76	2.13 +/- 0.36
0.50		2.81 +/- 1.88	2.64 +/- 0.49

In all tests, evidence of material being strained and displaced across the wear surface is seen. Figure 6.14 shows how the material is displaced to the edge of the pin. This type of deformation is characteristic of all the tests seen at and above 400 N. The lipping deformation was characteristic for all of the wear tests, with no such lipping was observed on the unworn pin. The higher speed tests show a more pronounced deformation at the pin edge. This material is typically thin and appears to be in the process of fracturing off, as seen in the high speed 0.5 test. A similar type of deformation, considered as 'shear tongues', was reported for laser-clad Stellites™™ by Persson [83].

In contrast, Figure 6.15 shows some example surfaces of pins operating under 160

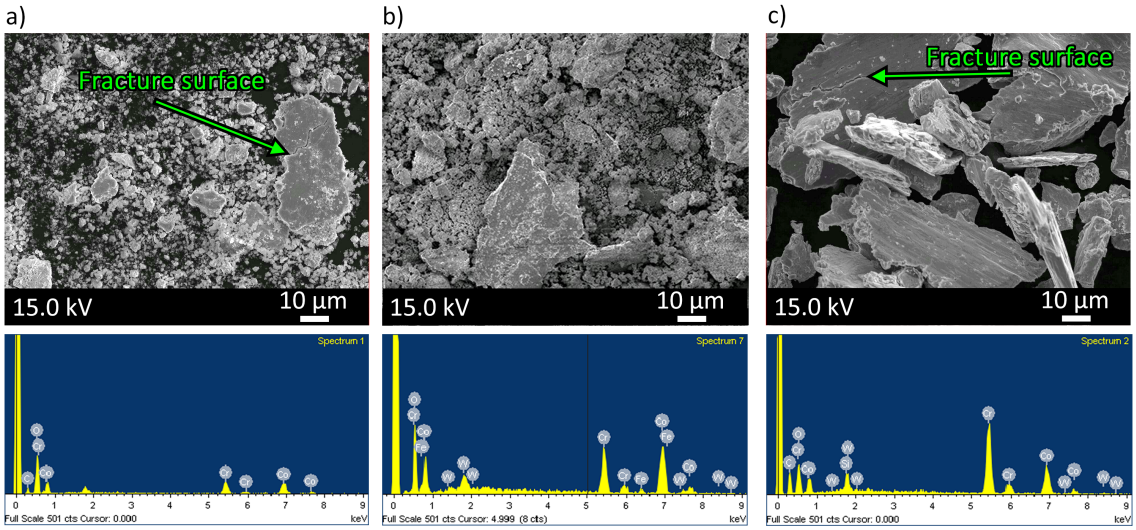

Figure 6.9: SEM micrograph of the wear debris from the variable speed tests with a corresponding EDX measurement below for (a) 0.05 m/s, (b) 0.10 m/s, and (c) 0.5 m/s.

N of load. This demonstrates that the primary wear mechanism in this regime is oxidative. For slow speeds of 0.05 m/s at 40 N, in Figure 6.15(a), there are clear signs of an oxide film covering a large portion of the surface. Where the oxide has failed by spalling [73], portions of the surface show an adhesive wear process. Grooving by hard, strain-hardened or oxidised, particles or material removal also be seen. These same mechanisms can be observed on the 0.1 m/s test, in Figure 6.15(b). More obvious is the existence of small-scale wear debris clustering around the oxide boundary. The wear debris for all of these tests, is large and takes on a more hemispherical nature, as demonstrated in Figure 6.15(c).

The EDX images shown in Figures 6.7 through 6.12 and Figure 6.15 give a broad measurement to the weight percentages of element present in the wear scars. For the 400 N tests shown throughout, and the high load 600 N to 1000 N tests, a much lower percentage of oxygen is seen in the wear scar when compared to the wear debris. This is not unusual as the high temperatures operating in the contact interface coupled with ejection and small surface area of wear debris makes them susceptible to oxidation after their formation. In contrast, at 40 N the EDX measurement shows a much more pronounced peak of oxygen throughout the pin, plate and debris than in the high load cases which is also reflected in the SEM images which show a dark, and thus insulating, surface layer. At such low loads and high speeds, it may be possible for oxides to form in the Stellite^{TM} without being destroyed or mechanical mixed into the surface.

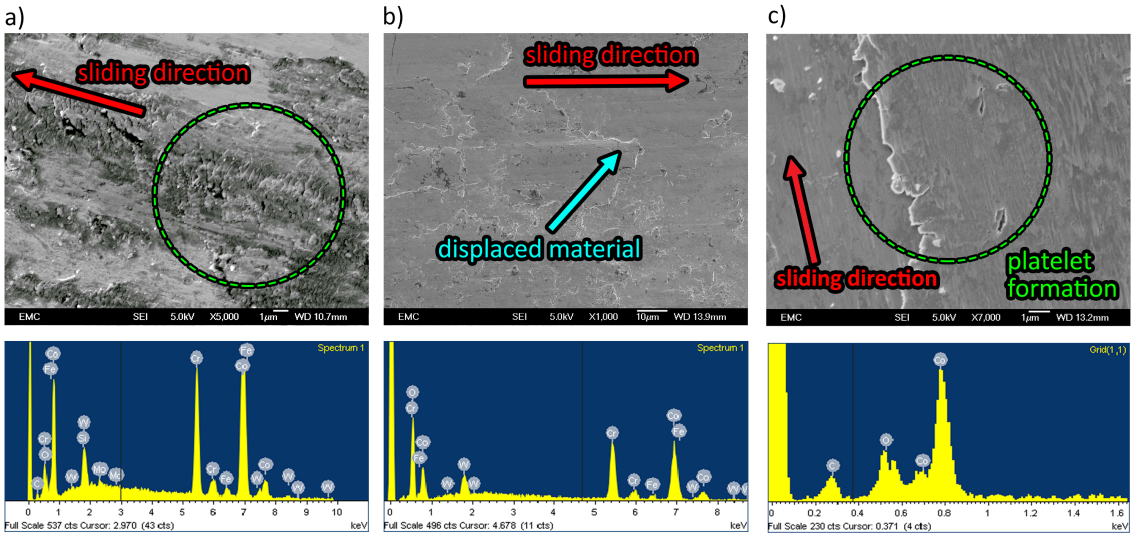

Figure 6.10: SEM micrograph of the wear surface on the pin for the variable load tests with a corresponding EDX measurement below for (a) 600 N, (b) 800 N, and (c) 1000 N.

Nano-indentation study

The nano-indentation data, resolving subsurface hardness and stiffness with respect to depth from the wear interface, is shown in Figures 6.17 and 6.16. Depending on the load conditions, it can be seen clearly that work-hardening was experienced, with higher hardnesses at lower depths owing to the stress distribution under the point of contact. Strikingly, the stiffness reduced closer to the wear interface.

The hardness values for the high load experiment, in Figure 6.17, show an increase in hardness with load but also the size of the transition between the interfacial hardness.

In order to estimate a value for the hardness and stiffness at the interface, the hardness and stiffness curves were fitted to a function of the form:

$$f(d) = p_{bulk} + \Delta p e^{-bd} \tag{6.1}$$

where d is depth, p_{bulk} is the bulk value of the material parameter we wish to fit to (in this case stiffness and hardness), Δp is the differences between the bulk value of the material parameter and its value at the interface, and b is a dimensionless parameter that controls the size of the transition zone between the interfacial and bulk hardness. The form of this equation was chosen due to it saturating to the bulk value at $d \to \infty$ and it's similarity to hardening functions appropriate for this alloy [111]. The values of the fitting parameters for hardness and stiffness in each of the tests are given in Table 6.3, all with a relative error $< 0.01\%$.

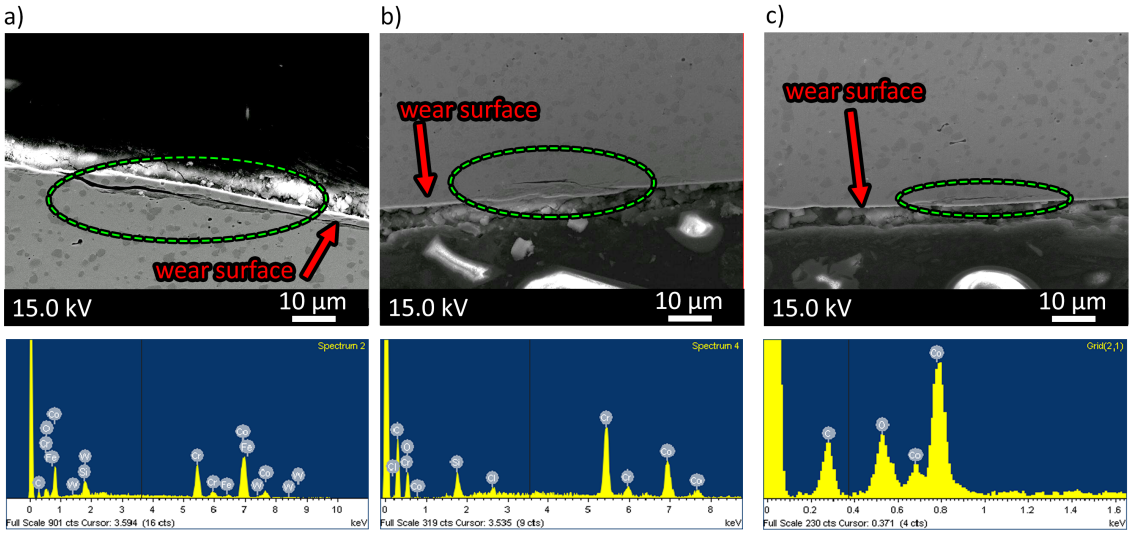

Figure 6.11: SEM micrograph of the pin cross-section for the variable load tests with a corresponding EDX measurement below for (a) 600 N, (b) 800 N, and (c) 1000 N.

Table 6.3: Table of the fitting parameter values for hardness and stiffness.

Load (N)	Speed (m/s)	H_{bulk} (GPa)	ΔH (GPa)	$H_{interface}$ (GPa)	b_H	E_{bulk} (GPa)	ΔE (GPa)	$E_{interface}$ (GPa)	b_E
400	0.05	6.380 ± 0.746	+2.728	9.108 ± 0.746	0.048	252 ± 14.7	-29	223 ± 14.7	0.015
	0.10	5.380 ± 0.978	+1.580	6.960 ± 0.978	0.007	243 ± 30.1	-78	165 ± 30.1	0.040
	0.50	5.416 ± 0.823	+1.758	7.174 ± 0.823	0.013	248 ± 20.4	-49	199 ± 20.4	0.042
600	0.02	6.310 ± 0.967	+2.740	9.050 ± 0.967	0.013	250 ± 26.2	-50	200 ± 26.2	0.034
800		5.887 ± 1.059	+2.624	8.511 ± 1.059	0.017	257 ± 19.9	-54	203 ± 19.9	0.019
1000		5.331 ± 0.785	+2.952	8.283 ± 0.785	0.016	258 ± 17.4	-47	211 ± 17.4	0.018

Additional macro-hardness values near the wear interface, taken using a Vickers indenter, are shown in Table 6.4.
It is interesting to note that the depth of hardening is reflected in the deformation of the pin itself, as shown in Figure 6.14 for the 600 N pin at 0.02 m/s.

6.5 Discussion

.

6.5.1 Friction, wear, and heat analysis

For all experiments, the observed friction coefficients were in the range of 0.25-0.50 and decreased with load [48, 49, 146, 83, 65]. This is consistent for what has been seen in the literature [84]. Due to the formation of an easy-shear layer, some several

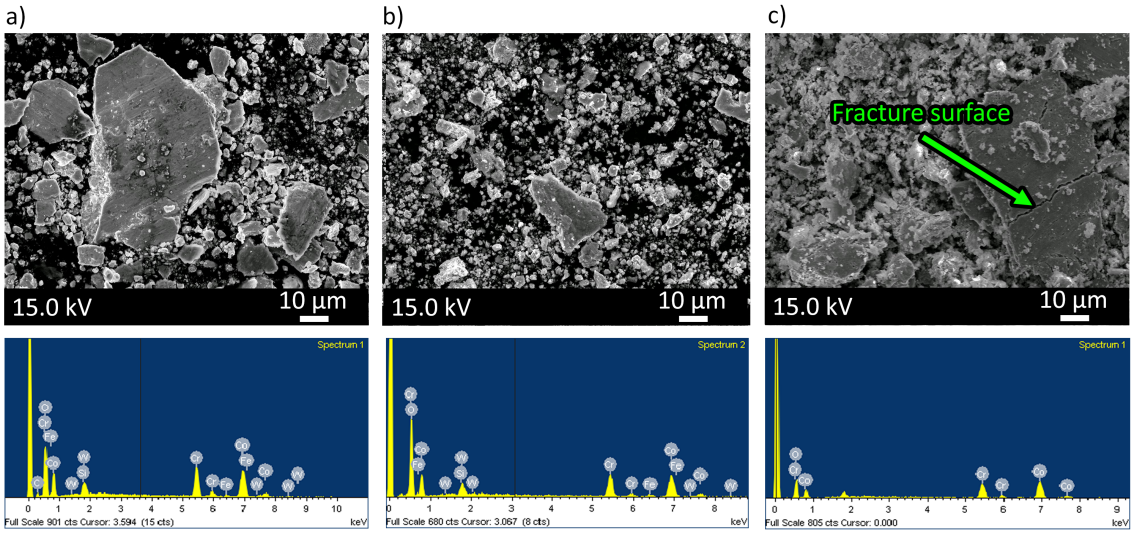

Figure 6.12: SEM micrograph of the wear debris from the variable load tests with a corresponding EDX measurement below. a) 600 N b) 800 N c) 1000 N

Table 6.4: Hardness values of Vickers indents corresponding to near-interface hardnesses.

Load (N)	Speed (m/s)	Distance (m)	Depth from wear interface (μm)	Macro hardness (GPa)
40	0.05	500	20	4.5
160			18	5.0
400			50	5.8
40	0.10		25	4.25
160			40	5.1
400			25	5.9
40	0.50		25	5.2
160			50	5.4
400			20	5.8

nanometres thick, where the plastic slip systems align parallel to the sliding direction of Stellite, there is less resistance to sliding [83]. According to Bowden and Tabor [68], if the contact interface is more easily deformed than the bulk of the material, we should expect the coefficient of friction to decrease. Consequently, these results run counter to the traditional notion that friction is constant with load. As this easy-shear layer is only several nano-meters thick [83], it is unlikely to be picked up on nano-indentation data.

For a majority of the tests, disparity between pin and plate wear increased with velocity. The reason behind this may lie in the frictional heat dissipation between the mated surfaces. For example, using thermal parameters from ref. [147] for a pin

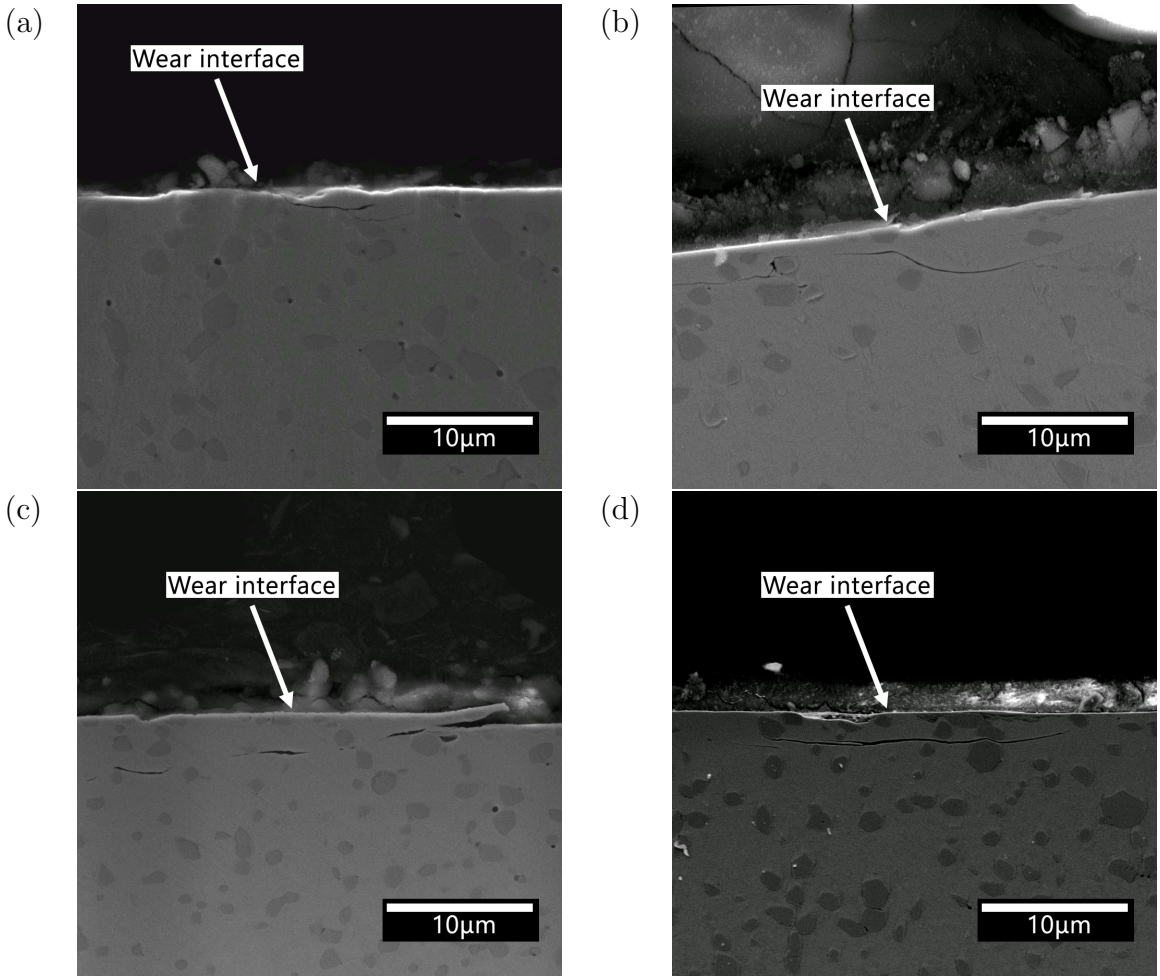

Figure 6.13: Scanning electron micrographs taken at a voltage of 5 kV showing cracks propagating in the subsurface, across different sections of the worn pins, for (a) 400 N at 0.05 m/s (b) 400 N at 0.10 m/s (c) 400 N at 0.50 m/s and (d) 600 N at 0.02 m/s. Crack branching can be seen, with propagation occurring at and around carbide boundaries, s well as material at the interface forming thin removable layers.

of diameter 10 mm, the ratio of heat between pin and plate are 0.6 : 0.4 and 0.9 : 0.1 for 0.02 m/s and 0.50 m/s respectively. As, at high velocities, the pin sees a greater percentage of heat for the test duration meaning the pin would become more ductile, easier to strain, and thus more susceptible to material removal.

The dominant wear mechanism in all tests at 400 N and above appeared to be plate-like wear, with subsurface cracks forming beneath the surface. Transitions to oxide-dominating wear were seen below loads of 160 N for speeds below 0.02. Perhaps at these lower loads, the oxides that form are more adherent and less likely to be removed during the test. For high speeds, no such wear regime is seen, with lamellar severe wear instead. Arguably, when plastic deformation and oxidation are seen on

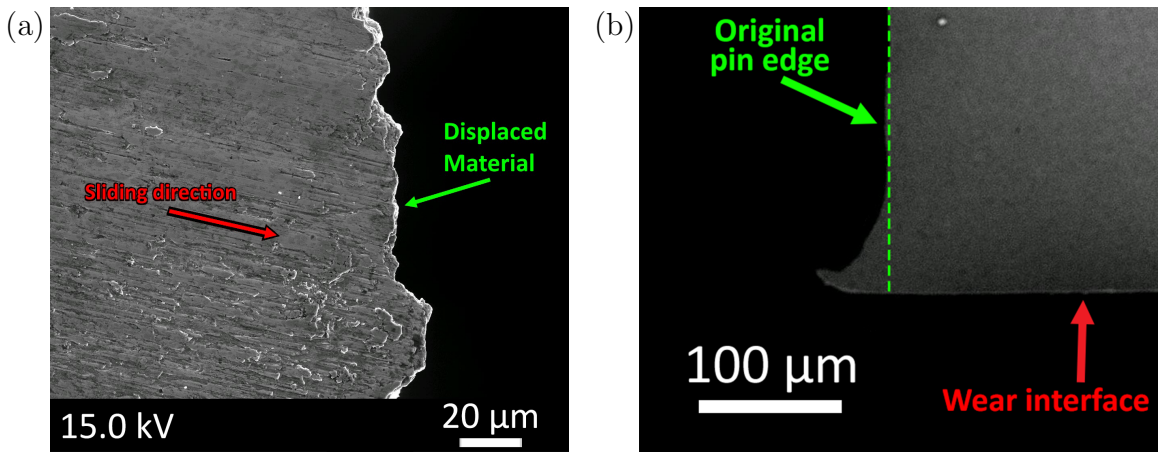

Figure 6.14: SEM micrograph of (a) material being displaced at the pin edge for the 600 N test and (b) SEM micrograph showing the scale of deformation towards the pin edge for the 600 N test. This type of 'lipping' was characteristic in all tests performed. Material has been displaced approximately 50 μm over the original pin edge as shown in (b).

a wear surface, this can lead to the formation of a mechanically-mixed-layer (MML) [70] that has markedly different material properties than the bulk material. Some mechanical mixing is seen (Figures 6.8 and 6.11), though was not predominant across tests.

All wear-rates were of the order 0.5×10^{-14}–10.0×10^{-14} m^3/Nm and 0.5×10^{-14}–1.0×10^{-14} m^3/Nm respectively, similar to those observed in the literature [48, 49, 146, 83, 65].

A wear map for the different tribological experiments is shown in Figure 6.18. These maps were simply constructed by plotting the wear-rate values for each respective load and velocity and then interpolating between each point using a spline interpolation; each point was then compared to the SEM data. Labels correspond to the type of wear mechanisms that were seen for that given condition. The dashed line separates each map where mechanisms associated with primarily oxidative or ratcheting were seen. Unfortunately, there is a lack of data for speeds between 0.10 m/s and 0.50 m/s and so further study could help elucidate the transitions between mechanisms in these areas.

Regarding the wear map, as the load increased oxidative wear mechanisms were less likely to be seen and plate-like wear particles were seen under these conditions, either as debris or adhered to the wear surface. The highest load and speed saw a lot of plastic deformation, with material being displaced to the edge of the pin. Regions where ploughing and platelet wear was observed were also associated with a high degree of deformation at the pin edge, as well as subsurface cracking. These conditions resulted in wear mechanisms similar to those seen on rail steels, as shown in Figure 3.7,

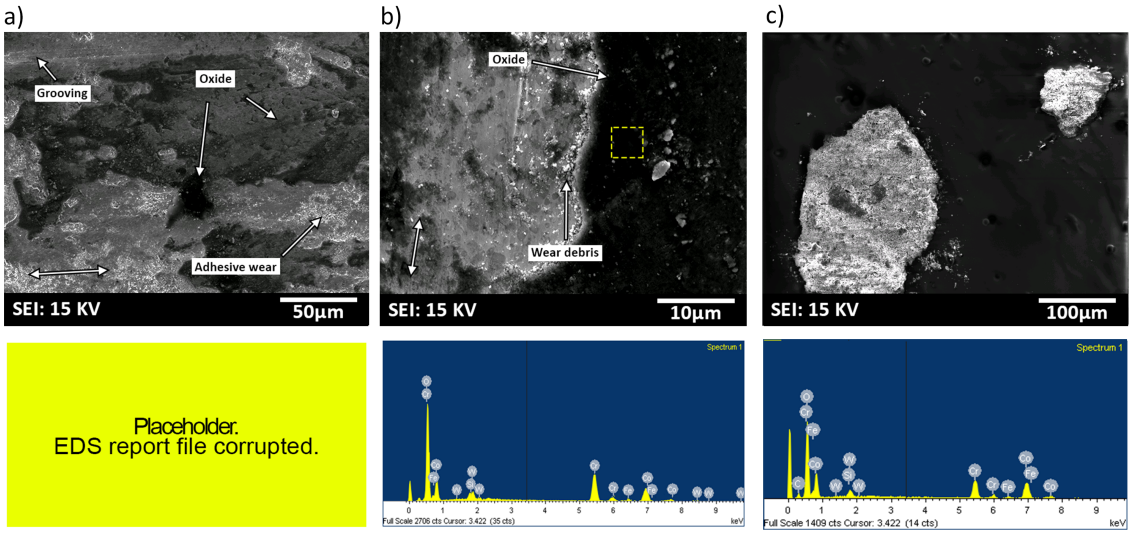

Figure 6.15: SEM micrograph of the (a) pin, (b) plate and (c) debris for a 40 N test at a speed of 0.10 m/s with corresponding EDX measurements below. In contrast to the tests at 400 N, a greater percentage of oxide is seen on the surface, particularly the darkened sections suggesting the presence of an insulating oxide.

where fatigue and ratcheting mechanisms dominate further suggesting the existence of ratcheting wear under these conditions.

A more in-depth study of the wear mechanisms concerning the wear debris and appropriate wear models are given in the next sections.

6.5.2 Archard wear analysis

In accordance to the research aims, we wish to determine if the wear behaviour of Stellite™ 6 is Archard-like to inform the future modelling approach. From all the tests done thus far, self-mated wear of Stellites™ is not Archard-like. The Archard wear equation posits that the wear volume is both linear with load and sliding distance, as in equation 4.7. From the wear-rate data in section 6.4.2 it can be seen that this is not the case, as for the high load we see a decrease in the wear-rate, or an increase as for the high speed data. For the 0.05 m/s and 0.1 m/s cases, the wear-rate may be constant, though the spread of data makes it difficult to determine. Instead, to understand if the Archard equation is appropriate for this system, it is pertinent to see if it satisfies the assumptions of Archard [120], primarily:

1. **The wear particles that are formed are hemispherical in nature.**

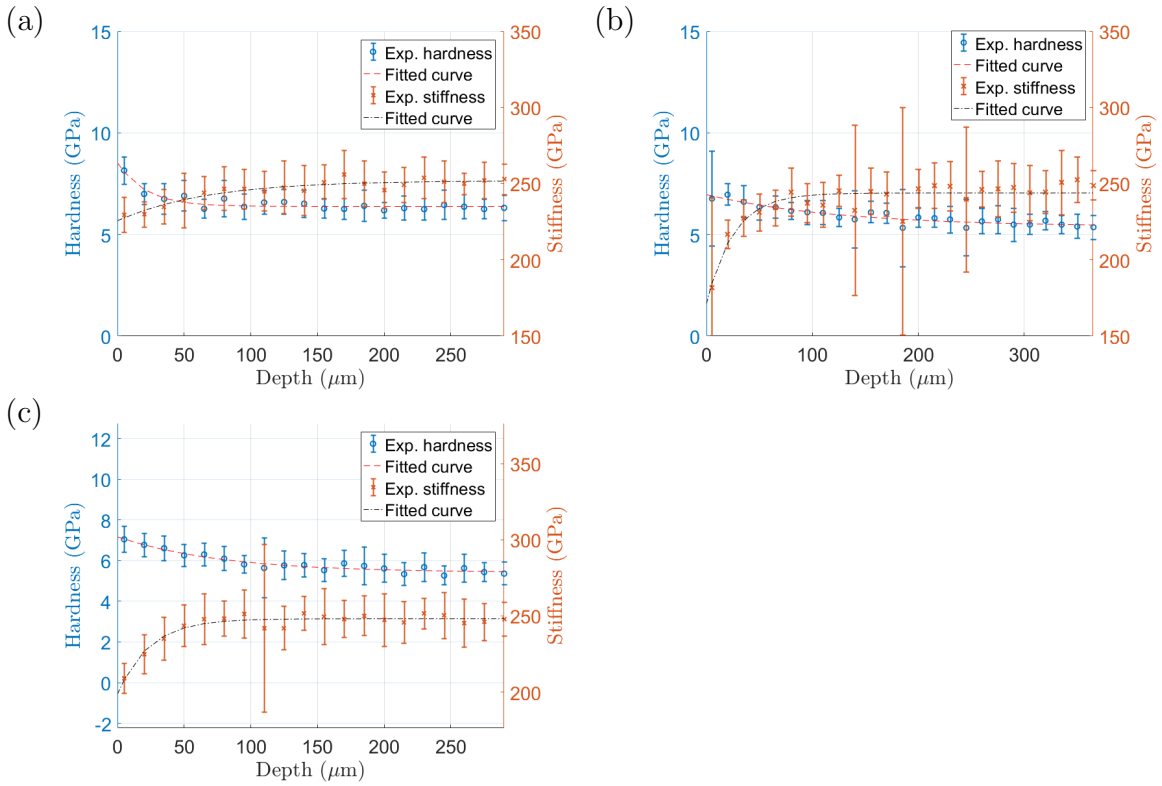

Figure 6.16: Nano-indentation results for the 0.05 m/s, 0.10 m/s, and 0.50 m/s at 400 N

2. **Wear particles are formed when the asperity load is equal to the flow stress of the softer material, assumed to be the hardness H.**

Regarding **(1)**, the wear particles are plate-like rather than hemispherical above 40 N load. This morphology is consistent to the laser-clad Stellite™ literature [58], and also similar to the sliding wear of pearlitic rail steels [148] and Al-Mg_2 si [149] where ratcheting occurs. In the latter case, the wear debris was formed due to the propagation of sub-surface cracks parallel to the sliding direction, similar to the micrographs in Figures 6.11 and 6.8. Regarding **(2)**, the indentation data shows work-hardening, and it is known that such hardening is important in governing the steady-state wear of Stellites™ [19]. Evolution of the hardening behaviour of Stellite™ 6 is not integrated into the Archard equation, and as does not capture the material response on the wear-rate. Implementing hardening effects, and its dependence on temperature, on wear could allow one to understand how Stellite™ may wear during high temperature applications.

In the modelling of Stellite™ wear, Ahmed et al. [50] employed a finite element method of wear and calculated wear depth using the Archard equation. They found that wear-rate, k_w, changed with time. To account for this, they manually entered

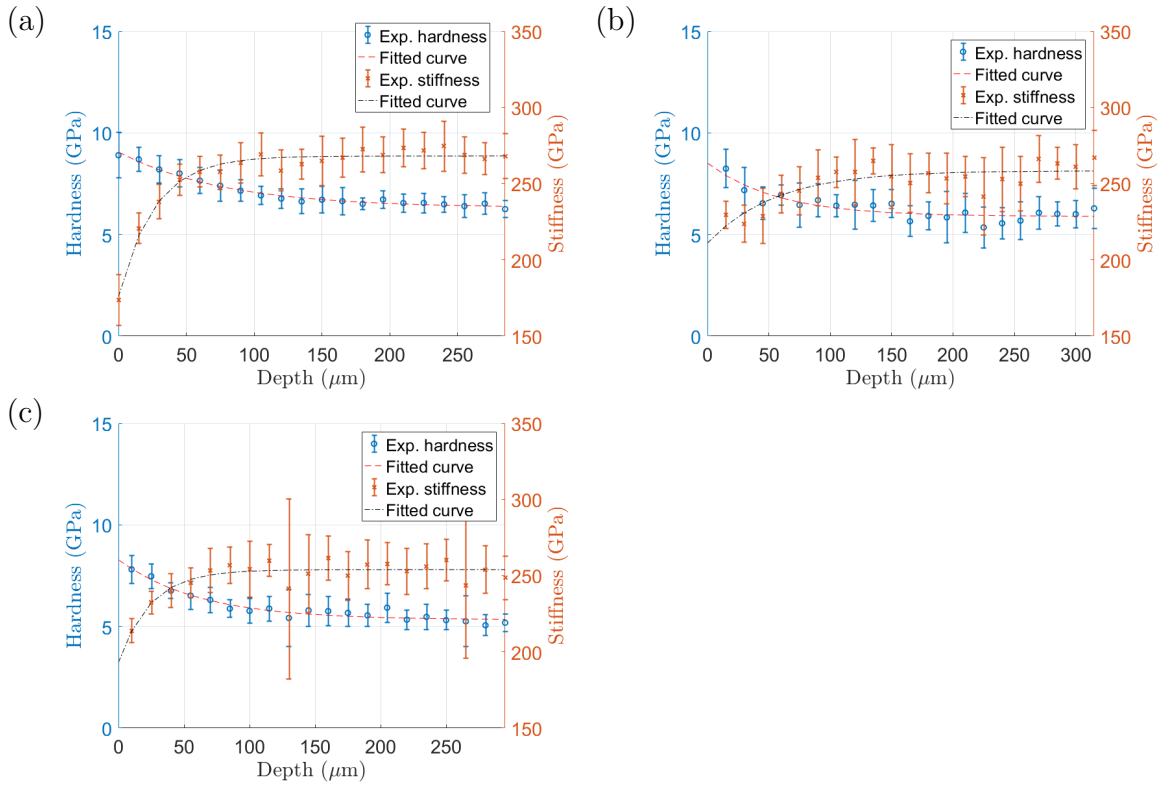

Figure 6.17: Nano-indentation results for the (a) 600 N, (b) 800 N, and (c) 1000 N tests at 0.02 m/s

different values of k_w during the wear simulation. While this recreated the results of their experiment, it meant that prediction of the model was only constrained to the results of their lab tests, severely limiting the applicability of the model, unless variability was built into k_w as a function of a controlled variable.

In conclusion, the basic Archard equation is not appropriate for making predictions for the wear of Stellite™ 6 and must either be extended or a different model that can capture the degradation of this material must be identified.

It is pertinent to ask why these wear particles form as platelet and how. Initially, it may seem that the wear particles occur as the result of mode II (shear) elastic fracture cracks as according to the, now discredited [116], "Suh delamination theory" of wear [150]. However, this is not possible, as the wear particles appear to form in highly strained and work-hardened material [116], where the cracks propagate on planes where frictional stresses suppress linear elastic shear cracks. It is more likely then, as the result of incremental plastic straining, as shown in Figure 6.14, that the cracks are rather instances of material rupture occurring when the strained material reaches a critical strain-to-failure [116]. The plate-like morphology is best explained

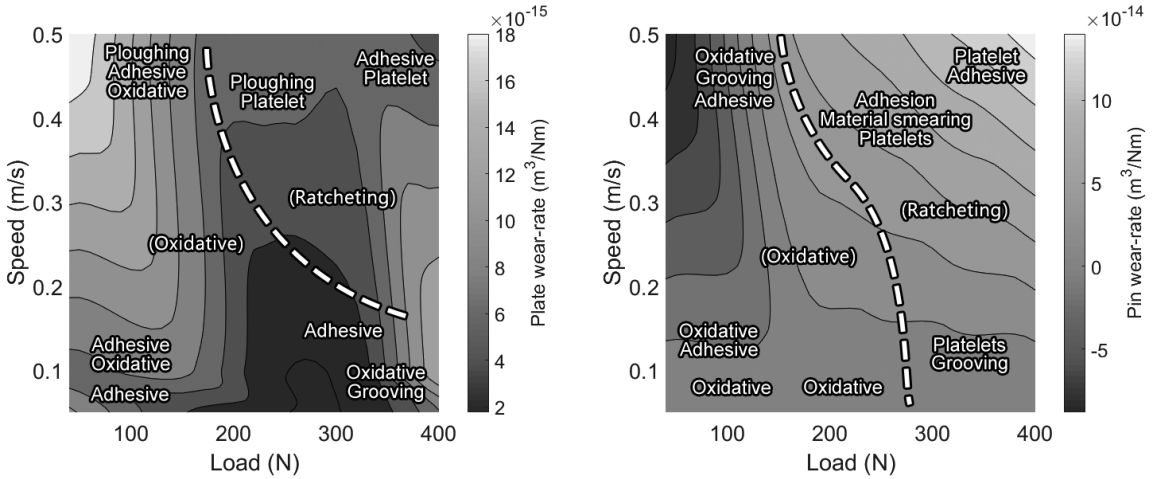

Figure 6.18: Wear-rate maps for the pin and plate of sliding speed vs load for the different tribological tests. These maps were simply constructed by plotting the wear-rate values for each respective load and velocity and then interpolating between each point using a spline interpolation. Each label corresponds to the type of wear mechanisms that were seen for that given condition. The dashed line separates each map where mechanisms associated with primarily oxidative or ratcheting, as shown in brackets, were seen. For the majority of the low load tests, the wear mechanisms were seen to be oxidative in conjunction with the standard modes of ploughing and adhesive. For higher loads, platelet wear dominated with a high degree of plastic deformation.

by the ratcheting wear theory of metals [125], where the applicability of this theory is explored in the next section.

6.5.3 Ratcheting analysis

The likelihood of ratcheting occurring for a given load condition can be determined using equation 4.9, the plasticity index for repeated sliding, repeated here for convenience:

$$\psi_s = \frac{E^*}{p_s}\sqrt{\frac{\sigma}{R}} \tag{4.9}$$

Importantly, for certain values of surface roughness, if this plasticity index exceeds a value of unity, then it can be expected that the mated pair will undergo continuous plastic deformation throughout the wear-test. The values of p_s can be determined from Figure 4.4, by selecting the appropriate p_s/k ratio for the given coefficient of friction and multiplying it by the shear strength at the interface, k, which is related to the hardness by $H/(3\sqrt{3})$. Using the nano-indentation data, the plasticity indices for Stellite™ 6 are shown in table 6.5:

Stellite™ 6 during sliding is undergoing ratcheting, as shown by the numerical analy-

Table 6.5: Table of the plasticity index for repeated sliding with respect to the hardness and stiffness at the pin interface after sliding. The first entry corresponds to unworn values of the pin.

Speed (m/s)	Load (N)	Stiffness (GPa)	Hardness (GPa)	σ (μm)	R (μm)	COF	p_s (GPa)	ψ_s
0	0	223	5.50	0.2	1.5	0.00	4.230	19.25
0.05	400	223	9.12	1.0	1.5	0.40	3.505	51.94
0.10	400	165	6.96	1.0	1.5	0.30	1.339	51.22
0.50	400	199	7.17	1.0	1.5	0.25	4.829	18.43
0.02	600	200	9.05	1.0	1.5	0.35	4.354	37.51
	800	203	10.70	1.0*	1.5*	0.35	5.148	32.20
	1000	193	8.283	1.0*	1.5*	0.35	3.985	39.54

sis using the ratcheting deformation theory. From table 6.5, it is clear that the plasticity index for repeated sliding is much greater than unity for these sliding conditions. This suggests that the wearing surface is undergoing progressive plastic deformation, which is further shown to be the case in Figure 6.14 where the pin has deformed as to form a 'lip' and displaced material can be seen on the pin edge. Further subsurface analysis of the specimens, after etching to reveal the grain structure or through measuring techniques such as electron backscattered detection, would reveal further plastic flow occurring at the surface following the analysis of Dautzenberg [88].

Furthermore, lamellar debris (small thickness relative to its lateral dimensions), can reveal a ratcheting mechanism. As shown in table 6.2, the depth of ductile cracks in the sub-surface of the pin appears to correlate closely to the thickness of the debris. For coefficients of friction above 0.25, the thickness of wear debris due to ratcheting is unbounded. For example, in pearlitic rail steels undergoing ratcheting, debris thickness can reach as high as 30 μm [148]. In other studies of laser-clad Stellites [83, 58] similar lamellar debris has also been observed.

The reason for the crack depth being approximately 3 μm is not entirely known; however it may be due to the presence of sub-surface voids or due to contact with a metallic carbide causing contact stresses to propagate much deeper than expected using a Hertzian contact analysis against a homogenous half-space. Typically, cracks would be expected to propagate from the highest value of strain, which is experienced at a depth of $0.3a$, where a is the contact radius, from the wear interface. For a cylinder of 1.5 μm radius against a half-space under a normal displacement of 0.2 μm, this gives a depth of 0.16 μm whereas, as shown in the simple finite element model in Figure 6.19, for an asperity contacting carbides embedded in an elasto-

plastic matrix, the maximum depth is 0.5 μm with strains as high as 0.2% at a depth of 2.0 μm. Consequently, this may result in larger wear particles and higher wear and highlights the importance of incorporating the influence of microscale heterogeneity onto the wear process.

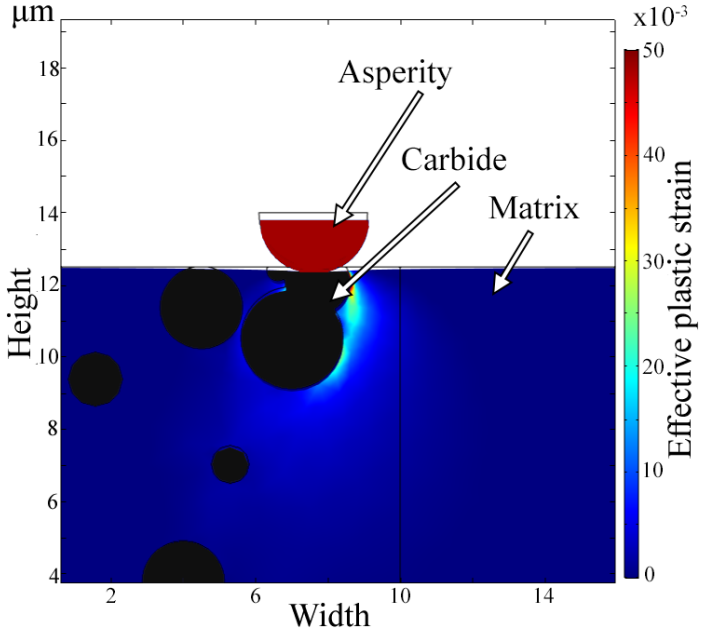

Figure 6.19: A simple finite element simulation of a carbide with Young's modulus 237 GPa indenting an elastoplastic half-space embedded with carbides. Here it can be see that the depth of maximum strain is much deeper than would be expected for a simple half-space as predicted by a Hertzian analysis.

6.5.4 Pin deformation and indentation data

After wear, the worn pins experienced a characteristic lipping deformation parallel to the sliding direction. This characteristic lipping effect is shown on the worn pins in Figure 6.14. This type of outflow has also been observed to occur lateral and parallel to the sliding direction in the case of pearlitic rail steels [151]. This type of flow was identified by Kapoor to be the consequence of ratcheting [125], and suggested that the extrusion of the pin caused thin and brittle material to detach via fracture to form a wear particle. In experiments with copper, Marui and Endo [152] observed a similar flow of material in the sliding direction for copper. They likened this to a combination of material heating allowing for greater ductility, along with ratcheting. Tarasov et al. [153] determined that material flow on the trailing edge occurred, with a strong dependence on crystallographic orientation, as the result of two forces: contact flow due to uniaxial compression and friction.

Table 6.6: Table of H/E, the elastic strain to failure, values.

Speed (m/s)	Load (N)	Stiffness (GPa)	Hardness (GPa)	H/E (μm)
0	0	223	5.50	0.025
0.05	400	223	9.12	0.041
0.10	400	165	6.96	0.042
0.50	400	199	7.17	0.036
0.02	600	200	9.05	0.045
	800	203	10.70	0.053
	1000	193	8.283	0.043

The stiffness at the wear interface drops appreciably as shown in the nano-indentation data in section 6.4.2. Reasons for the increased compliance could be due to material damage [154] and grain refinement. Cobalt-chromium alloys are known to undergo grain refinement, with nano-grains forming at the interface, during surface mechanical attrition [41, 155]. These grains are associated with nanoscale globular and highly charged, i.e. white, adhesive wear particles [45], which are seen in all tests in section 6.4.2. Additionally, numerical studies of grain-refinement show an inverse relationship on modulus with grain size, as grains become sufficiently small [156, 157]. Grain refinement would explain the increased hardness per the Hall-Petch effect [30, 31]. Material damage can also result in increased compliance .

Finally, this decrease in modulus gives an increase in H/E values as shown in Table 6.6, which are important in reducing incremental plastic deformation behaviour, as in Equation 4.9, and may be an additional reason behind the superior wear performance of Stellites™.

6.6 Conclusions

In summary, a new understanding of the wear behaviour for a HIPed alloy using a unique study has been established: it was seen that the formation of cracks, and wear particles, depended on the microstructure; that Stellite™ 6 undergoes considerable plastic straining; and there is hitherto an unknown decrease in the Young's modulus close to the wear interface. The wear mechanisms seen at loads above 160N, plastic straining and platelet wear particles, seen appear to suggest wear by ratcheting deformation.

Under reciprocated motion, performed at room temperature, between 40 N to 1000

N and 0.02 m/s to 0.50 m/s, wear-rates were of the order 10^{-15} m^3/Nm to 10^{-14} m^3/Nm, similar to the literature [48, 49, 146, 83, 65], and various wear mechanisms were seen, including: platelet, adhesive, and oxidative wear. The COF was seen to decrease with load from 0.70 to 0.25, similar to the literature [48, 49, 146, 83, 65]. Application of the ratcheting wear theory [125] to Stellites™, for loads above 40 N, has not been done prior to this thesis. Evidence supporting its usage are:

- **Wear-trends are not Archard-like according to Equation 4.7.**
- **Plastic deformation mechanism causing the initiation and propagation of ductile cracks in the subsurface; typically at carbide boundaries or voids.**
- **Debris are thin and plate-like with debris size being as large as 100 μm diameter in some cases, with debris thickness no deeper than 10 μm, comparable to the depth of cracking.**
- **Edge of the pin is severely deformed after each test as the result of cumulative plastic strain.**

It is expected that, in the case of a PWR, that the ratcheting mechanism will account in part for the purely mechanical part, W_0, of the tribocorrosion equation $S' = T - W_0 - C_0$, and so this study represents an important stepping stone to the desired outcome of modelling the wear of PWR components. However, for this thesis the desired outcome of our model is to predict the wear of Stellite™ in a simplistic dry sliding environment before any environmental complexity is introduced.
Cross-sectional material analysis of the worn pin using nano-indentation techniques revealed an increase in hardness but a decrease in stiffness. To date, this has not been reported for this system and is unique to this study. An explanation for the reduction in Young's Modulus may result from grain refinement [157, 156, 158, 45], or unseen subsurface damage, but further study is needed to clarify this hypothesis. Going forward a ratcheting model capable of incorporating the evolution of material properties may be better suited to predicting the wear of Stellites™. One such model, the numerical Franklin-Kapoor [23], can be used. However, this model suffers from 3 limitations, primarily: it requires full constitutive behaviour of the material, including strain-rates; it does not include microstructure; and it cannot be applied to general macroscopic geometries. Chapters 7 through 8 address these limitations.

Chapter 7
Extraction of Stellite™ 6 material properties using representative volume elements

7.1 Chapter introduction

Following on from the experimental work, it was demonstrated that a ratcheting wear mechanism was occurring for the Stellite™ pair. Importantly, elements of the microstructure — voids and carbides — were influencing the rupture path. The Kapoor-Franklin numerical model of wear is capable of capturing ratcheting wear in a mechanistic way, however the model requires knowledge of the wearing material's constitutive response, while assuming an homogeneous material. Therefore, to address these points, this chapter combines standard uniaxial materials testing (ISO 6892-1 and ISO 12106) with finite element simulations of microstructural representative volume elements for Stellite™ 6 to extract the material response for each metallic phase. Using MATLABs optimisation toolbox, material properties of the metallic phase in Stellite™ were searched for by adjusting material parameters until the over-all stress-strain curves matched between experiment and simulation, henceforth referred to as the "inverse analysis". It is shown that the plastic material response of Stellite™ 6 best follows the Voce hardening law in tension, and experiences non-linear kinematic hardening in cyclic tension-compression.

7.2 Objectives

- Outline the materials testing and the inverse analysis methodologies.
- Compare different hardening laws for the plastic response of Stellite™ 6, and identify the best law resulting in the smallest error.
- Use a statistical analysis on Stellite™ 6 microstructure to determine the size and spatial distributions of hard carbide inclusions and void imperfections.

- Using an inverse analysis, extract the material properties of the metallic phase for use in a modified Franklin-Kapoor model of wear.

7.3 Methodology

Despite there being mechanical testing data for HIP-consolidated Stellite™ 6 in the literature [19, 46, 61], to date no detailed analysis of the full constitutive behaviour of these alloys has been published. Therefore, standard material tests, i.e. tension and tension-compression, of Stellite™ 6 are performed in this chapter. Extraction of elasto-plastic material parameters from the stress-strain behaviour of this alloy will be important in the development of a mechanistic model of wear, as it would allow one to model how the stress-raisers produced by these imperfections produce material rupture, detachment, and therefore a wear-rate.
Furthermore, as was highlighted in the previous section, the role of hard inclusions and voids on the wear mechanisms for Stellite™ 6 are important particularly during plastic straining. However to date, no such data exists for the individual material response of the metallic phase for this material. To determine the elasto-plastic response of this phase, a combination of multi-scale materials modelling and nano-indentation data will be conducted.

7.3.1 Mechanical testing

A monotonic tension tests were performed following British Standard "ISO 6892-1" [142] on an INSTRON 5900 universal servo-electronic tension machine to determine the stress-strain response of Stellite™ 6 under load so that an appropriate hardening law can be determined. The displacement rate was chosen to be 0.4 mm / min to reduce any strain-rate dependant effects in the material, as stated in the standard. The material was taken up to failure in tension where the ultimate tensile strength (UTS) and strain-to-failure (stf) were seen to be the same. Proof stress of the material was calculated using the 0.2% yield offset method.
A cyclic tension-compression tests were performed in accordance to British Standard "ISO 12106" [143] on an INSTRON high-capacity hydraulic testing machine. This performed to determine the cyclic response of the material as, during reciprocated sliding, the contact interface is loaded and unloaded for many cycles due to surface roughness effects. Tests were run under strain-control up to a maximum strain of 0.3% and 0.75% for the low-strain and high-strain tests respectively, with one test

performed up to 1.0% strain, and were cycled until 100 cycles or failure was seen. A sinusoidal loading waveform, with a chosen frequency of 0.06 Hz, was used to ensure that the maximum speed was equal to 0.4 mm / min at 1.0% strain as to minimise strain-rate and inertial effects at the turning point.

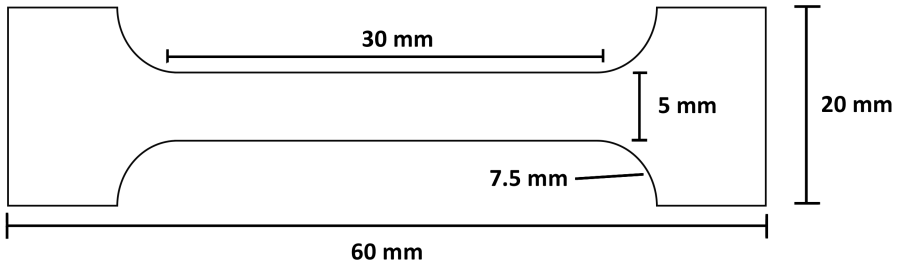

Figure 7.1: Schematic of the dog-bone geometry used in the tension and tension-compression tests. Thickness of the samples were 3 mm and 5 mm for the tension and tension-compression respectively to reduce geometrical effects and the likelihood of buckling as outlined in the standards [142, 143].

A schematic of the dog-bone sample used in both tests can be seen in Figure 7.1. The thickness of the dog-bone in the tension test was chosen to be 3 mm. The relative thinness of this sample meant that the tension test would be best approximated by plane-stress. Conversely, the thickness of the tension-compression sample was 5 mm. This gave a cross-sectional area of 25 mm^2 which, for the given gauge length, was enough to prevent the specimen from buckling when undergoing compression, according to ISO 12106 [143].
Lastly, to measure strain of the sample, an extensometer with gauge length 10 mm with an extension of 1 mm to give maximum output of 10% strain was placed onto the gauge of the sample and measured by the computer software.

7.3.2 Hardness simulation

To validate the hardening law at the microscale, a micro hardness simulation was conducted using the finite element method. Hardness, aka the resistance to permanent deformation, is typically calculated by performing indentations into metal using a diamond indenter and dividing the maximum load against the projected area, i.e. the area produced by the indentation, $H = F/A_p$. At this scale, the plastic deformations are expected to be finite, i.e. greater than 15%, so a finite-strain plasticity model was used. For these simulations, we are only interested in the *deformed* configuration of the surface.

The simulation geometry can be seen in Figure 7.2(a), and a 3D Vickers indenter is shown in Figure 7.2(b), where the blue domain represents the metal and red for the indenter. Given the symmetry of the Vickers indenter, it was sufficient only to simulate a quarter of its geometry. The half-space dimensions were 50 μm by 50 μm by 50 μm. The apex angle of the pyramidal indenter was 136°, resulting in a 22° angle between half-space and indenter, thereby matching the Vickers geometry.

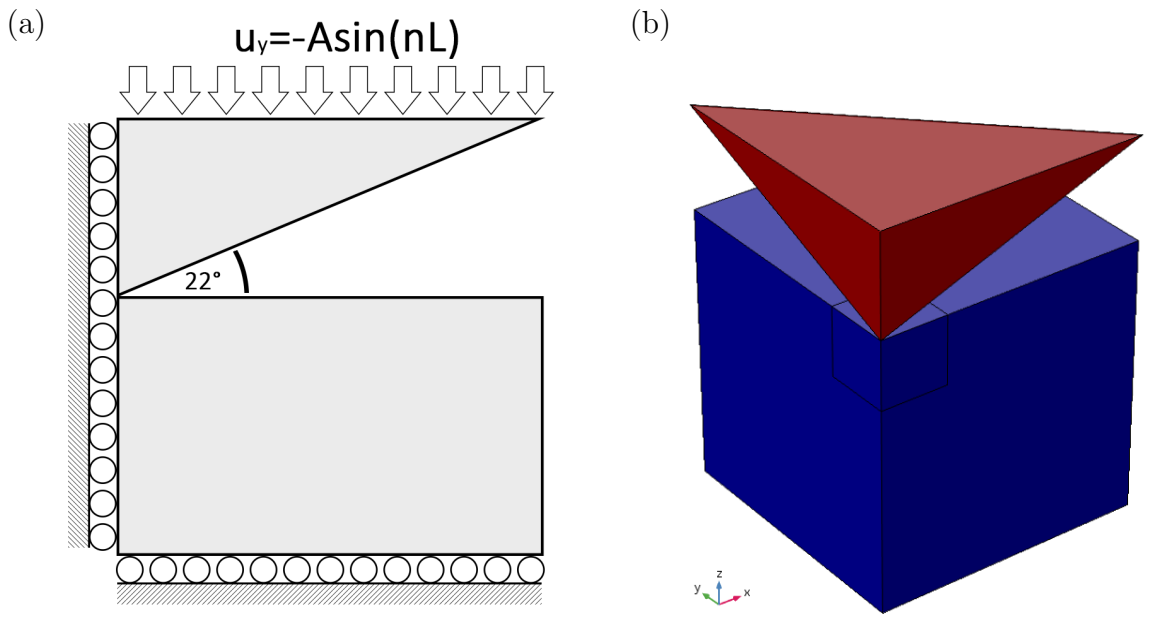

Figure 7.2: Geometry used in the finite element simulation of a Vickers indent showing (a) Boundary conditions of the indenter, where the top boundary was sinusoidally displaced up to a maximum amplitude of 1 μm (b) 3D view of geometry where the red and blue domains corresponds to the metal and diamond indenter respectively.

The boundary conditions are shown in the schematic of Figure 7.2(a). The top boundary of the indenter was loaded sinusoidally under displacement control, such that the maximum amplitude, A, was 1 μm. The left and bottom most boundaries were fixed in their lateral directions as to prevent free rotation of the body.

An augmented Lagrangian contact algorithm was selected to minimise over-closure between the indenter and metallic half-space. Hardness is calculated by taking the maximum applied load and dividing it by the projected area the point of unloading, and is the same method used in the calculation of Vickers hardness. The chosen Young's modulus and Poisson ratio for the indenter were 1141 GPa and 0.07 respectively, which are typical for a diamond indenter.

7.3.3 Statistical analysis of the microstructure

In order to build the representative volume element (RVE) of HIPed Stellite™ 6, it was decided that it would be best if carbide and void populations could be modified to delineate their effect on the over-all material response. Thus, instead of replicating the exact microstructural geometry as seen under SEM, a statistical analysis of the microstructure was performed to determine the spatial and size distributions of the carbide-phase and voids. Image analysis of the microstructure was performed using MATLAB 2016b on three SEM micrographs of the chosen Stellite™ 6 alloy, shown in Figure 7.3. A total of 3 micrographs were used with each image selected to be 935 by 935 pixels.

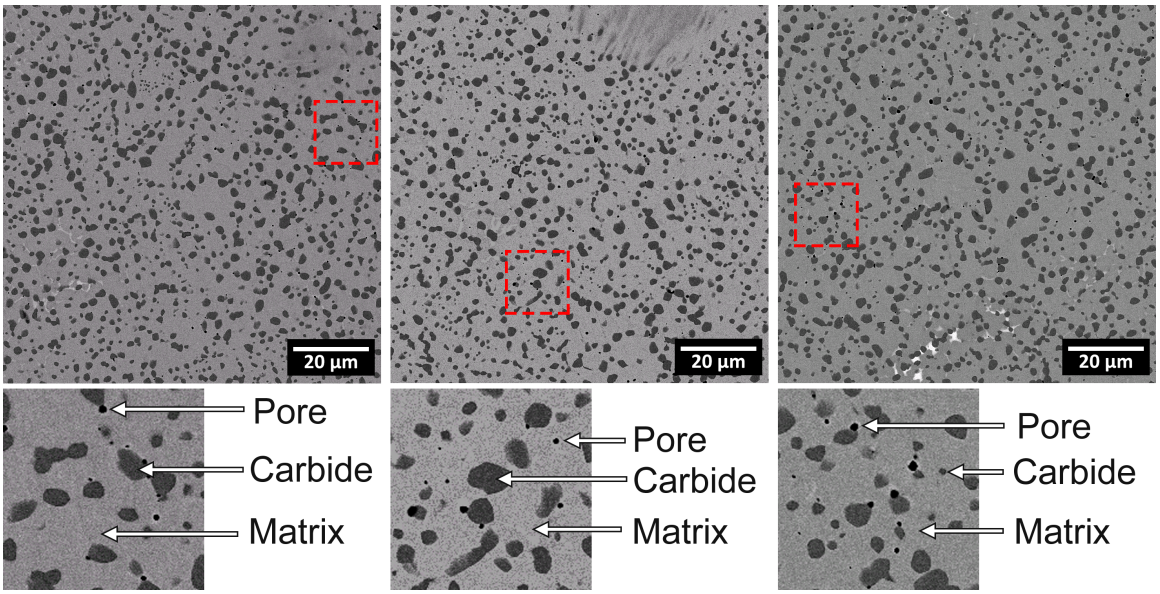

Figure 7.3: The 3 micrographs sampled for the statistical analysis of the microstructure. The red dotted line indicates the zoomed area shown beneath each respective micrograph to demonstrate the existence of voids or pores. The metallic matrix, carbides and voids are light grey, dark grey and black respectively. Pores are either angular or circular in nature.

The different greyscale values for the metallic matrix, carbides, and voids (light grey, dark grey, and black respectively) made it possible for each phase to be distinguished. The levels of each image were adjusted such that the metallic matrix was pure white, the voids pure black, and the carbides occupying any value in-between. The microstructural images were then loaded into Matlab in greyscale bit-mode, meaning each pixel in the image had 8 bits associated with its greyscale value, with the matrix and carbides/voids corresponding to colour values of 255 (black) and 0 (white) respectively. The result was a bitmap consisting of a series of "islands" in a "sea" of

white 255 bit values.

Using MATLAB 2016bs Image Analysis Toolbox, collections of pixels were identified, using *bwconncomp*, as belonging to a single carbide if they occupied any bit value between 1 to 254 and were adjacent to other pixels within this range. Likewise, the same analysis was performed for voids. To improve the analysis, coalesced carbides, or overlapping carbides, were partitioned by running ImageJs "Watershed" tool on the binary image. Each pixel also corresponded to an area of 0.78 μm^2, calculated by taking the ratio between the number of pixels in the scale bar and the distance it represented (in this case 20 μm/175 px). Each cluster of pixels constituting a carbide or void then had their centroid values calculated using *regionprops*, as well as their total surface area. Table 7.1 shows the area fraction and number of inclusions per unit area values for microstructure.

Table 7.1: Table of the area fractions of the individual phases extracted using image analysis of the microstructure and their respective standard deviations. Number density corresponds to the amount of carbides and voids per unit area.

Phase	Area fraction (%)	Number density (μm^{-2})	Max radius (μm)	Min radius (μm)
Matrix	0.8058	–	–	–
Carbide	0.1934 ± 0.0045	0.0939 ± 0.0125	2.987 ± 0.477	0.129 ± 0
void	0.0008 ± 0.0005	0.0029 ± 0.0021	0.727 ± 0.129	0.129 ± 0

To simplify the following analysis and the creation of an RVE, the carbide and void shape are assumed to be spherical given their spherical-like morphology in the SEM micrographs of Chapter 5. This allows one to then represent carbide sizes in terms of a radius, by taking the equation of $r = \sqrt{A/\pi}$, where A is the surface area of the corresponding carbide. A histogram of the spatial and size distributions of carbide and void then calculated using *histogram*, and then normalised to give probability density functions (PDFs) of the distributions (Figure 7.4).

The distribution of carbide and void radii corresponded best to a Gamma PDF of the form:

$$f(r;\alpha,\beta) = \frac{\beta^{\alpha} r^{\alpha-1} e^{\beta r}}{\Gamma(\alpha)} \tag{7.1}$$

where α and β are the distribution parameters, r is the range of radius values, and Γ is the gamma function. The parameters for both carbides and voids, of the above distribution, can be seen in Table 7.2.

Circularity is also shown in Table 7.2, which is a measurement of how close a shape

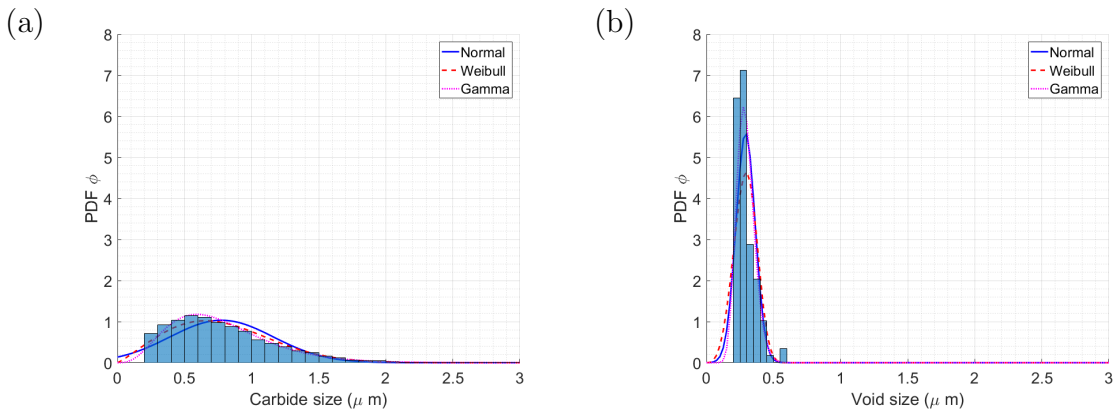

Figure 7.4: The statistical radii distributions of the (a) carbides and (b) voids. Several PDFs were tested against the histogram, and it was concluded that the Gamma distribution gave the best fit.

Table 7.2: Table showing the circularity, with standard deviation, and parameter values of the radii distributions for voids and carbides, analysed from Figure 7.4.

Phase	Circularity	α (μm)	β (μm)
Carbide	0.964 $\pm$ 0.207	5.001	0.148
Void	1.464 $\pm$ 0.307	19.91	0.015

is to a perfect circle with 1 being ideal. For carbides, this is 0.964 $\pm$ 0.207, further highlighting the assumption that carbides can be approximated as circles. However, for voids, the shape deviates from a circle. This indicates that voids may correspond to a more quadrilateral morphology, as seen in SEM micrographs, as well as circles.

7.3.4 Representative volume element construction

Using the statistical data from the previous section, the RVE can be constructed as shown in Figure 7.5. For this work, a total of 3 RVEs were used to account for the statistical variation of the microstructure. The creation of the RVE, using a geometry building subroutine, was built using COMSOL Multiphysics LiveLink for MATLAB. Tension tests are best approximated as plane-stress due to the relative thinness of the dog-bone sample, so a 2D plane-stress finite element model was used. Carbides and voids are approximated by circles as justified by the circularity measurement from the previous section.
To confirm the usefulness of the RVE, it must satisfy the following conditions [119]:

1. The RVE must be statistically similar to the microstructure.

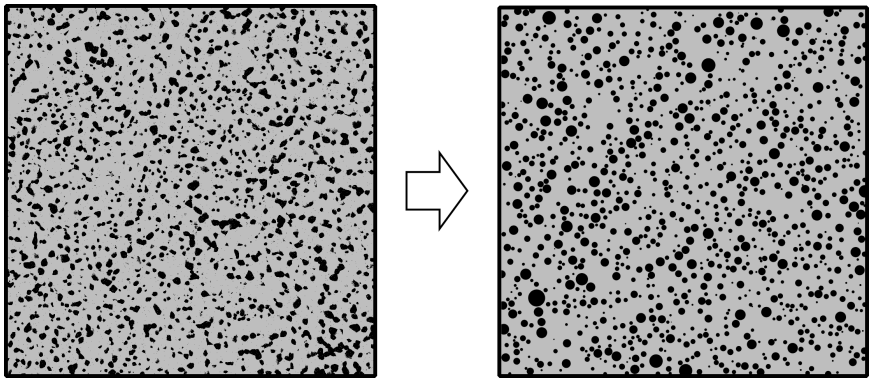

Figure 7.5: Left-hand microstructure sampled to produce the right-hand geometry used in the finite element simulation for the inverse analysis. The right-hand morphology has a different population to the left, and may be explained as a consequence of not discerning coalesced carbides in the experimental morphology.

2. The RVE must be large enough such that the boundary conditions do not influence the constitutive behaviour.

The first condition can easily be confirmed by performing the same statistical analysis, as in the previous section, on the generated RVE geometry. The number density, α and β statistical parameters of the FE model are shown in Table 7.3, with the relative error between experiment and simulation shown.

Table 7.3: Table showing the statistical values for the FEA geometry. The relative error corresponds to the difference between simulated and experimental values.

Phase	Number density (%)	Percent error (%)	α	Relative error (%)	β (μm)	Relative error (%)
Carbide	0.0878	6.41	5.42	8.37	0.145	1.97
Void	0.0029	5.13	21.2	6.47	0.016	10.2

Of note are the sizes of the relative errors, when compared to the experimental case, regarding the mean and variance in carbide and void radii. This may be explained due to the inability for the image analysis to separate coalesced carbides, which it then approximates as a single circle, as demonstrated in Figure 7.6. This would explain the relative closeness of simulation and experimental carbide number densities, but the drastic differences in the other values as shown in Table 7.3.

To satisfy the second condition, a minimum RVE size was chosen such that variation in the Young's modulus, determined by dividing the average stress by the average strain at the beginning and end of the simulation, within a section of material as to

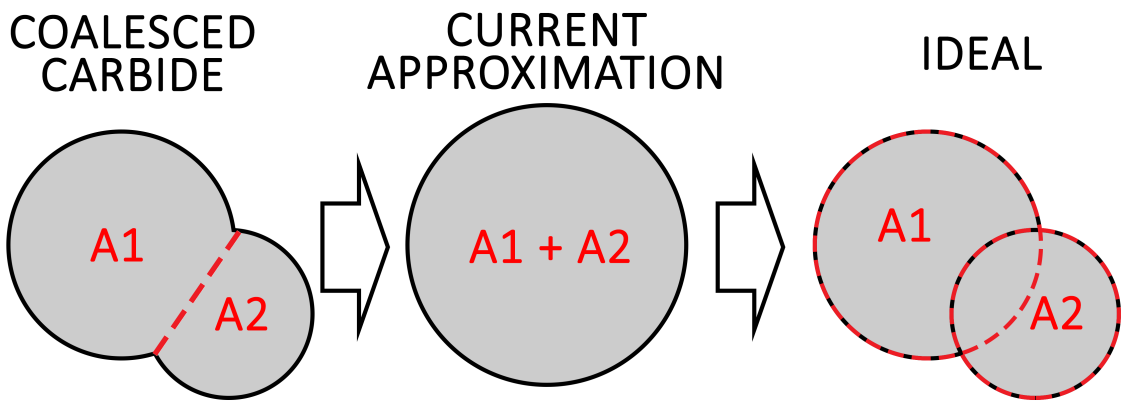

Figure 7.6: A diagram showing how the current geometry building subroutine approximates coalesced carbides of areas $A1$ and $A2$ as a single, larger, carbide of area $A1 + A2$. The ideal case would separate and then create two carbides of areas $A1$ and $A2$, which then overlap them as in the ideal case.

not include the boundary, became independent with scale. This was identified to be 100 μm by 100 μm.

For this work, 3 RVEs were used with different permutations of the microstructure in order to account for the statistical variation in the microstructure.

7.3.5 Inverse analysis

With the RVE selected, the inverse analysis is now conducted. At each load step, the stress and strain values on the RVE are averaged across a 50 by 50 point matrix to give the stress-strain at that load step, with the points chosen to minimise edge-effects. Despite the non-linear response of plasticity, averaging in the simulation makes sense if we consider that the strain measured in experiment is collected as an averaged response across an extensometer or strain-gauge.

The simulation boundary conditions are shown in the schematic of Figure 7.7. The left and bottom most boundary were fixed in the x and y direction respectively. The top-most boundary was then pulled vertically in tension in increments of n up to a maximum load of N_{max}. These boundary conditions were chosen as to reduce the off-axis strains as to emulate the tension test. The process for extracting the plastic parameters is then outlined in Figure 7.8 by minimising the difference between experimental and simulated stress-strain.

The four elasto-plastic variables to search for in the matrix were the Young's modulus, yield stress, and two plastic hardening parameters corresponding to an appropriately

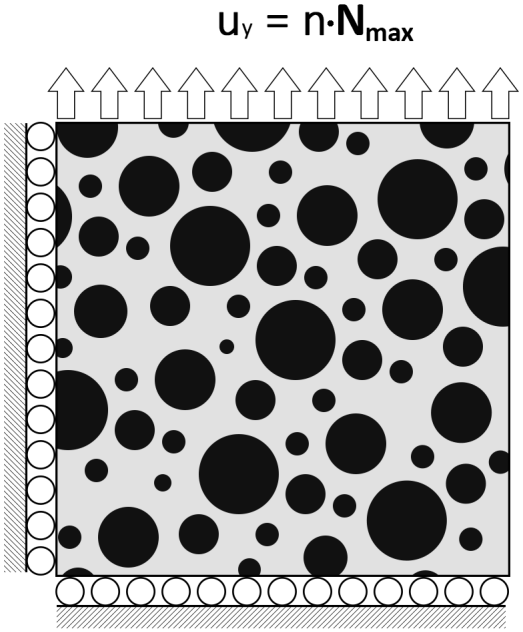

Figure 7.7: Schematic showing the boundary conditions for the RVE being pulled vertically in tension, where n is the incremental load step up to a maximum load N_{max}, with the left and bottom most boundaries constrained in the y and x axis respectively.

chosen hardening law from the experimental stress-strain data. The simulation was run with a finite-strain isotropic plasticity model with a Voce-like hardening function.

The material parameters for the carbides were collected from the literature [159, 160], with Young's Modulus and Poisson ratio 300 GPa and 0.33 respectively. The carbides were also assumed to be purely elastic, given their relatively high hardness and modulus compared to the matrix. Likewise, the voids were meshed with a Young's modulus of 1 Pa as to act like an exclusion of material.

The elastoplastic variables were searched for using MATLABs optimisation toolbox. Primarily, the difference between the simulated and experimental stress-strain curve was minimised using the Levenberg—Marquardt algorithm [161], which simply searches for the local minimum in a given parameter space by minimising the sum of the least-squares of deviations, i.e. the difference between the empirical and simulation data. To improve the robustness of the search for variables, a parameter space using Latin-hypercube-sampling of 20 samples for each variable was constructed. The relative error between the simulated and experimental stress-strain curves for this parameter space were plotted, an example is given in Figure 7.9. This allowed for an initial best guess of the material parameters by finding a local minimum.

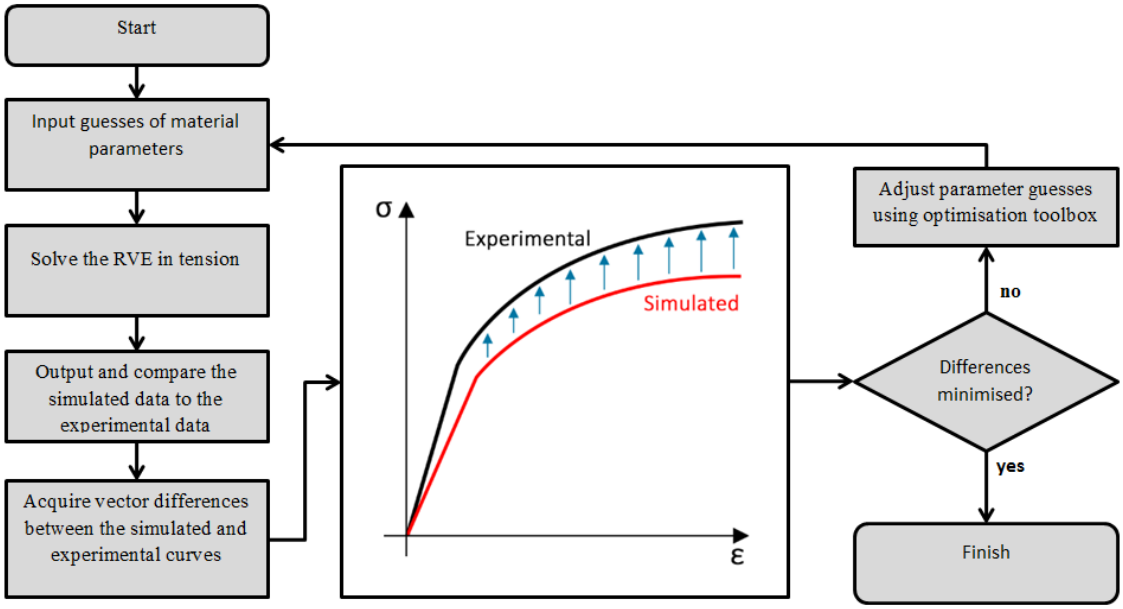

Figure 7.8: Flowchart outlining the general procedure employed to extract the material properties of the metallic phase.

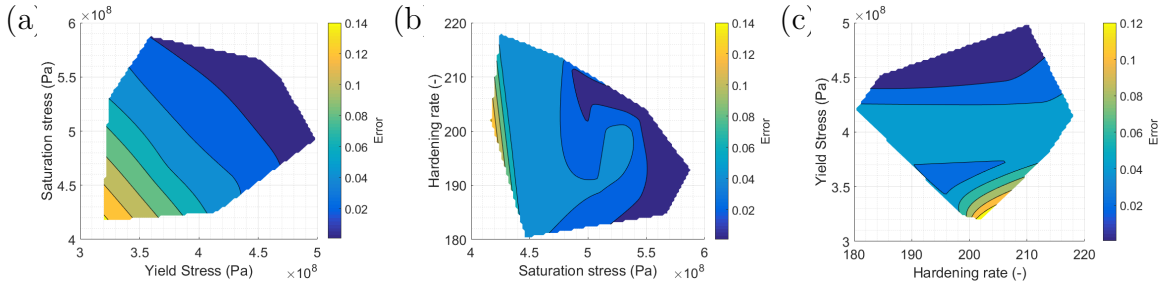

Figure 7.9: The parameter spaces used to find the best initial guess in the optimisation, showing (a) saturation stress versus yield stress, (b) hardening rate versus saturation stress, and (c) yield stress versus hardening rate.

7.3.6 Nano-indentation

Finally, to validate the extracted parameter values, a comparison to nano-indentation data is performed. The indentations were depth-controlled up to 50 nm indents as to minimise any potential influence of sub-surface carbides during matrix indentations, and likewise to prevent the matrix biasing the indentation values on carbides, so that individual phase mechanics could be extracted. A diamond berkovich indenter was used, with Young's modulus and Poisson's ratio of 1141 GPa and 0.07 respectively. Over 400 indents were performed in order to give a large spread of data.

As it is not possible to completely eliminate the influence of other material phases at any point during indentation, a statistical approach was used. The values of stiffness

and hardness measured across the indents were de-convoluted by measuring how many indents corresponded to a given mean of stiffness and hardness values, using MATLABs *kmeans* function. Each cluster of data was then counted using MATLABs *histogram* function. Each data cluster was then fitted to a chosen probability density, using the $fitdist$ function, which de-convoluted the nano-indentation data into high and low values of stiffness and hardness, assumed to correspond to carbide and matrix respectively.

7.4 Results

7.4.1 Mechanical testing

The results of the monotonic tension test can be seen in Figure 7.10. 5 tests were conducted to get a good idea of the stress-strain response of this material.

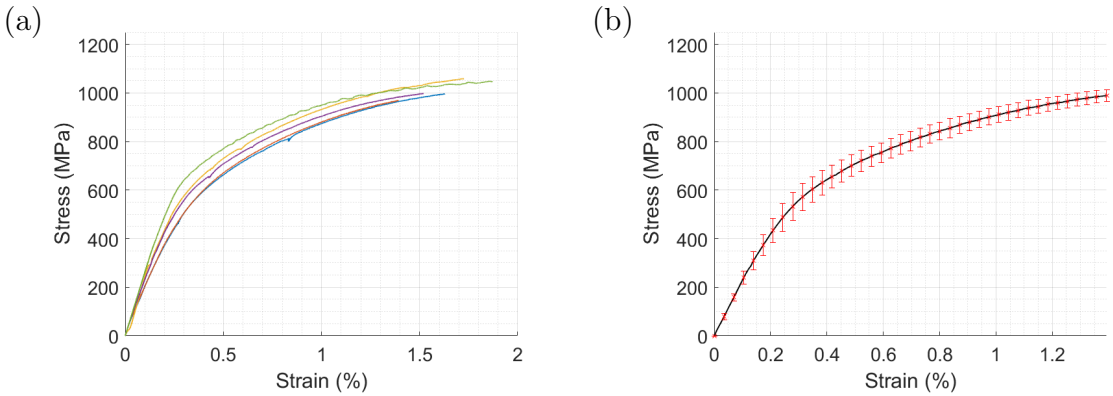

Figure 7.10: The stress-strain curves resulting from the monotonic tension tests, (a) all the individual tests, (b) the mean response of all the curves.

The general stress-strain response appears to correlate well with the materials data in the literature [61]. The Young's modulus for this material is 216 ± 30 GPa, which compares to a value of 237 GPa stated in the literature [61]. Using the 0.2% offset yield point, the proof stress of this material lies around 730 ± 30 MPa, resulting in only a 0.04% relative difference to the literature.
Determination of the yield stress in this material is defined as the point at which the stress-strain response diverges from linearity. In this case, it was calculated using an 0.01% offset yield point, rather than 0.2%, as this gives a better measurement of deviation from linearity. This gives a yield stress of 446 MPa for this material. Correspondingly, the hardening behaviour beyond yield was fitted to Voce, Ludwik, and linear hardening laws (as outlined in Section 4.4). The law giving the smallest

R^2 value was selected for the modelling of Stellite™ 6. The fitted curves can be seen in Figure 7.11.

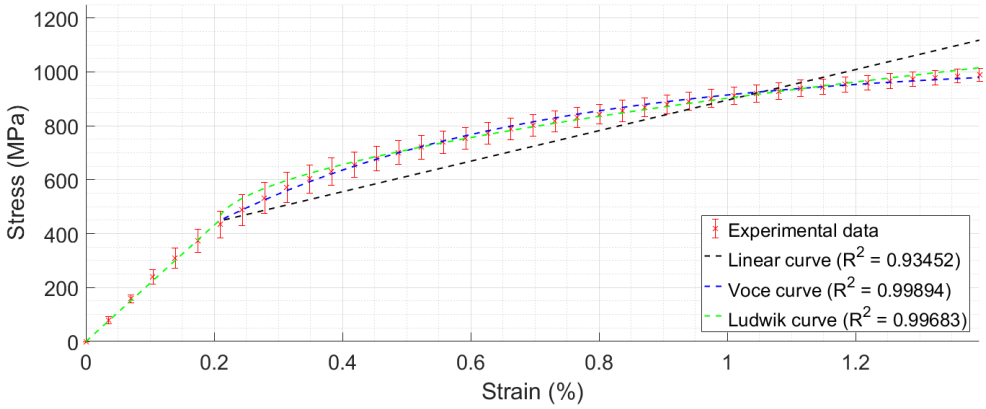

Figure 7.11: The stress-strain curve with the different hardening law fitted to the experimental data.

The R^2 of each fitted curve, corresponding to an particular hardening law, was calculated against the mean data as in Figure 7.11. The R^2 between the Voce and Ludwik laws are negligible, suggesting that either would be appropriate for modelling the plastic behaviour of Stellite™ past yield for this range of strain. For this project, the Voce hardening law was selected as it was seen to give good results. The linear law corresponded to a much less good fit as indicated by the R^2 value and would not be appropriate as an approximation for large strains. The elasto-plastic material parameters for the chosen hardening law are summarised in table 7.4.

Table 7.4: Table showing the elasto-plastic parameters determined from the tension tests.

Material Phase	Young's Modulus (GPa)	Yield stress (MPa)	Proof stress (MPa)	Strain-to-failure (%)	Saturation stress (MPa)	Hardening rate
Homogenised	215 ± 27	450 ± 12	720 ± 59	1.5 ± 0.19	586 ± 26	202 or 300 (FEA) ± 1.5

The cyclic stress-strain response of the alloy is slightly different to the monotonic response, and can be seen in Figure 7.12 for experiments strain controlled up to 0.3%, 0.75%, and 0.1%.

As demonstrated by the low-strain test in Figure 7.12, the yielding behaviour of Stellite™ happens much sooner than the typical 720 MPa proof stress given in the literature [46].

To capture this cyclic stress-strain behaviour, an Armstrong-Fredrick kinematic hardening model [162] was chosen, with perfect plasticity. This non-linear kinematic

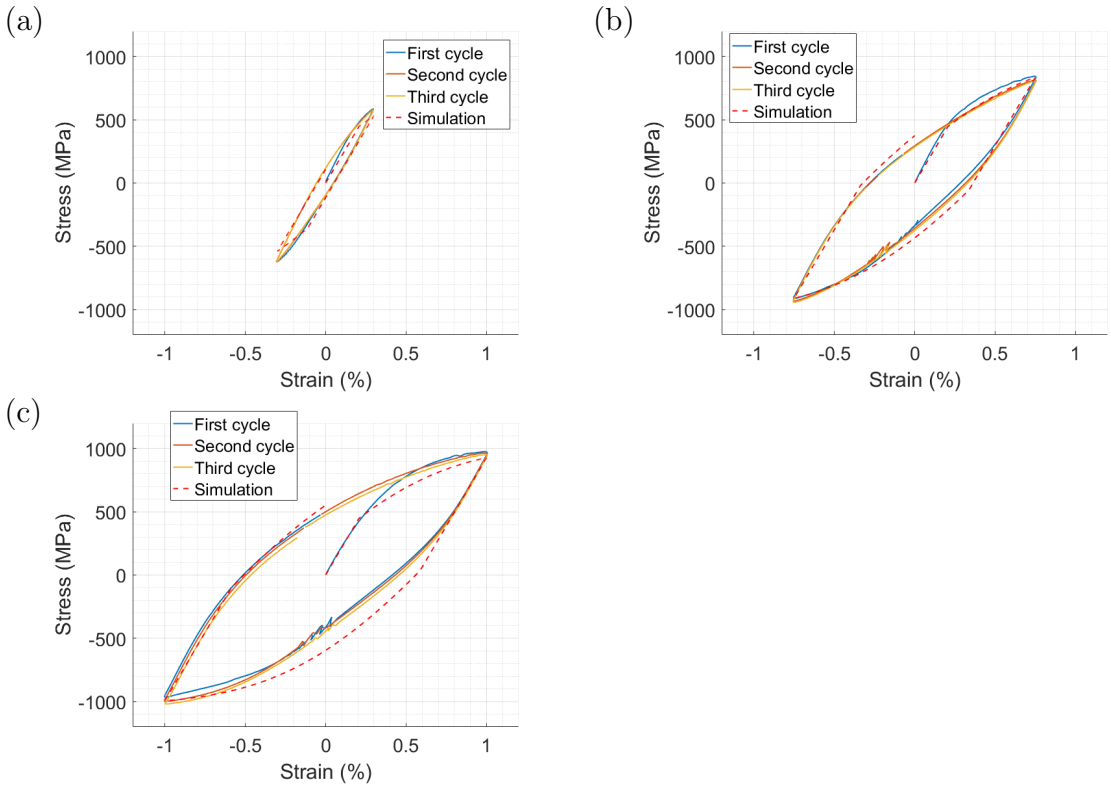

Figure 7.12: The stress-strain curves resulting from the cyclic tension-compression tests. (a) strain-controlled up to 0.03%, (b) 0.075%, and (c) 0.1%.

hardening model simulates the fact that, after tension, the yield stress is less in compression than in tension. This is known as the Bauschinger effect [24]. This is done by translating the locus of the yield surface in stress-space by the equation:

$$\dot{\sigma_b} = \frac{2C}{3}\dot{\varepsilon}_{pl} - \gamma_b \dot{\bar{\varepsilon}}_{pl}\sigma_b \tag{7.2}$$

where $\bar{\epsilon}^p$ is the effective plastic strain, σ_b and $\dot{\sigma_b}$ are the back-stress and back-stress rate respectively, and γ and α are kinematic hardening parameters. During monotonic tension, the stress-strain curve response of the Voce hardening model behaviour is similar to the kinematic hardening model. In fact, if one integrates equation 7.2 in time, the form of the integrand is identical to the Voce hardening model [163] and the hardening parameters can be related by $\gamma = Hb$ and $\alpha = b$. This fact is demonstrated in Figure 7.13. With this, the kinematic behaviour can be derived from the tension behaviour and is shown in Table 7.5.

Figure 7.12 shows the simulated cyclic stress-strain response overlaid on the experimental curves. Generally, the trends appear to match with slight differences in the hardening rates and Young's moduli. Generally, the hardening rate appears to be

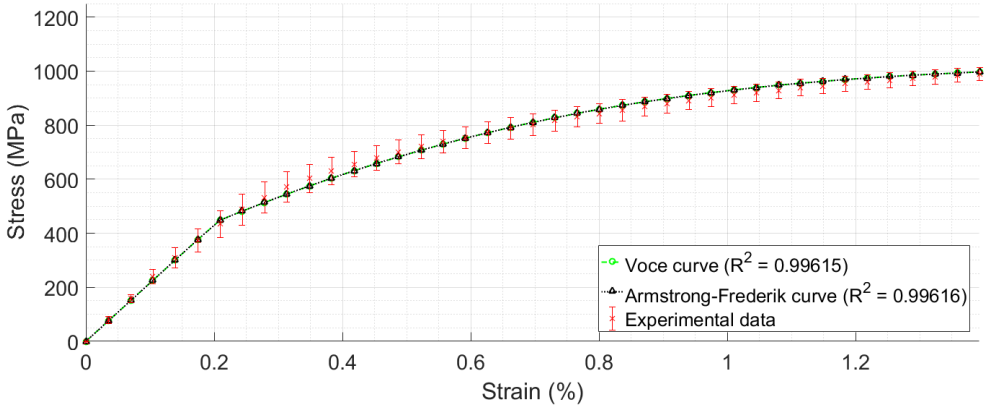

Figure 7.13: The parameters of the Voce and Armstrong-Frederick hardening laws can be related by $\gamma = Hb$ and $\alpha = b$ by integrating the back-stress equation in time. The stress-strain curve of Voce and Armstrong-Frederick with these selected values demonstrates this fact.

Table 7.5: Table showing the elasto-plastic parameters derived from the integral of equation 7.2.

Material Phase	Young's Modulus (GPa)	Yield stress (MPa)	Kinematic hardening parameter (MPa)	Back-stress rate (GPa)
Homogenised	215 ± 27	450 ± 12	118 ± 39	202 / 300 (FEA) ± 1.5

much higher than predicted in the simulation. Nevertheless, the response of the alloy during compression after the initial tension phase appears to deviate from linearity much sooner than would be expected, when compared to the simulated behaviour.
Interestingly, for the monotonic test, the finite element simulation gives a value for β which is 50% higher when fitted against experimental data than the value given by the least squares fit performed on the experimental data in Matlab. Reasons for the discrepancy between the value in Matlab and finite element simulation data are presently unclear. Thus, for the finite element simulations, all data will check against the 50% higher value of β.
The verification of the chosen hardening law are given in the following section.

7.4.2 Hardness analysis

The load and area response curves for the hardness indentation, in the deformed configuration, can be seen in Figure 7.14. The hardness simulation was ran using a finite-strain isotropic plasticity model with the plasticity parameters from the previous section used as input. For this analysis, we are only interested in stresses and strains

measured in the deformed configuration.

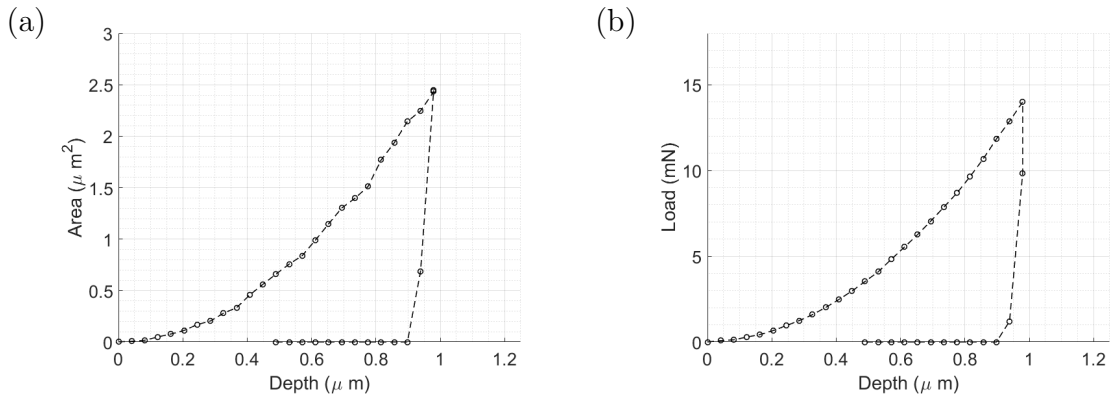

Figure 7.14: (a) The simulated area, and (b) load response curves to being indented with a Vickers hardness indenter.

The hardness of this material can thus be calculated using the $F/A = H$ formula, where F is the normal load and A is the projected area. Depending on the integration order chosen, the projected area values changed. Therefore, it was decided that a range of different projected areas should be used to give a range of the hardness of this material.

The final form of the indentation can be seen in Figure 7.15. As expected, the sub-surface of the material has yielded resulting in a spherical like region of plastic strain just below the point of contact. The effective plastic strain is quite high, about 83%, meaning the choice of a finite strain plasticity model was necessary.

The load and areas at the point of unloading were 3.58 mN and 6.67×10^{-13} m^2 or 8.02×10^{-13} m^2, depending on the integration order. This resulted in hardnesses of 4.46 GPa to 5.36 GPa, or 446 HV to 536 HV, which is exactly the range given for Stellites$^{\text{TM}}$ [46], with an example experimental indent shown in Figure 7.16. It is worth noting that the simulation strain is much higher, almost 54-fold, than the monotonic strain-to-failure which will be discussed later.

Particularly, the results of the indentation test demonstrate that the Voce hardening law is appropriate for Stellite$^{\text{TM}}$ 6.

7.4.3 Inverse analysis

Using the Voce hardening law, the plastic parameters to search for were the yield, σ_Y, the saturation stress, H, and the hardening rate, b, in addition to the Young's modulus, E. The best initial guesses given for the simulation are given in Table 7.6.

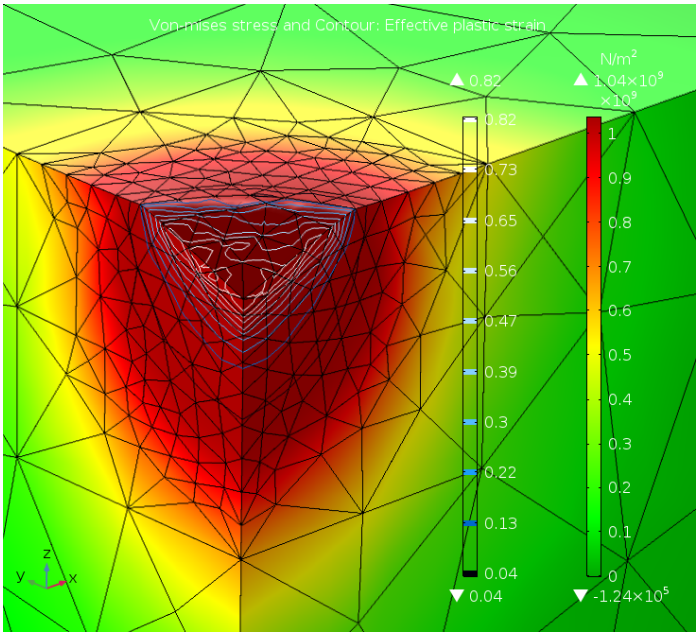

Figure 7.15: The final form after indenting the elasto-plastic half-space with a diamond indenter. The contour plot and gradient surface correspond to the effective plastic strain and the von Mises stress respectively.

The time taken to construct the initial guesses was approximately 10 hours, but in doing so the better initial guess would aid convergence of the optimisation routine.

Table 7.6: Table showing the initial guesses for the inverse analysis.

Material Phase	Young's Modulus (GPa)	Poisson Ratio	Initial yield stress (MPa)	Initial saturation stress (MPa)	Initial hardening rate
Homogeneous	215	0.3	450	586	202/300 (FEA)
Carbide	300 [159]	0.33 [159]	–	–	–
void	0.001	0.0	–	–	–
Matrix	204	0.3	470	548	203.6

Figure 7.17 shows the homogenised curve resulting from the average σ_{yy} and ϵ_{yy} components across a 50 μm by 50 μm section, as to minimise any edge effects. As it can be seen, it appears to fit well within the range given by the experimental data. This suggest the selected parameters correspond well to the constitutive behaviour of the metal matrix.

The resulting values of the parameters derived from the inverse analysis for each individual phase is given in table 7.7. It can be seen that the matrix has a reduced Young's modulus when compared to the macroscopic response, and a resulting increase in the yield stress. The hardening rate is also much slower in the matrix alone. It took several hours to search for these parameters using the optimisation routine,

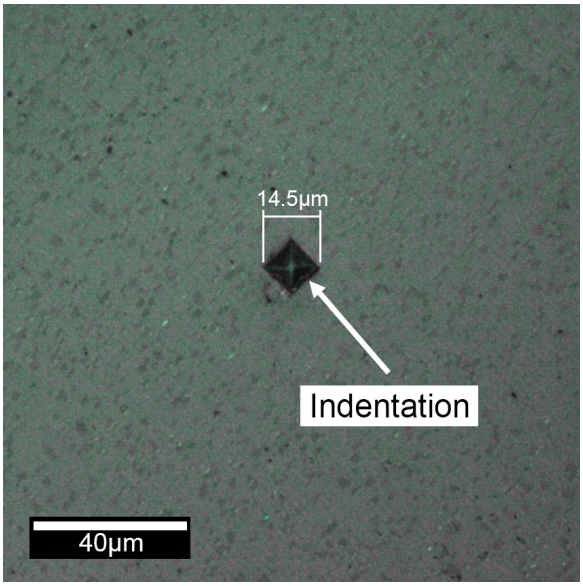

Figure 7.16: An optical micrograph showing the Vickers indentation on Co-Cr. This indent was made under 50 gf and resulted in an average diameter of 14.5 μm, which corresponds to a Vickers hardness of 449HV. Importantly, no cracking can be seen to emanate from the indenter edges.

which resulted in a relative error between the experimental data and simulated curves of $< 0.001\%$ and 0.05% for the elastic and plastic responses respectively.

The typical plastic strain field experienced during the tension test for the heterogeneous microstructure is displayed in Figure 7.18. It can be seen that the voids and hard phases act as stress-raisers with the plastic strain propagating preferentially around these regions. Interestingly, the plastic strain would propagate roughly 45° to the vertical axis, before connecting with other lines of strain. As the tension test continued, the strain paths would grow resulting in a cross hatch-like pattern.

The nano-indentation data used to validate the derived material parameters is shown

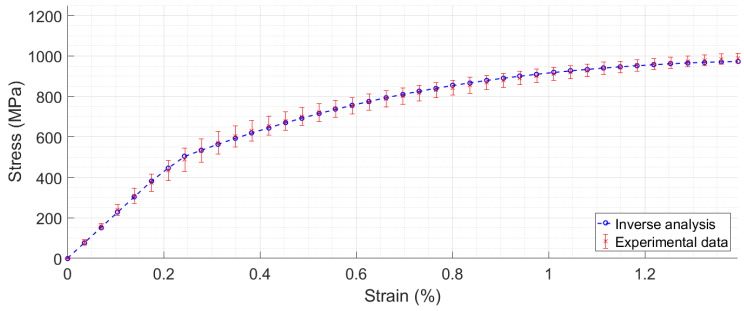

Figure 7.17: Stress-strain result from the inverse analysis after the error fell below a 1% error.

Table 7.7: Table showing the results from the inverse analysis.

Material Phase	Young's Modulus (GPa)	Poisson Ratio	Yield stress (MPa)	Saturation stress (MPa)	Hardening rate
Homogenised	215	0.3	–	–	202/300 (FEA)
Carbide	300	0.33	–	–	–
void	0.001	0.0	–	–	–
Matrix	203	0.3	481	544	101.7/201.7 (FEA)

in Figure 7.19, with the averaged values on table 7.8. The indents were separated into two clusters, using MATLABs *kmeans* function with the number of means assumed to be 2. This gave a bimodal distribution for the indents as shown. It is assumed that the peaks with the greater mean corresponded to the hard carbide phase, as carbides are known to have a higher stiffness and hardness factor than metal [159, 160]. The FCC matrix phase would less likely occur in this range, although a martensitic HCP matrix could occupy the higher range.

Determination of the plastic response in the nano-indentation data is more difficult, however hardness can help reveal the plastic response of the material. The higher mean of 15 GPa is more likely to correspond to the carbide phase which is almost 3 times higher than the matrix of 6.6 GPa, and corresponds to first principle calculations and other experimental data [159, 160]. The H/E (elastic-strain-to-failure) value is also shown given its importance in the plasticity index of repeated sliding [128], and other models of wear [109].

Table 7.8: Table showing the mean hardness and stiffness values, with standard deviation, for the homogenised, matrix, and carbide phases respectively, obtained from the nano indentation data.

Material Phase	Young's Modulus (GPa)	Hardness (GPa)	H/E (-)
Homogenised	217 ± 42.2	8.25 ± 4.02	0.038 ± 0.095
Matrix	194 ± 22.9	6.61 ± 1.58	0.034 ± 0.069
Carbide	267 ± 29.4	15.9 ± 2.87	0.059 ± 0.098

7.5 Discussion

The standard material tests have allowed for the determination of the necessary elasto-plastic material models needed to capture the load response of Stellite™ 6. Importantly, the yield stress in tension for Stellite™ 6 appears to be much lower than the

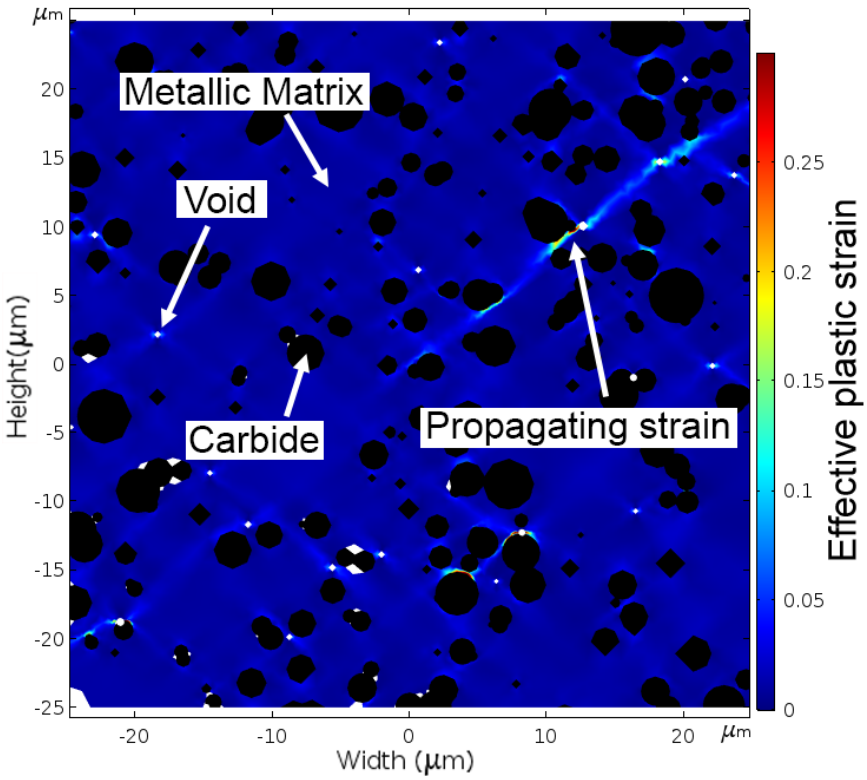

Figure 7.18: The finite element geometry corresponding to the effective plastic strain stress field. Under tension loading conditions, strain propagates from voids and around carbide boundaries at roughly 45° to give a cross-hatched like appearance.

commonly quoted yield stress (proof stress) in the literature [46], as shown in Figure 7.11. The best fit for the plastic phase followed a Voce-like hardening law, which suggests a theoretical ultimate tensile strength of 1100 MPa. Arguably, the average strain-to-failure of 1.5% for the chosen sample is lower than what is typical for this alloy (about 4%), but this may be a result of the short gauge length of the samples [142].

The tension-compression results demonstrate that Stellite™ 6 experiences the Bauschinger effect and therefore a non-linear kinematic hardening model was used, called Armstrong-Frederik. The finite element simulation with the chosen kinematic hardening parameters matches the trends of the experimental data, as shown in Figure 7.12. Reasons for Stellite™ 6 diverging from linearity much sooner in compression after a period of tension remains to be understood detail, but it likely due to the under-estimate in the hardening rate for these chosen experiments and not some non-linear elastic behaviour. It is unlikely to be softening considering the type of work-hardening, i.e. martensite formation, Stellites™ experience [41].

The Vickers hardness model demonstrates that the choice of isotropic elastic-plastic

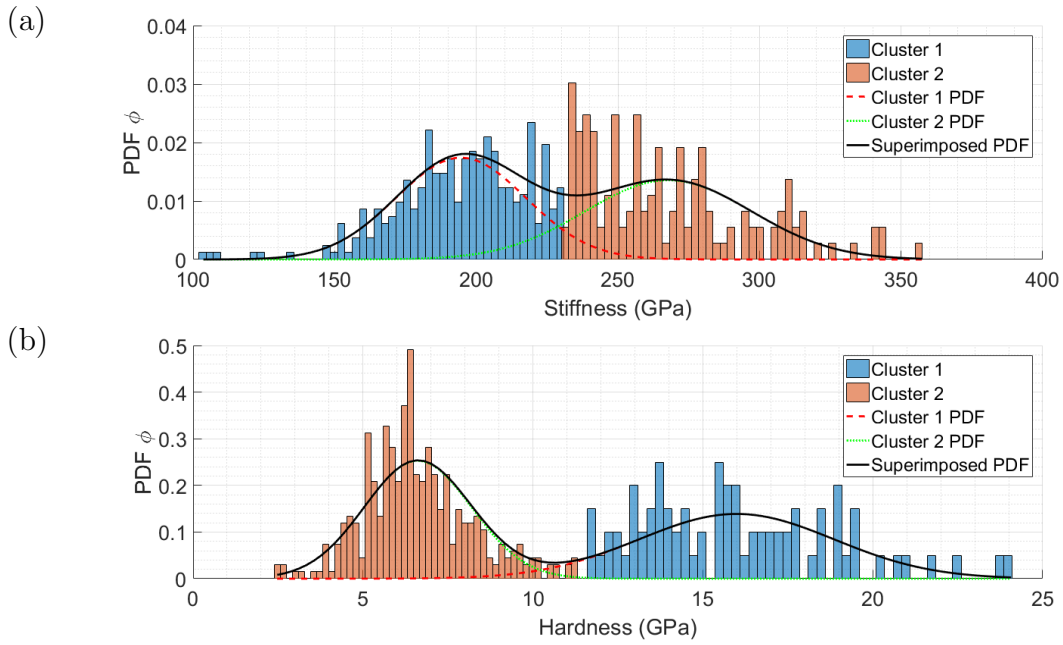

Figure 7.19: De-convoluted distributions of nano indentation results depth controlled up to 50 nm to resolve individual phase properties, (a) material stiffness, and (b) material hardness.

parameters are sound. The resulting hardness from this simulation was 4.46 GPa to 5.36 GPa, or 446 HV to 536 HV. These are close to the values of Vickers hardness as reported in the literature, as shown in Chapter 3 table 3.1, as well as the authors own measurements. This further confirms that the choice of yield stress and plasticity model correspond well to the stress-strain response of Stellite$^{\text{TM}}$ 6, even up to strains of 83%. The ability for Stellites$^{\text{TM}}$ to strain this high, without failure, may be a result of the high hydrostatic pressures produced during contact that suppress the propagation of failure [89] with no such cracking is seen from the indentation in Figure 7.16.

With the material models now validated, it was possible to continue with the inverse analysis to extract the material properties of the individual metallic phase such that the role of hard-inclusions and voids on the mechanical response of the alloy could be understood for future wear modelling.

The inverse analysis used a Young's modulus of 300 GPa for the carbide, in accordance to first-principles data [159, 160], and a negligible stiffness for the voids. The inverse analysis demonstrated that the rate of hardening for the matrix, when separated from the presence of hard-inclusions or carbides, was much reduced by about 30%. This makes sense however, as the introduction of hard-inclusions act as stress-raisers through the material. As a result, the average macroscopic response appears as

though hardening has been accelerated.

Additionally, the yield being higher for the matrix occurs for similar reasons. The high stress-concentrations around voids and carbides cause parts of the material to yield sooner, despite the applied displacement resulting on an average global stress below yield. The result of this is that the yielding of the metal matrix is accelerated by the presence of hard-inclusions. Furthermore, unlike the homogeneous case, there are off-axial stresses produced as a result of a heterogeneous microstructure which may cause the material to yield sooner, as the von-Mises criterion in principle plane-stress is given as:

$$\sigma_Y^2 = \sigma_1^2 - \sigma_1\sigma_2 + \sigma_2^2 \tag{7.3}$$

where σ_1 and σ_2 are the principle stresses. In order to offset this earlier yielding behaviour, it would be necessary for the matrix to be harder as seen in the inverse analysis.

The plastic strain field as shown in Figure 7.18, demonstrating how plastic strain can propagate from voids and grow around carbide boundaries, suggesting a potential rupture path in the material. This is not unlike the sort of cracking behaviour seen in Chapter 6.

The nano-indentation data in Figure 7.19 has been used to help validate the results of the inverse analysis. Importantly, the stiffness, i.e. Young's Modulus, of the metallic phase appears to match the simulation prediction of 203, corresponding to only a 1.4% difference. The modulus of the carbide phase, however, appears to be closer to 250 GPa on average. However, this type of spread is not unusual in the experimental literature, with the stiffness of chromium carbides typically corresponding to a range of 250 to 350 GPa [49, 164, 165, 166], in spite of first principle calculations.

With regards to the plastic response of the matrix, the mean hardness was 6.6 GPa. The relationship of $\sigma_Y \simeq H/3$ [68] is often cited in the literature. This equation gives $\sigma_Y \simeq 2.2GPa$, where it is immediately obvious that this is not valid for Stellites. Rather, we see $\sigma_Y \simeq mH$ where $m = 0.45/5.5 = 0.08$, however a more penetrating study must be conducted before such a value can be properly determined. Assuming this relationship, however, we see that an increase in yield stress causes an increase in hardness, a trend that is seen in the nano-indentation and inverse analysis data for the isolated matrix.

7.6 Conclusions

Through this study it can be concluded:

- The distribution of radius sizes for both voids and carbides follow a Weibull distribution function.
- That the hardening response of Stellite™ 6 follows a Voce-like curve in tension.
- The yield stress of Stellite™ 6 is as low as 450 MPa, which is 300 MPa less than the proof stress cited in the literature.
- Yield in compression happens much sooner than would be predicted using a kinematic hardening model, due to a conservative estimate in the hardening parameters.
- Voids and hard-phases act as stress-raisers which accelerate the hardening of the material, with the individual metallic phase hardening at 30% lower than the homogeneous macroscopic response.

Extraction of the individual material phases is important if one wishes to simulate microscale mechanics, where heterogeneity is important. As such, the role of inclusions on the wear process of the material at the microscale can now be captured.

Chapter 8
A macroscale model of ratcheting wear

8.1 Introduction

Using the materials analysis from the previous section, it is now possible to extend the Franklin-Kapoor model to include microscale heterogeneity and address limitation (2), which was shown to influence the rupture paths of Stellite™ 6. This is done by super-imposing the elastic stress field produced by voids of different morphologies on the Hertzian stress field produced during sliding. The influence of a circular and diamond void on wear-rates are compared to match the range of imperfections seen on the processed alloy. Secondly, the elastoplastic hardness law now allows for one to simulate the stresses and strains produced during the sliding of a cylindrical asperity — a contact geometry justified by the natural lay of the surface lapping method — and their contribution to the ratcheting strain and material rupture. This allows one to circumvent the simplistic analysis of Dautzenberg. Lastly, this Franklin-Kapoor is then used as a subroutine, which is then homogenised to the macroscale using the Greenwood-Williamson model of rough contact, in a macroscopic finite element model of wear. A finite element study of the asperity was performed and challenges to this approach are discussed. This allows one extrapolate microscale wear to laboratory conditions and perform sensitivity analysis with regards to material properties and pore morphology, thereby allowing greater predictivity otherwise not afforded in typical numerical models of sliding wear.

8.2 Objectives

- Perform the strain analysis required to determine the strain-rate per cycle of an asperity for using the Franklin-Kapoor model.
- Observe the changes in wear-rate for Stellite™ 6, in response to load, using the Franklin-Kapoor model of wear with the Stellite™ 6 structural data.

- Observe how the introduction of microscale heterogeneity, such as voids of differing morphology, influence the wear-rates in the ratcheting model.
- Determine the influence of strains other than shear on the accumulated strain using an elasto-plastic finite element model of a sliding asperity.
- Apply the modified Franklin-Kapoor model as a subroutine to a finite element model of wear using a homogenisation scheme.
- Compare the model results to laboratory experiments.

8.3 Methodology

8.3.1 Experimental strain analysis

Given the importance of plastic strain in the ratcheting wear model, the worn pins from Chapter 6 were mounted and cross-sectioned along the sliding axis and subsurface strain was observed.

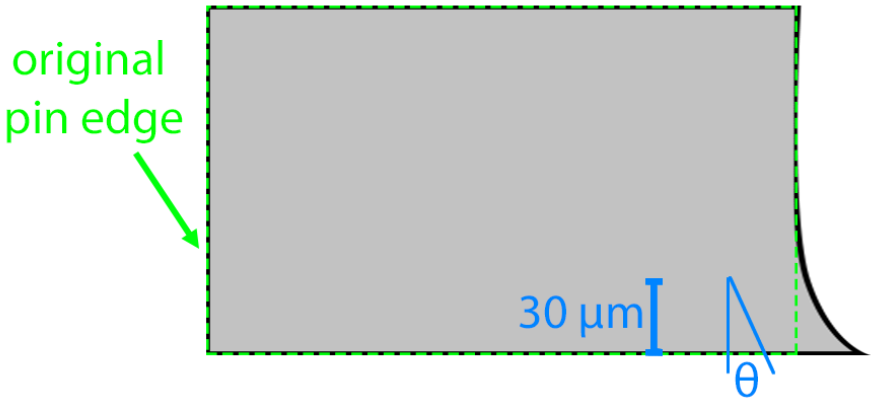

Figure 8.1: Schematic showing the angle measuring method employed on the strained pins.

To acquire the scale of plastic strain in the pin specimen, the methodology of Dautzenberg [88] was used:

$$\gamma_{xy} = tan(\theta) - tan(\eta) \tag{8.1}$$

where θ and η are the angles that the deformed and un-deformed material make with the normal to the wear interface, some 30 microns from the wear interface. For

this data, $\eta = 0$ and so $\gamma_{xy} = tan(\theta)$. This analysis holds for a perfectly plastic rigid material undergoing finite deformations in simple shear, which has been used by Cabrol et al. [66] and Kapoor et al. [127] to determine the tribological strain-to-failure for Stellite^{TM} 6 and pearlitic steels respectively.
In the ratcheting wear model [23], we are interested in the plastic strain per cycle, c. This is found by calculating the linear equation given by Tyfour et al. [94]:

$$c = \frac{\gamma_{xy}}{(p_0/k - p_r)N} \tag{8.2}$$

where γ_{xy} is the maximum plastic shear strain after sliding, p_0 is the mean contact pressure calculated from the methodology outlined in section 5.3, k is the shear strength of the interface calculated from hardness measurements using $k = \sigma_Y(H_f/H_i)$, N are the number of sliding cycles and p_r is the threshold of contact pressure required to make the material undergo ratchet deformation. This can be calculated by using the shakedown map for a rolling/sliding cylindrical asperity contact in Figure 4.4 and simply inputting value of p_0/k given by μ.

8.3.2 Void stress analysis

To account for the influence of void morphology on the stress-fields produced during mated contact and then wear, a finite element model of an asperity sliding over a half-space with a void was built using the material data derived from the inverse analysis. To simplify the analysis, an elastic plane-strain model was considered. This is justified considering that the plastic strain may be determined through elastic stresses, and the natural surface lay produced during lapping of the mated surfaces.
Two void morphologies were considered, primarily a circular void and a quadrilateral 'diamond' void, as shown in Figure 8.2. The contact interface was sufficiently meshed as to resolve the contact width. The material properties were 215 GPa and 203 GPa for the indenter and half-space respectively. The Poisson's ratio used was 0.3, typical for metals. The elastic properties for the void were a modulus of 1 Pa and Poisson's ratio of 0, to simulate the absence of material. To simplify the analysis, the cylindrical asperity and void were assumed to be 1.5 μm and 0.5 μm diameter respectively, in line with the experimental data.
As the stress field generated by a pore is influenced by a combination of penetration depth of the asperity, and the frictional coefficient, a Latin-hyper-cube sampling of friction coefficients and penetration depth was constructed with 20 samples varying from 0.25 to 0.70 and 0.05 μm to 0.50 μm respectively. The stress-field then had

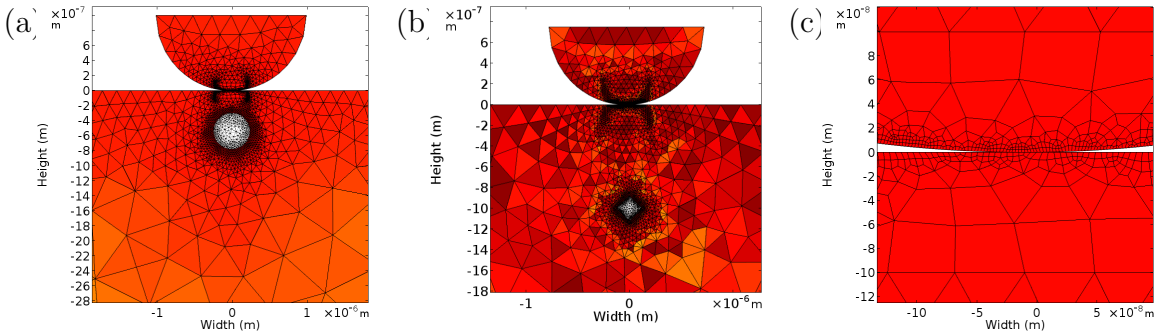

Figure 8.2: Mesh for the inclusion finite element model simulating the elastic contact showing (a) the circular void geometry, (b) the diamond void geometry, and (c) a close up of the contact zone.

a baseline analysis performed on it as to isolate the Hertzian stresses from those generated about the void.

With the stress-fields about the voids isolated, a Gaussian model was fitted to the data, of the form:

$$f(z;a,b,c) = ae^{\left(\frac{(z-b)^2}{c^2}\right)} \tag{8.3}$$

where a, b, and c are function parameters and z is depth from the interface. It was observed that a, b, and c depended on the value of void depth, friction coefficient, and asperity penetration. With a, b, and c plotted as a function of these values, it was seen that the magnitude of stress, a, varied exponentially with depth and varied linearly with friction and asperity penetration. The parameter b corresponded to the pore depth, and c remained constant.

An example result of the preceding analysis is shown in Figure 8.3, where the resulting Gaussian functions representing a stress-field around both a circular and diamond void has isolated from the Hertzian stress field, and has been plotted with respect to depth for a coefficient of friction of 0.25 and a penetration depth of 0.75 μ m.

8.3.3 Microscale wear models

Franklin-Kapoor ratcheting model

As Stellites$^{\text{TM}}$ appear to be undergoing ratchetting wear under high load dry sliding conditions, the Franklin-Kapoor model of wear is used [23], adapted to microscale wear. Primarily, the model uses an elastic half-space, divided up into layered elements, each of which track the amount of plastic shear strain accumulated using equation 4.19. Shear is focused on, as the subsurface cracks leading to the removal of layers

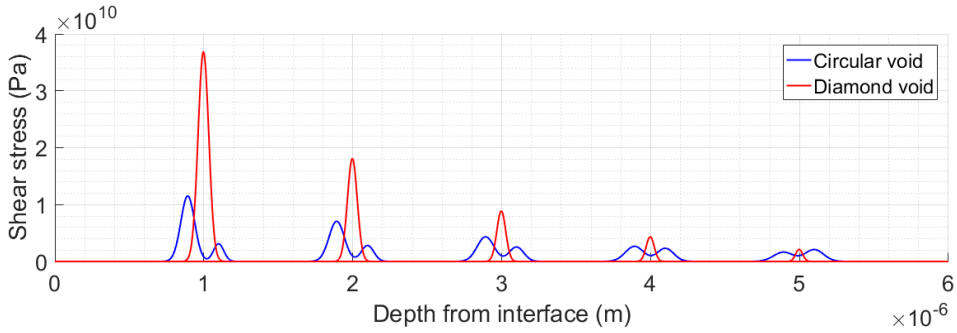

Figure 8.3: Plot showing the variation of shear stress fields, isolated from elastic stresses, produced by both a circular and diamond void at different depths.

propagate parallel and in the direction of sliding. When critical shear is reached in a given layer, it is removed along with all the layers above it, as to give wear depth. The numerical wear algorithm used in Franklin-Kapoor is outlined in Figure 8.4.

For this analysis, the asperity is assumed to be cylindrical plane-strain, as justified by the lapping procedure resulting in a prominent surface lay [116]. The size of the asperity is kept constant at 1.5 μm, thus restricting the wear model to the microscale. A further simplification is given, by restricting the microscale analysis to a strain-to-failure and strain-accumulation-per-cycle of 5.0 and 5×10^{-5} respectively. To calculate shear-strain in each layer, as a result of shear stress, a modified form of equation 4.19 is used:

$$\Delta\gamma_{i+1} = \begin{cases} c\frac{\tau_{xy}}{k_{eff}(\gamma_i)}, & \text{if } \tau_{xy} > k_{eff}. \\ 0, & \text{otherwise.} \end{cases} \tag{8.4}$$

where τ_{xy} and k_{eff} are the shear stress and shear strength respectively. Here, the shear strength is a function of the current value of accumulated shear strain at that point in the material as to simulate material hardening. If the shear stress does not exceed the value of shear strength, then there will be no accumulation of shear strain and the material response will be purely elastic.

In the case of Stellite™ 6, it has been demonstrated in Chapter 7 that Stellite™ 6 follows a Voce-like hardening curve. The function that represents this hardening is given as:

$$k_{eff} = \frac{\sigma_Y}{\sqrt{3}} + \frac{H}{\sqrt{3}}(1 - e^{-b\gamma}) \tag{8.5}$$

where σ_Y is the yield stress, H is the saturation stress, and b is the hardening rate. The factor of $1/\sqrt{3}$ here relates the values of yield stress and saturation stress to their

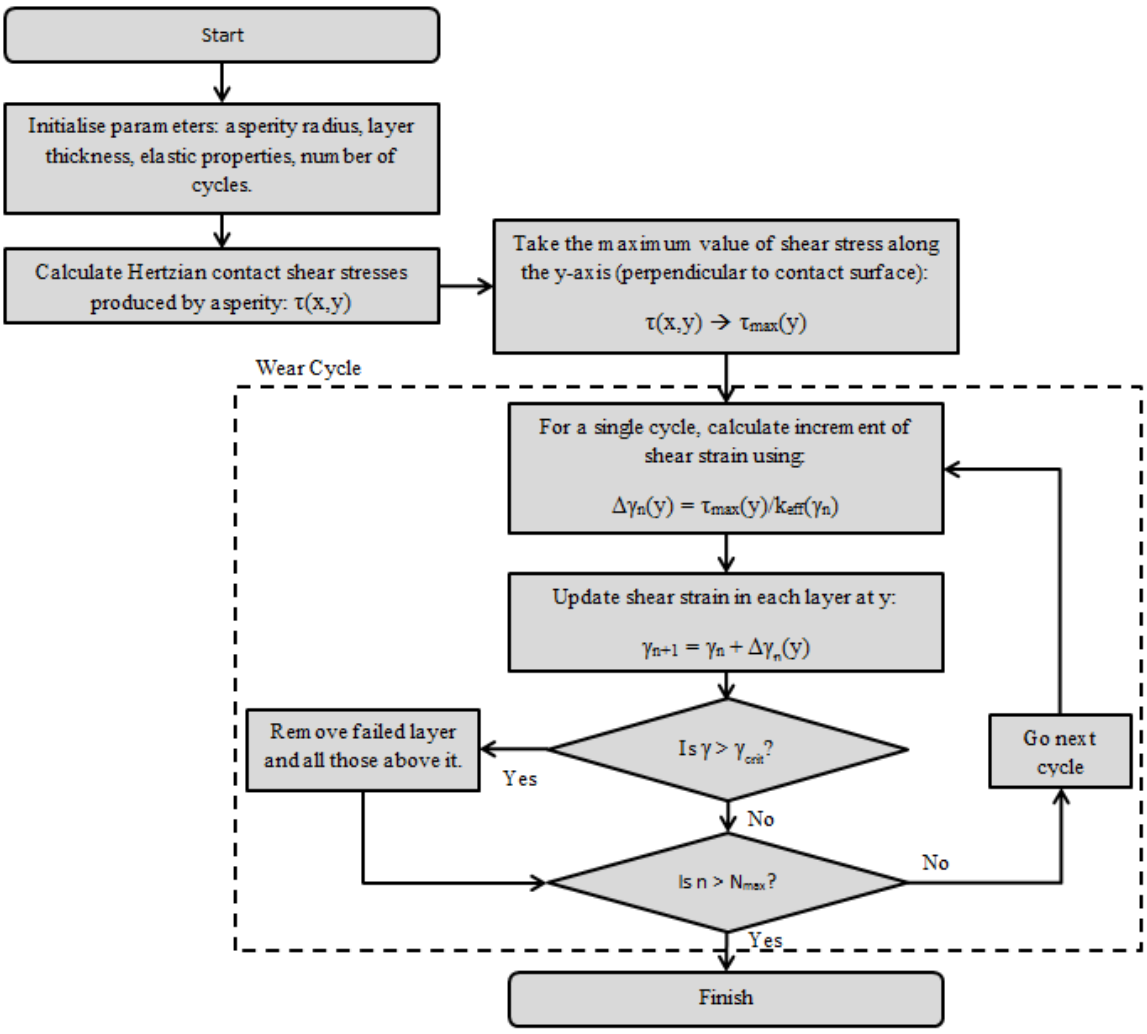

Figure 8.4: Schematic showing how the Franklin-Kapoor wear model works in MATLAB.

shear counter-parts.

Lastly, the influence of voids on the microscale wear was incorporated by superimposing the void stress fields, determined from the previous section, on the Hertzian stress field in the ratcheting wear model.

Finite element asperity model

To compare to the Franklin-Kapoor strain accumulation method, a finite element elastoplastic kinematic hardening model cylinder-on-flat slider model was built. The aim of the model was to capture the strain-accumulation-per-cycle by an asperity sliding over material, without using the analysis of Dautzenberg [88].

A plane-strain cylindrical asperity, of radius 1.5 μm, was slid over an homogeneous elastoplastic half-space, in load control, under reciprocated motion for one cycle.

One cycle was chosen for computational efficiency. The half-space was modelled as a homogeneous elastoplastic half-space with a non-linear kinematic hardening model, "Armstrong-Frederik", which was chosen to capture the effects of ratcheting [122]. The asperity was assumed to be purely elastic. The model was run under load control in plane-strain using an implicit quasi-static solver, with quadratic serendipitous triangular elements. The material properties were taken from the data in section 7.

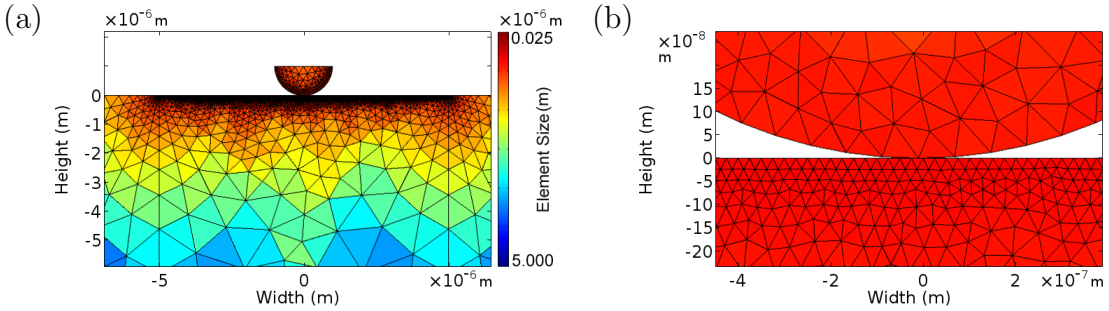

Figure 8.5: (a) Showcase of the FEA geometry used in the finite element slider model, and (b) a close up view of the mesh

To compare this data to the Franklin-Kapoor analysis [23], the plastic strains were related to the ratio of the maximum elastic stresses for an equivalent, but entirely elastic, geometry above yield at the point of maximum strain under the point of contact, by the equations:

$$\gamma_{xy}^{max} = C\left[\frac{\tau_{xy}^{max}}{k^{max}}\right] \tag{8.6}$$

and,

$$\epsilon_{pe}^{max} = C\left[\frac{\sigma_v^{max}}{\sigma_Y^{max}}\right] \tag{8.7}$$

where γ_{xy}^{max}, τ_{xy}^{max}, k^{max} are the maximum value of the shear strain, elastic shear stress, and yield stress in shear respectively. ϵ_{pe}^{max}, σ_v^{max}, σ_Y^{max} are the maximum value of the effective plastic strain, von Mises stress, and yield stress respectively. The factor C, the strain-per-cycle, scales the ratio of elastic stress above yield to the plastic strain.

8.3.4 Macroscale finite element sliding wear model

Homogenisation scheme

In order to homogenise the microscale wear, given by the Franklin-Kapoor ratcheting model [23], to a macroscopic wear-rate a finite element contact solution of the macro-

scale geometry was combined with the aforementioned true pressure computational methodology. In this way, a stress-field pertaining to microscale roughness, under the point of contact, could then be used as input into a Franklin-Kapoor wear model. This allows wear to be simulated in mechanistic terms, by observing how material is strained and ruptured due to the mean pressures generated by a rough surface leading to wear particle generation.

A finite element model of wear was built in Comsol Multiphysics with pre- and post-processing handled by Livelink for Matlab. The elements used in the finite element geometry were quadratic serendipity triangular elements. The simulation geometry and boundary conditions can be seen in Figure 8.6.

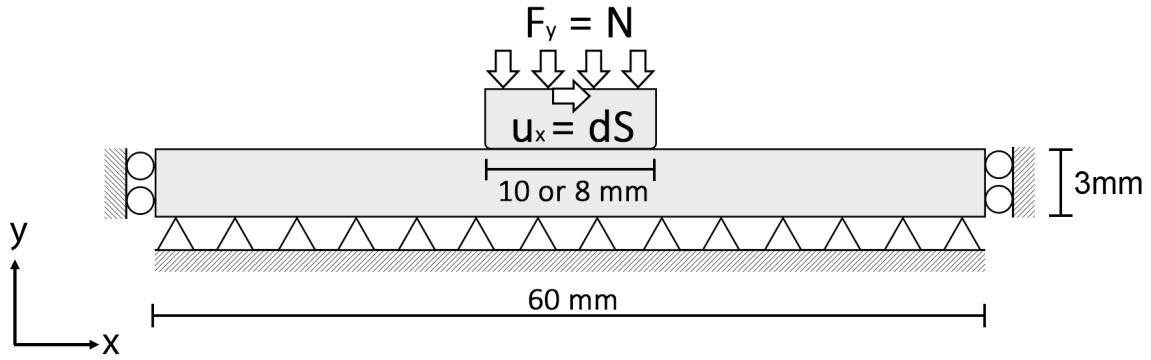

Figure 8.6: The boundary conditions and geometry used in the macroscopic finite element model of wear with a ratcheting subroutine.

First, a plane-strain finite element model of contact for the macro-scale geometry used in experiments was built. The finite element mesh at the contact boundary was chosen to be uniform in element size. This simplified the wear model, as for elements of varying size at the wear boundary it is necessary to interpolate the wear data onto a uniform grid [135]. The finite element contact problem for the macroscale smooth geometry was then solved for a given desired load in order to give the distribution over pressure across the contact. The pressure at each node, p_n, where n represents the specific node, was then multiplied by the width of the element boundary at the mating interface, w_n, in order to give the load density distribution at that specific node, $F_n/L = w_n p_n$, across the contact interface. The equation that represents this procedure is given as:

$$\frac{F_n}{L} = \frac{w_n(A_c/L)}{L} \int_{d_n}^{\infty} \phi(z) dF_n(z - d_n) dz \tag{8.8}$$

Then, for each node, the separation between the pin and plate surfaces at a specific

node can be calculated using the methodology outlined section 5.8 using the condition shown in equation 5.4 by searching for the separation that gives the correct force at a given node.

An example of the results of this procedure can be seen in Figure 8.7 for a macroscopic load of 40N applied over a boundary of 8mm. Importantly, the pressure values given here exceed a value of 60 MPa, whereas for the test geometry in ref. [1] of a pin with diameter 10mm the maximum pressure only reaches 0.5 MPa, thus highlighting how different the pressure profiles may be when one accounts for surface roughness in the analysis.

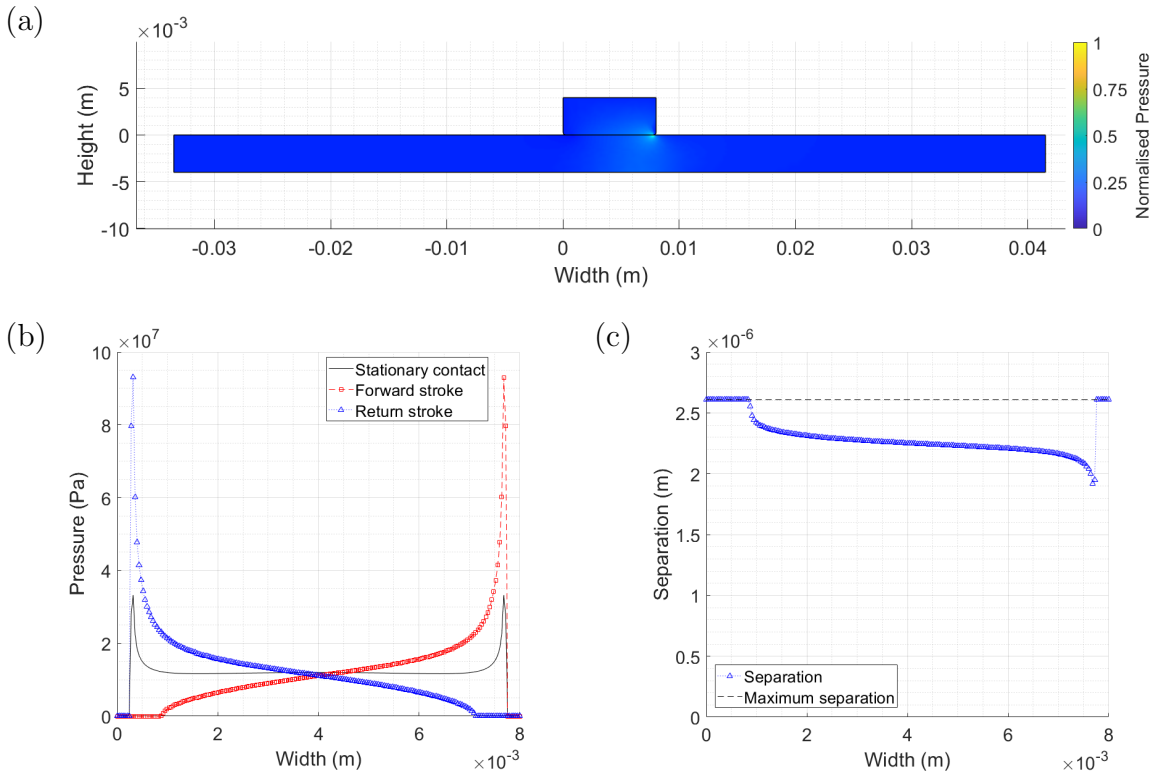

Figure 8.7: An example of the contact pressure experienced across the wear interface under a load of 600 N with a coefficient of friction 0.375, solved using FEA, showing the (a) macroscopic geometry used in the simulation, (b) the contact pressure across the interface before and after sliding thereby showing the influence of friction on the pressure distribution and (c) the separation between surfaces calculated from the pressure for each surface node using the Greenwood-Williamson model.

This data emphasises the importance of edge loading, as despite a chamfered edge, spikes in the pressure field are still experienced near the corners of the pin. It is striking that, for the stationary contact, the peak pressure reaches just above 30 MPa in contrast to the sliding contacts which experience a peak pressure of 100 MPa. Nevertheless, the mean value of pressure for all conditions considered is 12 MPa, as

would be expected for a load of 600 N for a cylindrical pin of diameter 8 mm. In addition, the profile is skewed towards from the leading edge of the contact, therefore giving a lower magnitude of stress at the trailing edge and presumably reduced wear. Correspondingly, the separation sees a similar skewing to the leading edge as would be expected; higher loads result in smaller separations.

With the separation-per-node found, the wear-rate could be determined. The shear stress field in the half-space, τ_{xy}, was then acquired by calculating the mean pressure at a given node by substituting the separation at each node, d_n, into equation 5.5 for real area. The mean pressure at this node can then be calculated via $p_{0,n} = F_n/A_{r,n}$ where F_n is the force carried at this node. Assuming this mean pressure is distributed uniformly across a given element, the shear stress can be the equations of ref. [108]. For normal loading of a uniform pressure distribution, where z is the depth from the contact interface:

$$\sigma_{xy,N} = -\frac{p_0 2z^2}{\pi} \int_{-w_n/2}^{w_n/2} \frac{(x-s)}{\left[(x-s)^2 + z^2\right]^2} ds \tag{8.9}$$

and shear loading, normally due to sliding friction forces given by $\mu p0$, where μ is the frictional coefficient:

$$\sigma_{xy,S} = -\frac{\mu p_0 2z}{\pi} \int_{-w_n/2}^{w_n/2} \frac{(x-s)^2}{\left[(x-s)^2 + z^2\right]^2} ds \tag{8.10}$$

which when superimposed give the shear stress solution for an elastic body being deformed by a normally loaded contact, sliding with a frictional coefficient, μ:

$$\tau_{xy} = \sigma_{xy,N} + \sigma_{xy,S} \tag{8.11}$$

Finally, we are only concerned with the maximum value of shear stress as a function of depth, as this will cause material straining and rupture. The maximum value of τ_{xy} may then be used in equation 8.4 to acquire the strain at a given node. Once this strain exceeds a critical strain to failure, the tribological layer at node n will be removed to give a corresponding wear-depth of h_n. An example of the stress field in the pin is shown in Figure 8.8.

Sliding wear routine

The finite element model of wear was built in Comsol Multiphysics with pre- and post- processing handled by Livelink for Matlab. The model geometry used a 2D

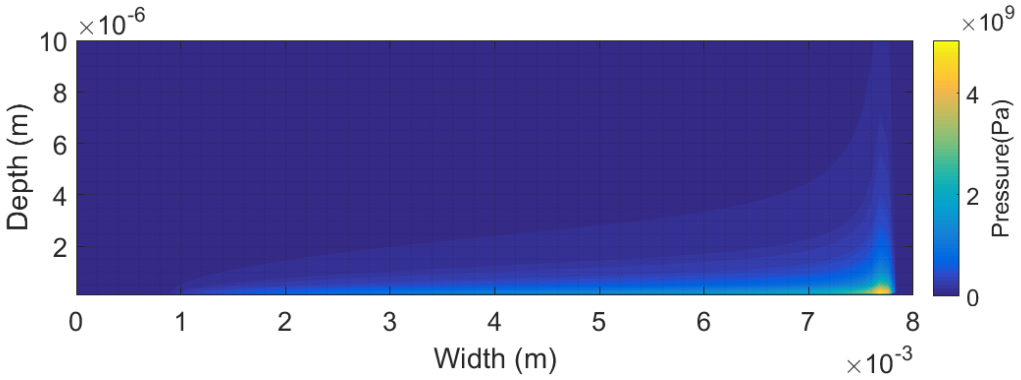

Figure 8.8: The Hertzian stress field under the point of contact using the homogenisation procedure. Note how the stress predicted using this method gives a much higher pressure, capable of yielding the material, when compared to the pressures calculated from the apparent area.

plane-strain finite element approximation, which can be justified by the nature of the surface lapping preparation giving the material surfaces a prominent surface layer [125]. The elements used in the finite element geometry were quadratic serendipity triangular elements.

Each simulation run was done to recreate each experiment. For speeds 0.05 m/s to 0.5 m/s, a contact length of 10 mm was used and slid for 10000 cycles for loads between 40 N and 400 N. For 0.02 m/s, the simulation was run for 5000 cycles using a contact length of 8 mm between loads of 600 N to 1000 N. A mesh sensitivity analysis was conducted. A simulation of the tribological geometry under a load of 600N, slid for 100m, with pin diameter of 8mm was used. Each simulation run was performed with a different number of elements at the contact interface, ranging from 10, 25, 50, 100, 200, 400 and 600 elements.

The standard approach to simulating wear using finite elements is to use the pressure distribution calculated from the macroscale geometry, in combination with a given wear subroutine. This subroutine is typically a modified form of the Archard equation, which describes wear depth in terms of pressure and velocity [135]. The wear depth per node, h_n, is calculated with each increment of sliding distance, ds, and then used to adjust the finite element geometry as shown in Figure 8.9 over the course of a simulation. In the case of the ratcheting subroutine, the wear depth, h_n is calculated from the height of the layer that is removed when the strain at a given node exceeds a critical strain to failure. The wear-rate can then be found at the end of the simulation by conducting an Archard-like analysis, by taking the wear volume, W_v and dividing it by the sliding distance and load.

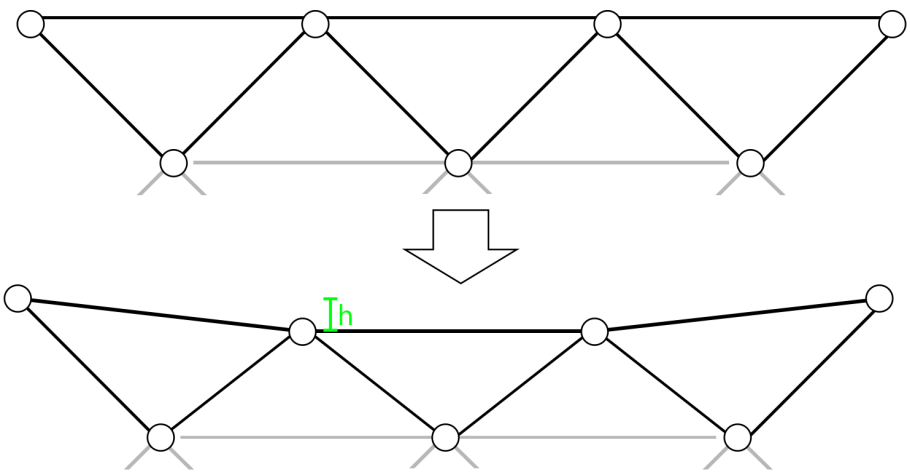

Figure 8.9: A schematic demonstrating how the finite element nodes are adjusted in response to a wear depth, h, determined using a degradation function and contact pressure. To prevent elements inverting when the wear depth exceeds the element size, the geometry was re-meshed.

Unique to this study is the replacement of the degradation function via a "ratcheting subroutine", using the homogenisation procedure outlined above in section 5.8 and 8.3.4. The stress field, corresponding to rough contact, solved for the given geometry and load is then plugged into a Kapoor-Franklin model of wear for each node in the contact interface. The shear-stress then maps to a value of shear strain at each node, which if greater than a critical strain to failure, results in the removal of worn layers at that node and therefore gives a wear-depth. This wear-depth is then used to adjust the node heights, as in Figure 8.9, and the geometry is updated. This procedure is repeated until the simulation reaches the maximum distance corresponding to the experimental test duration, with the full routine displayed in Figure 8.10.

Unlike the Franklin-Kapoor model, which assumes unidirectional sliding, the present macroscale model incorporates reciprocating motion into the sliding wear analysis. Given the near symmetrical lipping effect on the pin specimen, it is assumed that the material is strained equally in the opposite direction on the trailing pin edge to the stroke motion and vice versa for the returning stroke. This reflects the fact that misalignment effects can influence how the pin edge strains [152], whereas unidirectional sliding only sees a prevalent lipping effect on the trailing edge [167]. To account for this, it is assumed the pin only strains in one preferential direction, in this case during the forward stroke, and does not strain on the return stroke.

The finite element model had the pressure distribution updated 10 times throughout the course of the simulation, with the intervals between each solution increasing.

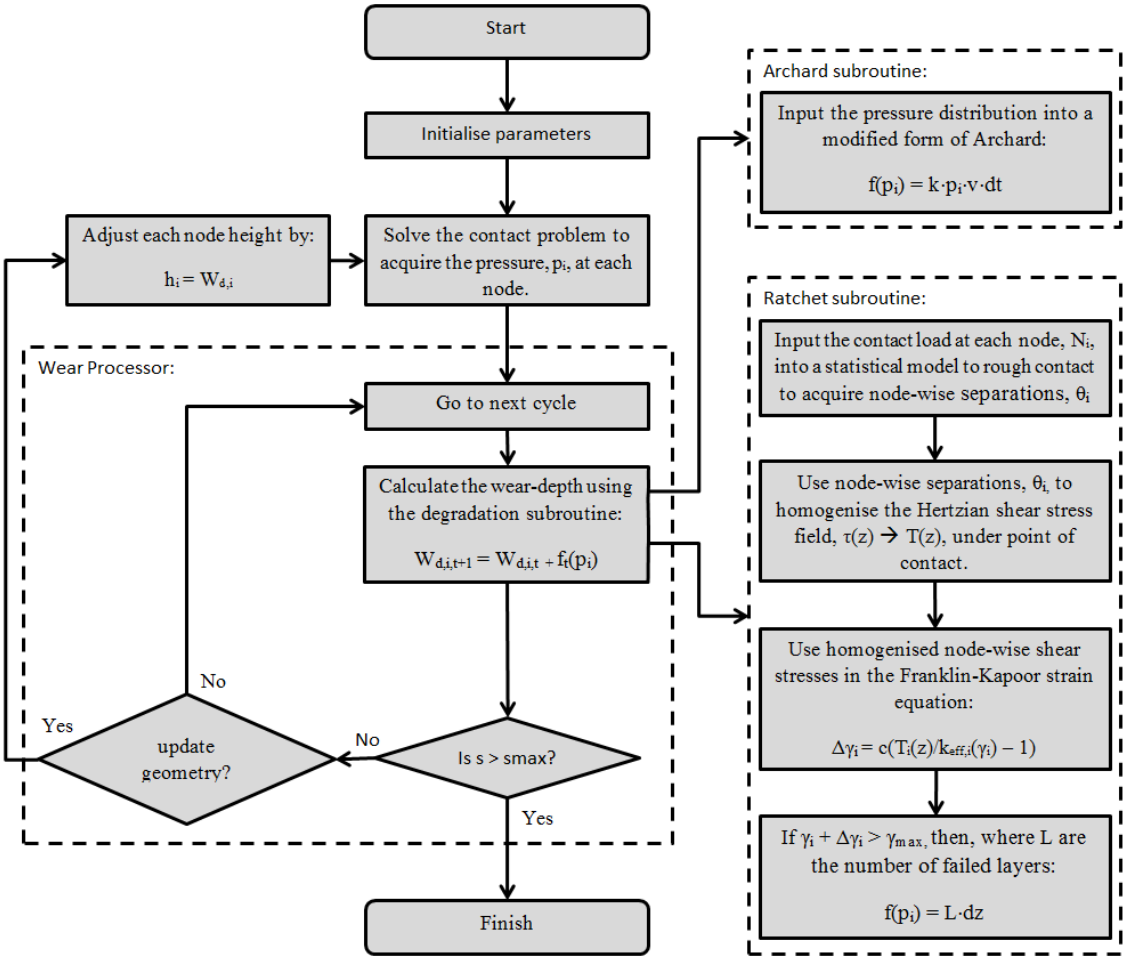

Figure 8.10: Schematic outlining the wear processor. As we can substitute the degradation for any function, both Archard and Kapoor-Franklin are shown for comparison.

The surface texture parameters were not updated throughout the simulation, with the end-of-test surface texture used from the experiments in Chapter 6. The input parameters for each simulation can be seen in table 8.1.

The role of voids could also be captured in the macroscale model using this same homogenisation procedure, and is outlined in Figure 8.11. For the sake of computational simplicity, voids, both diamond and circular, were modelled only on the pin. The voids were assumed to have diameter and half-width 0.5 μm.

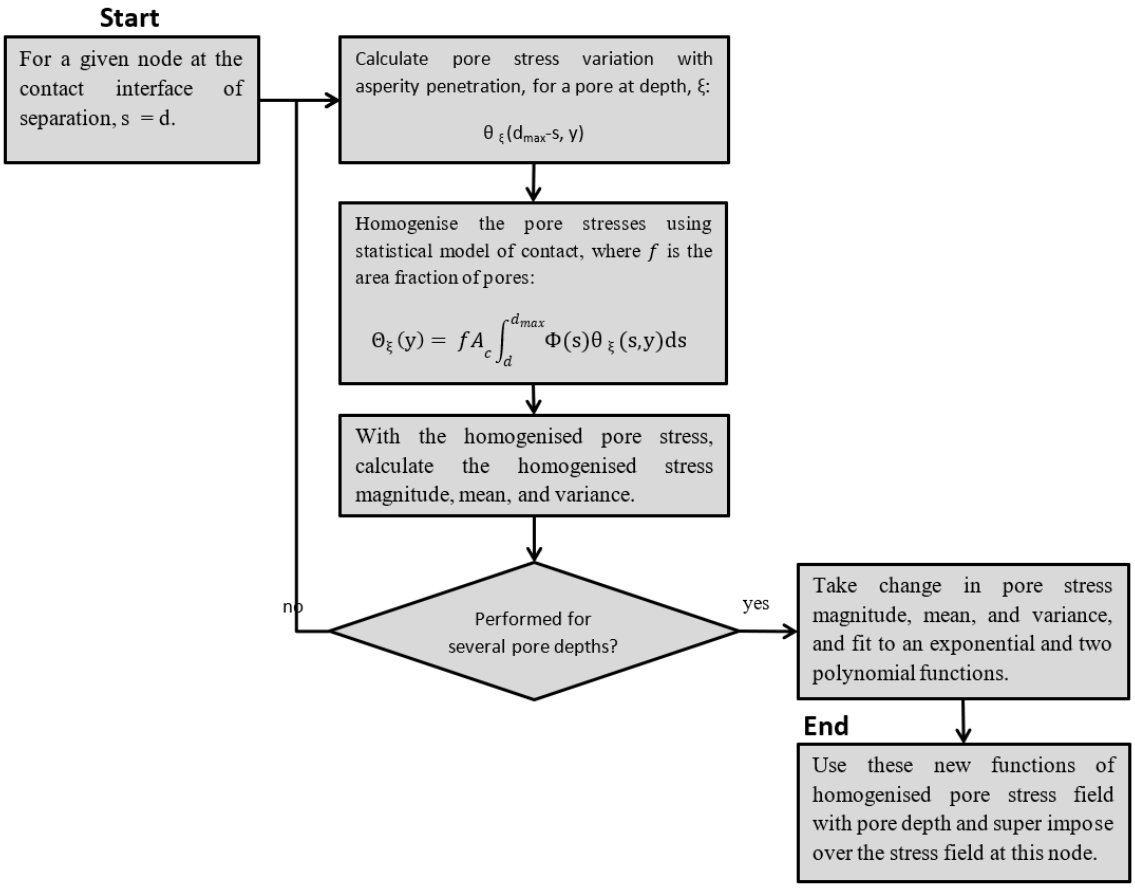

Figure 8.11: The process for scaling the void stress field so that they can be included in the macroscale wear processor.

8.4 Results

8.4.1 Experimental strain analysis

The typical strains observed at the pin edges can be seen in Figure 8.12 for the high load tests between 0.02 m/s between 600 N and 1000 N after sliding a distance of 100 m. Evidently, the higher load results in a larger deformation at the pin edge which would be expected.

In contrast the variable distance tests as shown in Figure 8.13, which were performed using a chamfered pin, under 1000 N. Noticeably, despite this, the pin displays the same kind of lipping as shown in the high load tests. It is noticeably less deformed than at 100 m for the lower distances.

Figure 8.14 shows plots for the strain of the pin after sliding for the variable speed tests, and the high load tests. As it can be seen, the scale of the pin deformation is

Table 8.1: Table of the input parameter values to the finite element model.

Load (N)	**Distance (m)**	**Speed (m/s)**	**E (GPa)**	**Yield (MPa)**	**k (MPa)**	$\mathbf{A}_c$	μ	$\mathbf{H}_i$ **(GPa)**	$\mathbf{H}_f$ **(GPa)**	$\mathbf{k}_{eff}$ **(MPa)**	**c** (1×10^{-6})	**STF**
40	500	0.05	215	450	259	4740	0.55	5.0	5.50	285	0.001	0.48
240						3510	0.62	5.0	6.29	326	7.72	1.95
400						2940	0.40	5.0	9.11	473	12.8	2.15
40	500	0.10				4250	0.70	5.0	5.45	282	8.31	1.43
240						3490	0.43	5.0	5.69	295	15.7	2.75
400						3260	0.30	5.0	6.96	361	29.9	5.15
40	500	0.50				2490	0.41	5.0	5.55	287	7.08	2.05
240						2830	0.30	5.0	6.09	315	10.0	2.90
400						2710	0.25	5.0	7.17	371	12.8	8.21
600	100	0.02				2640	0.38	5.0	9.05	470	28.4	1.24
800						2776	0.38	5.0	8.51	442	13.2	2.48
100						2624	0.39	5.0	8.28	430	22.5	3.73

significantly higher than what is possible in the monotonic tension test. The scale of this deformation is likened to the presence of high hydrostatic pressures (typically 1.5 GPa) under the point of contact which is known to make brittle materials more ductile [168, 169]. The scale of this deformation cannot be controlled frictional heating alone, and it is likely that the scale of deformation occurred as the result of a mechanism allowing for incremental accumulation of plastic strain, i.e. ratcheting.

8.4.2 Franklin-Kapoor ratcheting model

Results without a void are shown in Figure 8.16(a).

Interestingly, the wear-rate appears to have a periodic nature during the steady-state. This periodicity appears to be less pronounced at lower loads, with the form of periodicity changing over the course of the simulation.

To ensure accuracy of the inclusion model, the finite element contact between a cylinder and half-space without a void were compared to the Hertzian solution. The penetration depth used in the model was 0.3 μ m, with an indenter radius of 1.5 μm. The results of this analysis can be seen in Figure 8.17. The relative error between the two solutions is 0.98% suggesting a good fit between the two. With this, the void stress field could be super-imposed over the Hertzian solution.

Naturally, for real materials, one would not expect a single void to be present in the material. Rather, after enough time another void will reach the surface, and affect the wear-rate. Figure 8.16 shows the change in the total depth loss, after sliding 5000 cycles, as a function of asperity pressure for different subsurface voids rising to the surface every 500 cycles. The diamond void appears to generate an increase of about 25% in wear depth but only 20% for friction coefficients of 0.25 and 0.50 respectively.

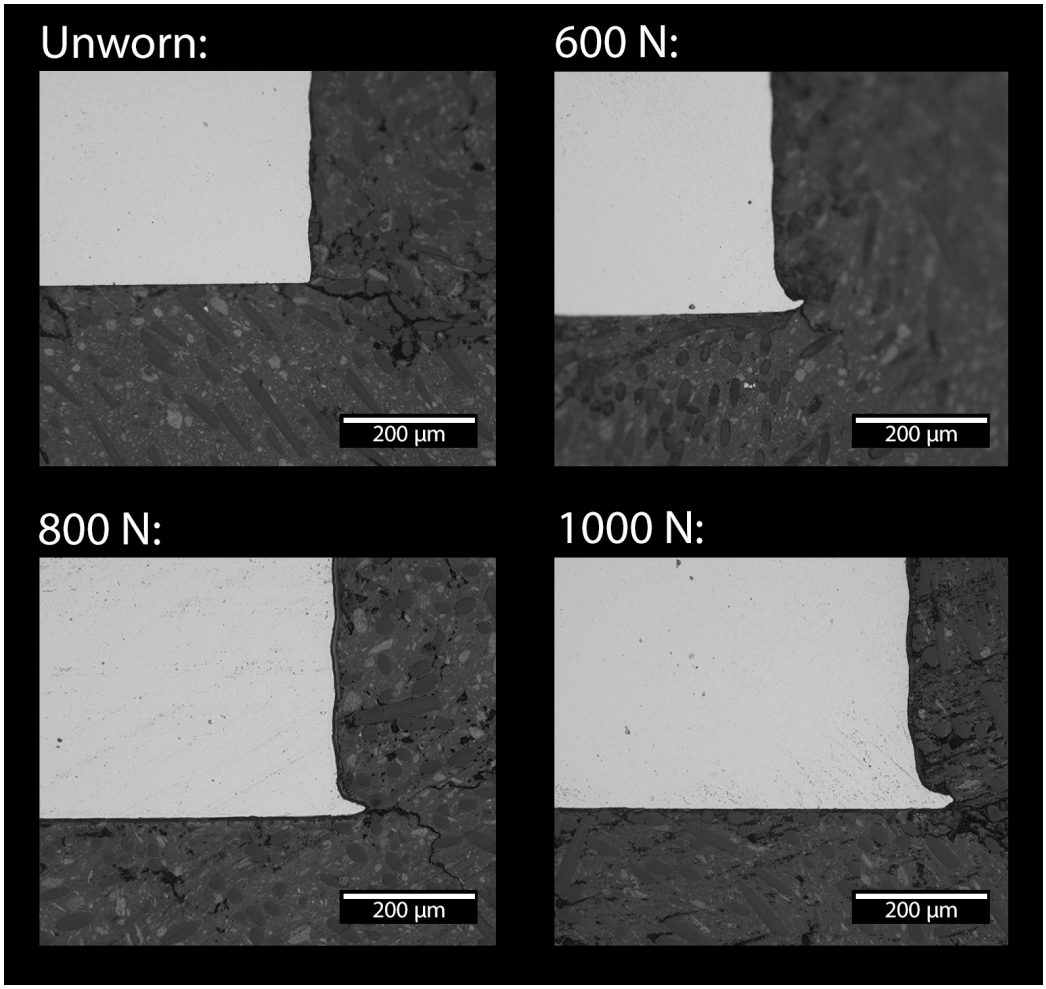

Figure 8.12: A series of optical micrographs showing the strain accumulation at the edge of the pins for the high load experiments.

The depth loss per cycle, or wear-rates, for an asperity sliding under a pressure of 20 GPa is shown in Figure 8.19. The spike in wear-rates does not appear to simply repeat itself, as each subsequent spike has a slight variation in behaviour. For instance, in the low coefficient of friction case, there is a period of low wear spikes from 2500 to 4000 cycles. At low coefficients of friction, the circular void does not necessarily wear less than the quadrilateral 'diamond' void. In contrast, at higher coefficients of friction, the spike in wear-rates for the diamond void are consistently bigger.

8.4.3 Macroscale finite element wear model

The wear-rate results from the wear simulations, comparing the ratchet and Archard subroutines using the strain data from Chapter 8 and the experimental wear-rates respectively, are shown in Figure 8.21. Importantly, these results demonstrate that

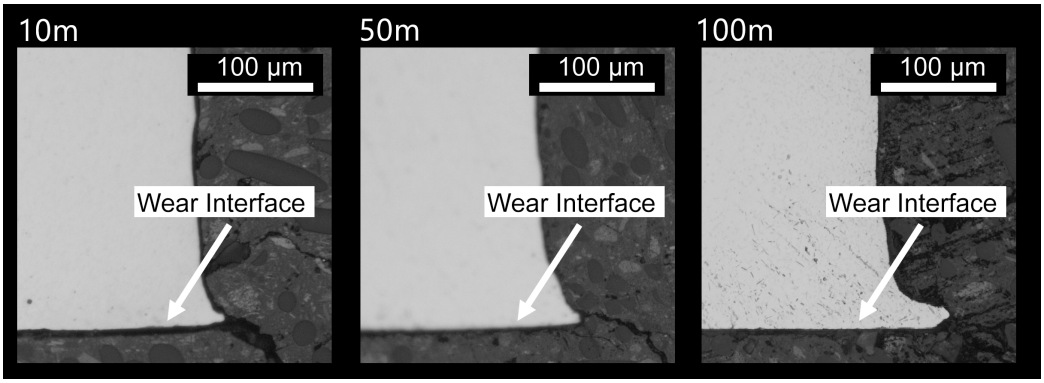

Figure 8.13: A series of optical micrographs showing the strain accumulation at the edge of a chamfered pin at 1000 N for 10 m and 50 m.

for speeds of 0.02 m/s to 0.05 m/s, the ratchet subroutine predicts the correct scale of wear. That is, they all lie within the range of 10^{-15} to 10^{-13}. Furthermore, the ratcheting subroutine predicts a difference in the wear-rates between the pin and the plate, with the plate wearing slightly less.

Results from the sensitivity analysis can be seen in Figure 8.20. The wear-rates have been normalised with respect to the wear-rate value corresponding to a mesh number of 10. With increasing element number, the value for wear-rate appears to tend to a value of 0.05.

In contrast the wear for the high speed, 0.05 m/s, case shows a large discrepancy between the magnitudes of wear albeit for the pin only. Likewise, the wear trends do not always agree, with the rate of wear increasing with load in the 0.02 m/s case. The reasons for these discrepancies will be discussed later.

Given the deviation of magnitude in the wear-rates and wear-volumes for the ratcheting subroutine, an optimisation procedure was executed to determine the values of the strain-per-cycle, c, that would be expected to give the wear-rates as seen in experiment. Importantly, this method of fitting is not performed to make any conclusions on the actual value of the strain-per-cycle as this would simply be recreating the method used to determine the wear-rate in Archard models of wear, rather this gives an expected value of the strain-per-cycle that would otherwise be reasonably obtained from materials data by using accurate measurements of strain, such as EBSD or grain deformation, in the subsurface of the worn material. In other words, this gives us a strain value to validate the ratcheting model against after using more accurate methods to determine strains from experiments.

The results for the strain-rate after using the optimisation procedure are shown in Figure 8.22. As expected, the strain-rates on both pin and plate are markedly differ-

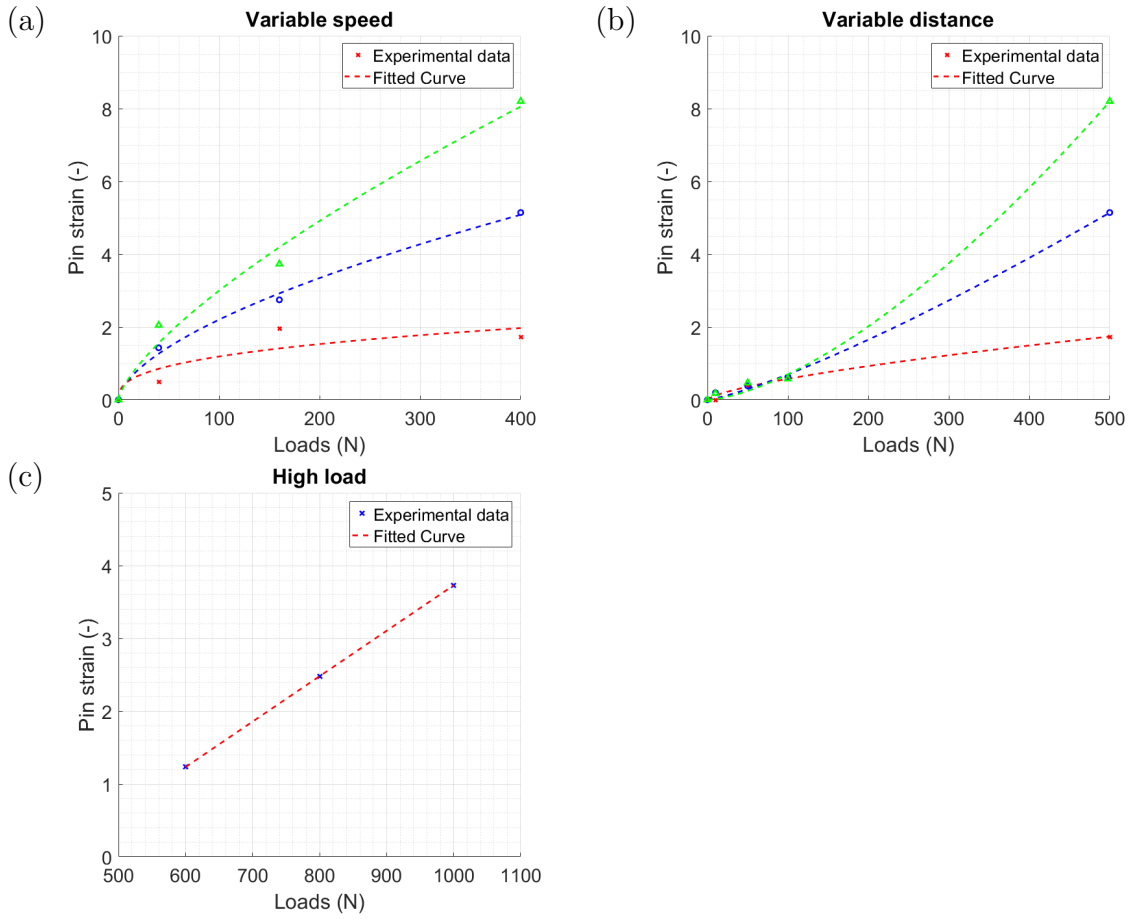

Figure 8.14: (a) Load vs strain graph for the worn pins for the variable speed test, (b) with the variable distance tests and (c) the 0.02 m/s tests between 600 N and 1000 N.

ent, with the the pin being strained more per cycle than the plate. The trends in the strain data all appear to be increasing with load, which reflects the increased strain seen in experiment. Additionally, at low loads and speeds, the strain-rate between pin and plate becomes similar perhaps suggesting the differences in strain stem from variations in heat generated between the mated surfaces. Studies of strain in the sub-surface, either using finite element models and phenomenological material models, or experimental studies using EBSD, would improve this analysis.

With the strain-rates corrected, these new values were used in combination with the void simulations of 5% area fraction. The wear-rates for the pin are shown in Figure 8.23. As expected, the introduction of voids onto the wear-process show an increase in the wear-rates on the pin. Generally, the increase is not too significant, with roughly a 0.5×10^{-14} increase over-all. The wear trends are maintained even with an introduction of a void, and appear to follow closely the trends in the surface texture parameters as seen in Figures 6.4 and 6.5.

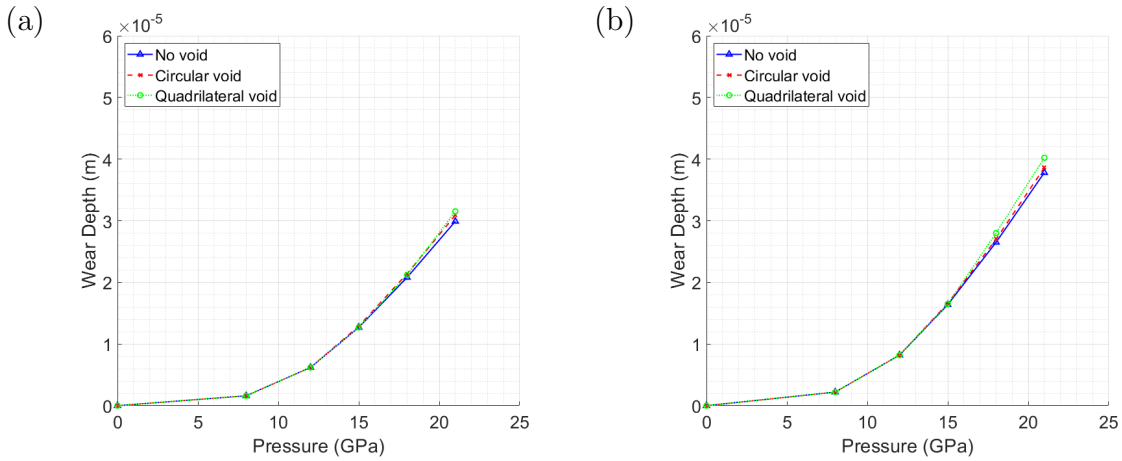

Figure 8.16: Variation in depth loss with the pressure experienced by an asperity of radius 0.75 μ for different void morphologies after 5000 cycles showing (a) the depth loss for $\mu = 0.25$ and (b) the depth loss for $\mu = 0.50$.

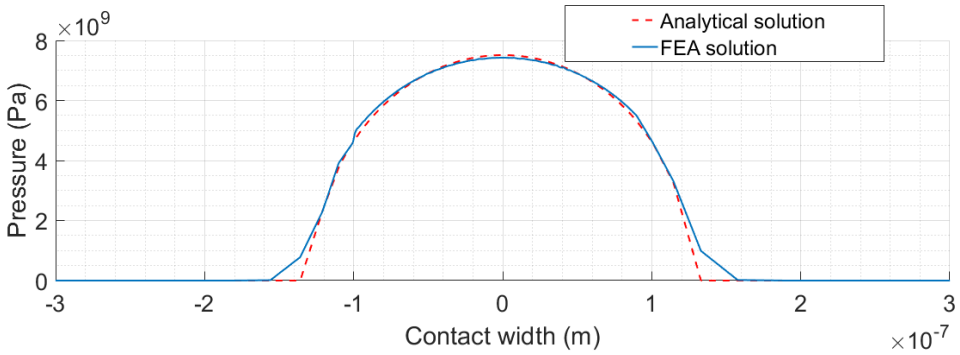

Figure 8.17: Comparison between the analytical Hertzian solution and the FEA simulation for a cylinder-on-flat under the same load conditions.

8.5 Discussion

8.5.1 Microscale ratcheting model

The Franklin-Kapoor model can help highlight how both friction as well as asperity load can interplay with one another to generate wear. Particularly, it was seen that at larger coefficients of friction the running-in occurred sooner, but the duration of running-in was shorter than in the low-friction case. This can be understood by the fact that at higher levels of friction, the magnitude of shear-stress increased as to cause the material to wear sooner. With regards to the duration of running-in, the greater magnitude of stress simply allowed the material to work-harden and remove material quicker to the point where the subsurface material was work-hardened the same amount before brought into contact with the asperity.

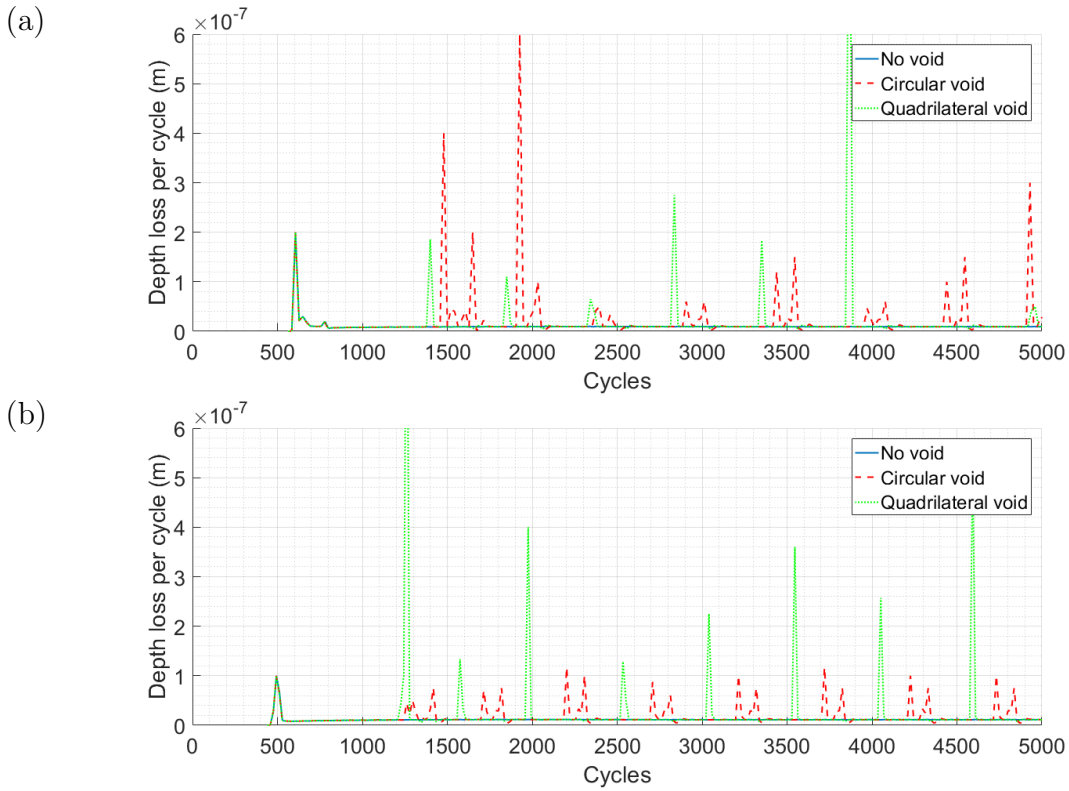

Figure 8.19: Cycles versus depth loss per cycle for different voids at friction coefficients for an asperity of radius 0.75 μm under a penetration depth of 1.0 μm (a) 0.25 and (b) 0.50 respectively.

Diamond voids appear to increase the wear-rate considerably, compared to circular, with the exception of higher coefficients of friction where the circular void appears to dominate. The increased wear-rate would be expected due to the sharper corners present on the diamond void when compared to circular voids. These sharper corners act as more severe stress-raisers than in the circular case. Interestingly the spikes in wear-rate, as seen in Figures 8.19 are much more transient than in the circular case. This may be explained by the sharper and narrower peaks in the stress data as shown in Figure 8.3. The circular voids have a much greater spread in stress with depth, and as such it takes longer for material removal to release the wearing material of these stresses.

With higher coefficients of friction, the gap in depth loss appears to diminish. Perhaps, looking at the wear-rate data in Figure 8.19, this may be explained in terms of a trade-off between the magnitude of wear-rate versus the duration that the void modifies the wear-rate.

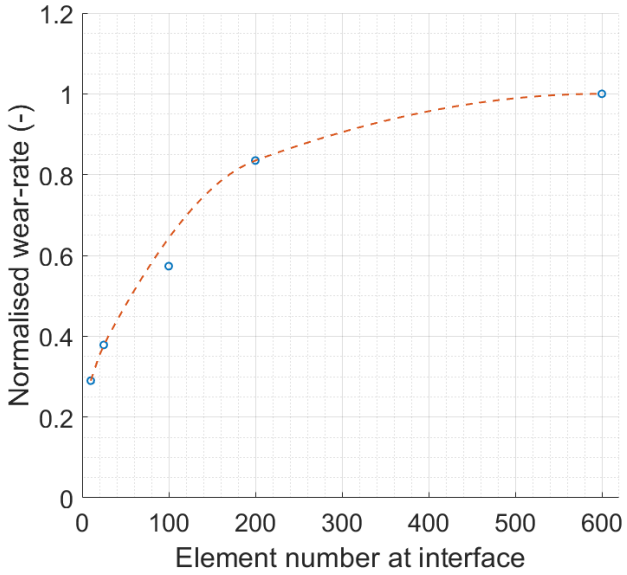

Figure 8.20: Mesh sensitivity analysis for a 600N test run for 100m on a geometry with pin diameter 8mm. The wear-rate values have been normalised against the wear-rate value corresponding to a mesh number of 10 at the wear interface.

8.5.2 Macroscale finite element model of wear

Most significant of the aforementioned analysis is that the ratcheting subroutine predicts the correct magnitude of wear for 0.02 m/s to 0.50 m/s. The wear-rate magnitude of $1{\times}10^{-14}$ m^3/Nm is typical for Stellite$^{\text{TM}}$ 6 [65, 58, 66]. This is important because the magnitude of wear-rates has essentially been determined through a mechanistic approach, which accounts for wear depth based on how much the material can strain before it ruptures to create a wear particle.

Initially, the rate of wear is not very high, due to the material starting at 0% initial strain. However, after a couple of cycles, the material begins to accumulate strain in the subsurface after which enough strain accumulates to liberate material from the wearing surface along with a corresponding increase in the wear-rate.

As expected, the introduction of voids into the wear process cause an increase in material damage. This is because the voids act as stress-raisers when subjected to load. Unlike other finite element models of wear, the method for the introduction of voids into the wear analysis is not clear. However, due to the mechanistic approach of the ratcheting sub-routine, their introduction is straight-forward. Primarily, changes in void morphology and their influence of wear may also be captured.

The percentage increase, comparing circular and diamond pores, are shown in table 8.2 and are calculated from the simulation results in Figure 8.23. The diamond void

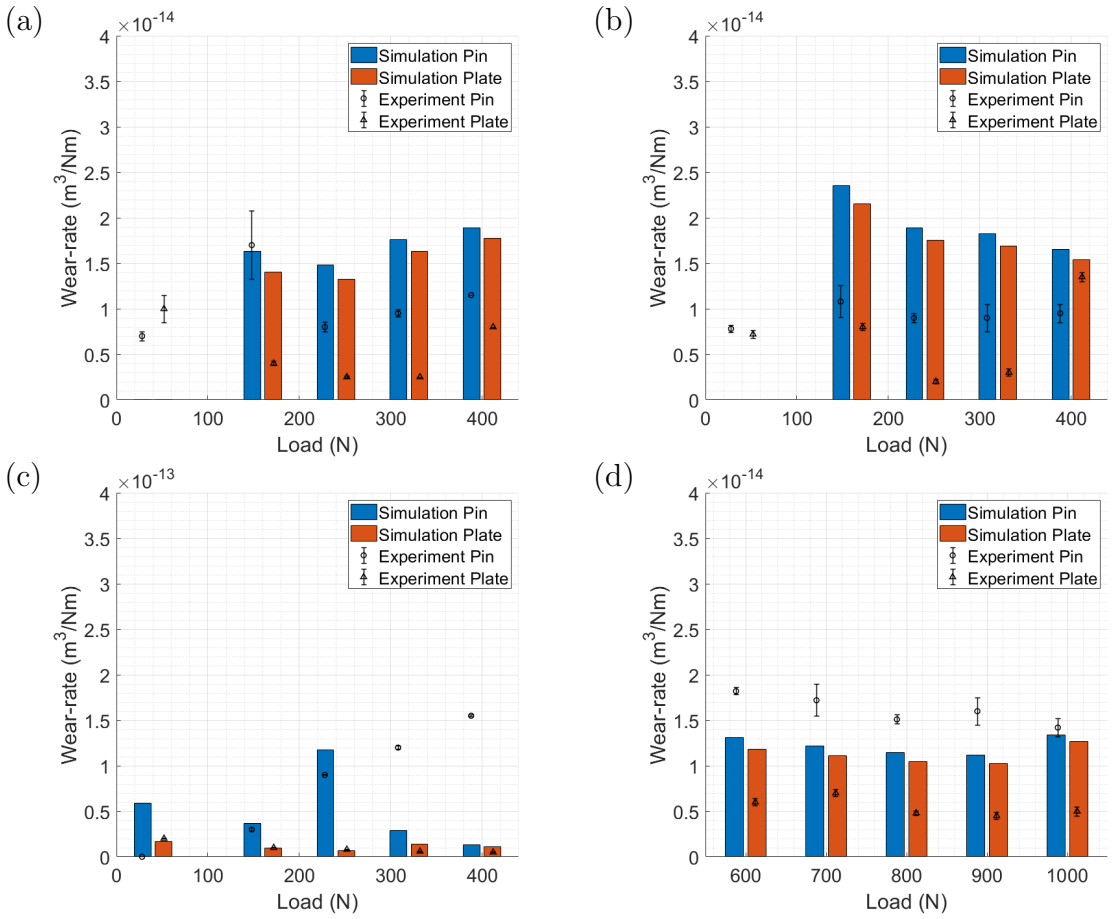

Figure 8.21: Wear-rates versus load of the simulation with the ratchet subroutine compared to the Archard routine for (a) 0.05 m/s, (b) 0.10 m/s, (c) 0.50 m/s, and (d) 0.02 m/s.

appears to result in a less extreme wear increase than the circular void, despite the much greater magnitude of stress produced by the diamond void (see Chapter 8 Figure 8.3). This could be due to the fact that the stresses produced by a circular pore are much less concentrated and spread out through the depth of the material.

The merits of this modelling approach are that it allows one to observe how wear is effected by material properties, microscale heterogeneity, and changes in surface roughness.

It is important to stress that this modelling approach only has a range of validity where ratcheting wear operates as the primary wear mechanism. As a result, loads below 160 N did not cause any wear to occur. This is expected, however, under these loads the primary wear mechanism was either oxide or fatigue driven. The high speed data is an exception, likely due to the high frictional heating changing the mechanical properties of Stellite. Furthermore, the current model does not account

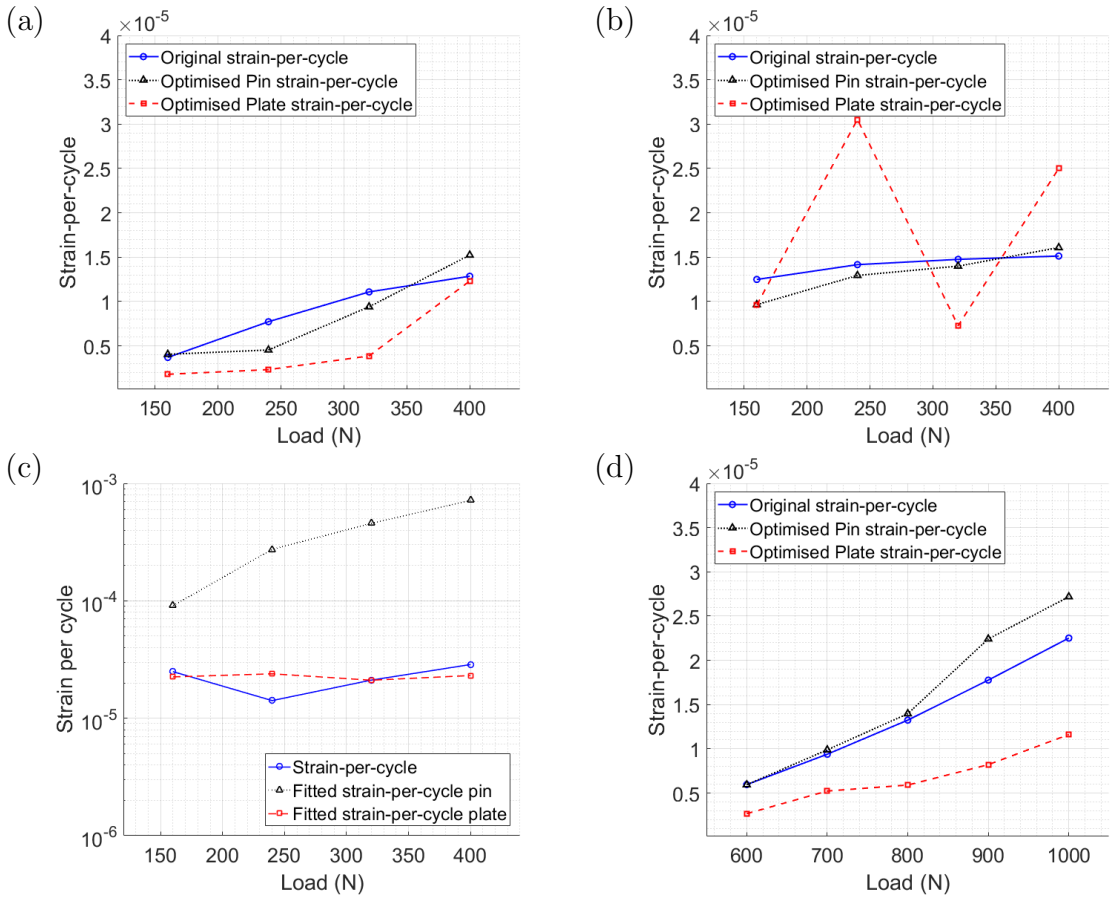

Figure 8.22: Comparison between the strain-per-cycle calculated from the worn pin and the strains determined from an optimisation routine for (a) 0.05 m/s, (b) 0.10 m/s, (c) 0.50 m/s, and (d) 0.02 m/s respectively.

for the reversal of strain due to reciprocated sliding motion.

Differences in the strain-rates, after the optimisation routine as shown in Figure 8.22, may be explained by a variety of physical phenomena not yet accounted for in the analysis. The higher strain-rate of the pin would likely be a consequence of the pin seeing more frictional heat throughout the analysis. Incorporation of such analysis has been done by Franklin [140] in their block model, and showed a marked increase in wear with sliding speed. It is likely that by incorporating changes in material properties with heat, that the 0.50 m/s simulation will showcase more appropriate wear-rates.

The discrepancies in the wear depths may be explained by typical procedure to select wear depth from the experimental data, and the simulations inability to capture extreme local variations in the profile. Relatively, the wear profile on the plate for the simulation is smoother than seen in experiment. As a result of the wear depth

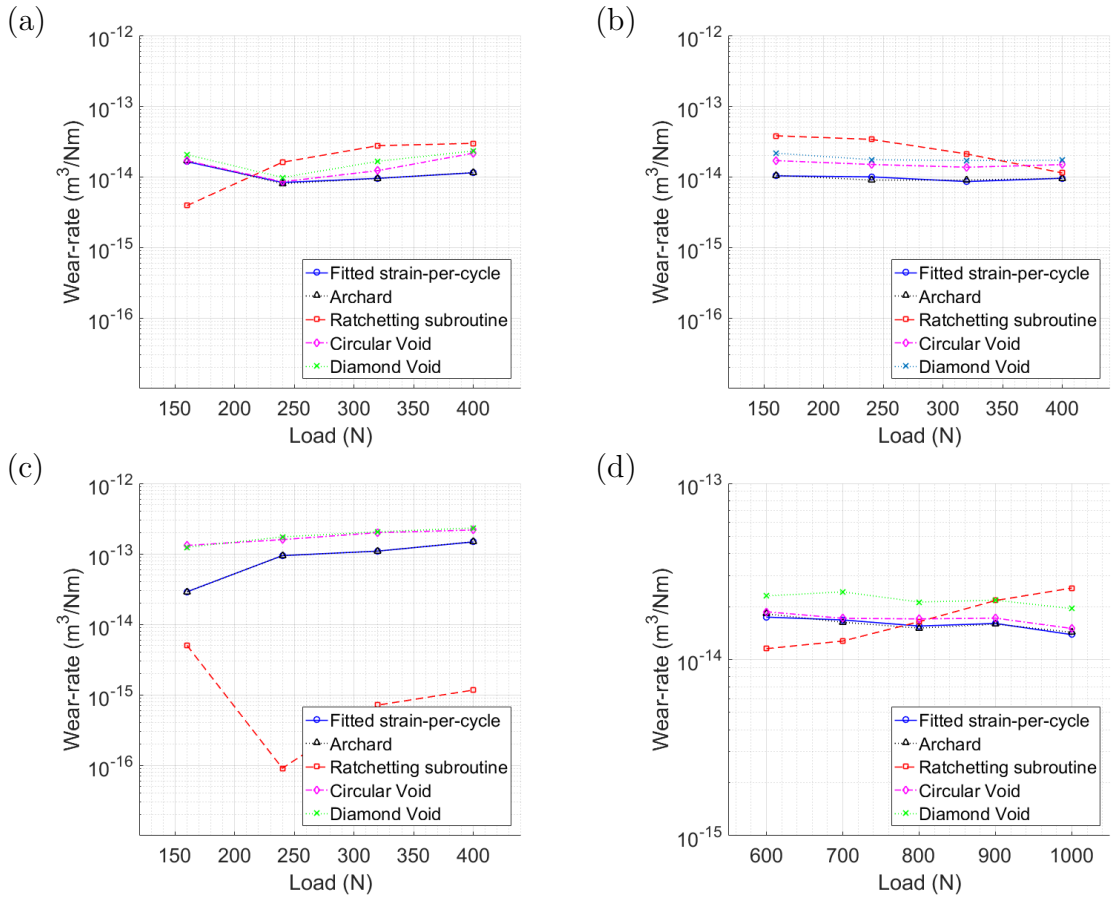

Figure 8.23: Results for the wear-rates after using the optimised strain values with the effects of voids included for (a) 0.05 m/s, (b) 0.10 m/s, (c) 0.50 m/s, and (d) 0.02 m/s respectively.

being determined as the lowest point on the wear profile, this could explain the differences in depths between simulation and experiment.

This modelling approach may be further improved by incorporating changes in surface roughness, and changes in material properties in response to frictional heating.

8.6 Finite element asperity model results and discussion

Results from the finite element slider model, showing the effective plastic strain and plastic shear strain factors, as calculated from equations 8.6 and 8.7, are shown as a Friction versus Load map in Figure 8.25. The values of strain were taken from the maximum value of strain under in the elastoplastic half-space at the centre of the stroke. The maximum strain is of interest here, as it would correspond to the value

Table 8.2: Table showing the increase in wear when circular and diamond voids are introduced onto the pin microstructure with an area fraction of 5%.

Load (N)	Speed (m/s)	Distance (m)	Experimental pin wear-rate (m^3/Nm)	Percentage increase (%)	
				Circular void	Diamond void
400	0.05	500	1.14×10^{-14}	87.8	102.0
	0.10		9.47×10^{-15}	56.6	80.8
	0.50		1.48×10^{-13}	46.5	56.6
600	0.02	100	1.82×10^{-14}	2.72	26.4
800			1.50×10^{-14}	12.8	40.6
1000			1.42×10^{-14}	5.01	36.2

of strain that causes initial material rupture and thus initiate wear particle creation. The strain factors are shown so that a comparison can be made against the strain-rate of Franklin-Kapoor.

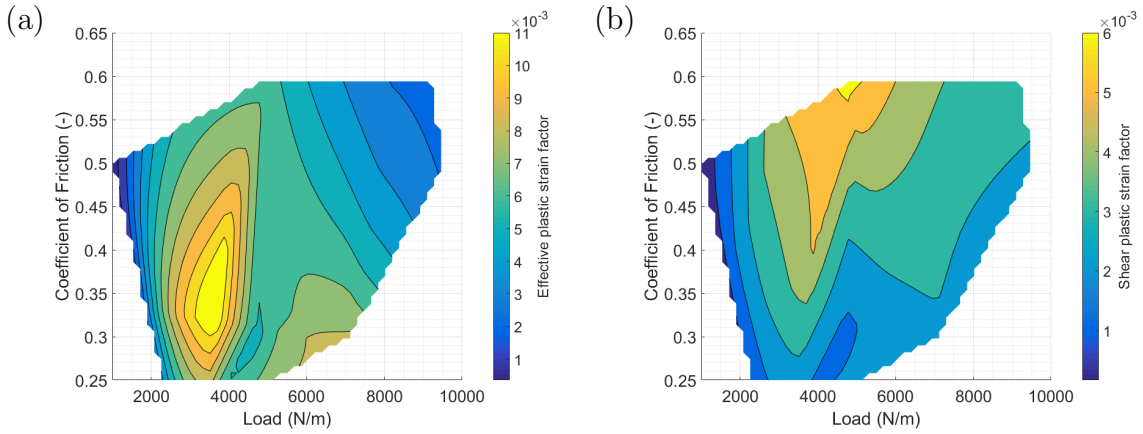

Figure 8.25: (a) The surface plot, interpolated from values obtained in the FEA simulation, for the plastic shear strain accumulated for a single cycle, (b) The strain factor corresponding to the strain and loading conditions.

While this model avoids the perfectly plastic small strain analysis of ref. [88], there are some short-comings with the given modelling approach. Firstly, the scale of the strains seen here quickly reach and exceed 15% strain before the simulation finishes a single cycle. This means that a finite strain model is required, and such models for non-linear kinematic hardening are not yet commercially ubiquitous. However, some exist in the literature [170, 171, 172] but require user subroutines for implementation. Furthermore, the model is also highly non-linear due to the interplay of plasticity and friction, and therefore runs into convergence problems, along with mesh distortion problems. Consequently, dynamics explicit modelling may be able to handle this

problem better [173]. In addition, the influence of hydrostatic pressure on the strain-to-failures is not known. As a result, further developments are required, such as a finite strain kinematic hardening model as well, before such a method can be employed to resolve the shear strains generated by an asperity ploughing into material for several thousand cycles under reciprocating motion.

8.7 Conclusions

A finite element model of wear, not based off the Archard wear equation, has been given. Primarily, one that is designed to capture a ratcheting wear process.
The benefits of this approach, which are not afforded by Archard, are thus:

- Evolution of surface roughness can be incorporated into the analysis.
- Influences of changes in material properties on wear-rates can be included, either through sliding or frictional heat.
- Different types of microscale heterogeneity can be implemented into the analysis, allowing one to better optimise the system in response to sliding wear.
- Coatings or wear-reducing oxides may easily be implemented into the analysis by modifying the contact stress equations appropriately.

As a result, this wear model affords a much greater range of predictability than would be possible with Archard. The specific wear rate used in the Archard wear equation has no clear physical interpretation. The mechanistic approach of the ratcheting sub-routine allows one to see how wear changes due to environmental changes in mechanical properties, microscale heterogeneity, or coatings. However, it must be stressed that this wear model is only valid under conditions in which ratcheting wear occurs.
Unfortunately, before finite element analysis can replace the dependency on a strain-per-cycle, c, as derived from wear experiments, further developments are required before such a model can be used. Primarily, the effective plastic strain exceeds 15% before a single cycle is completely which prevents the small strain assumption being used. This requires a user-implemented finite strain non-linear kinematic hardening model in the plasticity model in order to deal with the scale of deformations expected at this level. Given the scale of deformation, it would make more sense to employ dynamic explicit solvers typical for metal forming problems as this typically leads to better convergence, ableit longer solution times, of the model [173].

Chapter 9

Conclusions and future work

9.1 Introduction

This chapter takes the work presented in chapters 6 through 8, and gives an overall conclusion of the experimental and modelling work with relevance to the current literature. Unique to this thesis, Chapter 6 presented ratcheting wear as a main mechanism of wear for the Stellite™ system under a variety of loading conditions. This led to the study and application of the Kapoor-Franklin wear model [23]. It was seen that microstructure played a significant role in the wear process, so material properties of each phase were extracted in Chapter 7. Lastly, Chapter 8 provided extensions — the incorporation of microscale heterogeneity and scaling of macroscale wear — to the ratcheting wear model for Stellite™ 6. This section concludes with future developments on the experimental techniques and computational models presented.

9.2 Conclusions

The aim of this work was to build a predictive model of wear for HIPed Stellite™ 6 under self-mated dry sliding conditions by capturing the appropriate physics. Particularly, efforts to characterise the wear mechanism of Stellite™ 6 and then identify an appropriate modelling approach were lacking in the literature, with most work focused on laser-clad Stellites™. Thus, after conducting a series of systematic experiments and identifying a dominant wear mechanism, a wear model was built and validated against simplistic sliding conditions. Importantly, this model was developed using a mechanistic approach as to inform Rolls-Royce how Stellites™ may wear in response to changes in microstructure, environment, or tribological parameters.

As part of this work, Rolls-Royce were interested to know how manufacturing routes would affect the wear of Stellite™ 6. Therefore, the wear models presented incorporated elements of the microstructure into the analysis by first extracting the mechanics of each individual material phase. The work presented is not only limited to HIPed morphologies, either, as the same methodology may be applied for the sort of structures seen in laser-clad processing. By incorporating the effect of microscale features on a macroscopic wear-rate, it is now possible for Rolls-Royce to optimise wear in terms of microstructural parameters.

A literature review into the wear behaviours of Stellite™ 6, and current modelling efforts, were conducted in Chapters 2, 3, and 4. Further reciprocating tests were conducted in Chapter 6, which informed the modelling sections in Chapters 7 and 8. Section 9.2.1 presents the conclusions from the tribological study on self-mated HIPed Stellite™ 6. Section 9.2.2 gives conclusions for all the modelling work conducted after identifying a dominant wear mechanism. The wear model presented in Chapter 8 is a valuable extension to the current literature, as it now provides a means to predict wear based on physical changes within the material – or environment – when compared to other models of wear.

9.2.1 Experimental Conclusions

In Chapter 6, the wear response of Stellite™ 6 under self-mated dry sliding was performed for a variety of loads and speeds. The reasons for this were in order to observe how the wear mechanisms of Stellite™ 6 changed with tribological parameters, and to identify a dominant wear mechanism. It was concluded that Archard was not appropriate for modelling this system. Particularly, whether the Archard wear equation was an appropriate modelling approach was first tested by analysing trends in the wear-rates:

- **For 0.02 m/s, the wear-rate data showed a decrease in the wear-rate with load.**
- **For 0.05 m/s to 0.1 m/s, the wear-rate varied too much to make a reasonable conclusion on any trend.**
- **For 0.5 m/s, the wear-rate increased considerably with load as to reach severe wear.**
- **The pin generally wore moreso than the plate for every wear test.**

To further investigate the validity of Archard as a modelling procedure, several observations were made:

- **For low speeds and low loads, oxides formed on the surface remain well-adhered. Wear particles took on a large round morphology, suggesting a fatigue-dominant wear mechanism.**
- **As load or speed increased, material began to show signs of plastic deformation. Flake-like particles could be seen forming on the surface. Wear particle morphology began to take on a lamellar-like appearance.**
- **The pin edges appeared highly deformed, and strained much higher (some $> 100\%$ strain), than the reported strain-to-failure for this material [19].**

The latter mechanism was seen throughout most tests where oxide formation did not dominate. Given the plate-like morphology of the debris and variable wear-rate,

in contradiction to Archard's arguments, it was concluded that the Archard wear equation was not appropriate for modelling of Stellite™ wear.
Instead, the wear particle morphology and detachment mechanism pointed to a ratcheting-like wear mode [130], where this behaviour is typical of subsurface material being incrementally strained up to rupture to form plate-like wear particles [130]. Further experimental analysis was conducted to confirm this.

- **Subsurface analysis of the pin showed material being ruptured to form crack paths parallel to the sliding direction.**
- **These cracks would propagate from voids, sometimes carbides, and propagate around carbide boundaries.**
- **Nano-indentation was also performed to show that the material was failing in a highly work hardened layer.**

In some cases, highly-mixed material was also showed to have become adhered to the wearing pin to create a mechanically mixed layer (MML) which is suggested to wear off as a result of ratcheting [23].
Some additional observations were also made as part of the experimental work. Primarily:

- **Small globular adhesive wear was seen throughout all experiments, especially in the case of oxidative wear where these wear particles would cluster around oxide-matrix boundaries.**
- **The nano-indentation work also revealed that hardened layer also experienced a marginal decrease in the Young's modulus in this same layer, causing an increase in the H/E parameter.**

It is important to highlight that within the ratcheting model, the H/E factor [109] plays an important role in determining the plasticity index in repeated sliding [128]. A higher H/E value means that ratcheting will become less likely, however not enough to prevent it in the case of Stellite™ 6. This reduction in Young's modulus comes as a consequence of nano-grain formation during sliding, following many studies that demonstrate this to occur for Cobalt-based systems and led to 'globular' wear particles [155].
With the conclusion that a ratcheting wear mechanism was dominant throughout the wear tests, and that the wear was highly dependant on the morphology of the

microstructure and evolution of material properties such as hardness or stiffness, this led to developing models seen in Chapter 8 to capture Stellite™ 6 wear by modifying current numerical sliding and ratcheting wear methodologies. However, before models concerning the microstructure could be developed, knowledge regarding the material properties of each phase in Stellite™ 6 had to first be extracted, as was done in Chapter 7.

9.2.2 Modelling Conclusions

A precursory study of the literature with regards to ratcheting wear modelling led to the discovery of the Franklin-Kapoor ratcheting model [23]. This model was mechanistic in nature, i.e. wear was controlled as the result of changes in material properties that had clear physical interpretations. As a result, the Kapoor-Franklin model required a full understanding of the Stellite™ 6 material response during load, which led the author to conduct materials testing of Stellite™ 6 under tension and cyclic loading. These tests revealed that the yield stress of Stellite™ 6 was 450 MPa, much less than the offset yield, which was validated using hardness simulations against hardness data.
The Kapoor-Franklin model had to be extended due to several limitations of the model, which were addressed as part of this thesis, primarily:

1. **The existence of voids, and their morphology, in the microstructure is not incorporated into the wear analysis.**

2. **The strain-per-cycle, produced by an asperity was determined through a simplistic analysis [88], did not account for out-of-shear strains and finite strain plasticity.**

3. **The wear model only uses simplistic Hertzian contact geometries, such as cylinder-on-flat or sphere-on-flat.**

To address point (1), it was necessary to understand the mechanical response of each phase in the microstructure, the focus of Chapter 7. This led to the development of an inverse analysis model, wherein stress-strain curves from a tension experiment were matched to a simulation of an RVE of the Stellite™ 6 microstructure undergoing the same experimental conditions as in the tension test. The carbide phase material properties were chosen from the literature [159, 160, 165].

- **Several permutations of the Stellite™ 6 microstructure were subjected to the same loading conditions as in the tension test.**
- **The plastic parameters of yield, hardening rate, and saturation stress were adjusted until the experimental and simulated curves matched.**
- **Curves were considered matched if their relative error dropped below a 1% threshold.**

The values for the plasticity parameters, as well as their trends, were validated against experimental nano-indentation data. The nano-indentation data was de-convoluted in order to resolve the elastic modulus of each phase, which corresponded very closely to the extracted value from simulation. The yield in the inverse analysis of the matrix also increased when separated from the carbides, which would correspond to a higher hardness. Likewise, a higher hardness was seen for the de-convoluted matrix.
The inverse analysis allowed for the extraction of the material response of individual Stellite™ 6 phases, which is unique to this thesis. Furthermore, this will allow future modelling of the Stellite™ 6 microstructure.
With the microstructural material properties determined, the influence of circular and diamond-like voids on the Hertzian stress field could be conducted. This was the primary focus of Chapter 8. A methodology for super-imposing the stress-raisers from voids onto the Hertzian stress field of the Franklin-Kapoor model was outlined. Primarily this allowed for:

- **Comparison between wear-rates in the Stellite™ 6 as a function of load and friction.**
- **How wear-rates are affected by different void morphologies, such as a diamond or circle, to better understand how to optimise wear-rates in terms of microstructure.**

The major benefit of this methodology is that it allows one to incorporate the microstructure, as well as friction, to see how the wear-rate of Stellite™ 6 is affected in this ratcheting regime.
To address point (2), another focus of Chapter 8, a unit event of an asperity – assumed to be carbide – sliding over an elastoplastic half-space was simulated using the FEM. However, during loading, the scale of strain was much larger than 15% strain which required the usage of a finite strain plasticity model. Unfortunately, no such model existed for non-linear kinematic hardening. Furthermore, convergence of

such a model using an implicit quasi-static solver was exceptionally hard to achieve. It was concluded that, while this approach would be beneficial, it would require the development of a finite strain model to be solved using a more appropriate explicit dynamics solver [173].
Lastly, point (3) was addressed by using the microscale ratcheting models of the prior section, and incorporating them as a subroutine into a macroscale finite element model of wear using a statistical model of contact to upscale them. This allowed one to compare the simulated macroscale wear to experiments, thereby validating the previous approaches to wear.

- **Surface roughness was incorporated into the wear analysis, by using the Greenwood-Williamson statistical model of rough contact.**

- **The scale of wear, being $1\times10^{-14}m^3/Nm$, was captured by the ratcheting wear processor.**

- **It was possible to see the influence of the microstructure on the macroscopic wear process**

The wear model developed and presented in this thesis present a considerable improvement over the typical methods of wear prediction using finite elements. Arguably, for a model whose wear predictions depend only on how the material responds mechanically under load, the fact it is giving the right range of wear for 0.02 m/s to 0.10 m/s is a very good sign. Furthermore, because this wear model is mechanistic, it is possible to see how wear changes based off variations in microstructure (such as inclusion or void morphology) or changes in material properties (either through hardening or softening). This allows for much greater predictability over Archard wear, which offers no clear avenue on how to incorporate such physics into the wear process. However, the present model may be improved by incorporating frictional heating, carbides, and surface roughness evolution into its analysis.
It is suggested that this modelling approach will allow one to account for the purely mechanical wear component, W_0 in tribocorrosive wear, that is $S' = W_0 + C_0 + T$, to determine the synergistic term, S' [99, 22]. Coupling this model with the total tribocorrosive data, T, and corrosive data C_0, seen from a PWR may allow one to determine the form of this term and build a truly predictive model of Stellite$^{\text{TM}}$ wear in a PWR environment and aid in the development of cobalt alternatives.

9.3 Future work

While a lot of experimental research into the sliding wear of Stellite™ 6, particularly laser-clad, very little has been conducted for self-mated HIPed Stellite™ 6 systems with no real focus on understanding the mechanics behind wear. The work in this thesis identified a dominant wear mechanism and the mechanics behind it. Then, a mechanistic macroscale ratcheting degradation model, capable of outputting wear-rates as the material degraded due to plastic strain accumulation, was created. This model allows one to predict wear as a function of the straining of material in the subsurface, which may be easily modified in future work by introducing additional variables affecting the material properties at the interface, i.e. heating. Avenues of development on the work in this thesis are presented:

1. **Detailed identification of crack propagation in the subsurface via EBSD.**

Crack growth throughout the microstructure as a consequence of tribological experiments is difficult to identify, often with crack-like structures being identified post experiment. As part of the ratcheting model of wear, that wear particles may be generated through the incremental propagation of ductile cracks in the subsurface close to, and parallel to, the wear interface [116] where the cracks then turn up towards the wear interface and liberate material. Continuity of the microstructure around these so-called cracks suggests that the formation of these cracks is not the result of material adhering to the wear interface.
Experimental techniques such as EBSD or etching, can help identify cracks, as crack tips experience high levels of stress and so stress-driven material transformations, such as grain refinement or martensitic transformations, may be expected at the leading tip of the crack which would add credence to the suggestion of HIPed Stellite™ 6 undergoing ratcheting deformation, particularly if it can be demonstrated that such a crack exists within a highly compressive region of material [116].

2. **Use of a more robust experimental method, in conjunction with numerical modelling, for determining strain at the wear interface.**

Due to the lack of detailed strain data for self-mated HIPed Stellite™ 6 versus Stellite™ 6, it was necessary to analysis the lipping at the pin edge to approximate the strain after sliding. However, more appropriate methods for determining

the strain after sliding – particularly in the highly work-hardened layer – such as observing the deformed grains after etching the material using SEM or back scattered diffusion (EBSD) methods could be used.
In order to capture the strain mechanics of ratcheting in simulations, it is necessary to employ either perfectly plastic or non-linear kinematic plasticity models. Unfortunately, the strains generated at the asperity scale are exceptionally large, even without sliding and so a finite strain model is necessary. Development of such a model that shows how strain accumulates with many cycles of an asperity would be beneficial as it would replace the strain methodology of Franklin-Kapoor [94] and allow one to come up with more physically appropriate models of strain accumulation during ratcheting.

3. **Improved hardening function in the Franklin-Kapoor model that accounts for the reversal of strain during reciprocated sliding motion.**

The present ratcheting subroutine using a hardening function procedure as outlined by Kapoor-Franklin [23], does not account for the reversal of strain when the load is removed from contact. This could be implemented by replacing the Voce-like hardening curve in Chapter 8 with one that models the evolution of back-stress. This would be particularly useful as it would capture the reversing strains present in a reciprocating sliding stroke.

4. **Application of the more general 2D brick model [140] to capture the influence of microstructure in the ratcheting wear processor.**

Presently, carbides were ignored from the inclusion model with voids merely to keep the work simplistic. The influence of carbides on the wear process could be implemented using the Franklin brick model [140]. Such a model relies on various heuristics to control the likelihood of material failure around microstructural defects, and so these heuristics for Stellite™ 6 may be better determined by analysing strain-data from finite element simulations for carbides.

5. **Add the influence of material heating due to friction and ambient temperature on the material properties at the wearing interface in the ratcheting wear processor.**

Due to the lack of meaningful data regarding how the material properties, such as yield and hardening rates, of Stellite™ 6 change when subjected to increasing temperature it was not possible to incorporate meaningfully the influence of frictional

heat. However, the development would be possible if one were to collect such data from their own material tests. Analytical equations for heating due to friction exist [174], and could be used in conjunction with this data to better see how wear-rates change with increasing sliding speed or ambient temperatures.

6. **Incorporation of a oxide growth subroutine in the macroscale wear model to capture the interplay between oxide formation and ratcheting wear.**

Oxides are known to play an important role in mitigating wear. Particular, the ratcheting wear model could be extended to the oxide regime by simplying incorporating a mechanism for oxide growth on the macroscale model which prevents the substrate (Stellite$^{\text{TM}}$ 6) from being highly strained. Growth models, such as in the form of a transfer layer [124] or oxide itself [175] in the context of sliding wear have already been done and so such an extension may prove simple.
These models may be further improved if combined with a better constitutive model that captures how stress within the substrate is modified when a coating or oxide is introduced into the system, as well as the mechanics behind coating failure [176, 177]. Particularly useful is that ratcheting, or incremental collapse, may be determined through Hertzian considerations [116] and such analytical extensions to the stress field of an elastic half-space with a coating being subjected to loading have been done [178].

Chapter A
Methodologies

A.1 Derivation of the force function

The derive the equation for the pressure between two cylinders under contact as a function of displacement, the RHS of the equation for two cylinders in contact [128] was plotted in Matlab on the y-axis and the LHS on the x-axis. This was done so that the plot was expressed in terms of the inverse solution. This analytical equation is:

$$\frac{\delta}{R} = \left(\frac{p_0}{E^*}\right)^2 \left[2\ln\left(\frac{4E^*}{p_0}\right) - 1\right] \tag{A.1}$$

where δ is the interference or penetration between the contacting bodies, R is the radius, $p0$ is the maximum pressure.

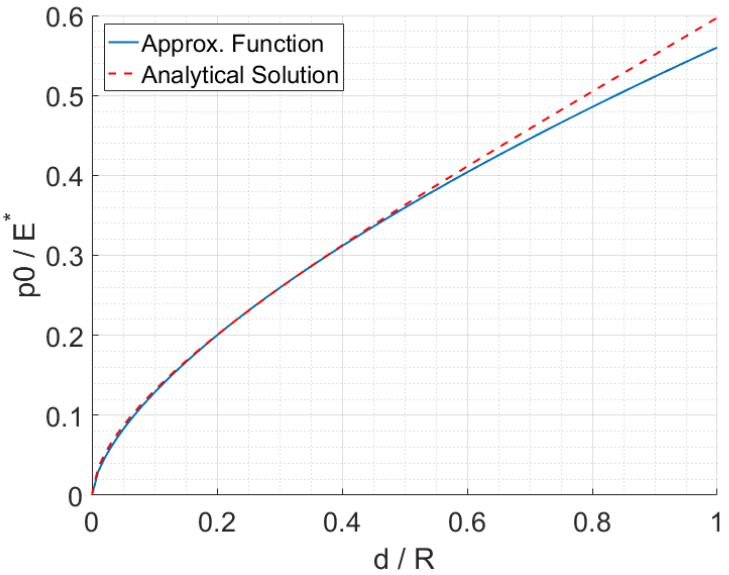

Figure A.1: The fitted function, blue, plotted against normalised pressure values with the analytical form from equation A.1 also plotted.

Once plotted, as shown in Figure A.1, a function of the form $f = ax^b$ was fitted to the analytical solution as this appeared to give a reasonable fit, where $x = \delta/R$

and $f = p0/E^*$. The fitting range was $0 \leq p0 \leq 5 \times 10^{10}$ Pa. The reason for this chosen pressure range is that, at values above this, the logarithmic term in the equation causes the analytic solution to deviate from the fitting function form, thus the fitted form only has this range of validity. Nevertheless, provided the maximum pressure values are within this range (which they often are) then the function gives a reasonable fit. The fitting results were:

$$p_0 \simeq 0.56E^*\Big(\frac{\delta}{R}\Big)^{0.64} \tag{A.2}$$

With this equation, it is now possible to express the contact force resulting from a desired interference, as well as the radius of contact, by using the equations for cylindrical contact force, F, and area, a, from Johnson [115]:

$$F/L = \frac{\pi R}{E^*}{p_0}^2 \tag{A.3}$$

$$a/L = 2\Big(\frac{4FR}{\pi E^*}\Big)^{0.5} \tag{A.4}$$

Substituting equation A.2 into equation A.3, and expanding out the squared term, gives:

$$F/L \simeq \pi R E^* 0.31\Big(\frac{\delta}{R}\Big)^{1.28} \tag{A.5}$$

Chapter B
Experimental data

B.1 Frictional traces

The full frictional traces for every dry sliding experiment are shown in Figure B.1.

B.2 2D profilometry

The profile of the plate for 0.05 m/s after sliding 500 m are shown in Figure B.2.
The profile of the plate for 0.10 m/s after sliding 500 m are shown in Figure B.3.
The profile of the plate for 0.50 m/s after sliding 500 m are shown in Figure B.4.
The profile of the plate for 0.01 m/s after sliding 100 m are shown in Figure B.5.

B.3 Scanning electron microscopy

Scanning electron microscopy

The SEM micrograph for the low load 40N, or nominal pressures of 0.5 MPa, tests for the pin and plate are shown in Figure 6.15.
The SEM micrograph for the low load 40N tests for the plate are shown in Figure B.7.

B.4 Statistical distributions

The statistical distribution of asperity heights for the 0.05 m/s and 0.10 m/s tests are shown in Figure B.8.

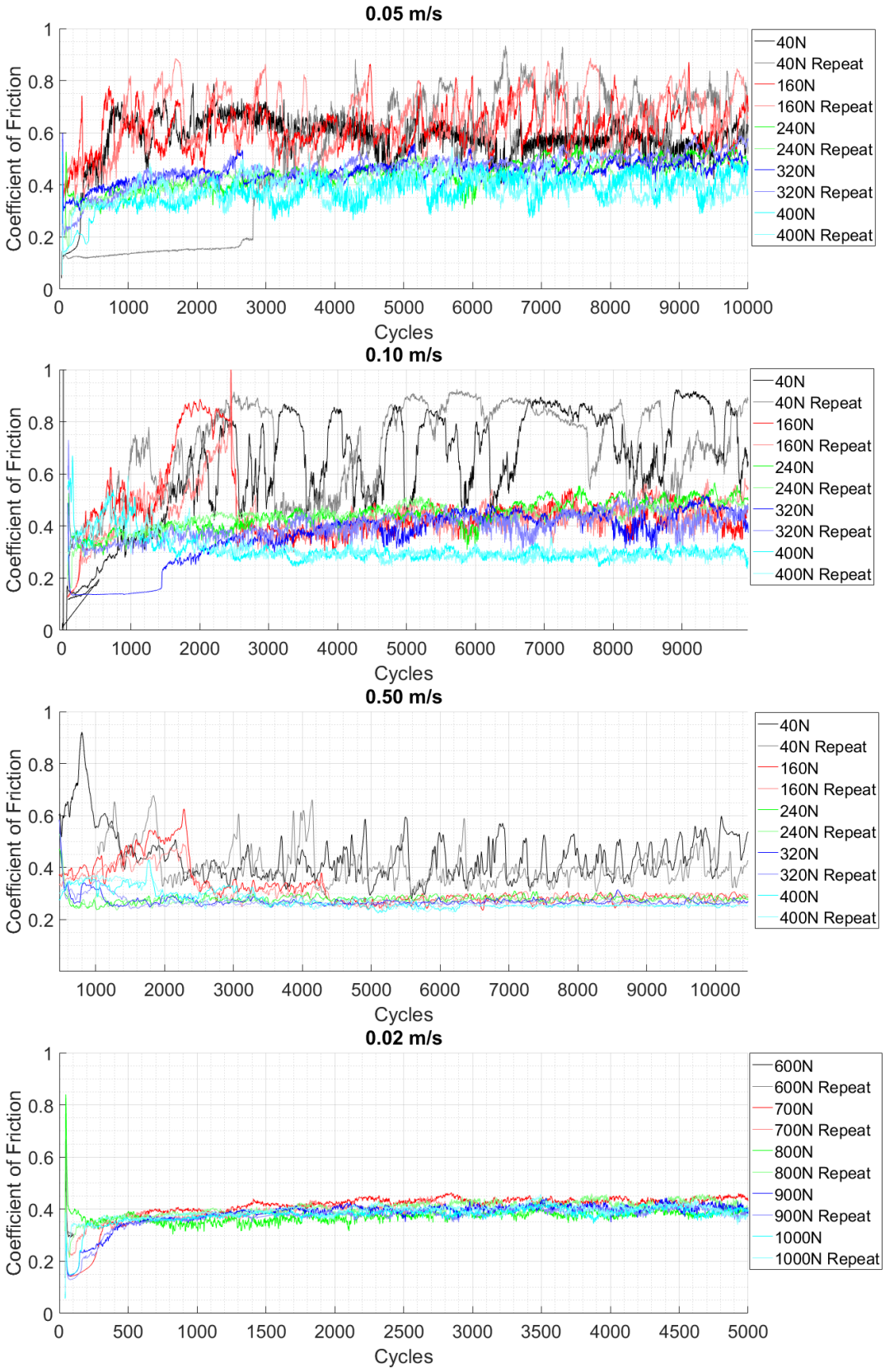

Figure B.1: The frictional traces for every dry sliding experiment.

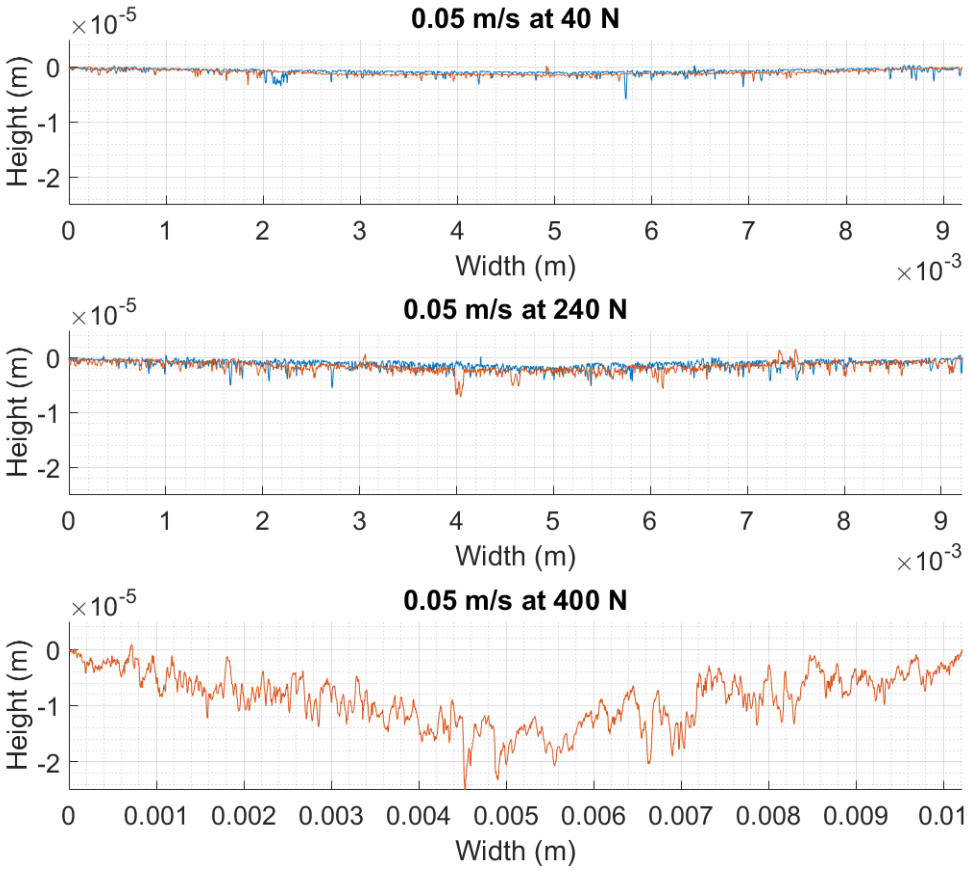

Figure B.2: Profilometry traces for the 0.05 m/s after 500 m tests are shown as the blue and red lines for the first and second runs respectively under (top) 40 N, (middle) 240 N, and (bottom) 400 N.

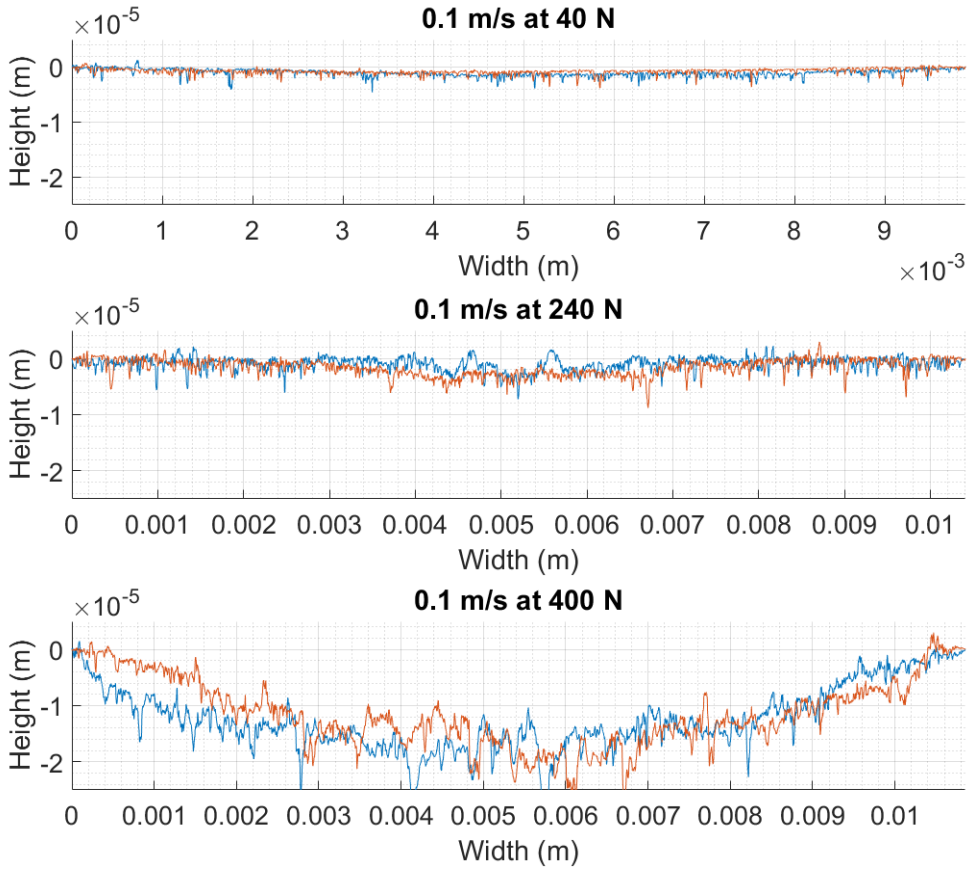

Figure B.3: Profilometry traces for the 0.10 m/s after 500 m tests are shown as the blue and red lines for the first and second runs respectively under (top) 40 N, (middle) 240 N, and (bottom) 400 N.

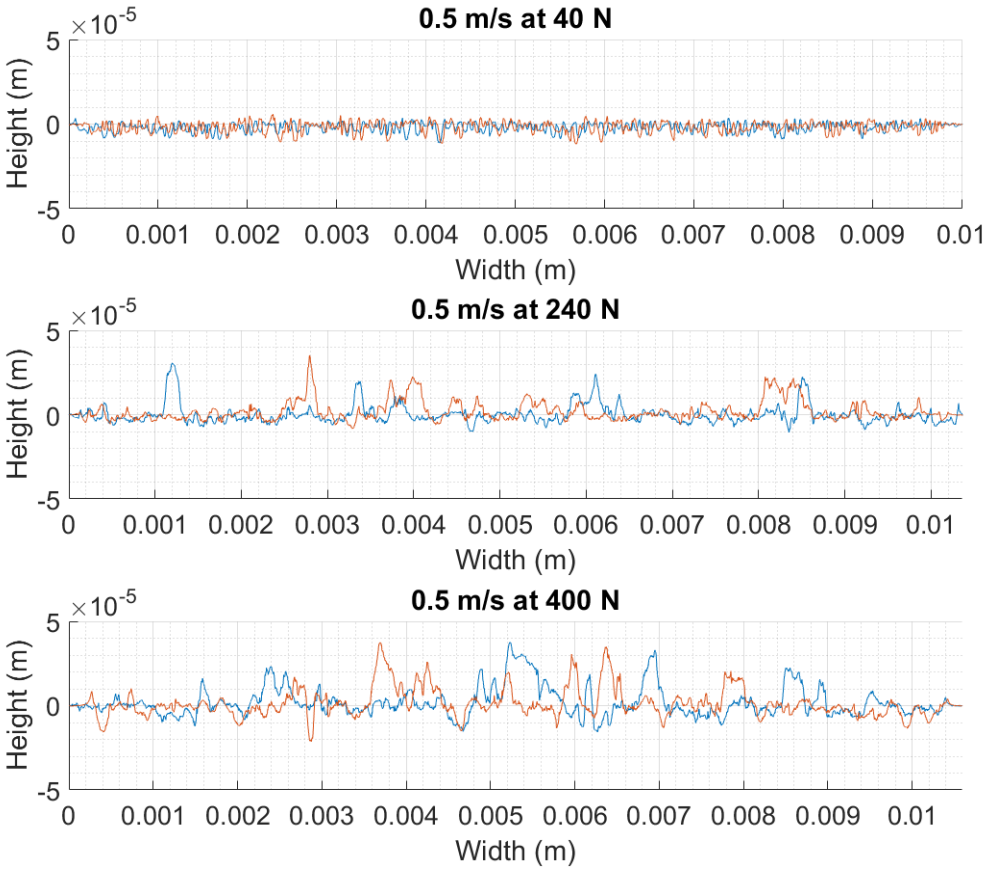

Figure B.4: Profilometry traces for the 0.50 m/s after 500 m tests are shown as the blue and red lines for the first and second runs respectively under (top) 40 N, (middle) 240 N, and (bottom) 400 N.

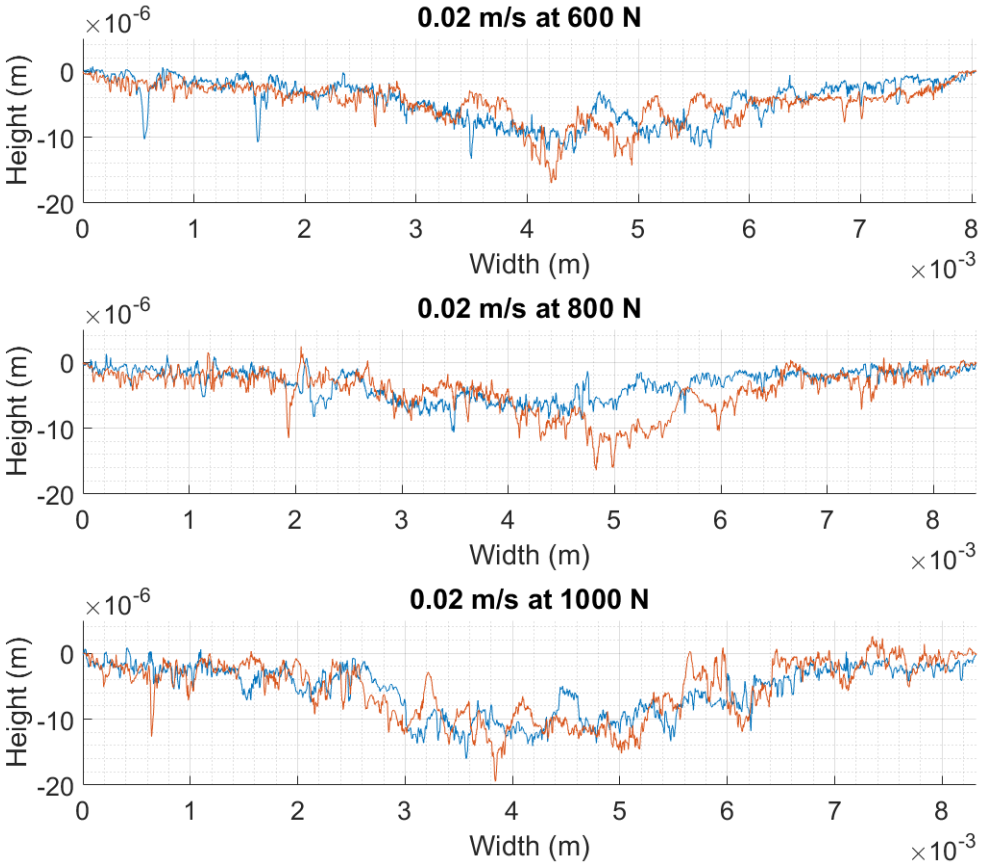

Figure B.5: Profilometry traces for the 0.02 m/s after 100 m tests are shown as the blue and red lines for the first and second runs respectively under (top) 600 N, (middle) 800 N, and (bottom) 1000 N.

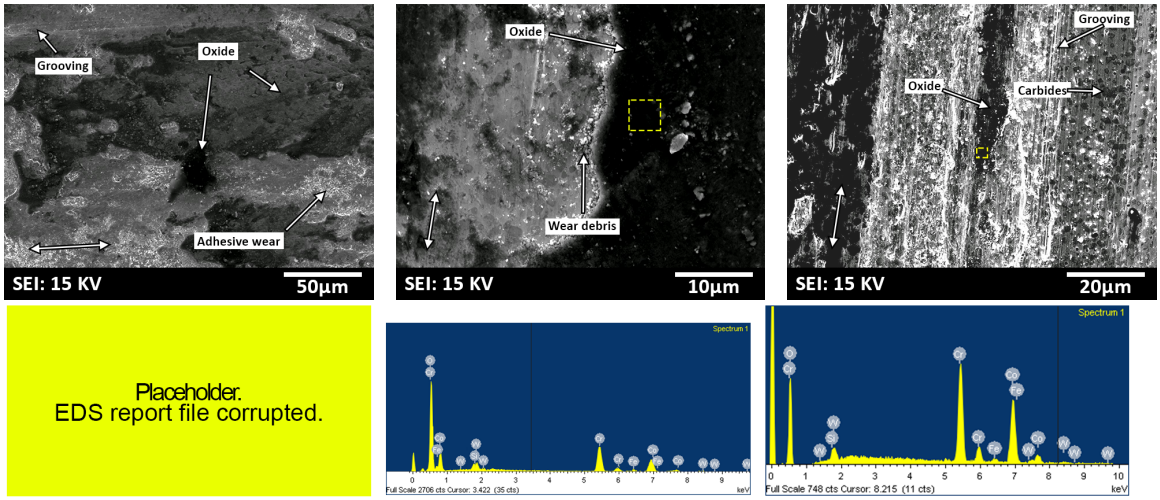

Figure B.6: SEM micrographs for the 40 N tests pin. Left) 0.05 m/s. Right) 0.10 m/s. Right) 0.50 m/s. Below each micrograph is its corresponding EDS spectra.

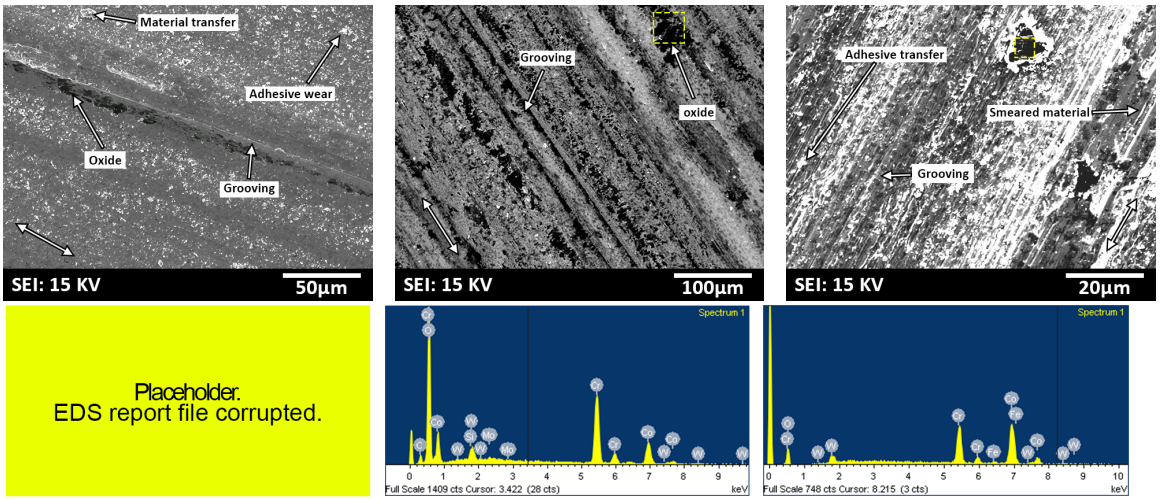

Figure B.7: SEM micrographs for the 40 N tests plates. Left) 0.05 m/s. Right) 0.10 m/s. Right) 0.50 m/s. Below each micrograph is its corresponding EDS spectra.

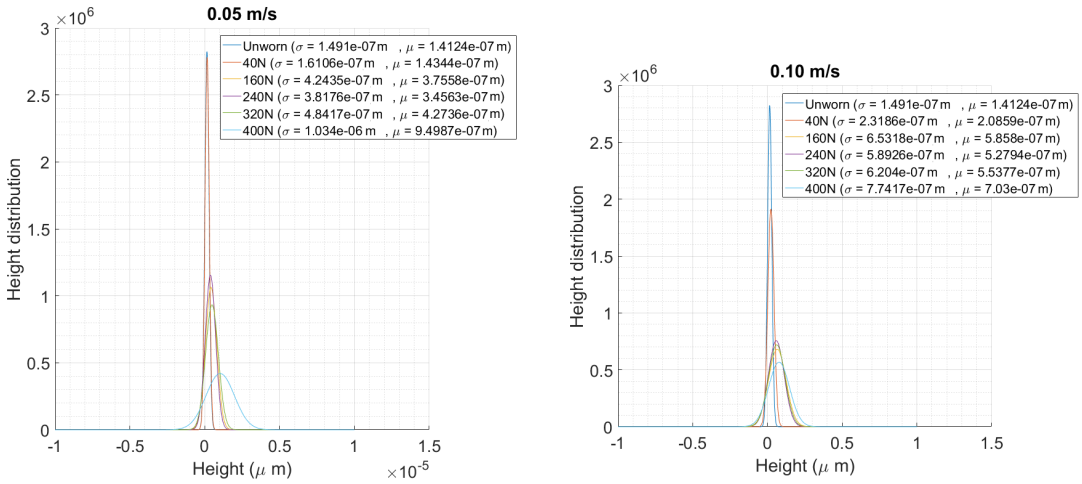

Figure B.8: Statistical distributions of asperity heights for the sliding wear tests.

.

Bibliography

[1] P.S.G. Cross et al. "Ratcheting wear of a cobalt-chromium alloy during reciprocated self-mated dry sliding". In: *Wear* 426-427 (2019), pp. 1142 –1151.

[2] P.S.G. Cross et al. "Extraction of material properties for a cobalt-chromium alloy using inverse analysis". In: *Journal of Solids and Structures* (Submitted).

[3] P.S.G. Cross et al. "A finite element model of wear for materials undergoing ratcheting deformation". In: *Wear* (Submitted).

[4] *Nuclear Power Generation*. `https://www.clpgroup.com/NuclearEnergy/Eng/power/power4_1_2.aspx`. Accessed: 2019-02-06.

[5] B. Pastina, J. Isabey, and B. Hickel. "The influence of water chemistry on the radiolysis of the primary coolant water in pressurized water reactors". In: *Journal of Nuclear Materials* 264.3 (1999), pp. 309–318.

[6] Walter D. Loveland, David J. Morrissey, and Glenn T. Seaborg. "Modern Nuclear Chemistry". In: John Wiley & Sons, Inc., 2005, pp. 465–496.

[7] A. Lina et al. "The influence of water flow on the impact/sliding wear and oxidation of PWR control rods specimens". In: *Wear* 251 (2001), pp. 839–852.

[8] E. Lemaire and M. Le Calvar. "Evidence of tribocorrosion wear in pressurized water reactors". In: *Wear* 249.5-6 (2001), pp. 338–344.

[9] P. R. Rubiolo and M. Y. Young. "On the factors affecting the fretting-wear risk of PWR fuel assemblies". In: *Nuclear Engineering and Design* 239.1 (2009), pp. 68–79.

[10] P. J. Blau, A. V. Hayrapetian, and M. J. Demkowicz. "Development of a Predictive Wear Model for Grid-to-Rod Fretting in Light Water Nuclear Reactors". In: *Tribo-Corrosion: Research, Testing, and Applications* 1563 (2013), pp. 139–158.

[11] P. Crook. "Cobalt-Base Alloys Resist Wear, Corrosion, and Heat". In: *Advanced Materials & Processes* 145.4 (1994), pp. 27–30.

[12] K. F. Dufrane and H. Ocken. "Measurements of Wear in Nuclear-Components". In: *Wear* 101.1 (1985), pp. 13–31.

[13] W. B. Burdett. “Development of Cobalt Free Wear Resistant Alloys for Nuclear Applications”. In: *Surface Engineering* 8.2 (1992), pp. 131–135.

[14] K. Y. Lee et al. “Sliding wear behavior of hardfacing alloys in a pressurized water environment”. In: *Wear* 262.7-8 (2007), pp. 845–849.

[15] H. Ocken. “Reducing the Cobalt Inventory in Light Water-Reactors”. In: *Nuclear Technology* 68.1 (1985), pp. 18–28.

[16] J. K. Kim and S. J. Kim. “The temperature dependence of the wear resistance of iron-base NOREM 02 hardfacing alloy”. In: *Wear* 237.2 (2000), pp. 217–222.

[17] *Scopus*. 2019. URL: `http://www.scopus.com`.

[18] B.V. Cockeram. “Development of wear-resistant coatings for cobalt–base alloys”. In: *Surface and Coatings Technology* 120-121 (1999), pp. 509 –518.

[19] S. Atamert and J. Stekly. “Microstructure, Wear Resistance, and Stability of Cobalt Based and Alternative Iron Based Hardfacing Alloys”. In: *Surface Engineering* 9.3 (1993), pp. 231–240.

[20] J. L. Sulley et al. “Introduction of Hot Isostatically Pressed, Reactor Coolant System Components in Pwr Plant”. In: *Proceedings of the 18th International Conference on Nuclear Engineering 2010, Vol 5* (2011), pp. 357–367.

[21] W. J. Chitty and J. P. Vernot. “Tribocorrosion issues in nuclear power generation”. In: *Tribocorrosion of Passive Metals and Coatings* (2011), pp. 424–440.

[22] A.J Gant, M.G Gee, and A.T May. “The evaluation of tribo-corrosion synergy for WC–Co hardmetals in low stress abrasion”. In: *Wear* 256.5 (2004), pp. 500 –516.

[23] A. Kapoor and F.J. Franklin. “Tribological layers and the wear of ductile materials”. In: *Wear* 245.1 (2000), pp. 204 –215.

[24] J. Lubliner. “Plasticity Theory”. In: Dover Publications, Inc., 2008, pp. 75–100.

[25] W. Püschl. “Models for dislocation cross-slip in close-packed crystal structures: a critical review”. In: *Progress in Materials Science* 47.4 (2002), pp. 415 –461.

[26] N. N. Greenwood and A. Earnshaw. “Chemistry of the Elements”. In: Butterworth-Heinemann, 1997, pp. 1113–1143.

[27] Lizarraga et al. “First Principles Theory of the hcp-fcc Phase Transition in Cobalt”. In: *Nature Scientific Reports* 7 (2017).

[28] Su Leen Wong et al. “A crystal plasticity model for twinning- and transformation-induced plasticity”. In: *Acta Materialia* 118 (2016), pp. 140 –151.

[29] X. Wu et al. “Strain-induced grain refinement of cobalt during surface mechanical attrition treatment”. In: *Acta Materialia* 53.3 (2005), pp. 681 –691.

[30] E. O. Hall. “The Deformation and Ageing of Mild Steel: III Discussion of Results”. In: *Proceedings of the Physical Society. Section B* 64.9 (1951), pp. 747–753.

[31] N. J. Petch. “The Cleavage Strength of Polycrystals”. In: *Journal of the Iron Steel Institute, London* 127 (1953), pp. 25–28.

[32] C.S. Pande and K.P. Cooper. “Nanomechanics of Hall–Petch relationship in nanocrystalline materials”. In: *Progress in Materials Science* 54.6 (2009), pp. 689 –706.

[33] K. Ishida and T. Nishizawa. “The Co-Cr (Cobalt-Chromium) system”. In: *Bulletin of Alloy Phase Diagrams* 11.4 (1990), pp. 357–370.

[34] K. J. Bhansali and A. E. Miller. “The Role of Stacking-Fault Energy on Galling and Wear Behavior”. In: *Wear* 75.2 (1982), pp. 241–252.

[35] D. L. Klarstrom. “Wrought cobalt- base superalloys”. In: *Journal of Materials Engineering and Performance* 2.4 (1993), pp. 523–530.

[36] D. Hull and D.J. Bacon. “Chapter 5 - Dislocations in Face-centered Cubic Metals”. In: *Introduction to Dislocations (Fifth Edition)*. Ed. by D. Hull and D.J. Bacon. Fifth Edition. Oxford: Butterworth-Heinemann, 2011, pp. 85 – 107.

[37] W. D. Callister. “Fundamentals of Materials Science and Engineering, Fifth Edition”. In: John Wiley & Sons, Inc., 2001, pp. 197–233.

[38] “Deformation induced FCC to HCP transformation in a Co–27Cr–5Mo–0.05C alloy”. In: *Materials Science and Engineering: A* 528.7 (2011), pp. 3037 –3043.

[39] Marko Knezevic et al. “Deformation behavior of the cobalt-based superalloy Haynes 25: Experimental characterization and crystal plasticity modeling”. In: *Acta Materialia* 63 (2014), pp. 162 –168.

[40] H. M. Tawancy, V. R. Ishwar, and B. E. Lewis. "On the fcc → hcp transformation in a cobalt-base superalloy (Haynes alloy No. 25)". In: *Journal of Materials Science Letters* 5.3 (1986), pp. 337–341.

[41] Ping Huang and H.F Lopez. "Strain induced ϵ-martensite in a Co–Cr–Mo alloy: grain size effects". In: *Materials Letters* 39.4 (1999), pp. 244 –248.

[42] Righdan Mohsen, Peng Zeng, and W Rainforth. "Correlation of the wear transition in CoCrMo alloys with the formation of a nanocrystalline surface layer and a proteinaceous surface film". In: *Wear* 376-377 (Apr. 2017), pp. 223–231.

[43] H. Kashani, A. Amadeh, and A. Ohadizadeh. "Effect of temperature on the strain induced $\gamma \rightarrow \epsilon$ phase transformation in Stellite 21 during wear test". In: *Materials Science and Engineering: A* 435–436 (2006), pp. 474 –477.

[44] E.P. Butler and M.G. Burke. "Chromium depletion and martensite formation at grain boundaries in sensitised austenitic stainless steel". In: *Acta Metallurgica* 34.3 (1986), pp. 557 –570.

[45] R. Büscher et al. "Subsurface microstructure of metal-on-metal hip joints and its relationship to wear particle generation". In: *Journal of Biomedical Materials Research Part B: Applied Biomaterials* 72B.1 (), pp. 206–214.

[46] *Stellite 6 Alloy: Technical Data*. 2008. URL: `http://stellite.co.uk/Portals/0/Stellite\%206\%20Final.pdf`.

[47] S. Kapoor et al. "Temperature-Dependence of Hardness and Wear Resistance of Stellite Alloys". In: *Engineering and Technology* 6.68 (2012), pp. 800–809.

[48] H. Yu et al. "Influence of Manufacturing Process and Alloying Element Content on the Tribomechanical Properties of Cobalt-Based Alloys". In: *Journal of Tribology-Transactions of the Asme* 131.1 (2009).

[49] R. Ahmed et al. "Influence of Re-HIPing on the structure-property relationships of cobalt-based alloys". In: *Tribology International* 57 (2013), pp. 8–21.

[50] M. A. Ashraf et al. "Finite Element Modeling of Sliding Wear in a Composite Alloy Using a Free-Mesh". In: *Journal of Tribology-Transactions of the Asme* 137.3 (2015).

[51] Rong Liu, Matthew X. Yao, and Xijia Wu. "Influence of Carbon Content in Cobalt-Based Superalloys on Mechanical and Wear Properties ". In: *Journal of Engineering Materials and Technology* 126.2 (Mar. 2004), pp. 204–212.

[52] Linchun Wang and D.Y. Li. “Effects of yttrium on microstructure, mechanical properties and high-temperature wear behavior of cast Stellite 6 alloy”. In: *Wear* 255.1 (2003), pp. 535 –544.

[53] J. C. Shin et al. “Effect of molybdenum on the microstructure and wear resistance of cobalt-base Stellite hardfacing alloys”. In: *Surface & Coatings Technology* 166.2-3 (2003), pp. 117–126.

[54] V.L. Ratia et al. “The effect of temperature on sliding wear of self-mated HIPed Stellite 6 in a simulated PWR water environment”. In: *Wear* 420-421 (2019), pp. 215 –225.

[55] E. P. Degarmo, J. T. Black, and R. A. Kohser. “Fundamentals of Casting”. In: Wiley, 2003. Chap. 13.

[56] A.D. Sarolkar and K.P. Kolhe. “A review of (GTAW) Gas Tungsten Arc Welding and its Parameters for Joining Aluminum Alloy”. In: *IJSART* 3 (8 2017), pp. 361 –368.

[57] R. Singh et al. “Laser cladding of Stellite 6 on stainless steel to enhance solid particle erosion and cavitation resistance”. In: *Surface & Coatings Technology* 251 (2014), pp. 87–97.

[58] A. Frenk and W. Kurz. “Microstructural Effects on the Sliding Wear-Resistance of a Cobalt-Based Alloy”. In: *Wear* 174.1-2 (1994), pp. 81–91.

[59] Mohammed Mohaideen Ferozhkhan et al. “Plasma Transferred Arc Welding of Stellite 6 Alloy on Stainless Steel for Wear Resistance”. In: *Procedia Technology* 25 (”2016”), pp. 1305 –1311.

[60] H. V. Atkinson and S. Davies. “Fundamental aspects of hot isostatic pressing: An overview”. In: *Metallurgical and Materials Transactions a-Physical Metallurgy and Materials Science* 31.12 (2000), pp. 2981–3000.

[61] M. A. Ashworth et al. “Microstructure and property relationships in hipped Stellite powders”. In: *Powder Metallurgy* 42.3 (1999), pp. 243–249.

[62] F. Rosalbino and G. Scavino. “Corrosion behaviour assessment of cast and HIPed Stellite 6 alloy in a chloride-containing environment”. In: *Electrochimica Acta* 111 (2013), pp. 656–662.

[63] W.H. Hocking et al. “Mechanisms of corrosion of stellite-6 in lithiated high temperature water”. In: *Corrosion Science* 25.7 (1985), pp. 531 –557.

[64] U. Malayoglu, A. Neville, and H. Lovelock. “Assessing the kinetics and mechanisms of corrosion of cast and HIPed Stellite 6 in aqueous saline environments”. In: *Corrosion Science* 47.8 (2005), pp. 1911–1931.

[65] H. So, C. T. Chen, and Y. A. Chen. “Wear behaviours of laser-clad stellite alloy 6”. In: *Wear* 192.1-2 (1996), pp. 78–84.

[66] E. Cabrol et al. “Plastic strain of cobalt-based hardfacings under friction loading”. In: *Wear* 330 (2015), pp. 354–363.

[67] J.F. Archard. “The temperature of rubbing surfaces”. In: *Wear* 2.6 (1959), pp. 438 –455.

[68] John Williams. “Engineering Tribology”. In: Cambridge University Press, 1994. Chap. 5.

[69] Ruby McCarron et al. “Sliding wear analysis of cobalt based alloys in nuclear reactor conditions”. In: *Wear* 376-377 (2017). 21st International Conference on Wear of Materials, pp. 1489 –1501.

[70] “The generation of mechanically mixed layers (MMLs) during sliding contact and the effects of lubricant thereon”. In: *Wear* 246.1 (2000), pp. 74 –90.

[71] Ian Inman et al. “Microscopy of glazed layers formed during high temperature sliding wear at 750 degrees C”. In: *Wear* 254 (Mar. 2003), pp. 461–467.

[72] T. F. J. Quinn. “Oxidational Wear”. In: *Wear* 18.5 (1971), p. 413.

[73] H. So. “The Mechanism of Oxidational Wear”. In: *Wear* 184.2 (1995), pp. 161–167.

[74] J. F. Archard and W. Hirst. “The Wear of Metals under Unlubricated Conditions”. In: *Proceedings of the Royal Society of London A: Mathematical, Physical and Engineering Sciences* 236.1206 (1956), pp. 397–410.

[75] N. S. McIntyre, D. Zetaruk, and E. V. Murphy. “X-Ray photoelectron spectroscopic study of the aqueous oxidation of stellite-6 alloy”. In: *Surface and Interface Analysis* 1.4 (1979), pp. 105–110.

[76] T. F. J. Quinn. “Review of Oxidational Wear .1. The Origins of Oxidational Wear”. In: *Tribology International* 16.5 (1983), pp. 257–271.

[77] T. F. J. Quinn. “Review of Oxidational Wear .2. Recent Developments and Future-Trends in Oxidational Wear Research”. In: *Tribology International* 16.6 (1983), pp. 305–315.

[78] F. H. Stott. “The role of oxidation in the wear of alloys”. In: *Tribology International* 31.1-3 (1998), pp. 61–71.

[79] M. Vardavoulias. “The role of hard second phases in the mild oxidational wear mechanism of high-speed steel-based materials”. In: *Wear* 173.1–2 (1994), pp. 105–114.

[80] Zhu Zhiyuan et al. “Wear Characteristic of Stellite 6 Alloy Hardfacing Layer by Plasma Arc Surfacing Processes”. In: *Scanning* (2017), p. 7.

[81] D.H.E. Persson, S. Jacobson, and S. Hogmark. “The influence of phase transformations and oxidation on the galling resistance and low friction behaviour of a laser processed Co-based alloy”. In: *Wear* 254.11 (2003), pp. 1134 –1140.

[82] D H. E. Persson, Staffan Jacobson, and Sture Hogmark. “Investigation of anti-galling and low friction properties of laser processed co-based materials”. In: *International Congress on Applications of Lasers & Electro-Optics* (Jan. 2001), pp. 685–693.

[83] Daniel H. E. Persson. “On the Mechanisms behind the Tribological Performance of Stellites”. Uppsala University. Thesis. 2005.

[84] Staffan Jacobson and Sture Hogmark. “Surface modifications in tribological contacts”. In: *Wear* 266.3 (2009), pp. 370 –378.

[85] D. H. Buckley and Robert L. Johnson. “Friction and Wear of Hexagonal Metals and Alloys as Related to Crystal Structure and Lattice Parameters in Vacuum”. In: *Tribology Transactions* 9.2 (1966), pp. 121–135.

[86] Marco Sebastiani et al. “Wear mechanisms and in-service surface modifications of a Stellite 6B Co–Cr alloy”. In: *Wear* s 290–291 (June 2012), 10–17.

[87] V. M. Desai et al. “Effect of Carbide Size on the Abrasion of Cobalt-Base Powder-Metallurgy Alloys”. In: *Wear* 94.1 (1984), pp. 89–101.

[88] J.H. Dautzenberg and J.H. Zaat. “Quantitative determination of deformation by sliding wear”. In: *Wear* 23.1 (1973), pp. 9–19.

[89] M J. Zehetbauer et al. “The Role of Hydrostatic Pressure in Severe Plastic Deformation”. In: Jan. 2005, pp. 433–446.

[90] B.J. Roylance and S. Raadnui. "The morphological attributes of wear particles — their role in identifying wear mechanisms". In: *Wear* 175.1 (1994), pp. 115 –121. ISSN: 0043-1648. DOI: https://doi.org/10.1016/0043-1648(94)90174-0. URL: http://www.sciencedirect.com/science/article/pii/0043164894901740.

[91] K. Hokkirigawa and K. Kato. "An experimental and theoretical investigation of ploughing, cutting and wedge formation during abrasive wear". In: *Tribology International* 21.1 (1988), pp. 51 –57.

[92] R. Ahmed et al. "Structure-property relationships in a CoCrMo alloy at micro and nano-scales". In: 80 (2014), pp. 98–114.

[93] WJ Wang et al. "Effect of laser quenching on wear and damage of heavy-haul wheel/rail materials". In: *Proceedings of the Institution of Mechanical Engineers, Part J: Journal of Engineering Tribology* 228.1 (2014), pp. 114–122.

[94] W.R. Tyfour, J.H. Beynon, and A. Kapoor. "Deterioration of rolling contact fatigue life of pearlitic rail steel due to dry-wet rolling-sliding line contact". In: *Wear* 197.1 (1996), pp. 255 –265.

[95] L. Ma et al. "Study on wear and rolling contact fatigue behaviors of wheel/rail materials under different slip ratio conditions". In: *Wear* 366-367 (2016). Contact Mechanics and Wear of Rail / Wheel Systems, CM2015, August 2015, pp. 13 –26.

[96] W. J. Wang et al. "Influence of Different Application of Lubricants on Wear andPre-existing Rolling Contact Fatigue Cracks of Rail Materials". In: *Tribology Letters* 65.58 (2017).

[97] N.K. Taylor and I. Armson. "Corrosion product release from stellites and stainless steel in high pressure, high temperature lithiated water". In: *Proceedings of the Water Chem.Nucl. React. Syst. 3 International Conference* (1983), pp. 141 –151.

[98] Vilma L. Ratia et al. "Comparison of the sliding wear behaviour of self-mated HIPed Stellite 3 and Stellite 6 in a simulated PWR water environment". In: *Wear* 426-427 (2019). 22nd International Conference on Wear of Materials, pp. 1222 –1232.

[99] D Landolt, S Mischler, and M Stemp. "Electrochemical methods in tribocorrosion: a critical appraisal". In: *Electrochimica Acta* 46.24 (2001), pp. 3913 –3929.

[100] A.I. Vakis et al. "Modeling and simulation in tribology across scales: An overview". In: *Tribology International* 125 (2018), pp. 169 –199.

[101] J. A. Greenwood, J. B. P. Williamson, and Frank Philip Bowden. "Contact of nominally flat surfaces". In: *Proceedings of the Royal Society of London. Series A. Mathematical and Physical Sciences* 295.1442 (1966), pp. 300–319.

[102] David J. Whitehouse, J. F. Archard, and David Tabor. "The properties of random surfaces of significance in their contact". In: *Proceedings of the Royal Society of London. A. Mathematical and Physical Sciences* 316.1524 (1970), pp. 97–121.

[103] B.N.J. Persson. "Contact mechanics for randomly rough surfaces". In: *Surface Science Reports* 61.4 (2006), 201–227.

[104] Robert Jackson and Jeffrey Streator. "A Multi-Scale Model for Contact Between Rough Surfaces". In: *Wear* 261 (Dec. 2006), pp. 1337–1347. DOI: 10.1016/j.wear.2006.03.015.

[105] Vladislav Yastrebov, Guillaume Anciaux, and Jean-François Molinari. "Contact between representative rough surfaces". In: *Physical review. E, Statistical, nonlinear, and soft matter physics* 86 (Sept. 2012), p. 035601. DOI: 10.1103/PhysRevE.86.035601.

[106] Martin Müser et al. "Meeting the Contact-Mechanics Challenge". In: 65 (Aug. 2017), p. 118.

[107] J. J. Kauzlarich and J. A. Williams. "Archard wear and component geometry". In: *Proceedings of the Institution of Mechanical Engineers Part J-Journal of Engineering Tribology* 215.J4 (2001), pp. 387–403.

[108] K. L. Johnson. *Contact Mechanics*. Cambridge Books Online. Cambridge University Press, 1985. ISBN: 9781139171731. URL: http://dx.doi.org/10.1017/CBO9781139171731.

[109] A. Leyland and A. Matthews. "On the significance of the H/E ratio in wear control: a nanocomposite coating approach to optimised tribological behaviour". In: *Wear* 246.1-2 (2000), pp. 1–11.

[110] P. Ludwik. "Elemente der Technologischen Mechanik". In: Springer, Berlin, 1909.

[111] E. Voce. “The relationship between stress and strain for homogeneous deformations”. In: *J Inst Metals* 74 (1948), pp. 537–562.

[112] C.O. Frederick and P.J. Armstrong. “A mathematical representation of the multiaxial Bauschinger effect”. In: *Materials at High Temperatures* 24.1 (2007), pp. 1–26.

[113] E. Melan. “Zur Plastizitat des raumlichen Kontinuums”. In: *Ing. Arch.* 9 (1938), 116–126.

[114] W.T. Koiter. “Progress in Solids Mechanics”. In: John Wiley & Sons, Inc., 1963. Chap. General theorems for elastic-plastic solids, 165–221.

[115] K L Johnson. “The Strength of Surfaces in Rolling Contact”. In: *Proceedings of the Institution of Mechanical Engineers, Part C: Mechanical Engineering Science* 203.3 (1989), pp. 151–163.

[116] K.L. Johnson. “Contact mechanics and the wear of metals”. In: *Wear* 190.2 (1995), pp. 162 –170. ISSN: 0043-1648. DOI: https://doi.org/10.1016/0043-1648(95)06665-9. URL: http://www.sciencedirect.com/science/article/pii/0043164895066659.

[117] K.L. Johnson and H.R. Shercliff. “Shakedown of 2-dimensional asperities in sliding contact”. In: *International Journal of Mechanical Sciences* 34.5 (1992), pp. 375 –394.

[118] Frederic Feyel. “A multilevel finite element method (FE2) to describe the response of highly non-linear structures using generalized continua”. In: *Computer Methods in Applied Mechanics and Engineering* 192 (July 2003), pp. 3233–3244.

[119] R. Hill. “Elastic properties of reinforced solids: Some theoretical principles”. In: *Journal of Mechanics Physics of Solids* 11 (1963), pp. 357–372.

[120] J. F. Archard. “Contact and Rubbing of Flat Surfaces”. In: *Journal of Applied Physics* 24.8 (1953), p. 981.

[121] P. J. Blau. “How common is the steady-state? The implications of wear transitions for materials selection and design”. In: *Wear* 332 (2015), pp. 1120–1128.

[122] J. A. Williams. “Wear modelling: analytical, computational and mapping: a continuum mechanics approach”. In: *Wear* 225 (1999), pp. 1–17.

[123] J. F. Molinari et al. “Finite-element modeling of dry sliding wear in metals”. In: *Engineering Computations* 18.3-4 (2001), pp. 592–609.

[124] Daniel Sutton. “Wear modelling of diamond-like carbon coatings against steel in deionised water”. University of Southampton. Thesis. 2014.

[125] A. Kapoor. “Wear by plastic ratchetting”. In: *Wear* 212.1 (1997), pp. 119 – 130.

[126] A.F. Bower and K.L. Johnson. “The influence of strain hardening on cumulative plastic deformation in rolling and sliding line contact”. In: *Journal of the Mechanics and Physics of Solids* 37.4 (1989), pp. 471 –493.

[127] A. Kapoor. “A RE-EVALUATION OF THE LIFE TO RUPTURE OF DUCTILE METALS BY CYCLIC PLASTIC STRAIN”. In: *Fatigue & Fracture of Engineering Materials & Structures* 17.2 (1994), pp. 201–219.

[128] A. Kapoor, J.A. Williams, and K.L. Johnson. “The steady state sliding of rough surfaces”. In: *Wear* 175.1 (1994), pp. 81 –92.

[129] “A model for the mild ratchetting wear of metals”. In: *Wear* 200.1 (1996), pp. 38 –44.

[130] A. Kapoor and Kenneth Langstreth Johnson. “Plastic ratchetting as a mechanism of metallic wear”. In: *Proceedings of the Royal Society of London. Series A: Mathematical and Physical Sciences* 445.1924 (1994), pp. 367–384.

[131] B J Roylance, JA Williams, and Rob Dwyer-Joyce. “Wear debris and associated wear phenomena: Fundamental research and practice”. In: *Proceedings of The Institution of Mechanical Engineers Part J-journal of Engineering Tribology* 214 (Jan. 2000), pp. 79–105.

[132] E.K. Francis. “Frictional Heating and Contact Temperatures”. In: CRC Press LLC, 2001. Chap. 6.

[133] P. Podra and S. Andersson. “Simulating sliding wear with finite element method”. In: *Tribology International* 32.2 (1999), pp. 71–81.

[134] S. Mukras et al. “Numerical integration schemes and parallel computation for wear prediction using finite element method”. In: *Wear* 266.7-8 (2009), pp. 822–831.

[135] V. Hegadekatte, N. Huber, and O. Kraft. “Finite element based simulation of dry sliding wear”. In: *Modelling and Simulation in Materials Science and Engineering* 13.1 (2005), pp. 57–75.

[136] S. Fouvry et al. “An energy description of wear mechanisms and its applications to oscillating sliding contacts”. In: *Wear* 255.1 (2003), pp. 287 –298.

[137] S. Fouvry, Ph. Kapsa, and L. Vincent. “An elastic–plastic shakedown analysis of fretting wear”. In: *Wear* 247.1 (2001), pp. 41 –54.

[138] A.R.S. Ponter, A.D. Hearle, and K.L. Johnson. “Application of the kinematical shakedown theorem to rolling and sliding point contacts”. In: *Journal of the Mechanics and Physics of Solids* 33.4 (1985), pp. 339 –362.

[139] F.J. Franklin, I. Widiyarta, and A. Kapoor. “Computer simulation of wear and rolling contact fatigue”. In: *Wear* 251.1 (2001). 13th International Conference on Wear of Materials, pp. 949 –955. ISSN: 0043-1648. DOI: https://doi.org/10.1016/S0043-1648(01)00732-3. URL: http://www.sciencedirect.com/science/article/pii/S0043164801007323.

[140] F. J. FRANKLIN, T. CHUNG, and A. KAPOOR. “Ratcheting and fatigue-led wear in rail–wheel contact”. In: *Fatigue & Fracture of Engineering Materials & Structures* 26.10 (2003), pp. 949–955.

[141] B. G. Mellor. “Understanding surface wear in engineering materials”. In: Woodhead Publishing, 2006. Chap. 1.

[142] British Standards Institution. *6892-1: Tensile testing*. 2016. URL: https://www.iso.org/standard/61856.html.

[143] British Standards Institution. *ISO 12106: Fatigue testing*. 2017. URL: https://www.iso.org/standard/64687.html.

[144] K. A. O’Donnell. “Effects of finite stylus width in surface contact profilometry”. In: *Appl. Opt.* 25 (1993), pp. 4922–4928.

[145] Andrej-Nikolai Spiess and Natalie Neumeyer. “An evaluation of R2 as an inadequate measure for nonlinear models in pharmacological and biochemical research: A Monte Carlo approach”. In: *BMC pharmacology* 10 (June 2010), p. 6. DOI: 10.1186/1471-2210-10-6.

[146] A. Frenk and J. D. Wagniere. “Laser Cladding with Cobalt-Based Hardfacing Alloys”. In: *Journal De Physique Iv* 1.C7 (1991), pp. 65–68.

[147] Y. Birol. “Thermal fatigue testing of Inconel 617 and Stellite 6 alloys as potential tooling materials for thixoforming of steels”. In: *Materials Science and Engineering a-Structural Materials Properties Microstructure and Processing* 527.7-8 (2010), pp. 1938–1945.

[148] W.R. Tyfour, J.H. Beynon, and A. Kapoor. “Deterioration of rolling contact fatigue life of pearlitic rail steel due to dry-wet rolling-sliding line contact”. In: *Wear* 197.1 (1996), pp. 255 –265.

[149] M. Ebrahimi et al. “Correlating the microstructure to mechanical properties and wear behavior of an accumulative back extruded Al-Mg2Si in-situ composite”. In: *Tribology International* 115 (2017), pp. 199 –211.

[150] Nam P. Suh. “The delamination theory of wear”. In: *Wear* 25.1 (1973), pp. 111 –124.

[151] W.R. Tyfour, J.H. Beynon, and A. Kapoor. “The steady state wear behaviour of pearlitic rail steel under dry rolling-sliding contact conditions”. In: *Wear* 180.1 (1995), pp. 79 –89.

[152] Etsuo Marui and Hiroki Endo. “Effect of reciprocating and unidirectional sliding motion on the friction and wear of copper on steel”. In: *Wear* 249.7 (2001), pp. 582 –591.

[153] S. Yu Tarasov et al. “Subsurface structural evolution and wear lip formation on copper single crystals under unlubricated sliding conditions”. In: *Wear* 410-411 (2018), pp. 210 –221.

[154] J. Lemaitre. “A Continuous Damage Mechanics Model for Ductile Fracture”. In: *Journal of Engineering Material Technology* 107.1 (1985), pp. 83–89.

[155] Righdan Mohsen, Peng Zeng, and W Rainforth. “Correlation of the wear transition in CoCrMo alloys with the formation of a nanocrystalline surface layer and a proteinaceous surface film”. In: 376-377 (Apr. 2017), pp. 223–231.

[156] “The effects of grain size and porosity on the elastic modulus of nanocrystalline materials”. In: *Nanostructured Materials* 11.3 (1999), pp. 361 –367. ISSN: 0965-9773.

[157] Tae-Yeon Kim, John E. Dolbow, and Eliot Fried. “Numerical study of the grain-size dependent Young’s modulus and Poisson’s ratio of bulk nanocrystalline materials”. In: *International Journal of Solids and Structures* 49.26 (2012), pp. 3942 –3952. ISSN: 0020-7683.

[158] “Effect of grain size on the elastic properties of nanocrystalline alpha-iron”. In: *Scripta Materialia* 48.5 (2003), pp. 611 –615.

[159] Chao Jiang. “First-principles study of structural, elastic, and electronic properties of chromium carbides”. In: *Applied Physics Letters* 92.4 (2008), p. 041909.

[160] Yefei Li et al. “The electronic, mechanical properties and theoretical hardness of chromium carbides by first-principles calculations”. In: *Journal of Alloys and Compounds* 509.17 (2011), pp. 5242 –5249.

[161] William H. Press et al. “Modelling of Data”. In: Cambridge University Press, 1992. Chap. 15.5.

[162] C.O. Frederick and P.J. Armstrong. “A mathematical representation of the multiaxial Bauschinger effect”. In: *Materials at High Temperatures* 24.1 (2007), pp. 1–26.

[163] J.L. Chaboche. “Time-independent constitutive theories for cyclic plasticity”. In: *International Journal of Plasticity* 2.2 (1986), pp. 149 –188.

[164] Vanesa Martinez Nogues. “Nano-scale tribocorrosion of CoCrMo biomedical alloys”. Southampton University. Thesis. 2016.

[165] Ken Hirota et al. “Simultaneous synthesis and consolidation of chromium carbides (Cr3C2, Cr7C3 and Cr23C6) by pulsed electric-current pressure sintering”. In: *Materials Science and Engineering: A* 399.1 (2005), pp. 154 –160.

[166] J. Esteve et al. “Cathodic chromium carbide coatings for molding die applications”. In: *Surface & Coatings Technology* 188-189 (2004), pp. 506–510.

[167] C. Subramanian. “Wear lip formation during dry sliding”. In: *Wear* 126.1 (1988), pp. 57 –67. ISSN: 0043-1648. DOI: https://doi.org/10.1016/0043-1648(88)90108-1. URL: http://www.sciencedirect.com/science/article/pii/0043164888901081.

[168] F. P. Bullen et al. “The effect of hydrostatic pressure on brittleness in chromium”. In: *The Philosophical Magazine: A Journal of Theoretical Experimental and Applied Physics* 9.101 (1963), pp. 803–815.

[169] M. Yajima, M. Ishii, and M. Kobayashi. “The effects of hydrostatic pressure on the ductility of metals and alloys”. In: *International Journal of Fracture* 6.2 (1970), pp. 139–150.

[170] A.V. Shutov and R. Kreißig. “Finite strain viscoplasticity with nonlinear kinematic hardening: Phenomenological modeling and time integration”. In: *Computer Methods in Applied Mechanics and Engineering* 197.21 (2008), pp. 2015 –2029.

[171] J. Arghavani, F. Auricchio, and R. Naghdabadi. “A finite strain kinematic hardening constitutive model based on Hencky strain: General framework, solution algorithm and application to shape memory alloys”. In: *International Journal of Plasticity* 27.6 (2011), pp. 940 –961.

[172] Ivaylo N. Vladimirov, Michael P. Pietryga, and Stefanie Reese. “On the modelling of non-linear kinematic hardening at finite strains with application to springback—Comparison of time integration algorithms”. In: *International Journal for Numerical Methods in Engineering* 75.1 (2008), pp. 1–28.

[173] A.Erman Tekkaya. “State-of-the-art of simulation of sheet metal forming”. In: *Journal of Materials Processing Technology* 103.1 (2000), pp. 14 –22.

[174] I.M. Widiyarta, F.J. Franklin, and A. Kapoor. “Modelling thermal effects in ratcheting-led wear and rolling contact fatigue”. In: *Wear* 265.9 (2008). Contact Mechanics and Wear of Rail/Wheel Systems - CM2006, pp. 1325 –1331.

[175] J Ding et al. “A multi-scale model for fretting wear with oxidation-debris effects”. In: *Proceedings of the Institution of Mechanical Engineers, Part J: Journal of Engineering Tribology* 223.7 (2009), pp. 1019–1031.

[176] S.A. Silling. “Reformulation of elasticity theory for discontinuities and long-range forces”. In: *Journal of the Mechanics and Physics of Solids* 48.1 (2000), pp. 175 –209.

[177] N. Moes and T. Belytschko. “Extended finite element method for cohesive crack growth”. In: *Engineering Fracture Mechanics* 69.7 (2002), pp. 813–833.

[178] M J Matthewson. “The effect of a thin compliant protective coating on Hertzian contact stresses”. In: 15.2 (1982), pp. 237–249.